Holistic Physics-of-Failure Approach to Wind Turbine Power Converter Reliability

SMITH, CHRISTOPHER,JOHN

Holistic Physics-of-Failure Approach to Wind Turbine Power Converter Reliability

Christopher John Smith

Thesis submitted towards the
degree of Doctor of Philosophy

Energy Group
School of Engineering and Computing Sciences
Durham University
United Kingdom

September 2017

Dedicated to

Katherine and our families

Holistic Physics-of-Failure Approach to Wind Turbine Power Converter Reliability

Christopher John Smith

Abstract

As the cost of wind energy becomes of increasing importance to the global surge of clean and green energy sources, the reliability-critical power converter is a target for vast improvements in availability through dedicated research. To this end, this thesis concentrates on providing a new holistic approach to converter reliability research to facilitate reliability increasing, cost reducing innovations unique to the wind industry. This holistic approach combines both computational and physical experimentation to provide a test bench for detailed reliability analysis of the converter power modules under the unique operating conditions of the wind turbine.

The computational models include a detailed permanent magnet synchronous generator wind turbine with a power loss and thermal model representing the machine side converter power module response to varying wind turbine conditions. The supporting experimental test rig consists of an inexpensive, precise and extremely fast temperature measurement approach using a PbSe photoconductive infra-red sensor unique in the wind turbine reliability literature. This is used to measure spot temperatures on a modified power module to determine the junction temperature swings experienced during current cycling.

A number of key conclusions have been made from this holistic approach.

- Physics-of-failure analysis (and indeed any wind turbine power converter based reliability analysis) requires realistic wind speed data as the temporal changes in wind speed have a significant impact on the thermal loading on the devices.
- The use of drive train modelling showed that the current throughput of the power converter is decoupled from the incoming wind speed due to drive train dynamics and control. Therefore, the power converter loading cannot be directly derived from the wind speed input without this modelling.
- The minimum wind speed data frequency required for sufficiently accurate temperature profiles was determined, and the use of SCADA data for physics-of-failure reliability studies was subsequently shown to be entirely inadequate.
- The experimental emulation of the power converter validated a number of the aspects of the simulation work including the increase in temperature with wind

speed and the detectability of temperature variations due to the current's fundamental frequency.

Most importantly, this holistic approach provides an ideal test bench for optimising power converter designs for wind turbine, or for other industries with stochastic loading, conditions whilst maintaining or exceeding present reliability levels to reduce wind turbine's cost of energy, and therefore, society.

Declaration

No part of this thesis has been submitted elsewhere for any other degree or qualification. The content of this thesis is all my own work unless referenced to the contrary in the text.

Acknowledgements

Whilst the authorship of this thesis may imply a solo effort, by no means has this work been an individual's endeavour. Rather, without the help, support and patience shown by people from all aspects of my life, this work would not have come to fruition. Whilst I will inevitably miss some people out due to the fallibility of memory, I have tried my best to mention as many contributors as possible.

Firstly, I want to thank my supervisors Dr Christopher Crabtree and Dr Peter Matthews for being the best supervisors any PhD student could ask for. Their constant enthusiasm and willingness to discuss the research up to several times a week has gone above and beyond the requirements of any supervisory team and has certainly minimised the pressures felt during such a long undertaking. They have frequently encouraged me to present at conferences, to publish, and to discuss my research with industrial partners which has highlighted their desire for me to feel like a part of the research team at Durham, and not just another student.

Secondly, I want to thank the technicians in the School of Engineering for their patience, skill and (somewhat) willingness to help produce the experimental rig constructed for this research. Without their expertise and time this research would simply not possible. I want to particularly thank Ian Hutchinson for willingly designing a number of PCBs and discussing improved designs on a regular basis, Ian Garrett for much of the electrical construction of the rig and making sure I was safe throughout the process, Alan Styles for his expertise in noise reduction turning disaster to success at the eleventh hour, and Colin Wintrip and the mechanical workshop team for regularly slotting my jobs into the smallest of timetable gaps to ensure that I was without equipment for as little time as possible. I also want to extend my gratitude to all the technicians for their friendship throughout the process, as in their own unique way they brought on a smile even on the most disastrous days. I must also apologise to Neil Clarey for continuously breaking his intricate soldering, and I am grateful to him for missing my head with those pliers.

Thirdly, I want to thank a number of the researchers at Durham. The THz electronics group are worth a special mention for the idea of using a photo-conductive sensor as a temperature measurement device and allowing me to borrow their optical equipment for much of the experimental work. Thanks are also due to Dr Donatella Zappalá for her support and time throughout much of the set-up and calibration of the photo-conductive sensor.

Finally, I want to thank my very close friends and family who have supported me throughout this PhD. I want to thank Katie for her love, support and humour throughout the ups and downs

over the past four years, and for creating a beautiful home to come to at the end of the day. I want to thank my mother for her continuing unconditional love since I was born and always supporting my decisions unwaveringly, and my late father for his support and encouragement of my ambitions. My gratitude also extends to Andrew and Lisa for being wonderful in-laws, for listening to me ramble about all things wind turbine related, and allowing me to escape to Surrey on a regular basis without hesitation. Finally, special mention goes to Danny, Rich, Rob and Tim who have been subjected to my unique taste in music, my inability to take losing well, and whose friendship and faith throughout this time have been invaluable.

"*He gives strength to the weary and increases the power of the weak. Even youths grow tired and weary, and young men stumble and fall; but those who hope in the LORD will renew their strength. They will soar on wings like eagles; they will run and not grow weary; they will walk and not grow faint.*"

Isaiah 40:29-31

Contents

List of Figures

List of Tables

Acronyms

3L-ANPC-VSC 3 level, active neutral point clamped, voltage source converter

3L-HB-VSC 3 level, halfbridge, voltage source converter

3L-NPC-VSC 3 level, neutral point clamped, voltage source converter

CAD computer aided design

CAPEX capital expenditure

CCP common collection point

CORPE Centre of Reliable Power Electronics

CPM constant power mode

CTE coefficients of thermal expansion

CTM constant torque mode

DCB direct copper bond

DDTRET Durham drive train reliability evaluation tool

DFIG doubly fed induction generator

DUT device under test

EENS expected energy not supplied

ELGC expected loss of generation capacity

ESR equivalent series resistance

EOL end of life

EOS electrical overstress

ESD electrostatic discharge

EU European Union

FEA finite element analysis

FEM finite element method

FRC fully rated converter

FRSCIG fully rated squirrel cage induction generator

FSSCIG	fixed speed squirrel cage induction generator
GSC	grid-side converter
IG	induction generator
IEC	International Electrotechnical Commission
IGBT	insulated gate bipolar transistor
IGCT	Integrated Gate-commuted Thyristors
IR	infra-red
LCoE	levelised cost of energy
LOLE	loss of load expectation
LOEE	loss of energy expectation
LUT	look-up table
LWK	LandwirtschaftKammer
MOS	metal-oxide semiconductor
MOSFET	metal-oxide semiconductor field-effect transistor
MPPF	metallized polypropylene film
MPPT	maximum power point tracking
MPT	maximum power tracking
MSC	machine-side converter
MTBF	mean time between failure
MTTF	mean time to failure
MTTR	mean time to repair
MV	medium voltage
O&M	operations and maintenance
OPEX	operational expenditure
PCB	printed circuit board
PI	proportional-integral
PMI	power module IGBT
PMSG	permanent magnet synchronous generator
PMSM	permanent magnet synchronous machine
PoF	physics of failure
PPI	press packed IGBT

PWM	pulse width modulation
RC	resistor-capacitor
SCADA	supervisory control and data acquisition
SCIG	squirrel cage induction generator
SG	synchronous generator
SnAg	tin-silver
SPWM	sine-wave pulse width modulation
WMEP	scientific measurement and evaluation programme
WRSG	wound rotor synchronous generator
WSD	WindStats Germany
WSDK	WindStats Denmark
WSTS	wind speed time series
ZOH	zero-order hold

Chapter 1

Introduction

The human race has always required energy for survival and societal improvement, whether that is for cooking, heating, transport or light. For millennia humanity has worked tirelessly to gather and process fuel to provide for their basic needs. Today, however, large proportions of the world have a relative abundance of comparatively cheap and convenient sources of energy at their disposal. Nowhere has this development been better illustrated than through the seemingly simple task of providing light. It requires approximately 60 hours of chopping wood to provide 1000 lumens of light from fire; a modern light bulb produces 1000 lumens in just 54 minutes [1].

Through innovation in energy production reducing the required effort for survival significantly, the human race has been able to technologically and socially expand at an unprecedented rate, particularly since the industrial revolution. This is highlighted by the increasing usage of energy since the 19th century (Figure 1.1). This development has led the world today to be unrecognisable to those living just a century ago.

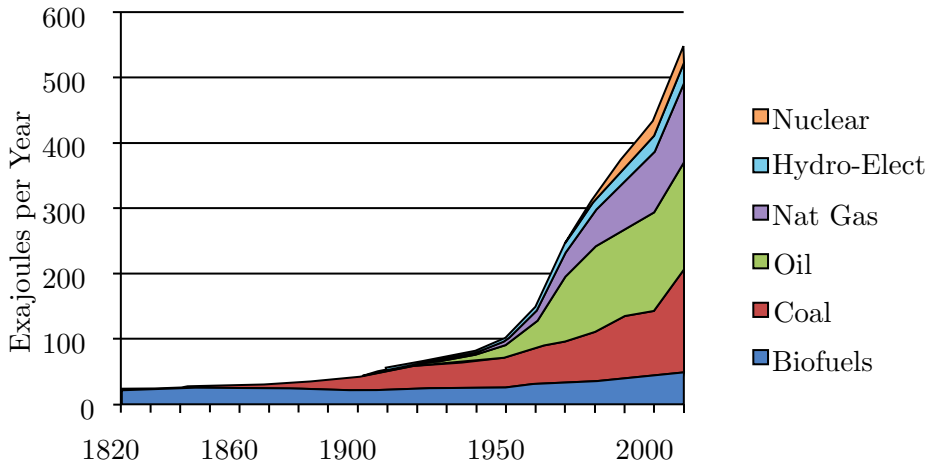

Figure 1.1: World energy consumption by source since 1820 [2].

Unfortunately, this thirst for energy has come at a price. This chapter explores these issues,

often labelled the energy trilemma (Section 1.1). The expansion of renewable energy resources to combat these issues is then examined (Section 1.2), with a particular focus on wind and its move from onshore to offshore sites (Section 1.3). The reliability challenges that these offshore wind farms face are discussed (Section 1.5). This thesis is focused on tackling these reliability issues, particularly in the power conversion stage. The outline for this wind turbine reliability based thesis is presented (Section 1.6), along with the original contributions achieved through this research (Section 1.7).

1.1 The Energy Trilemma

Many of the modern world's issues are inextricably linked with the need to solve the challenges of meeting high energy demands that such abundant energy usage presents. These challenges are often grouped into three main categories [3]: security of supply, sustainability, and cost. As these issues are rarely mutually exclusive and improvement in one area is often detrimental to another, they are labelled the energy trilemma (Figure 1.2).

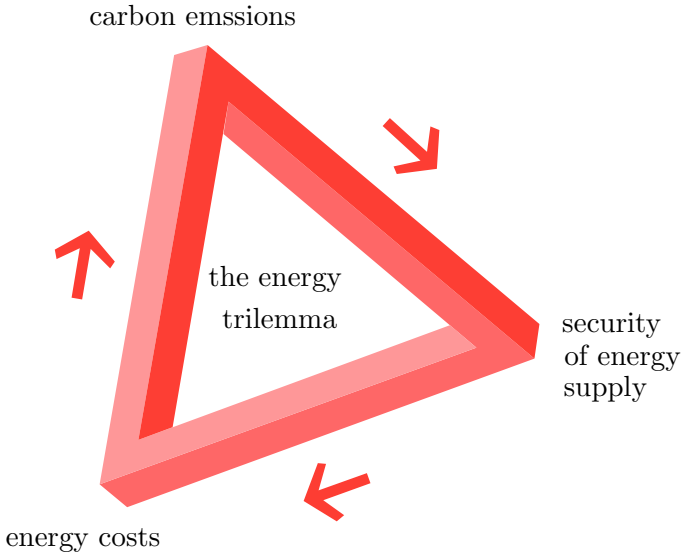

Figure 1.2: The energy trilemma, based on [3].

Security of supply is greatly impacted by geopolitics. As countries such as the UK become more reliant on fuel imports, political instability in Eastern Europe and the Middle East can affect fuel prices and even threaten the stability of economies far from the fuel source. A classic example is the ongoing political tensions between the Ukraine and Russia; the supply of gas between the two nations is frequently a source of economic and political tension [4]. Therefore, there is a push in many countries to provide locally sourced energy supplies, such

as the controversial pursuing of extracting natural gas through hydraulic fracturing in the USA and the UK [5].

The geopolitical issues are compounded by the fact that new generating technologies such as wind and solar are often intermittent, increasing the potential for demand outstripping supply, resulting in higher electricity costs. The potentially increasing costs of energy can have a profound impact on society as a whole. In many advanced economies, the cost of energy affects the operating costs of other industries, affecting their global competitiveness. The cost of energy also impacts the populations' quality of life as it has a direct impact on cost of services and goods, disposable income, and even whether people are able to meet their basic needs.

The third component in the trilemma is sustainability and the environmental cost, from a local to global scale. Locally, challenges include changing landscapes from fuel extraction, loss of animal habitat, and various forms of pollution, particularly with regards to fossil fuels. Human health can also be severely affected. Diesel cars have recently been attributed to dangerous levels of air pollution, and air pollution as a whole is attributed to 40 000 early deaths a year in the UK alone [6]. The economic and socio-political benefits of fuel extraction and consumption must therefore be balanced with the cost to the local environment and human health.

Globally there is arguably a greater challenge: climate change. There is ever-growing evidence that this phenomenon is anthropogenically driven [7], and is linked particularly with greenhouse gas levels, such as CO_2, in the atmosphere (Figure 1.3). This is attributed primarily to the burning of fossil fuels in energy production. Due to the potentially catastrophic impact on human civilisation, the United Nations has ratified the Paris Agreement to limit the increase in average global temperatures to well below 2°C compared to pre-industrial levels, with an aim of reaching only 1.5°C.

1.2 The Renewable Energy Uptake

Climate change and the need to reduce dependency on fossil fuels have become major forces for change in the European Union (EU). One of the key moves to implement this was the introduction of the EU community 20/20/20 by 2020 targets [9]. These targets require a 20% reduction in CO_2 emissions, a 20% increase in the uptake of renewable energy generation, and a 20% increase in energy efficiency compared to a 1990 aggregate EU benchmark. In the UK this has led to the setting of a legally binding target of an 80% reduction compared to 1990 levels of

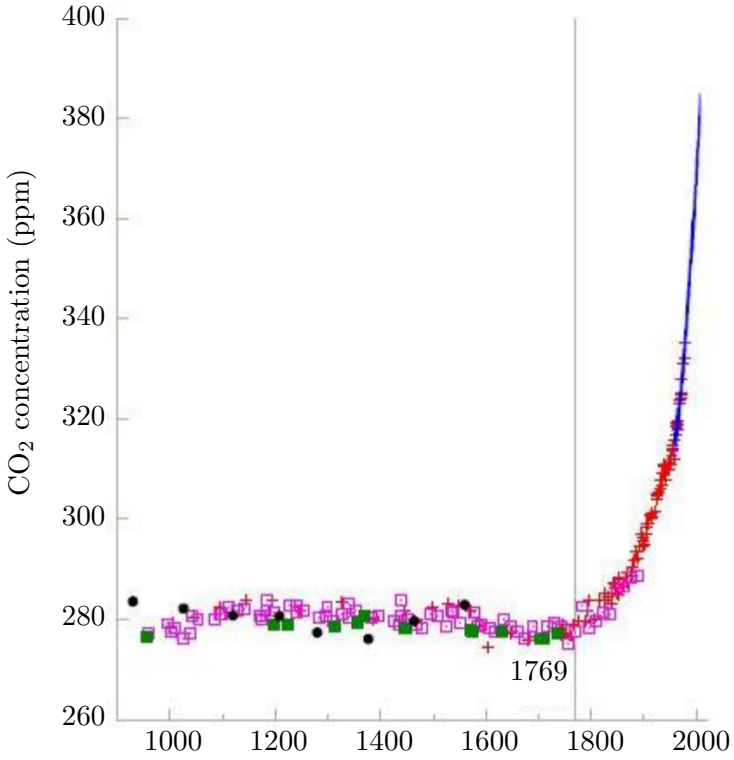

Figure 1.3: Atmospheric CO_2 concentration over the past millennium [8].

greenhouse gas emissions by 2050 [10].

To have a net reduction in greenhouse gas emissions, de-carbonisation of generation is essential. De-carbonisation has galvanised the uptake of renewable resources in generation mixes. Furthermore, renewable energy sources are typically locally situated, improving political security of supply. It is projected that the share of the UK's electricity generation from variable renewables could be as much as 64% by 2040 [11]. Wind energy in particular has seen huge growth to meet this demand and will be discussed in the next section (Section 1.3).

Renewable energy sources do not come without their disadvantages. Due to their low energy densities, renewable energy sources have been traditionally more expensive than conventional fossil fuel plants, though this is changing [12]. Renewable energy sources are also generally intermittent due to the inherent variability of the primary energy source, impacting the security of supply. Therefore any innovation in renewable energy that reduces the levelised cost of energy (LCoE) and reduces downtime to minimise the impact of intermittency will help address the issues highlighted in the energy trilemma.

1.3 Wind Energy

Onshore wind energy has become the most competitive renewable resource, alongside geothermal, in terms of the LCoE of various renewable energy resources (Figure 1.4). This low LCoE has seen wind generation become a major part of various countries' generation fleets; in certain parts of Germany the grid load is temporarily matched by the area's total wind generation [13]. Indeed, in the UK onshore wind has reduced its LCoE considerably as indicated by the UK strike price of around £80/MWh [14]. This means onshore wind is now competitive with the more expensive forms of conventional generation such as nuclear energy.

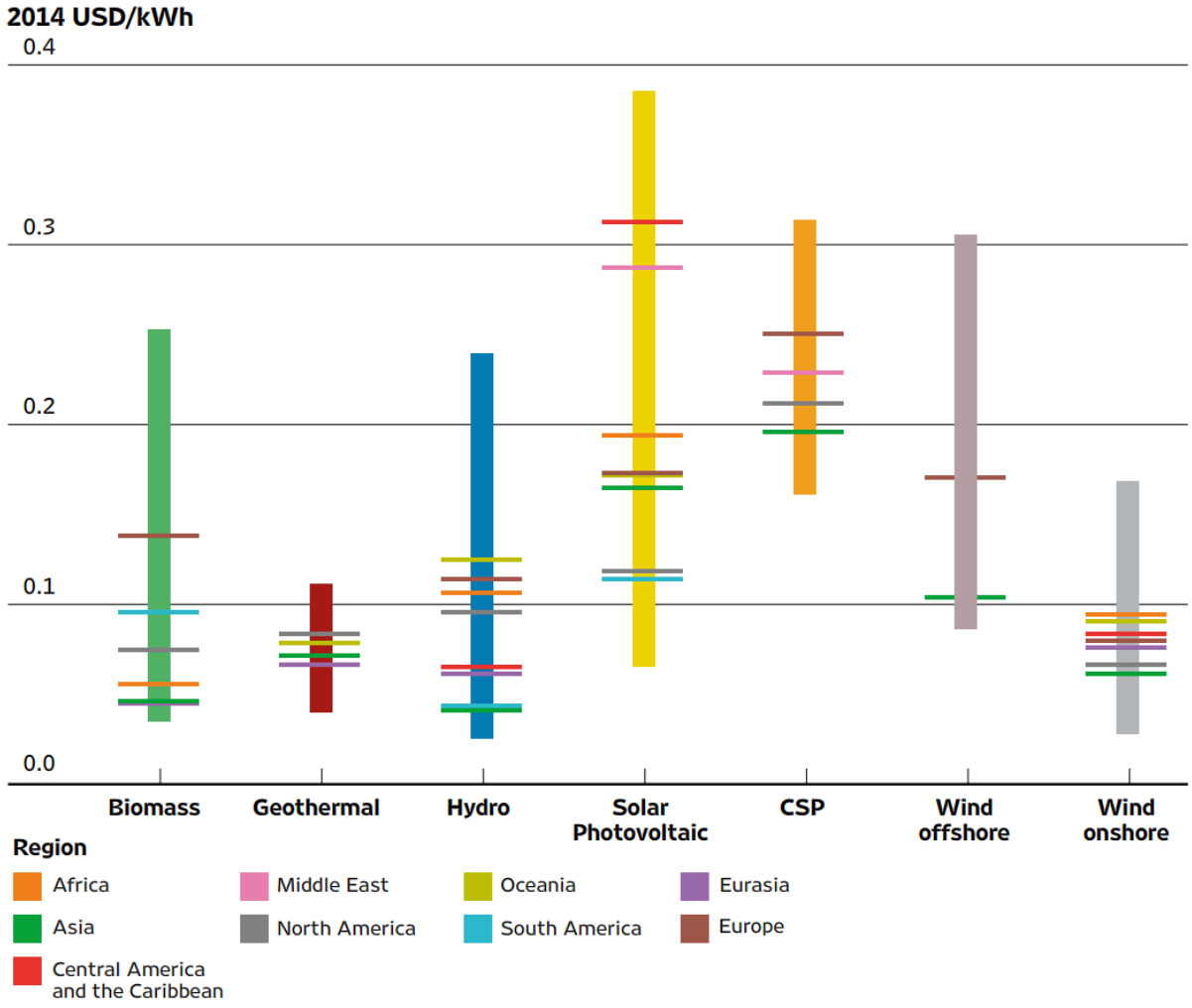

Figure 1.4: LCoE of various renewable energy sources [15].

In the early development of wind power, large wind farms were constructed onshore due to their relatively high accessibility [16]. As such, onshore wind turbines have benefited from high availability of 95-99% due to periodic maintenance and short repair times after a fault [17].

However, suitable sites for onshore wind farms are becoming rare [16] and the visual impact of onshore sites has brought increasing public opposition [18]. In contrast, offshore sites do not suffer from these drawbacks [19]. Offshore wind generation boasts higher and more consistent wind conditions due to reduced surface roughness, allowing for both greater energy yields and enabling large-scale renewable generation integration [20] and is now the focus of future development.

Due to these advantages and carbon reduction targets, a number of regions of the world are looking to develop offshore wind farms. Northern Europe has given much attention to offshore wind; it is believed that the EU wind market will consist of 40% offshore wind by 2030 [21]. The UK has set out to be a leader in offshore wind farm projects with its Round 3 offshore wind site selection; the Crown Estate is leasing out large areas of seabed for development by various companies and consortia [22]. This shift to offshore wind can also be seen in the installed capacity of commissioned sites for round 2 for both onshore and offshore wind [23]; 4.5GW for offshore and only 0.2GW for onshore wind.

Nevertheless, offshore wind farms are not without their own challenges, mainly brought about by the harsh marine environments and remote locations [24]. These challenges include more demanding installation processes [16], complex maintenance procedures due to wind and wave heights [19], and longer repair times from the need to wait for appropriate weather windows [25]. As such, offshore wind turbines have lower availability (90-95% compared to 97% for onshore [26]) due to their increased time to repair from poor accessibility [17, 25].

It has been reported that the increase in operational expenditure (OPEX) incurred by offshore wind farms could be as much as 30% higher compared to onshore [27] and capital expenditure (CAPEX) anywhere between 30-60% higher [18]. Without innovation to reduce the OPEX and CAPEX, offshore wind will struggle to be an economically sustainable source of renewable energy. As such, offshore wind still requires further technological development.

1.4 Power Converters in Wind Turbines

Offshore wind turbines have changed significantly since their first installation off the Danish coast in 1991 [28]. One of the key changes in wind turbine technology is the progressive move from fixed speed wind turbines, through partial speed control, to full speed control [29]. This ever increasing speed control allows for increased power production, reduced structural loads [30]

and reduced noise [31], but at the cost of increasing complexity. This change has also correlated with the introduction of direct drive concepts, which remove the gearbox from the nacelle. The removal of the gearbox reduces the need for heavy lifting equipment when conducting maintenance [32]. As such, wind turbine designers have options in terms of the level of speed control and the requirement of a gearbox.

To allow for this variable speed control, power converters have been introduced to the drive train. In a fixed speed machine, the rotational speed is determined by the grid frequency. The power converter allows the decoupling of the wind turbine from this grid frequency by providing an intermediate DC bus (Figure 1.5.a). With this decoupling, the machine-side frequency can be varied using the MSC. This is performed by switching a series of transistors to provide a square wave from the DC voltage. By varying the square wave duty cycle with time, a sinusoidal voltage can be emulated. This is generally performed by using some form of pulse width modulation (PWM) (Figure 1.5.b,c). The frequency can then be varied by varying the reference wave frequency. The voltage can also be varied by reducing the magnitude of the voltage reference by a multiplier known as the modulation index (m).

This introduction of power conversion has also changed the use of generators. There are four types of generators used for wind turbines: squirrel cage induction generator (SCIG), doubly fed induction generator (DFIG), wound rotor synchronous generator (WRSG) and permanent magnet synchronous generator (PMSG) . The drive train configurations possible for each generator type are outlined in Table 1.1. It is expected that fully rated converters with a synchronous generator (SG) or SCIG will come to dominate the offshore wind market in the near future [28].

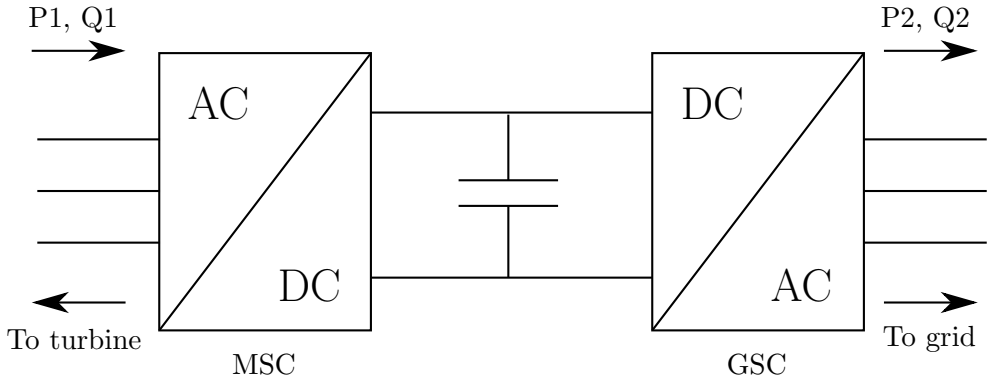

(a)

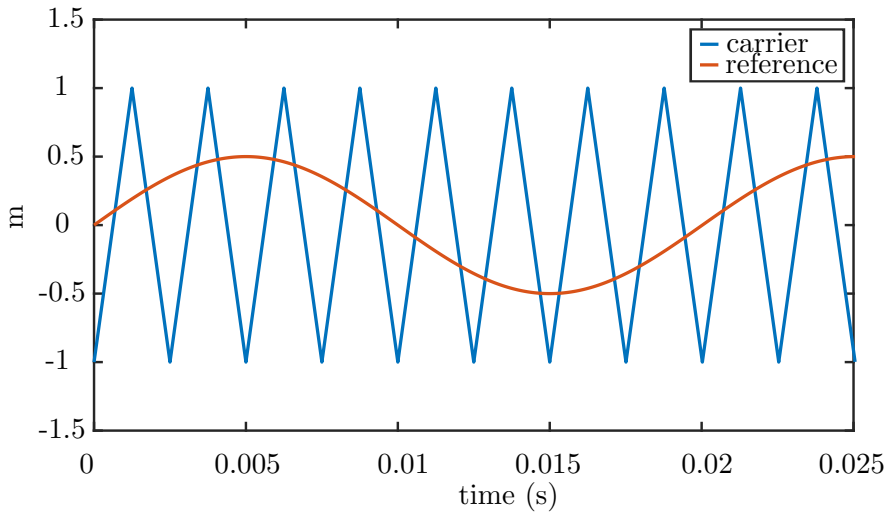

(b)

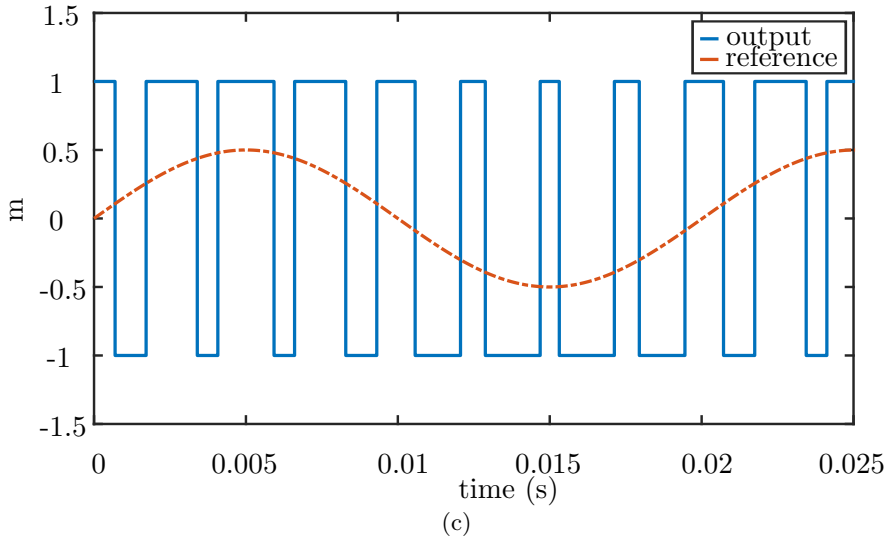

(c)

Figure 1.5: (a) Block diagram of typical converter with MSC and grid-side converter (GSC). (b) Control signals for one leg of the three phase converter. The reference wave is modulated using a carrier wave; in this case a triangular wave. (c) The resulting modulated signal as compared to the original reference wave. This also represents the shape of the output voltage pre-filtering.

Generator	Control	Conversion	Gearbox	Advantages	Disadvantages	Figure	Example
SCIG	Fixed	None	Yes	• Low cost • Robust • Torque damping	• Limited power extraction efficiency	Fig. 1.6.a	Viking 25
DFIG	Partial speed	Partial	Yes	• Partial MPPT • Smaller converter	• Poor ride-through • Costly maintenance • Complex gearbox	Fig. 1.6.b	Vestas V110-2.0 MW
SCIG	Full speed	Full	Yes	• Torque damping • Robust generator • MPPT	• Converter complexity and cost	Fig. 1.6.c	Siemens SWT-4.0-130
WRSG	Full speed	Full	Optional	• MPPT • Direct drive possible • Avoid magnets	• Converter complexity and cost • Lower efficiency	Fig. 1.6.c	Enercon E-141 EP4
PMSG	Full speed	Full	Optional	• MPPT • Direct drive possible • High efficiency	• Converter complexity and cost • High cost magnetic materials	Fig. 1.6.c	GE Haliade 150-6MW

Table 1.1: Wind turbine drive train topologies.

Power converters provide a number of services to the turbine. They allow for full reactive power control to satisfy grid requirements for both normal and fault operations [34]. This means more efficient PMSGs can be used instead of wound rotors [35], as the loss of reactive power control in the generator is compensated for by the converter. However, power converters have a number of disadvantages. Firstly, power converters that operate at lower power levels have a lower efficiency, and cause harmonic voltages on the grid due to PWM [30]. Secondly, the higher the rating of the converter, the higher the failure rate [35].

1.5 Reliability Critical Components in the Wind Turbine

The reduction in reliability when moving to offshore is a key driver for the increased operations and maintenance (O&M), and therefore OPEX costs [36]. This is due to the aforementioned increased repair times and cost to repair [37]. The impact of this can be demonstrated by any high failure rate, low mean time to repair (MTTR) components. Onshore, the high failure rate component's reliability can be considered to have no significant on production or costs as repairs and replacements can be scheduled relatively flexibly due to the ease of access. Therefore their impact on the LCoE is negligible. However, with reduced accessibility, a failure offshore is much more critical to the overall performance of the turbine [38]. For example, a small failure in bad weather could lead to a logistical delay of up to six months in extreme circumstances [19], leading to a loss of power generation and subsequent loss of revenue [39]. Therefore it is important to determine the components that have the highest failure rates for offshore wind farms and the conditions that drive these failures.

The literature has revealed that the wind turbine is the reliability critical system within the offshore wind farm infrastructure [40, 41]. In response, a number of studies looked at past reliability data of wind turbines to try and deduce which components are the source of failure.

Spinato et al. analysed the LandwirtschaftKammer (LWK) data using the failure rate and MTTR [42]. The electrical system, rotor and converter were found have the highest failure rates (0.32, 0.19 and 0.24 failures/per/year respectively), but the MTTR was significantly higher for the generators, electrical systems and gearboxes (175, 260 and 330 hours/failure respectively). Data from Swedish wind farms over the same period was also analysed [43]. It was found that the gearbox, electric system and control systems were the greatest source of total downtime with 6057, 4479 and 5724 hours/year respectively (256.7, 106.6 and 184.6 hours/failure respectively).

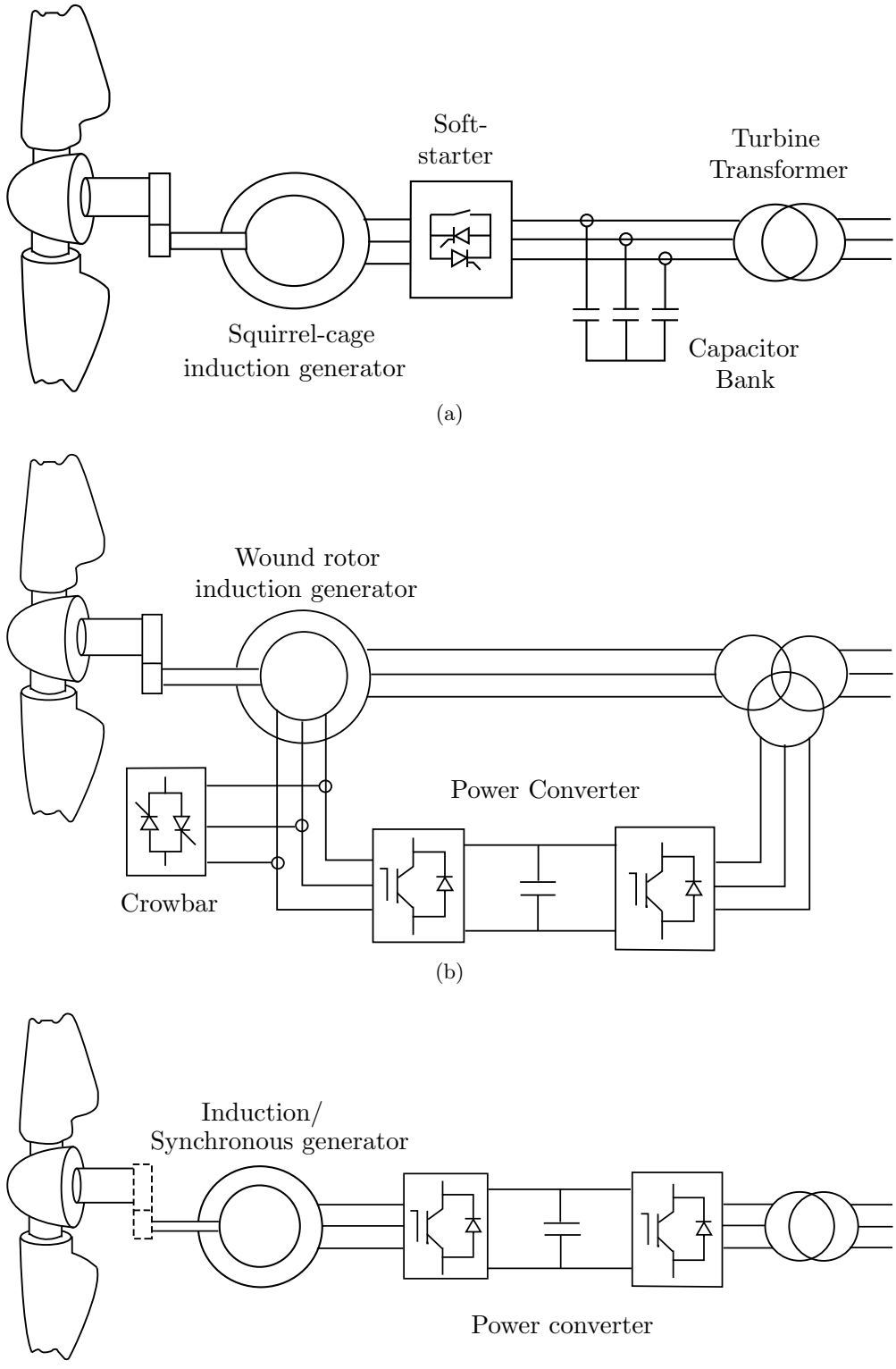

Figure 1.6: Typical drive train topologies: (a) fixed speed squirrel-cage induction generator, (b) partially rated converter doubly-fed induction generator, (c) fully rated converter induction/synchronous generator [33].

The analysis of the LWK data set and that of another dataset, from the scientific measurement and evaluation programme (WMEP), is represented in Figure 1.7 [44]. It is clear from this figure that the electrical system, including converter components, and control have the highest failure rates. Therefore, these sub-systems will impact the LCoE dramatically offshore.

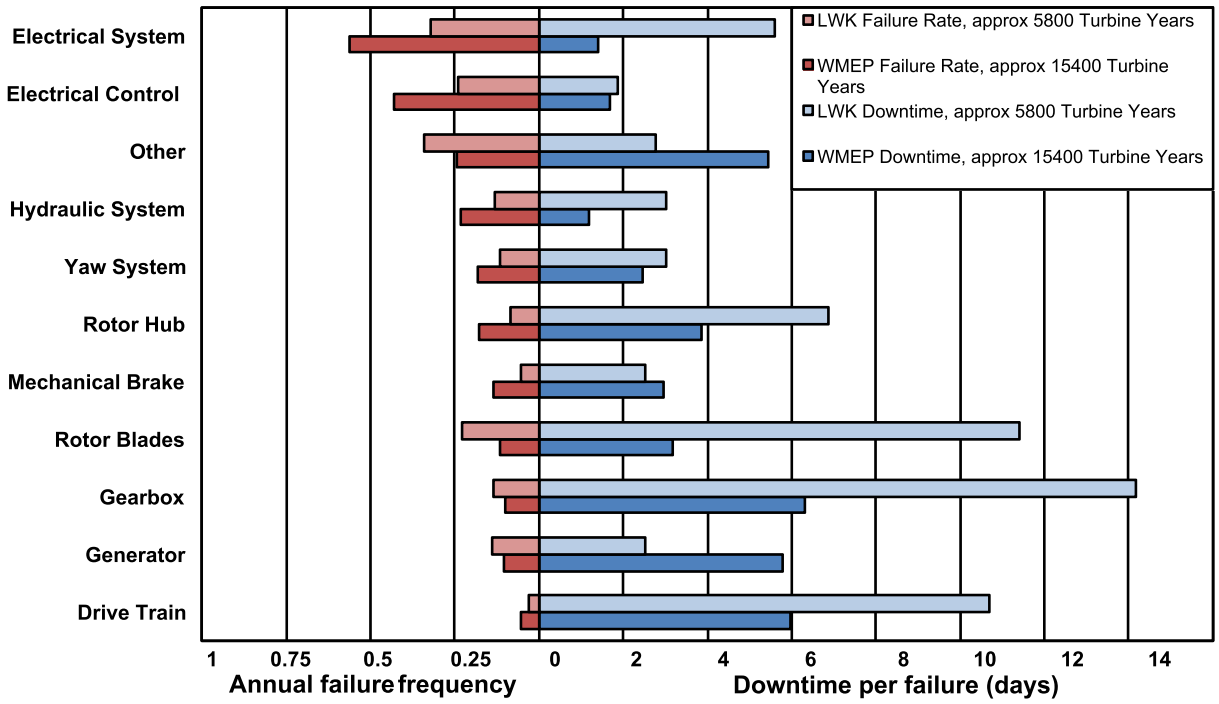

Figure 1.7: Annual failure rate and downtime per failure for various components of a wind turbine [44].

Therefore, it can be concluded that the electrical and control systems have the highest failure rates. However, it is worth noting that these analyses only consider data from pre-2006 onshore turbines with technologies that include fewer power electronic components than modern, multi-megawatt wind turbines. As such the results may actually underestimate the failure rates of electrical components for offshore wind.

In response, a few studies have analysed more recent data and focused on offshore wind turbines. Carroll et al. examined a large offshore wind turbine dataset with varying turbine technologies to determine the main causes of failure and concluded that the power converter had a typical failure rate of approximately 0.2 failures/turbine/year, which was much lower than the highest failure rate of >1 failures/turbine/year for the pitch system [45], and on par with the results in [43]. However, a more focused study on turbine type [46] found that the failure rate of fully rated converter (FRC) in PMSG turbines was 0.593 failures/turbine/year compared to the

0.106 failures/turbine/year for partially-rated converters in DFIG turbines. This would suggest that the system topology of the PMSG-FRC is causing higher failure rates.

Furthermore, Spring et al. examined large datasets of wind turbines and consulted expert knowledge to determine the impact of component failure on turbine downtime, compiling a top 30 list of turbine failure sources [36]. It was concluded that the power converter was the highest failure source to turbine downtime, with its failure modes occupying the top 15 positions. This is supported by data from RenewableUK and the German Wind Energy Institute showing that the converter accounts for 17-25% of all failures, and 3-8% of OPEX [47].

These studies demonstrate that the power converter has one of the highest failure rates in the wind turbine. Furthermore, the failure rate of power converters increases with increasing turbine power rating and wind speed due to higher stressing and higher number of components [48]; the current trend in offshore wind farms. Therefore the power converter, particularly in PMSG machines, is reliability critical and must be examined to maximise the impact of improving reliability on the LCoE of wind.

The challenge with wind turbine power converters and their reliability is variability of the loading profile. Unlike a number of other converter operating conditions such as industrial drives, the power converter loading is stochastic in nature due to the wind speed applied to the turbine rotor. This is highlighted by the variability of the electrical power output of a wind turbine over a 5 minute period (Figure 1.8). Furthermore, the wind speed input to the wind turbine is not directly correlated to the current throughput of the converter due to the complex drive train dynamics of the wind turbine (Figure 1.9). Therefore, this must be considered when developing approaches to reliability evaluation of power converters in wind turbines through a holistic approach.

1.6 Thesis Structure

Chapter 1 has introduced the importance of energy in human development, the current energy trilemma and the potential for wind energy to be part of the solution to these challenges. The growth of wind energy and the move towards offshore wind has also been outlined, alongside the challenges that face offshore wind with a focus on turbine reliability. Finally, the power converter has been identified as a reliability critical component that needs further investigation.

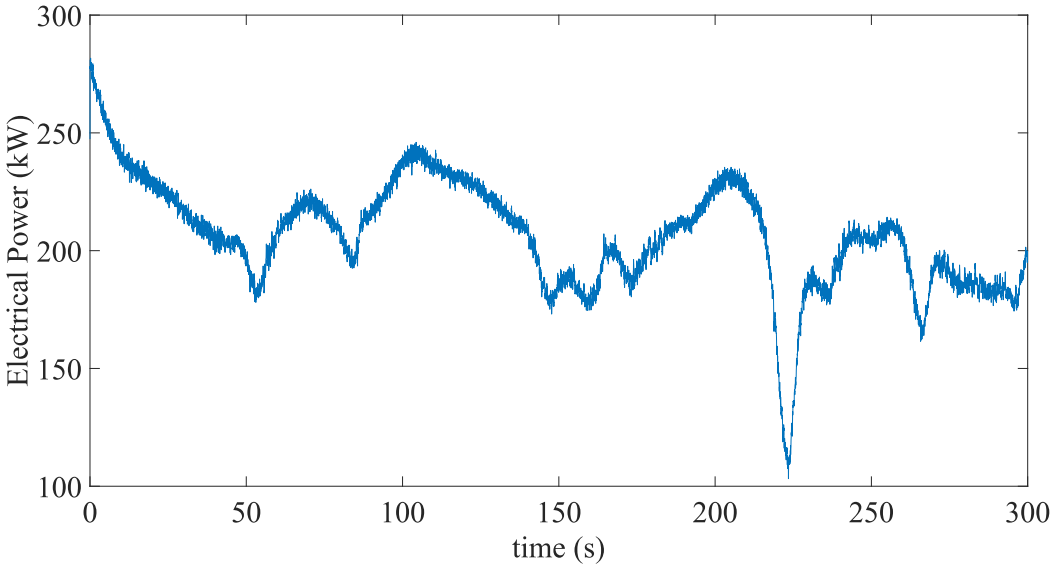

Figure 1.8: Electrical power output of wind turbine over 5 minutes (30Hz data) from the ReliaWind dataset.

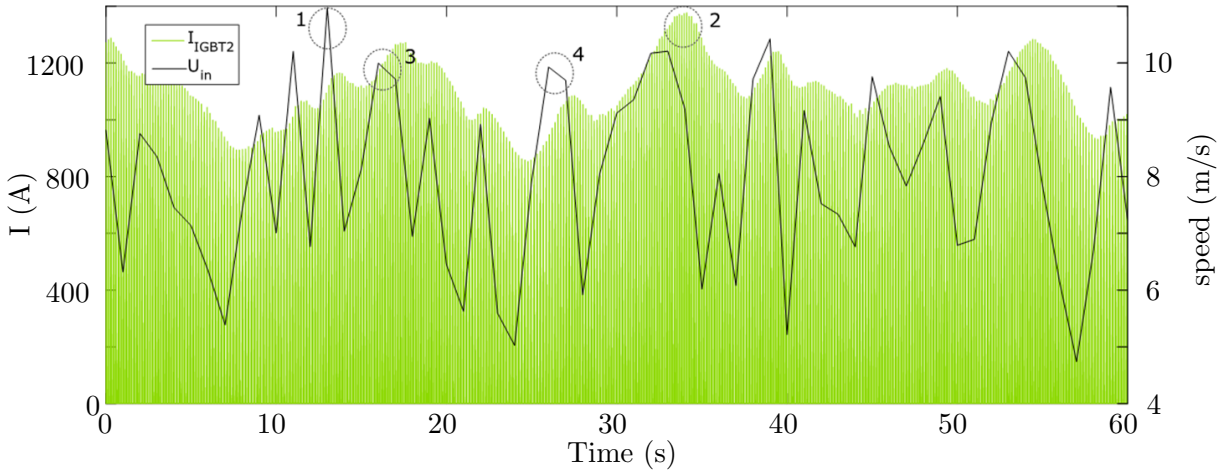

Figure 1.9: IGBT current response to turbulent wind speed (See Chapter 5 for further information).

Chapter 2 provides a detailed review of the current reliability literature on wind turbine power converters. Surveys of power converter failures in both conventional and wind turbine specific studies are outlined. The typical power converter failure modes and their root causes are discussed. The statistical and physical approaches for determining the impact of power converter failures on the LCoE and their limitations are reviewed. In response to these limitations, the research approach is outlined.

With the research approach outlined in Chapter 2, Chapter 3 details the first stage of the contribution to knowledge: the simulation of a wind turbine drive train model with a specific

features to support power converter reliability studies. This includes a description of the physical fundamentals behind each stage of the drive train. A thermal model of the power converter, and its integration with the drive train model, are also detailed.

An experimental rig is designed in Chapter 4 to produce practical temperature measurements for comparison with the theoretical results. A review of various methods for temperature measurement is carried out and a novel approach for measuring power converter temperatures is introduced. The chosen temperature measurement approach is then validated against a modified power converter test bench.

Chapter 5 applies the theoretical model to evaluate the theoretical impact of various wind speed conditions on the power converter thermal loading and the impact on the remaining life of the converter. This includes a comparison of converter critical components' thermal profiles, the temperature variations found over different time periods, and the thermal response at a range of wind speed frequencies and magnitudes. These results are then validated against a selection of results from the experimental rig.

Chapter 6 outlines the ongoing work inspired by this research project, including the experimental design for turbine emulation in the lab and work into power converter condition monitoring. Chapter 7 concludes the findings from the previous chapters.

Appendix A includes the publications produced during the research for this thesis. This includes a conference publication outlining work carried out in wind speed modelling for reliability analysis that was not included in the final version of this thesis.

1.7 Original Contributions

Chapter 2 will highlight the limitations of present approaches to reliability estimation of power converters. To summarise, present statistical approaches are over-reliant on out-of-date, onshore data, whilst physics-of-failure approaches are based on constant current operating conditions which are unrepresentative of the conditions under which a wind turbine power converter is operated. Furthermore, studies which use physics-of-failure approaches have little exploration into the impact of wind speed temporal fidelity on the thermal loading of the devices and are shown to overestimate the life span of these devices.

As such, there is a need for up-to-date power converter reliability data that has been produced under realistic operating conditions and an improved understanding of the affects of wind loading

on the life span of power converters. In response, this thesis focuses on facilitating the collection of this data. The research can be summarised in the following contributions:

- The first presentation of the impact of wind speed temporal fidelity on the theoretical thermal loading of power converter devices in the wind turbine. This includes a discussion of the attributes that cause the greatest damage to the power converter based on traditional modelling techniques. This discussion highlights that aspects such as temperature variations due to sinusoidal currents cannot be neglected.

- The application and validation of infra-red sensors for high frequency response temperature monitoring of power modules in a wind turbine to provide direct, non-contact temperature measurements of the power converter devices.

- The design of an experimental rig to allow for the emulation of wind turbine specific operating conditions on a power converter in a laboratory setting. This includes a novel approach of emulating the generator via an AC drive, supported by a model, and inductor to allow for easy machine parameter variation without the need to construct a new electrical machine for each new test.

The overall contribution of this thesis is a comprehensive approach to power converter reliability assessment under the unique operating conditions of a wind turbine. This allows for the development of improved, and verified, power converter reliability models, the construction of more robust converter experimental testing regimes, and provide opportunities for further research into novel monitoring approaches under a controlled, but realistic, environment.

Chapter 2

Approaches to Converter Reliability Analysis

In Chapter 1 the impact of overall power converter reliability on wind turbine operation was discussed. This chapter reviews the critical sub-components which determine power converter reliability (Section 2.1) and the root causes of these failures (Section 2.2) to ensure that the thesis concentrates on the reliability-critical components of the converter.

With the root causes of converter failure determined, wind turbine specific power converter reliability studies are critiqued. This includes how power converters are modelled in reliability simulations (Section 2.3) and the details of tests that have been carried out in the literature to diagnose root causes of failures in power converters (Section 2.4). The limitations of the existing research are discussed (Section 2.5), and are used to shape the subsequent research approach taken in this thesis (Section 2.6).

2.1 Surveys of Power Converter Failures

A starting point for surveying the power converter failures in wind turbines is the older turbine databases such as LWK and WMEP. Lyding et al. concentrated on the limited wind turbine converter failure data found in the WMEP database [49]. Lyding et al. found that over half of failures in the power converters could be attributed to semiconductor failure. This information is a useful starting point, but the results are of limited value due to the turbines found in the WMEP; the majority are onshore wind turbines with fixed speed wind turbines from 1989 to 2006 and therefore there are few power converter failures to sample from.

Surveys of power converter failures in other applications can be used to verify the findings of [49]. Wolfgang has gathered information on power converter failures of 200 products from 80 companies [50], and Yang et al. details the results of an industrial questionnaire handed out to various power converter industries, particularly device manufacturers, to discover which components the industry perceive to be the most fragile [51]. This data is qualitative and hence may not be accurate, but still provides relevant insight. The results of these studies are summarised in Figure 2.1.

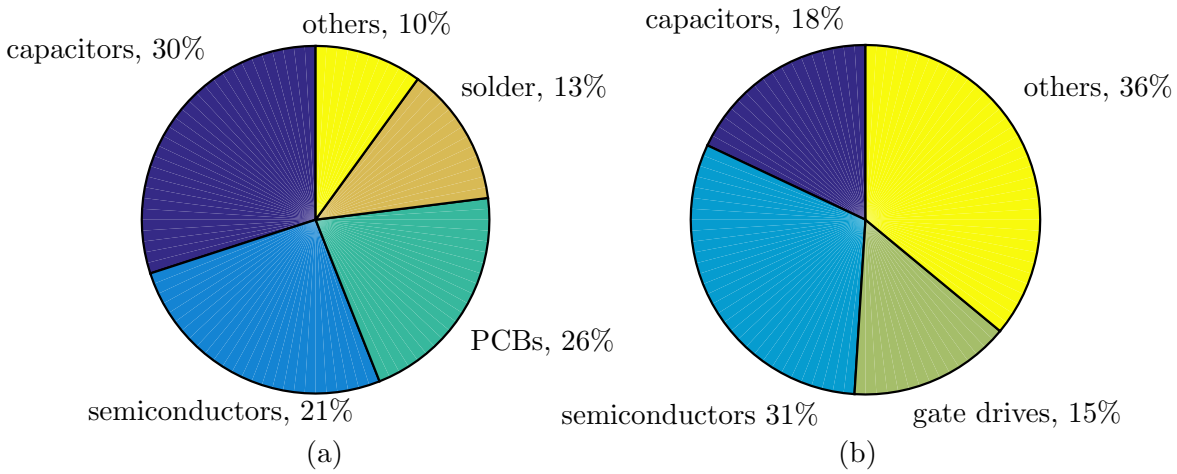

Figure 2.1: Results of surveys on failures within power converter devices: (a) [50], (b) [51].

The results of these two surveys agree that semiconductor devices and capacitors are two of the main sources of power converter failure. Therefore, there is a qualitative trend between the surveys that the semiconductor devices and capacitors are the main cause of failures in power converters in industry and, potentially, for wind turbines. However, the number of failures of semiconductors devices is less than 50%, which disagrees with the results in [49]. This is not to say that the findings of [49] are unfounded as, as discussed in Chapter 1, the high variability of wind turbine loading profiles may have a different impact on converter reliability when compared to converters operated in other industries.

2.2 Traditional Failure Mechanisms of Sub-components

Based on the findings in the previous section, the failure modes and root causes for failure of capacitors and semiconductors are detailed here.

2.2.1 Capacitors

The DC link capacitors used in power converters come in two forms: aluminium electrolytic and film type [17]. Electrolytic capacitors are characterised by their high capacitance, high voltage rating, high volumetric efficiency and low cost, but are deemed highly unreliable [52]. In contrast, the film capacitor is characterised by high reliability (except for rare catastrophic explosions), high lifetime, and the ability to withstand both large voltage and current surges [53], but come in low power densities [17]. The device also has self-healing, whereby separate segments in the capacitor passively disconnect themselves when the material melts, acting like a fuse. This ages the capacitor by reducing capacitance, but the device remains intact. This section details the failure modes of both capacitor types in detail.

Electrolytic capacitors have a large number of failure modes and root causes for these failures, summarised in Figure 2.2. A large number of these failures can be attributed to manufacturing defects and mishandling of the device, leading to very early failures. In contrast, the main wear out mechanism is electrolytic vaporisation, which is exasperated by ripple currents and thermal stressing through mishandling. This leads to capacitance drop and an increase in equivalent series resistance (ESR). Both of these are the main measures for ageing; a 20% drop in capacitance or doubling of ESR is an indicator of the end-of-life of the capacitor [52]. Therefore, manufacturing defects, mishandling, ripple currents, insulation breakdown due to high temperatures and voltages, and thermal stress are main causes of electrolytic capacitor failure.

For film capacitors (specifically metallized polypropylene film (MPPF) capacitors), the main failure modes are dielectric film breakdown, sprayed end detachment from capacitor roll, and excessive capacitive loss [53]. The dielectric film breakdown can be due to poor self-healing. In this case the capacitor enters either an open circuit or closed circuit. A closed circuit failure can have a much more serious consequence than an open circuit failure as, if the supply remains energised, heat dissipation can lead to more dielectric film melting, releasing explosive hydrocarbon gas. In extreme cases, the power converter can be blown from the machine [53]. Dielectric melting is also the cause for excessive capacitance loss. Sprayed end detachment is caused by environmental, thermal and mechanical stress leading to fatigue. This is particularly an issue when there are high current peaks in pulsed power applications. MPPF capacitors are therefore resistant to failure at the sacrifice of capacitance, suffer fatigue in high current pulsing

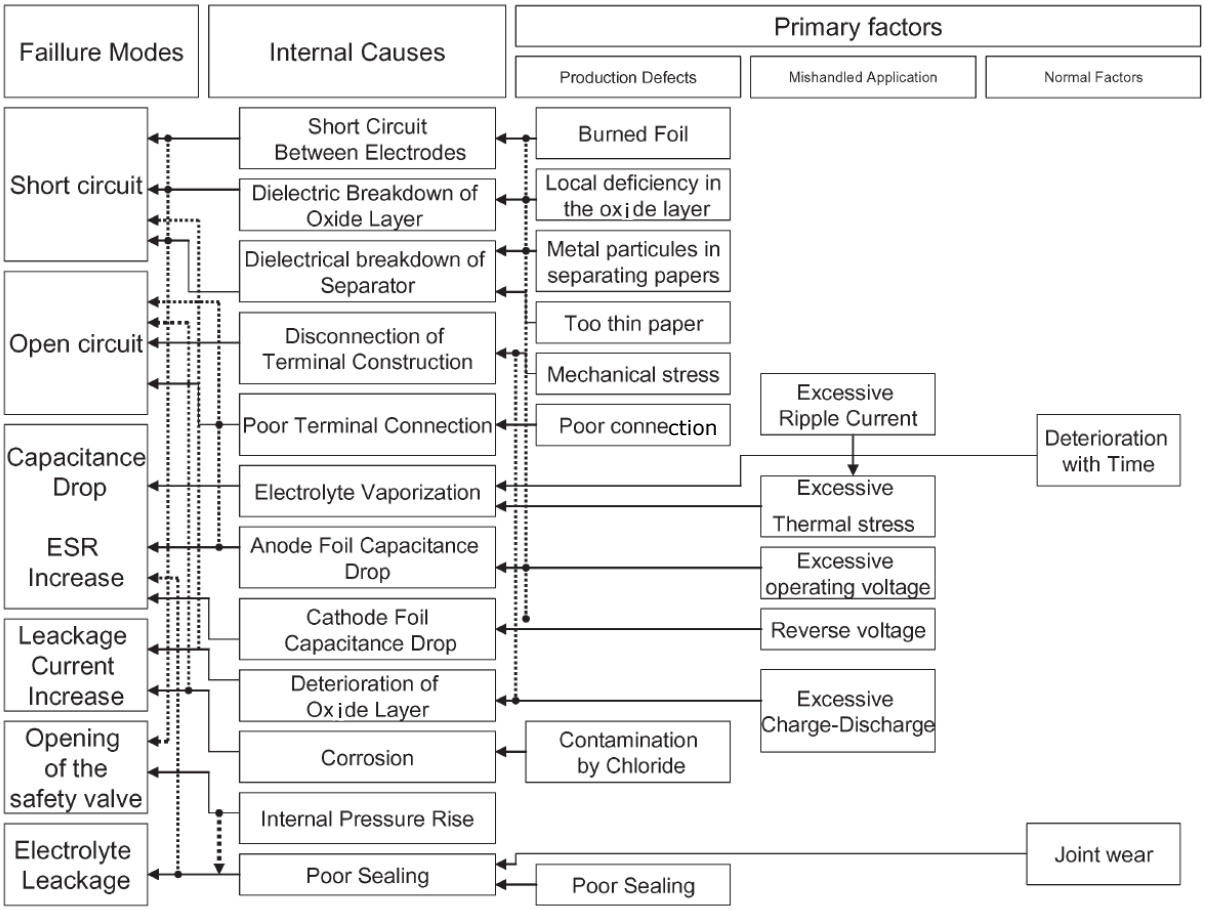

Figure 2.2: Failure modes and root causes for typical aluminium electrolytic capacitors. Figure presented as found in [52], original in [54].

applications, and can explode due to excessive dielectric melting [53].

In summary, electrolytic capacitors are inexpensive devices that boast high volumetric efficiency, high capacitance and high voltage rating, but suffer from a number of manufacturing defects and are susceptible to mishandling which can lead to early failure. In contrast, MPPF capacitors are highly resistant to current and voltage surges, but have low power densities. They are characterised by long lifetimes and high reliability, but can suffer from rare catastrophic explosions that can cause huge damage to surrounding components.

2.2.2 Semiconductor Devices

In power converters, there are a number of types of semiconductor that can be used for the switching devices. Generally, IGBTs are the most popular choice for the switching device [51] as they have high current density and are voltage driven [55]. Integrated Gate-commuted Thyristors (IGCT)s are another option for medium voltage (MV)-level wind power converters, and have

been used in oil and gas applications. However, their high cost has hindered their uptake and so they will not be explored further here. Instead the failure modes of IGBTs is the focus of this section.

The failure modes of semiconductor devices can be characterised into two groups, chip-related and package-related. An extensive summary of these failure modes has been outlined in [56]. Chip-related failures are those that destroy the device, whilst package-related failures affect the fatigue experienced by the device. As fatigue leads to eventual device failure, the two failure mode groups are not always mutually exclusive [56]. These are summarised in Table 2.1. In general, chip-related failures are activated by extremes in electrical operation, or thermal cycling.

Failure Mode	Root Cause
Over-heating	Electrical overstress (EOS) through over-voltage and over-current conditions, electrostatic discharge
Secondary breakdown	EOS, electrostatic discharge (ESD)
Gate shorting	ESD with excessive voltage applied to unprotected gate
Latch-up, triggering of parasitics (IGBT acting as thyristor)	Too high a dv/dt during turn off sequence
Ionic contamination leading to device performance shift and degradation	High temperature operation, most common for metal-oxide semiconductor (MOS) devices
Hot carrier injection leading to device performance shift and degradation	High temperature operation, most common for MOS devices
Metallization (rare for power devices)	Atomic migration from electromagnetism, inter-diffusion and manufacturing stress
Accelerated degradation	Thermal activation through temperatures
Single event induced burnout	Cosmic rays
Increased ESR from aluminium pad reconstruction	Repeated short circuits and high temperature

Table 2.1: Failure modes and root causes for chip-related failures in semiconductor devices [56].

Package-failure modes are often due to thermal-mechanical stress between different materials with varying coefficients of thermal expansion (CTE) under oscillating operating temperatures. This causes degradation over time. Humidity can also affect this packing degradation. Package-failure modes can also lead to accelerated chip failure and performance modification

from electrical stress triggered by package thermal expansion. Therefore, package-failure modes are attributed to gradual module degradation [56].

IGBTs come in two forms of packaging; power module IGBT (PMI), and press-pack IGBT (PPI). The PMI design is characterised by contacts between chip, di-electric and heat sink connected via solder, whilst the PPI design is held together by pressure only. The packaging type used in wind industry, and other applications, is dependent on a number of factors. PPIs have higher power density, better cooling and, according to industrial experience, are more reliable than PMIs. However, PMIs are preferred due to their low cost and easier mounting. These differences in packaging lead to difference failure modes for both of these devices, as summarised in Tables 2.2 and 2.3.

Failure Mode	Root Cause
Bond wire lift-off	Crack growth between silicon and aluminium from temperature cycling
Solder joint fatigue	Crack (void) growth between silicon die and copper substrate from temperature cycling
Bond wire heel cracking	Temperature cycling, especially when ultrasonic bonding process not optimised (rare in modern devices)

Table 2.2: Failure modes and root causes for package related failures in PMI devices [55, 56].

Failure Mode	Root Cause
Fretting damage	Temperature cycling
Spring fatigue	Power cycling leading to large number of compression expansion cycles
Spring stress relaxation	Temperature and time dependent

Table 2.3: Failure modes and root causes for package related failures in PPI devices [55].

2.2.3 Summary

In summary, temperature variations play a major role in package failure of IGBT devices, regardless if a PPI or PMI is used so it is likely that a detailed understanding of operational condition is required in order to fully understand component damage in any given application. Temperature causes accelerated fatigue of the device, and can exasperate chip-related failures. Chip-related failures, which are responsible for the final failure of the device, are driven both by temperature cycling and extremes in electrical operation. These root causes of power converter failure are in keeping with the conditions power converters are faced with in real applications [51].

2.3 Power Converters in Reliability Analysis

It is important to quantify the impact of power converter reliability on wind turbine and wind farm power production and operation. This can be carried out using modelling and simulation. In the literature, three methods of modelling power converter reliability have been used:

- The assignment of a statistical reliability index based on large dataset data.
- The modification of failure rates (λ_f) based on reliability handbooks. The following section outlines these three methods in greater detail.
- A physics of failure (PoF) approach which aims to link operation of the converter to its effect on remaining useful life.

2.3.1 Statistical Failure Rate Modelling

A common reliability modelling technique for a power converter is to assign a reliability value and distribution of failures to the power converter. The reliability value is generally assumed to be a constant λ_f, with an assumed exponential distribution of failures. This λ_f can be used either as an indicator of converter reliability or, more commonly, as part of a larger reliability analysis to produce other reliability indices. These may include the repair rate (μ_r) of components and/or sub-systems. λ_f and μ_r can be calculated using (2.1) and (2.2) respectively.

$$\lambda_f = \frac{1}{MTTF} \tag{2.1}$$

$$\mu_r = \frac{1}{MTTR} \tag{2.2}$$

Bala et al. used the λ_f of various sub-systems, including the power converter, in an expected energy not supplied (EENS) calculation for various wind farm converter-collection architectures where turbines are clustered together [28]. Examples of these architectures can be found in Figure 2.3. The reliability data used was mostly taken from [57]. This λ_f and μ_r data was not offshore wind farm data, but derived from existing onshore wind farm data and modified using industrial experience. In [28], the λ_f for power converters was independent of power rating or operational conditions, but μ_r was lower for architectures where the power converters were situated on the offshore platform rather than in the turbine nacelle. The results revealed that cluster architectures had lower EENS due to the reduced impact of feeder outages as each

turbine was independently connected to the offshore platform. However, the effects of varying operating conditions were neglected making this unsuitable for determining the end of life of components at a specific site with a specific wind speed profile.

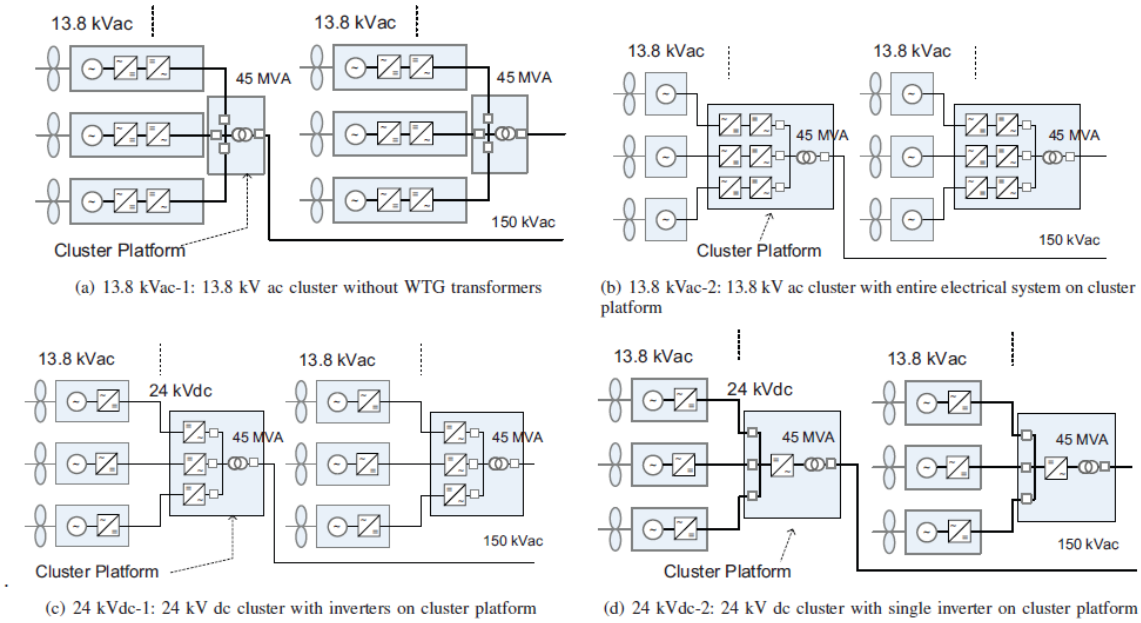

(a) 13.8 kVac-1: 13.8 kV ac cluster without WTG transformers

(b) 13.8 kVac-2: 13.8 kV ac cluster with entire electrical system on cluster platform

(c) 24 kVdc-1: 24 kV dc cluster with inverters on cluster platform

(d) 24 kVdc-2: 24 kV dc cluster with single inverter on cluster platform

Figure 2.3: Cluster designs considered in [28].

A similar approach to that found in [28] was used in [58] to calculate expected loss of generation capacity (ELGC) for various converter-collection architectures. These architectures included radial and ring feeder connections, and power converters situated at the turbines or at the common collection point (CCP) (Figure 2.4). This time λ_f was not used, but availability (A_v) and unavailability (U_a) values for wind turbine, power converter and feeder cable were stated. The reliability indices were varied to simulate the wear out of components over time in the second part of the study. However, no statement was made as to where this data was collected from. The study concluded that, rather intuitively, systems with a higher reliability level would be more reliable than a lower reliability level, with the difference between the reliability levels increasing with time. This was a simple analysis that aimed to produce results for wind farm layout decision making, but is not a suitable approach for capturing the effect of various operating and environmental conditions on power converter, and wind farm, reliability and therefore has limited practical application.

The use of statistical reliability indices has also been used in redundancy optimisation calculations. In [47], the value of including redundant power converters into the nacelle of the turbine

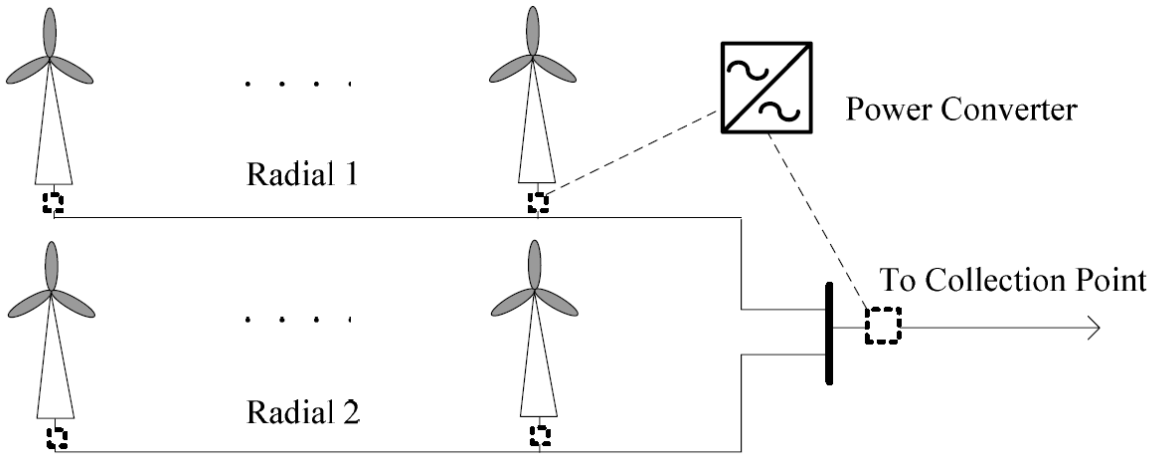

Figure 2.4: Example of possible positions for power converter analysed in [58].

was assessed using a minimum long run expected cost calculation. This included the cost of the added converters, and the costs associated with sending a maintenance team to repair the converter. In this analysis, the mean time to failure (MTTF) for the power converter was assigned as 200 days, and the lifetime of the power converters was assumed to be exponential. This data is reported to be from [59] which used onshore turbine data from the WMEP, LWK, WindStats Germany (WSD), WindStats Denmark (WSDK) and Felanalys databases. This information was used in an analytical equation for long-run average cost for a range of redundant converter numbers. In this case, it was found that using two actively redundant converters in the nacelle of the turbine had the lowest long run expected cost. The use of reliability indices such as MTTF in a redundancy optimisation is useful for macro-scale decision making, but cannot be used to predict the end of life of specific components under part.

Statistical reliability modelling can also include Monte-Carlo simulation. In [60], a sequential Monte-Carlo simulation was carried out to produce the loss of load expectation (LOLE) and the loss of energy expectation (LOEE) for various wind farm collection topologies and generator types with a simulated wind speed time series (WSTS) and grid load. Various components of a wind farm were modelled using Markov processes. For example, the power converter was modelled using a two state Markov process with the states indicating either full operation or failed. The original data, in the form MTTF and MTTR, came from a number of sources with the converter data from [42], itself derived from the onshore wind turbine failure data in LWK, WSD and WSDK. By using a Markov process sequential Monte-Carlo simulation, the model was able to evaluate the effect of variable environmental conditions and the reliability of

sub-systems on wind farm power output. However, the sub-systems, including the converter, still failed independently of sequential turbine operation and therefore cannot give an accurate prediction of converter failures.

The reliability of a power converter can be modelled as a number of smaller components to produce an overall converter λ_f. Arabian-Hoseynabadi et al. used Markov models for various sub-assemblies in the wind turbine drive train, including the power converter [61]. The λ_f and μ_r for the power converter were not given as a figure, but a Markov model was constructed for the converter using a number of λ_f and μ_r for various components in the power converter; namely the power electronics (inverter and rectifier), control unit and the DC-link. This was combined with other Markov models, such as for the generator, and used to calculate and compare the A_v of various electrical drive train sub-assembly topologies. The topologies included were DFIG, PMSG, fixed speed squirrel cage induction generator (FSSCIG) and a modified DFIG. The data used was from the operations and maintenance reports of the onshore Manjil wind farm, Iran, and from [62], which is derived from the LWK, WSD and WSDK onshore datasets. The results of the analysis indicated that the modified DFIG was deemed to have the highest A_v, as the converter could be disconnected and the generator operated as a FSSCIG. This construction of sub-systems from constituent parts allowed for the analysis of which components could cause the highest downtime, but again did not consider the effect of operating conditions on the failure modes of the sub-systems or their constituent parts.

Markov based models have also been used to assess the potential improvement in reliability of power converters through the introduction of redundancy. Redundancy can justify a modified λ_f value. Zhang et al. evaluated the reliability of modular converter topologies [63]. These converters were constructed from a number of identical power modules in parallel, with a minimum of 6 for the MSC and 6 for the grid-side converter (GSC) (termed a 6:6 power converter model). There was also a degraded performance state where the power flow was restricted, with the limit for total failure set at 5 operational modules on both sides. Reconfigurable modules (able to be used for either GSC or MSC) were introduced to add the desired redundancy. The redundant modules were actively redundant, and therefore the λ_f were reduced for modules that were sharing power flows between more than 6 modules on that side of the converter. λ_f and a reconfiguration rate were used in a Markov process to calculate the probability of being in a fully operational, degraded or failed state at a given point in time to assess the benefit of redundancy.

it was found that the larger number of modules, the higher the reliability performance. The (8:6 or 6:8) configuration performed the best, with a probability of at least degraded operation at 15 years of 0.949 compared to 0.713 for the 6:6 configuration. Note, the converters were not modelled as repairable and it was stated that the values are with reference to present standards in the electronic industry, but no reference was given. Therefore the results for a power converter in real operating conditions may vary significantly from these results. However the concept of reduced stress on components leading to a higher lifetime for a component has potential for more accurate reliability analysis, if the results can be validated. It cannot, however correct the failure rate for varying operating conditions.

This has been partly address by Li, where the λ_f has been modified to account for prevailing wind conditions, assuming higher power production and loading is going to place more stress on the system [64]. Li has developed a reliability model for DFIG drive trains, including the power converter. The work evaluated the U_a of various induction generator (IG) and DFIG configurations, including the effect of using a crowbar to operate the DFIG as an IG. Each sub-system in the turbine drive train was assigned a λ_f based on [43, 61, 65, 66]. The λ_f were modified with a correction factor that depended on current wind speed and whether there was a short circuit at a given point in time. However, there was no quantitative justification for the value of the correction factors chosen. The results showed that introducing reactive power support for an IG increased A_v from 0.9622 to 0.9624, and a DFIG has greatly increased availability (from 0.9230 to 0.9316) when a crowbar is allowed to operate when a converter fault occurs. Interestingly, the author states that the data used may not be suitable for real applications due to continual improvements to reliability, changing operational environments and variations in DFIGs between manufacturers. However, there is scope to use variable λ_f that are dependent on operating conditions to allow for a better link between harsher operating and more frequent failures.

Most modelling techniques in statistical reliability analysis are concerned with how to construct the reliability models for the various sub-systems in the offshore wind farm in order to evaluate the power output of the farm. Only two models was concerned with the impact of operation and environmental conditions on the reliability of the power converter. These two studies were limited as the correction factors determining the failure rates at various wind conditions were arbitrary and not linked to the actual loading of the devices. The impact of operation

and environment on the reliability of the power converter sub-system must be explored for more accurate reliability modelling.

All of these methods require large data sets of wind turbine power converter failures to ensure that the results are valid. In this literature the data was almost exclusively from onshore wind farm databases, with some onshore data modified to emulate offshore data based on industrial experience. Some papers made no statement of where their data came from. Therefore, no offshore wind farm data has been used in the reliability evaluation of these offshore wind farms. This makes the data unsuitable for modern, offshore wind farms. There is therefore scope to explore the impact of using data from a different application in reliability evaluation of wind farms.

2.3.2 Reliability Studies Using Handbook Data

Reliability analysis using handbook data uses similar concepts to those found in Section 2.3.1 as it considers the system reliability in terms of λ_f. However, the source of these λ_f is quite different. In Section 2.3.1 λ_f was derived from large datasets of wind turbine and/or power converter failures. In contrast, handbook methods derive the λ_f for a subsystem from a number of λ_f for components that make up the device. These are then modified with correction factors to reflect the operating conditions the device is experiencing. This produces a variable λ_f for use in a reliability analysis.

To demonstrate the use of handbook methods being used in wind turbine reliability analysis, two examples are given here. Zhu et al. carried out a reliability analysis of a fully rated converter using a modular converter structure (Figure 2.5) and the MIL-HDBK-217K and Bellcore SR-332 reliability handbook to produce λ_f for various components in the converter [67]. It was found that mean time between failure (MTBF) was 7325 hours. As this was less than a year, it was stated as pessimistic and therefore a 'field factor' of 2-3 should be used to correct this number. The λ_f were also used to determine which components could be considered the weakest. These were the gate drive board, the IGBT chip, the DC link capacitor and control board. A reliability model of the converter was then produced in ReliaSoft BlockSim using these λ_f, and μ_r to produce various converter reliability indices, including the A_v. The paper also outlined a number of experimental testing procedures, but had not carried out these tests at time of writing.

Xie et al. modified FIDES models to incorporate the operational profile of a wind turbine [48].

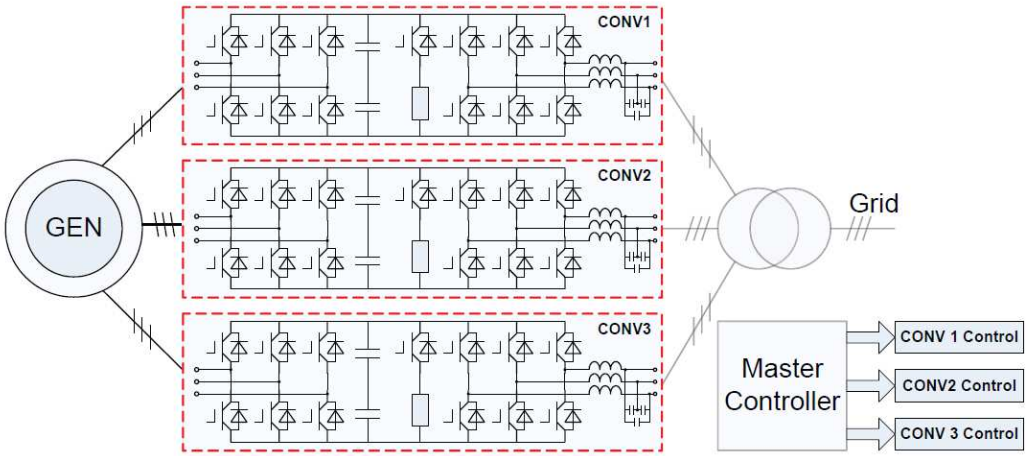

Figure 2.5: Modular power converter for analysis in [67].

Firstly, the wind speed was converted into a output power, frequency and voltage for the power converter. This was used in a power loss model for the IGBT, which considered conducting and switching losses as a function of power, frequency, current (function of power and voltage) and voltage. These power losses were converted into a T_j and board temperature (T_b) using (2.3) and (2.4).

$$T_j = T_a + R_{th,ha}P_{total} + R_{th,jh}P_{d/IGBT} \tag{2.3}$$

Where $R_{th,ha}$ is the thermal resistance between heat sink and ambient, P_{total} is the total converter power loss, $R_{th,jh}$ is the thermal resistance between junction and heat sink, and $P_{d/IGBT}$ is the power loss over the diode and IGBT.

$$T_b = T_a + R_{th,ha}P_{total} \tag{2.4}$$

With these temperatures and the λ_f equations from FIDES, the modified λ_f for all wind speed states of a wind turbine were calculated for a fully rated PMSG. This was used to calculate the λ_f for two wind farm sites based on their wind speed distribution. The work also investigated the effect of cut-in, rated and cut-out wind speeds, and seasonality on λ_f of the power converter. This model was modified in [68] to include wind turbulence intensity in the power loss calculation.

The use of handbook methods appears to provide a bridge between physical and statistical reliability models for power converters. However, the literature is often critical of, for example,

the military handbook [69–72] as the reliability results are often pessimistic and have no way of accounting for thermal cycling. The root cause of failures cannot be investigated either so cannot be used to perform reliability enhancement.

2.3.3 Physics of Failure Approach

Whilst the previous two sections detail reliability studies that use reliability data to produce reliability indices values, PoF focuses on producing the reliability data. PoF approaches aim to link the operation of the system, in this case the power converter, to the stress experienced by the system. The accumulated stress can then be attributed to the failure of the system. The basic principle is that the harder the system is operated, the higher the stresses that will be experienced, and the sooner the end of life (EOL) will be reached.

In general, the PoF models follow the same steps, but use different methods at each of these steps. The steps are as follows:

1. The operational profile of the wind turbine power converter needs to be decided upon and simulated.

2. The input operational profile is converted into power losses through an electrical loss model in the selected components.

3. The electrical losses are converted into temperature cycles in the component.

4. The temperature cycles are used to determine the life lost in the devices through life-cycling models.

This section looks at the various methods at each of these steps in turn. The methods used in each individual work are summarised at the end of the section.

Operational Profiles

Each of the PoF models require an input that drives the failure mechanisms. In most cases this was an operational profile driven by the wind speed experienced by the wind turbine. However the operational profile models used come in a number of forms, often driven by how the operational profile is used:

- **Fixed wind speed.** In order to capture the worst case scenario of wind turbine power loading, the rated wind speed was used as a constant input [73]. As the wind turbine is

commonly below this rated wind speed, this approach has little practical application.

- **Range of drive frequencies.** Instead of using a wind speed, the drive frequency was directly applied to the device to see which frequencies would cause the most damage [74]. To use this practically the wind speeds would need to be converted into drive frequencies.

- **Range of wind speeds.** To provide an understanding of the impact of varying wind speeds on converter loading, the wind speeds can be varied. This can between two wind speeds [75] or all wind speeds from cut-in to rated wind speed [76, 77]. This gives more information than the fixed wind speed, but cannot be used to analyse the impact of a real wind speed profile.

- **Wind speed distribution.** This is similar to using a range of wind speeds but with an added probability of that loading occurring. Normally in the form of a Weibull or Rayleigh distribution for the wind speed, these distributions have either been produced from generic wind speed profiles [78], a range of generic International Electrotechnical Commission (IEC) wind speed classes [79], or using a real wind speed profile [80]. Using a wind speed distribution is useful for quickly determining the expected lifetime of the power converter through summation of the products of the distribution and the corresponding cost of life at each wind speed. However, this approach assumes ageing effects are time independent.

- **Wind Speed Time Series (WSTS).** The use of WSTS can be either be generic [81] or real [82–88]. The time step of these WSTS varies between studies from seconds [81, 84, 88], 3-hourly [82, 83], or a combination of seconds, minutes and 3-hour data [85]. No statement of the time period was given in [86, 87]. Using the raw temporal wind speed data will give a better understanding of when a power converter will fail and can account for time dependency. However, the use of real wind speed data is limited to whether the wind speed at a given site has been recorded and the length of the dataset.

The above operational profile data types range in complexity, with the complexity linked to the required outcomes of the study. Therefore it is worth considering what the purpose of study is before deciding upon which operational profile is suitable. However, the use of WSTS has the potential to produce the most accurate results as it can capture the impact of moving

between wind condition extremes in the estimated end-of-life of the device, whilst the other approaches assume that the damage accumulated at a given wind speed is independent of wind speed history. Unfortunately, there is currently no consensus on the most appropriate wind speed data time step to use for this type of analysis.

Electrical Loss Models

To convert the operational profiles into temperature rises in the power converter components, the operational profile input must be transformed into a power throughput and loss in the component.

Electrical loss models have the same general layout; the loading of the power converter is calculated using a simulated generator and power converter under a particular control strategy to provide the converter loading profile. The loading profile is then converted into a total power loss profile for the power electronic module, ready for the calculation of thermal cycling.

The chosen generators in almost all cases are DFIG [74, 75, 78, 80, 84, 86] and PMSG [73, 76, 77, 79, 82, 83, 85, 88], or a comparison of the two [87]. There is only one exception where the generator type is neglected as only the grid-side converter is analysed [81]. Both the PMSG and DFIG are popular modern wind turbine generator topologies, with the DFIG analysed in these cases due to the unique rotor loading and subsequent electrical characteristics.

The turbine control algorithms required differ between the two generator types, but the control aims remain similar. In most cases the turbine is operated in maximum power tracking (MPT) mode [75–78, 80, 82, 83, 86–88], with grid code requirements also included [79]. There are some exceptions. Musallam et al. also includes a constant power mode (CPM) and constant torque mode (CTM) [84]. Ma et al. does not include a complex drive train model, but uses the turbine power curve to produce the power generated from a wind speed, and directly applies this power to the converter for long-term loading, with a 20 second inertia time constant for medium-term loading [85]. Arifujjaman et al. only considers rated power operation for a PMSG and directly applies this to the power converter [73].

The electrical loss models used in the literature considered similar semiconductor losses. These were conduction losses and switching losses of the IGBT and conduction and reverse recovery losses of the diode devices. These losses are calculated as functions of input parameters, with the functions differing depending on the IGBT used (Semikron [75], Infineon [82] or ABB [79]). However, in general, the input parameters considered are consistent and include current

throughput, device voltage drop, driving frequency, switching frequency, and rated switching energy loss. The losses are summed to produce the electrical losses of the device given the current loading conditions.

In most cases a drive train topology is chosen alongside a control strategy. The drive train is simulated to convert the operational profile into the electrical signals experienced by the power converter components. These electrical signals are used to calculate losses experienced by the IGBTs and diodes, with the conduction, switching and reverse recovery diode losses calculated in most instances. However, the choice and extent of the drive train model will greatly impact the calculated electrical losses.

Thermal Models

With electrical losses calculated, the temperature changes inside the device can be simulated by applying a thermal model. In all cases the aim of the thermal models was to estimate junction temperature (T_j) and ΔT_j as these variables are used in life cycle estimations. The thermal models come in three categories: thermal equivalent circuits, thermal diffusion equations and finite element analysis (FEA). The details of each of these methods are given below.

1. **Thermal Equivalent Circuits.** This is by far the most popular thermal modelling used in the literature. These circuits represent the thermal paths in a component as a number of resistor-capacitor (RC) connections, with the resistance representing a constant thermal parameter and the capacitor representing a thermal cycling parameter. These circuits come in two forms, Foster and Cauer networks (Figure 2.6), and can be combined to produce hybrid networks. Cauer networks have nodes that represent real physical thermal points in a component, but are more complex to solve than Foster networks. Foster networks are mathematical representations of the component and the internal nodes have no physical meaning. Power sources are used to represent power inputs which, in this case, are the electrical losses of the component. Voltage sources are used to represent constant temperature sources.

   In the literature these networks are used to convert the electrical losses into various temperatures in the devices, with the most important being T_j. These models have a wide range of networks used with varying complexity depending on how much of the device is modelled and how it is modelled:

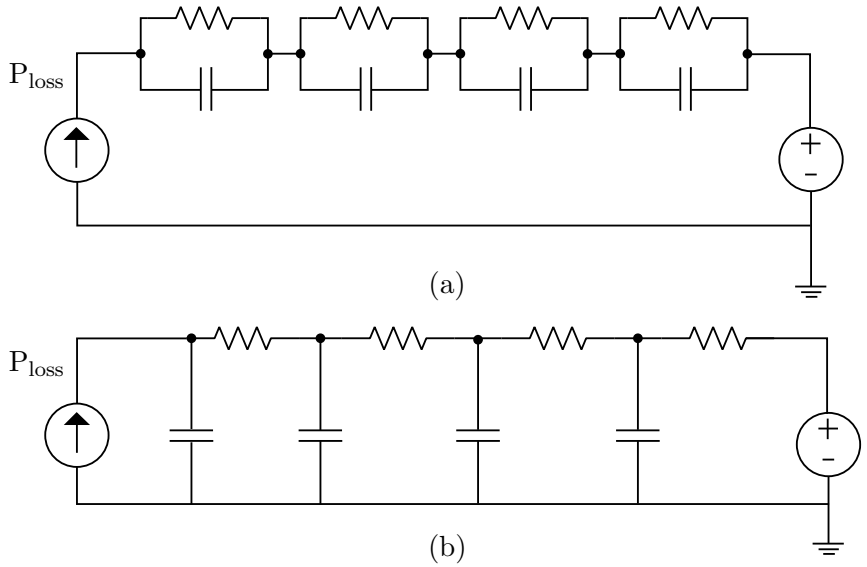

Figure 2.6: Thermal equivalent circuits in (a) Foster and (b) Cauer network from [75].

- Arifujjaman et al. used a single equivalent resistance between ambient temperature and junction temperature [73].
- Kostandyan et al. used a multi-layer Foster network for IGBT and diode with T_j, ambient temperature (T_a), heat sink temperature (T_h) and T_c included [82, 83]. The network was converted into a Cauer network to estimate the parameters outside the case.
- Senturk et al. used combined Foster networks for the IGBT-diode pair, including cooling plate, that were simplified into two dependent Foster networks for ease of calculation [81].
- The thermal model used in [81] was developed further in [89], where the scale was reduced from component level to chip level thermal models. For this, a physical Cauer model was used. As the PPI thermal impedance is related to clamping pressure, the thermal impedance at different clamping pressures was calculated.
- Fuchs et al. used a multi-branch foster network attached to a liquid cooling system to produce T_j for all diodes and IGBTs simultaneously [80]. The T_j against wind speed results were used in [86, 87].
- Lei et al. used a 4th order Cauer network, which modelled temperatures throughout the IGBT module [75]. This network was converted from a Foster network containing manufacturer's data.

- Isidori et al. used a Foster network for an IGCT module, including the case to heat-sink thermal impedance [77].
- A modified Foster RC network was used in [76]. The modifications added simple thermal grease and heat sink RC models, and an ambient temperature model.
- Wei et al. used a Foster network that included thermal impedances for junction to case, case to heat sink, and heat sink to ambient conditions [78]. The chips were assumed independent so no thermal coupling between chips was modelled.
- Ma et al. used two different thermal models depending on the time constants considered [85]. The T_j and T_c were calculated for the loss profile using the thermal equivalent model used in [88] and [82] but with C_{th} neglected as the temperatures were only considered at 3-hourly intervals. For the medium time-scale, the thermal model was modified as the C_{th} could no longer be neglected, and it was deemed that existing Cauer and Foster networks were limited. Therefore, the thermal model in [90] was used, which has one thermal path to estimate the T_j from T_c and another to estimate the T_c and T_h. This was also used by [79].

Whilst most of the literature have varying degrees of complexity to their thermal equivalent circuit model, they are all based on either a Foster or Cauer network, with the Cauer networks physically related to the internal structure of the device. The overall applicability of each network is determined by the number of thermal steps included e.g. inclusion of the heat sink parameters.

2. **Thermal Diffusion Equations.** This method, whilst common in a number of other applications, has only been implemented in [84] for wind turbine power converters. T_j of the IGBT module was estimated by solving the thermal diffusion equation for the module, with the simplified version given in (2.5) for a given region. Using a Laplace transform, a transfer function was used to represent the thermal paths in the module with the electrical losses and ambient temperatures acting as heat sources. The transfer function parameters were determined using experiments to calculate the observable average temperatures through electrical measurement (validated using an IR camera), and FEA in Flowtherm to simulate the hidden temperature points, with curve fitting to extract model parameters. The results were verified with an IGBT under test [91].

$$D(\frac{\delta^2 T}{\delta x^2} + \frac{\delta^2 T}{\delta y^2} + \frac{\delta^2 T}{\delta z^2}) = \frac{\delta T}{\delta t} \tag{2.5}$$

Where D is the diffusion coefficient.

3. **FEA.** FEA was used by [74] for a Mitsubishi IGBT. Flomerics "Flotherm" FEM-program was used to simulate the convection, thermal conduction, radiation and air flow effects on a detailed device computer aided design (CAD) model when the input frequency was varied. This detailed model gave the time dependent T_j needed.

The choice of thermal model appears to be based on the availability of data. The thermal equivalent circuits are generally used when available manufacturing data includes Foster network RC parameters. Modifications are then made to improve the accuracy of the networks, which often involves converting to a Cauer network. If this data was not available, or if detailed analysis of the device in question was required, the thermal diffusion equations and FEA were used. However, these methods still require data, either from manufacturers or experimental work.

Life Cycle Models

The final step is to estimate the remaining life of the components based on the T_j profiles produced by the thermal equivalent models. T_j was used as it was assumed that the main failure mechanisms are driven primarily by temperature cycling (Section 2.2.2). The main methods used for life estimation are detailed here.

- **Fatigue due to cycling of plastic strain.** This method relates the cycling of plastic strain of a material to the number of cycles until the component fails. This is a popular method used in fatigue analysis and has been adapted for use in power electronic devices.

  Typically a failure mode must be chosen to provide the material parameters required in the analysis. A typical failure mode is the cracking of the solder joining the baseplate and ceramic inside the IGBT chip [82].

  In [82] the plastic strain applied to this solder based on the ΔT_j was defined by (2.6) [92], which was derived from the results of a FEA in [93].

$$\Delta \mathcal{E}_p = A(\Delta T)^B(\alpha_{Cu} - \alpha_{Si})e^{(-\frac{Q}{RT_m})} \tag{2.6}$$

$\Delta\mathcal{E}_p$ is the plastic strain, α_{Cu} , α_{Si} are CTE of copper and silicon, ΔT is the temperature range, T_m is the mean temperature, and A, B, Q and R are constants derived using FEA [93].

This plastic strain was converted into a number of cycles until failure per plastic strain magnitude using the Coffin-Manson model (2.7). In [82] the failure mode was set as a 20% reduction of total interconnection area of solder due to solder cracking between baseplate and ceramic in the chip. This equation has been parametrised for tin-silver (SnAg) solder in [94], based on an experimental data point for three temperatures where the solder was cycled at that temperature until failure.

$$N_L(\Delta\varepsilon_p) = \frac{L}{a(\Delta\varepsilon_p)^b} \tag{2.7}$$

$N_L(\Delta\varepsilon_p)$ is the number of cycles to end of life for a given plastic strain as calculated by the Coffin-Manson model, L is the solder interconnect length, and a and b are constants related to the SnAg solder.

Deterministic EOL was calculated using the above equations and the Palmgren-Miner rule (2.8).

$$D(t) = \sum_{alli \subset t} \frac{n_i(\Delta T_i, T_{m,i})}{N_i(\Delta T_i, T_{m,i})} \tag{2.8}$$

$D(t)$ is the deterministic damage failure criteria calculated by the Palmgren-Miner rule, n is the number of cycles at that operating temperature profile that have been experienced, and N is the number of cycles to failure at that operating temperature profile.

The EOL is reached when $D(t)$ equals 1. The T_j operating profile was converted into these temperature cycles using a rain-flow counting algorithm.

A model for aluminium bonding wires was also used alongside the solder failure model in [84] (2.9), parametrised using curve fitting of four cycles-to-failure versus temperature cycling data points for aluminium bonding wires [95].

$$N_f = (1.4 \times 10^{11})\Delta T^{-3.597} \tag{2.9}$$

N_f is the number of cycles to failure, and the constants found in [95].

Whilst this approach is based on well established engineering fatigue principles, it has yet to be validated for power converters. Furthermore, to provide an accurate result for the whole power module every possible failure mode has to be modelled. This would produce a very complex and computational expensive simulation making it impractical for end-of-life predictions of components.

- **Exponential relationship between T_j and nominal life.** This is a simple method whereby T_j is directly linked to nominal life cost for an event via (2.10) [73].

$$L(T_j) = L_0 exp\left(\frac{\frac{E_A}{K_B}}{\Delta T_j}\right) \tag{2.10}$$

L_0 is the nominal life of the component based on statistical failure data, E_A is the activation energy, and K_B is Boltzmann's constant.

To note, no reason was given for using this exponential model in [73].

- **Manufacturer's/Experimental relationship between T_j and nominal life.** This is similar to the exponential method, but fits curves to manufacturer's, or experimental, cycles to failure against ΔT_j using well defined fatigue relationships. In Senturk et al. [81] both exponential (2.11) and a curve based on the Coffin-Manson law were considered for switching failure cycling data. In this case an exponential model proved to be the better fit, whilst others find models built using the Coffin-Manson law were preferable [77–80, 85–87]. The life consumption is then calculated using rain-flow counting and the Palmgren-Miner rule as in the fatigue cycling case.

$$N_{f,exp} = ae^{b\Delta T_j} \tag{2.11}$$

Where $N_{f,exp}$ is the number of cycles until failure, and a and b are constants.

Whilst this data is easily validated for simple cases as it is based on real experimental data, it has not been validated against a more complex loading profile that can be found in a wind turbine setting (Chapter 1).

- **Direct comparison of thermal cycles.** Instead of estimating life expectancy, in some

cases the thermal loading is directly compared to indicate which loading profile will likely cause the most damage [75, 76]. This method is not usable for prognosis of converter end of life without this life estimation as only relative life costs can be produced.

The life estimation methods each have advantages, along with some key drawbacks. The direct comparison of thermal cycles gives an indication of which loading profiles may cause the most damage, but the lack of component life estimation means the method cannot be used in detailed reliability models. The use of manufacturer's data is a relatively simple way to predict the life of a component, but there is a question as to whether data from a consistently loaded device can be applied to a component that has a highly variable loading profile. The use of an exponential relationship between ΔT_j and nominal life is a similar method to the manufacturer's/experimental relationships. The use of fatigue cycle analysis is a well defined reliability assessment used in engineering. However, the complexity of the method means that only a select number of failure mechanisms can be analysed, missing key potential failure modes.

Summary of POF Models

Table 2.4 provides an overview of the models used in combination in the literature.

Model Parameter	[74]	[85]	[73]	[75]	[76]	[77]	[78]	[79]	[80]	[81]	[82]	[83]	[84]	[86]	[87]	[88]
Operational Profile	**x**	**x**	**x**	**x**	**x**	**x**	**x**	**x**	**x**	**x**	**x**	**x**	**x**	**x**	**x**	**x**
Fixed Wind Speed			x													
Range of Drive Frequencies	x															
Range of Wind Speeds				x	x	x										
Wind Speed Distribution							x	x	x							
WSTS		x								x	x	x	x	x	x	x
Generator	**x**	**x**	**x**	**x**	**x**	**x**	**x**	**x**	**x**	**n/a**	**x**	**x**	**x**	**x**	**x**	**x**
DFIG	x			x			x		x				x	x	x	
PMSG		x	x		x	x		x			x	x			x	x
Control	**n/a**	**n/a**	**n/a**	**x**	**x**	**x**	**x**	**x**	**x**	**n/a**	**x**	**x**	**x**	**x**	**x**	**x**
maximum power point tracking (MPPT)				x	x	x	x	x	x		x	x	x	x	x	x
CPM/CTM													x			
Thermal Model	**x**	**x**	**x**	**x**	**x**	**x**	**x**	**x**	**x**	**x**	**x**	**x**	**x**	**x**	**x**	**x**
Thermal Equivalent Circuit		x	x	x	x	x	x	x	x	x	x	x		x	x	x
Thermal Diffusion Equations													x			
FEA	x															
Life Modelling	**x**	**x**	**x**	**n/a**	**n/a**	**x**	**x**	**x**	**x**	**x**	**x**	**x**	**x**	**x**	**x**	**n/a**
Fatigue Cycling											x	x	x			
Manufact./Exp. Relationship	x	x				x	x	x	x	x				x	x	
Arrhenius Equation			x													
Direct comparison				x	x											

Table 2.4: Summary of POF models used in the wind turbine converter literature. 'n/a' indicates where no model was used, and 'n/i' indicates where there is not enough information given to determine the model used.

The PoF model used is highly dependent on the focus of the work carried out, and the data available for the simulations. However, some general conclusions can be drawn.

- If the PoF model is to be used in a detailed reliability analysis for estimating EOL of the power converter, a realistic wind speed model is needed. Preferably this would be in the form of a WSTS. Interestingly, less than half of the publications include some form of WSTS (Table 2.4), and they have very different time steps between data points. This highlights a lack of consensus on the most appropriate wind speed data time step for determining sufficiently accurate thermal loading profiles in the converter.

- A detailed drive train and control model is required to produce the electrical signals experienced by the converter. In almost all cases, this is based on MPPT in the literature (Table 2.4).

- The electrical losses that are considered are well defined as the conduction, switching and reverse recovery diode losses of the IGBT-diode modules.

- Thermal models are used for converting electrical losses into T_j in the IGBT-diode modules. Thermal equivalent circuits from manufacturing data are the most popular thermal models used (Table 2.4).

- For cost-to-life estimation calculations, the use of cycles to EOL against temperature relationships in manufacturing data is the most popular, as is the estimation of plastic strain in key components such as solder joints (Table 2.4).

In general, the PoF models used in the literature assume that the failure modes are all driven by the cycling of T_j in the IGBT and diode modules. As discussed in Section 2.2.2, there are a number of other failure modes that are driven by other root causes that cannot be captured by thermal cycling. Therefore these models can be used to estimate the EOL of a component if the thermal cycling is the root cause of failure, but cannot be used in isolation for converting loading patterns into life expectancy of the power converter. PoF also require sequential calculations which can lead to high computation time.

2.3.4 Conclusions of Reliability Analysis Approaches

This section has summarised the three reliability analysis approaches applied in the literature; statistical failure rate modelling, PoF models and handbook approaches.

Statistical failure rate modelling was the simplest to scale to wind farm level and takes advantage of the large wind farm datasets. However, the data was exclusively from onshore wind farm sites and the offshore component data is currently not publicly available in large enough datasets. Furthermore, little work has been done to include operational and environmental impacts on the λ_f of the wind turbine components.

PoF models are promising as they can directly link loading profiles, assuming that the failure modes are all driven by the cycling of T_j in the IGBT and diode modules. These models are also generally complex and may not scale well to a whole wind turbine due to their requirement of sequential computations leading to potentially high computation time.

The use of handbook methods appears to provide a bridge between physical and statistical reliability models for power converters but the literature is often critical of handbook methods. This is as the reliability results are often pessimistic or have outdated information. The root cause of failures cannot be investigated either so cannot be used to perform reliability enhancement.

Of these three methods, a PoF model is the most promising as it is able to provide useful information to wind farm operators on how the operation of wind turbines impacts the reliability of the power converter.

2.4 Experimental work in Power Converter Failure Diagnosis for Wind Turbines

There are a number of universities and collaborative groups that have research interests in power converter reliability for wind turbine applications and this section describes the research facilities available.

2.4.1 Institute for Power Electronics & Electrical Drives, Aachen University

The work at Aachen University concentrated on the effect of specific converter-generator operation on generator-side converter reliability for DFIGs. Bartram et al. used a finite element method (FEM) to simulate the temperature rise and cycling under different load conditions in a Mitsubishi IGBT [74]. The simulation results were compared to an experimental set up where the same IGBT was opened up and temperature measured using a single-crystal infra-red imaging system. The IGBT was modified by etching away any silicon gel, and vacuum-dried silicon-oil was added to ensure insulation of DC link voltage. The temperature rise was measured

at 18.1K for 1Hz, 200A, 1100V_{DC} conditions, whilst the simulation produced a temperature rise of 19.6K. The disparity was assumed to be due to the etching away of the silicon gel.

Bartram et al. also detailed a long-term test bench for reliability analysis of IGBTs [74]. This rig tested for the minimum lifetime of various IGBT modules by driving them at DFIG-unique operating conditions that were assumed to stress the modules the greatest; a 0.4Hz operating frequency at 200A, a DC-link voltage of 1100V (790V for the Semikron devices) and a $-20°$ phase angle to simulate the inductive behaviour of the induction machine close to synchronous speed. The saturation voltage of the IGBTs was measured and was used to indicate when failure occurred. Modules from Semikron, Mitsubishi and Eupec were tested.

The results of the test rig in [74] are given in more detail in [96], with diagnosis of in-field failed power converters also used in the analysis. The results of this study are summarised by [97], and the following results are taken from that summary:

- Observed ΔT_j on the IGBTs of 34K.
- The Mitsubishi IGBT module could cope with between 4×10^7 and 2×10^8 cycles; 3-7 years under minimal lifetime operation.
- The IGBT chip was more reliable than other components in the experiment, whilst the driver boards suffered the greatest number of failures.
- Degradation of thermal grease was found in all the IGBT modules that were tested, indicating poor thermal dissipation.
- Explosion due to a fault arc was a typical failure event. This was due to bondwire lift-off, particularly for the emitter bonds, and was observed for ΔT_j as low as 35K.
- No solder failure occurred. This was expected as solder failure generally occurs at ΔT_j of 40K or above.
- In-field power converters were found to have insufficient switch-off procedures as large currents were still present in failed modules before the turbine was disconnected.
- In-field power converter drive boards had large amounts of dust and flies, the latter being attracted by the silicon gel. It was suggested that the flies caused reduced creepage between collector and emitter of the IGBT chip, causing spark-over and destruction. With this in mind, suggestions for improvements to converter design were proposed.

2.4.2 Elforsk, Sweden

Elforsk has begun work on classifying failure modes and root causes for power converters specific to wind turbines [97]. Three types of data were used: 10-minute supervisory control and data acquisition (SCADA) data and maintenance reports of failed converters, on-site weather conditions, and forensic analysis of 11 replaced power converters from operating wind turbines. This information was taken from seven wind farm sites; five onshore and two offshore. From these sites, two converter-generator topologies were investigated; DFIG and fully rated squirrel cage induction generator (FRSCIG). The results have been separated by turbine type and are summarised below.

For the sites where DFIG turbines were operating, the following conclusions were made:

- From SCADA data and weather data at one site, a statistically significant correlation between monthly converter failure and monthly mean ambient temperature was found. This was not the case for monthly wind speed or relative humidity.
- Inspection of replaced power converters found that failures in DFIGs were dominated by non-switching of IGBTs which may be caused either by chip, printed circuit board (PCB) or the interconnection between faults. It was suspected that it was not the IGBTs in the non-destructed modules as IGBTs tend to fail explosively due to short circuit. Diodes were not found to be susceptible to failure.
- Forensic analysis of the destructed power converters indicated presence of 20kV voltages. It was suspected that this could be due to lightning strikes, but no data for the site was available. The correlation with higher ambient temperatures and converter failures was thought to be an indication of periods of lightning (high pressure systems).
- Degraded thermal grease and abrasion-wear spots in heat conducting areas were found, indicating poor heat dissipation.
- Forensic analysis of two non-destructed failed modules did not find any classic ageing/ failure modes.
- Corrosion was found on one of the power converters, but not on the other converters at same site. It was suspected that this corrosion could be due to how the power converter module was handled, but further investigation would be required.

- Insects were found inside the power converters and were suspected of having potential to cause failures, but further investigation would be required.

For the sites where FRSCIG turbines were operating the following conclusions were made:

- A correlation between lightning strikes and converter failures, particularly destructive failures, was found. This would indicate sudden death failures due to electrical overstress were occurring.

- A correlation between daily mean wind speed and non-destructive failures was also found. This would suggest that electrical overstress was causing degradation to failure, but further investigation is required.

2.4.3 CORPE, Department of Energy Technology, Department of Physics and Nanophysics, Aalborg University

A large amount of work has been carried out on converter reliability by the CORPE, the Department of Energy Technology and the Department of Physics and Nanophysics at Aalborg University, Denmark.

One of the main focuses of the research is in online and offline methods of measuring collector-emitter voltage (V_{ce}) of the IGBT chip:

- Beczkowski et al. used the V_{ce} measurement as both an estimate of T_j and to indicate failure due to degradation [98].

- Ghimire et al. used this V_{ce} measurement to perform a V_{ce}-T_j calibration exercise [99]. The experimental rig consisted of a wind turbine power converter, control circuitry, water cooling and the V_{ce} measurement system. The power converter consisted of a 1700V/1000A IGBT power module with two IGBT chips, two diodes and 20 bond wires per section. The power converter was arranged in a half-bridge topology. The converter was run in its lower frequency range, 6 to 20Hz, at 1000V_{DC} and 630A_{rms} to emulate the highest thermal stresses when operating with a DFIG.

- Ghimire et al.'s rig was also used to verify a FEM that aimed to capture the relationship between V_{ce} and T_j. The peak T_j reached in the FEM simulation matched well with the experimental results.

- The experimental rig was also used alongside an offline measurement system [100] for an accelerated test of high power IGBT modules [101], with an updated cooling system. Four IGBT modules were tested to different wear out levels; 2500kcycles, 3500kcycles, 4500kcycles and to failure (5100kcycles, or approximately 9.8 days). V_f was recorded for each of these tests.

- No change in V_f was found up to 3500kcycles. V_f increased linearly between 3500 and 4500kcycles, which was attributed to reconstruction of the metallization surface. The V_f changed rapidly between 4500 and 5100kcycles, which was assumed to be due to bondwire lift-off. These assumptions need to be verified through diagnosis of the modules.

- Mismatched degradation between IGBTs and diodes was also found, with more degradation on the diodes, and more degradation was found on the low voltage side of the modules compared to the high side. The future work for this experimental rig is to emulate real mission profiles for DFIG connected power converters.

Aalborg University also has three other wind turbine specific experimental rigs:

- The first of these rigs applied double-pulse tests for switch loss characterisation of a prototype 3 level, active neutral point clamped, voltage source converter (3L-ANPC-VSC) IGBT module to provide data for power loss and static thermal models and to compare the performance with a 3 level, halfbridge, voltage source converter (3L-HB-VSC) module [102]. The tests involved varying collector current (I_c) up to 2000A at a V_{ce} voltage of 2500V on a single phase of the module. Temperature dependency was also included by repeating the test at T_j between 25°C and 125°C. In this case, the module was used to emulate the generator side converter.

- The second rig carried out non-destructive testing of short circuit responses of IGBT modules in a wind turbine [103]. This rig applies a 6kA, 1.1kV signal to an IGBT module from a charged capacitor bank to simulate a short circuit. The protection equipment removes the signal almost immediately to avoid explosion of the IGBT.

- The third rig used an experimental rig to validate the short and medium term thermal modelling techniques used in a detailed reliability analysis (details can be found in Section 2.3.3) [85]. A 3 level, neutral point clamped, voltage source converter (3L-NPC-VSC)

with metal-oxide semiconductor field-effect transistor (MOSFET) components was opened and a 3kHz FLIR X8400sc infra-red thermal camera was used to measure the T_c and T_j under a 600V DC link voltage and 20A load current. It was found that the temperature cycling followed a similar pattern to that of the thermal model, though the magnitude of the currents were lower due to the lower loading current.

2.4.4 Beuth University of Applied Sciences

A test bench for power cycling at varying frequencies to emulate real converter operation for a DFIG has been developed by [104] at Beuth University. The aim of this project was to provide a way to re-characterise the thermal IGBT degradation models for DFIG specific operation. One phase of the power converter in a half-bridge configuration was built. The experimental rig was designed to run the device at full load condition whilst only consuming the power required for losses of the semiconductors and inductor. The test bench is water cooled and controlled by LabVIEW. The temperature is measured using thermocouples, but non-contact temperature measurement methods have been experimented with, focusing on thermal impedance and V_{ce} measurement. The development of this advanced temperature measurement was one of the aims of the project. Currently there are no results of operation from this experimental rig but it is open for future experimental work.

2.4.5 Conclusions of Wind Turbine Reliability Experimental Research

This section has detailed the work of institutions who have carried out experimental research or failure diagnosis of power converters used in wind turbines.

Diagnosis has been carried out on real wind turbine power converters by a number of institutions. It was found that:

- The presence of insects attracted by the silicon gel was suspected of causing a short circuit.
- There was evidence of poor heat dissipation in the power modules.
- Lightning strikes were a suspected cause of electrical overstress.
- There was no consensus over whether thermal loading was the cause of module failures. This was compounded by the fact that it was often impossible to diagnose the root cause of failure due to explosion damage.

As these results show, there is still much work to be done in determining the failure modes, and finding alternative ways of determining the root cause of failure other than post-failure inspection.

There are also a number of institutions that focus on characterising the reliability of power converters in wind turbine. Whilst each institution had different approaches, there were some general themes:

- The power converters used in the experiments were set up for a DFIG.
- V_{ce} measurements were used for the estimation of IGBT T_j.
- Experimental rigs were used for accelerated testing of IGBT modules under constant loading conditions.
- It was found that thermal overstress was experienced when the modules were cycled systematically. These findings disagreed with the findings of Elforsk.
- The emulation of real wind turbine mission profiles has not been achieved experimentally.

Interestingly, little research effort has been applied to the effect of PMSG mission profiles on converter reliability. Furthermore, none of the experimental rigs have attempted to apply varying wind conditions onto the power converter to see their effect on the thermal loading of the devices. The scale of the test benches used for this analysis are also prohibitive due to the large currents and voltages required and thus work into down-scaling of test benches could be of use. Therefore, there is scope for research into effects of PMSG under realistic operating conditions, and for scaling the experiment to a more appropriate test bench size.

2.5 Current Research Limitations

The research into power converter reliability is extensive, with PoF approaches being the most promising approach. However, there are a number of limitations with the existing approaches that must be addressed.

Firstly, the PoF studies use a range of wind speed time steps to produce their results, with the time step determined by the data available rather than based on wind speed characteristics that are critical to the reliability of the power converter. This is problematic as this implies that a wind speed characteristics over one second has the same impact as a variation over three

hours. Therefore, a study is required to determine the wind speed temporal fidelity that must be considered to provide the relevant temperature variations for converter reliability.

Secondly, PoF studies that examine the wind speed operating conditions that theoretically cause the most damage generally only look at static wind speeds, or draw conclusions about the impact of wind conditions by examining just one WSTS, such as in [88]. Indeed, the study in [77] is the only study that looks at more than one WSTS, with three times series produced from one WSTS modified using various roughness classes. Even with this limited dataset Isidori et al. shows that the operating conditions have an impact, with increasing roughness reducing the cycle life of the device. Therefore, there is a need to examine more closely the impact of wind conditions on the cycle life of power converter devices.

Thirdly, the minimum ΔT_j for converter damage considered in PoF studies varies substantially. Studies either only consider a minimum ΔT_j taken from the lowest recorded in the manufacturing cycles-to-failure data, typically 30K, or extrapolate to include all ΔT_j swings. Therefore, developing an experimental procedure that would be able to determine the impact of ΔT_j cycles-to-failure under realistic operating conditions would help determine the operating conditions that are causing the most damage with confidence.

Finally, manufacturing cycles-to-failure are gathered under constant current, constant frequency conditions with unrealistic heating and cooling profiles [105]; this is very unlike how a power converter in a wind turbine is operated (Chapter 1). Furthermore, no experimental studies have successfully emulated the wind turbine power converter operating conditions in an experimental rig, or provided an appropriately scaled test bench for feasible laboratory studies. As such, due to the models not being verified using realistic operating conditions, there is a question about the validity of the temperature profiles that are produced by the PoF models. Therefore, there is a need to verify these temperature profiles.

2.6 Research Questions

It is clear from the above limitations that PoF modelling and experimental emulation have been treated separately by research groups. In response, a holistic approach to wind turbine power converter reliability is proposed. This includes a combination of effective drive train modelling, simulation, and emulation of the power converter under realistic wind turbine operating conditions. This will allow for developments in either computational or experimental fields to inform

the formulation of results of the other. With this in mind, the following research questions are examined in this thesis:

1. Which wind speed operating conditions theoretically cause the greatest thermal loading to the power modules in the power converter and why?

2. Can the junction temperature be measured in order to verify the simulation models cost effectively?

3. How can wind turbine operating conditions be emulated in a a scaled down test bench?

4. What can be learnt by comparing the results of wind turbine simulations with those of an experimental rig?

To answer these questions a number of steps must be taken. Firstly, a wind turbine drive train model with a power converter thermal model is required in order to simulate the converter under realistic operating conditions. Based on the findings of Chapter 1, this drive train will be modelled based on a FRC PMSG turbine design. This drive train model is outlined in Chapter 3.

Secondly, a method for measuring junction temperature directly in a cost effective manner is required which could be potentially implemented in a real wind turbine. A review of existing temperature measurement techniques is carried out, with the chosen approach tested on an experimental rig to determine the effectiveness of the chosen approach (Chapters 4 and 5).

Finally a proposed test bench that allows for these emulated wind turbine conditions to be applied to a scaled down power converter is outlined in Chapter 6, including a novel approach for generator emulation.

2.7 Conclusions

The importance power converter reliability, particularly in PMSG wind turbines, was outlined in the previous chapter. In this chapter the failure modes of power converters have been given in detail, the experimental work specific to reliability of power converters used in wind turbines has been summarised, and the methods for reliability analysis of offshore wind turbines and wind farms have been detailed to explore the present state of the art and their corresponding weaknesses and merits.

It was found that the main sources of failure of power converters are the semiconductor devices and capacitors, with current industrial surveys indicating that semiconductors may cause over 50% of wind turbine power converter failures.

Capacitors used in wind turbines come in two types; electrolytic and MPPF capacitors. MPPF capacitors are deemed the more reliable of the two technologies but electrolytic capacitors are generally preferred due to their lower cost.

IGBTs are the semiconductor of choice in wind turbine power converters. Temperature variations play a major role in package failure of IGBT devices. Temperature causes accelerated fatigue of the device and can exasperate chip-related failures. Chip-related failures, which are responsible for the final failure of the device, are driven both by temperature and extremes in electrical operation.

Research has been carried out into the diagnosis of failures in wind turbine power converters. The presence of insects were suspected of causing a short circuit, lightening strikes were correlated with converter failures, and signs of damage from poor heat dissipation in the modules was found. There were also disparities between studies on the extent to which thermal loading caused device failure, and which devices were most prone to these failures.

There are a number of research institutes with experimental rigs developed to explore the reliability of IGBT power modules in wind turbines. This includes V_{ce} measurement for estimation of IGBT T_j and accelerated testing of IGBT modules. It was found that thermal loading-related failure modes were dominant, and diodes had a greater degradation in performance with age, disagreeing with the findings of in-field diagnosis. In all cases, the power converter was set up for a DFIG topology, but the emulation of real DFIG mission profiles has not yet been achieved. Interestingly, little research effort has been applied to the effect of PMSG mission profiles. The scale of the test benches used are also prohibitive. Therefore, there is scope for research into effects of PMSG under realistic conditions and for scaling the experiment to a more appropriate test bench size.

The semiconductor devices are the focus of research in wind turbine specific reliability analysis (both experimental and simulation). Statistical failure rate modelling was the simplest to scale to wind farm level and takes advantage of the large wind farm datasets. However, the data was exclusively from onshore wind farm sites and offshore component data is currently not available in large enough datasets. Furthermore, little work has been done to include operational and

environmental impacts on the λ_f of the wind turbine components.

Handbook methods appear to provide a bridge between physical and statistical reliability models for power converters but the literature is often critical of handbook methods. This is as the reliability results are often pessimistic or have outdated information. The root cause of failures cannot be investigated either so this method cannot be used to perform reliability enhancement.

For reliability analysis of the wind turbine/wind farm, the PoF models were the most promising as they are able to provide useful information to wind farm operators on how the operation of wind turbines impacts the reliability of the power converter. The limitations of the current research approaches have been outlined, including the present lack of a holistic approach for power converter reliability analysis specific to wind turbine power converters, and the disparity between experimental and in-field testing results.

In response a number of research questions have been detailed which aim to provide a holistic approach to wind turbine power converter reliability research which considers realistic operating conditions of the wind turbine being emulated in a laboratory environment. This involves simulation work in the form of a drive train model and power converter thermal model. An experimental rig has been designed for temperature measurement validation to allow for thermal monitoring of the device under test. A second test bench has also been proposed for emulating the wind turbine specific operating conditions in a laboratory environment. These models and experimental rigs are detailed in the following chapters.

Chapter 3

Drive Train and Power Converter Thermal Modelling

3.1 Introduction

Power converter reliability has been linked to thermal loading of power converters (Chapter 2). Thermal loading is determined by the electrical loading experienced by the converter's power module devices. In a wind turbine, this electrical loading is highly variable and is determined not only by the wind speed, but also the wind turbine configuration and control strategies employed (Chapter 1). Therefore to provide wind turbine representative electrical loading profiles and an application-specific power module thermal response, a drive train model is required with a power module thermal model.

The approach chosen to determine the thermal loading of a wind turbine power converter with a new focus on wind speed characteristics is outlined in the following five main steps:

1. Model a wind turbine drive train to calculate the current throughput of the converter based on turbine mechanical and electrical dynamics (Section 3.2).

2. Model the resultant power losses in the converter due to the current profile (Section 3.3).

3. Model the power module T_j thermal loading in response to the power losses (Section 3.3).

4. Simulate power module thermal responses to characteristic wind speed profiles (Chapter 5).

5. Calculate the expected life of the power module from these simulations (Section 3.4).

This chapter outlines the key features of the models used for the simulation work (points 1-3 above) and methods for calculating remaining useful life (point 5). The drive train, thermal and life estimation model will be collectively referred to as the Durham drive train reliability evaluation tool (DDTRET). The operation of the drive train is verified in Section 3.5. Finally, section 3.6 summarises the key features of the combined model.

3.2 DDTRET: Drive Train Model

To ensure relevance to the modern wind turbine industry a PMSG drive train with FRC was chosen to be modelled. The state-of-the-art offshore wind turbines being constructed are now reaching 8MW, however there is not enough data freely available to be able to simulate this size in appropriate, reliable detail. Therefore a 2MW PMSG-FRC drive train was modelled.

The drive train model can be split into eight sub-systems; illustrated in Figure 3.1:

- Rotor power extraction (Section 3.2.1).
- Drive train dynamics (Section 3.2.2).
- Generator (Section 3.2.3).
- MSC (Section 3.2.4).
- DC link (Section 3.2.5).
- Turbine control (Section 3.2.6).
- Sensors and sampling (Section 3.2.7).
- Simulation details (Section 3.2.8).

Section 3.2.9 provides a summary of the key features of the drive train model.

3.2.1 Rotor Power Extraction

First the turbine mechanical power extracted from the wind by the turbine rotor (P_t) is calculated using (3.1) [106].

$$P_t = 0.5 C_p(\lambda, \beta) \rho \pi r^2 u^3 \tag{3.1}$$

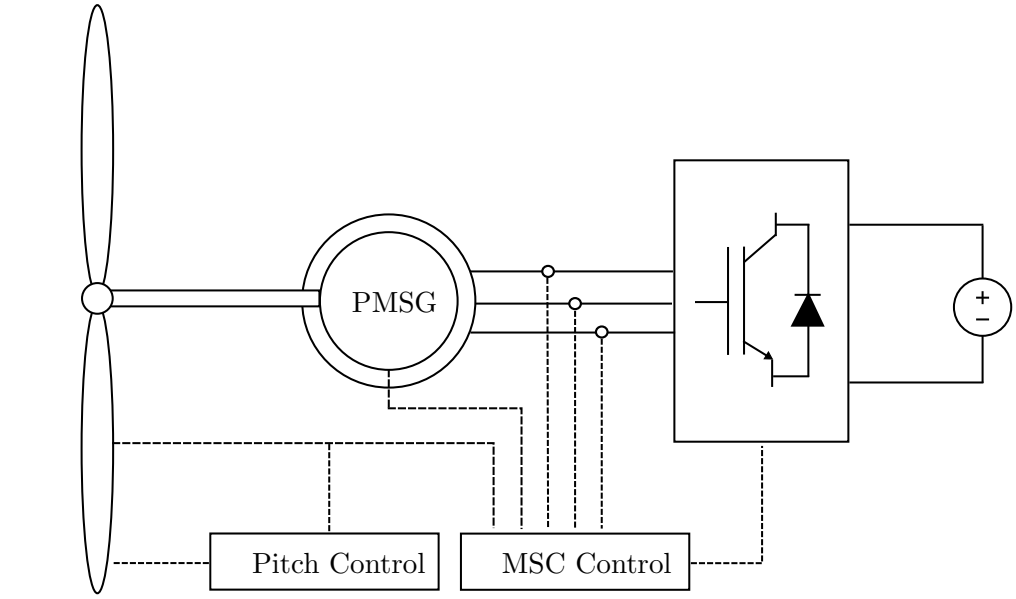

(a)

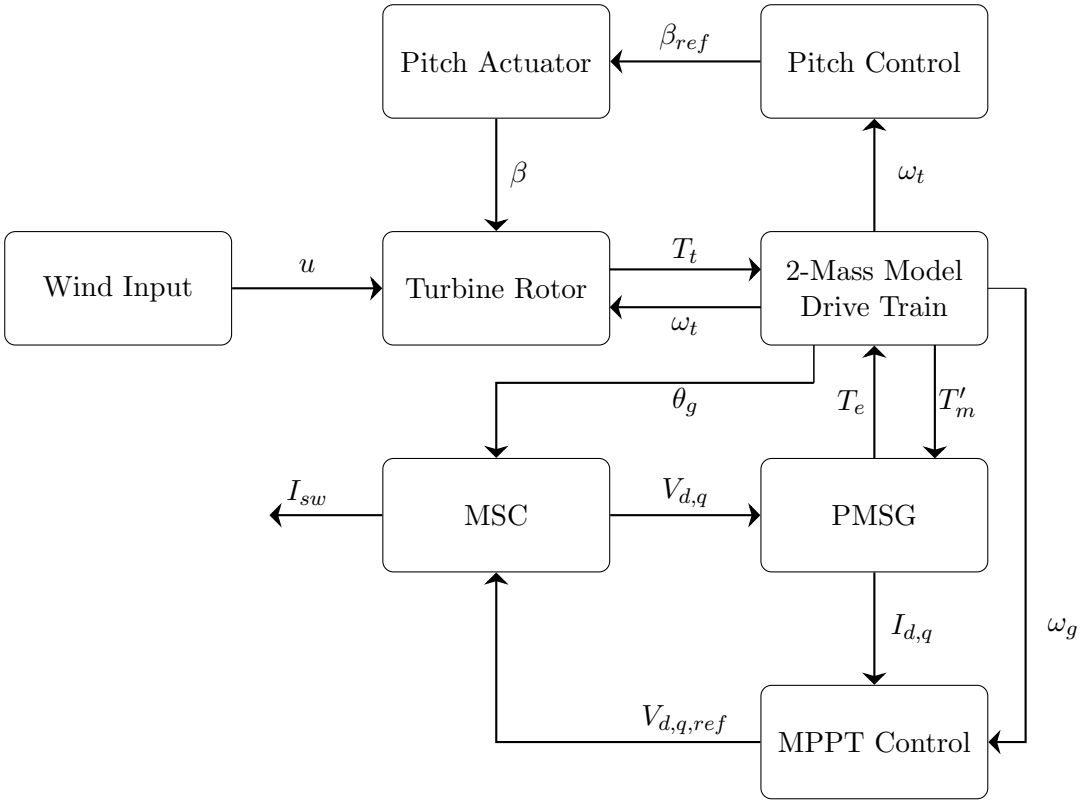

(b)

Figure 3.1: Drive train model summary. u is the incoming wind speed, T_t is the turbine torque extracted from the wind, T'_m is the mechanical torque resulting from the shaft stiffness and damping, T_e is the electromagnetic torque, ω_t is the turbine rotational speed, ω_g is the generator rotational speed, θ_g is the generator angular displacement, β is the pitch angle, β_{ref} is the reference pitch angle, $I_{d,q}$ is the generator output current, I_{sw} is the current through the power modules $V_{d,q}$ is the generator terminal voltage applied by the MSC, and $V_{d,q,ref}$ are the reference MSC output voltages.

Where C_p is the coefficient of performance of the turbine which is a function of λ, the tip speed ratio, and β, the blade pitch angle, ρ is the air density, r is the radius of the turbine rotor, and u is the wind speed.

The $C_p(\lambda, \beta)$ function is turbine-specific but can be expressed numerically using (3.2) [107].

$$C_p = C_1(C_2 - C_3\beta - C_4\beta^{C_5} - C_6)e^{-C_7(\lambda,0)} \tag{3.2}$$

Where C_{1-7} can be replaced to give the following expression (3.3).

$$C_p = A_t(\frac{B_t}{\lambda_i} - C_t\beta - D_t\beta^{E_t} - F_t)e^{\frac{-G_t}{\lambda_i}} \tag{3.3}$$

Where $A_t - G_t$ are turbine-specific constants, and λ_i is given by (3.4).

$$\frac{1}{\lambda_i} = \frac{1}{\lambda + H_t\beta} - \frac{K_t}{\beta^3 + 1} \tag{3.4}$$

Where H_t and K_t are turbine-specific constants.

The $C_p(\lambda, \beta)$ has been plotted for the example turbine used in this work [108] (Figure 3.2). $C_{p,max}$ is the maximum C_p for this turbine, and is found at the optimum λ (λ_{opt}).

λ is the ratio between the turbine rotational speed (ω_t) and u and is calculated using (3.5).

$$\lambda = \frac{\omega_t r}{u} \tag{3.5}$$

The resultant turbine torque (T_t) is calculated using (3.6).

$$T_t = \frac{P_t}{\omega_t} \tag{3.6}$$

Figure 3.3 summarises the turbine rotor model described in this section. $C_{p,betz}$ is the Betz limit [109]. Parameters for this part of the model can be found in Table 3.1.

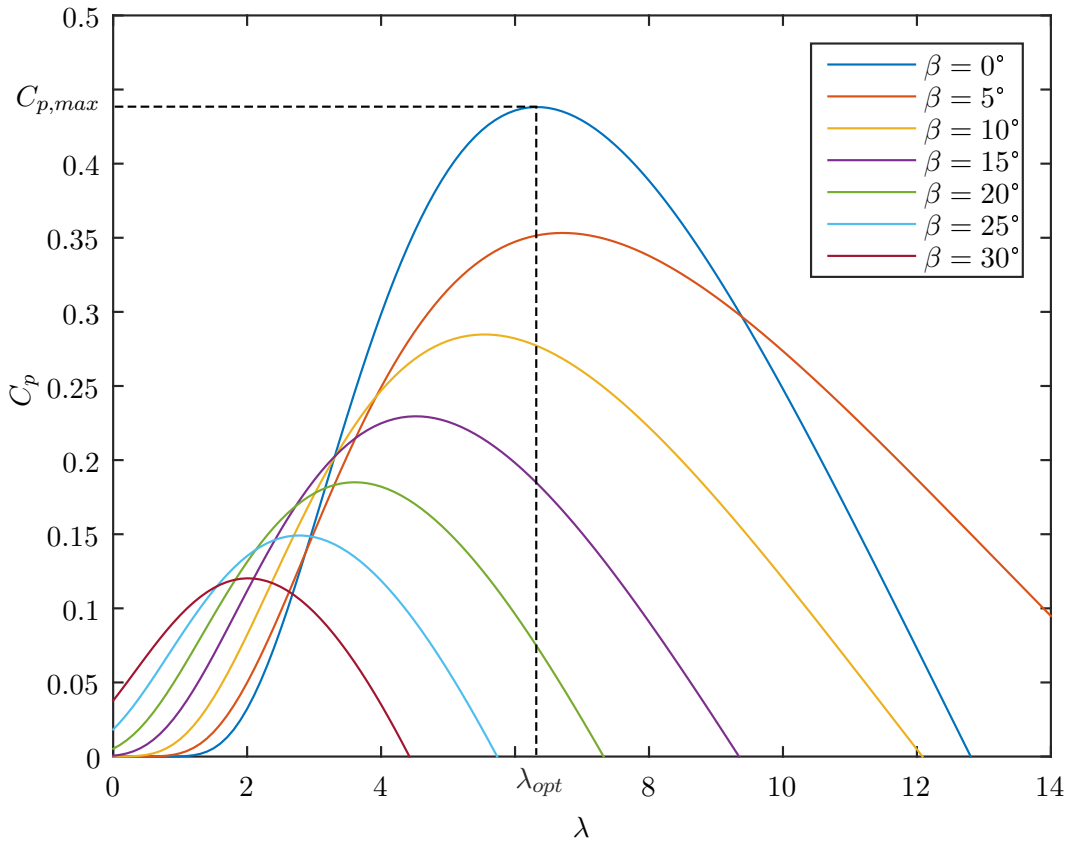

Figure 3.2: Example $C_p(\lambda, \beta)$ function. This figure was produced using the $A_t - H_t, K_t$ constants found in Appendix B.

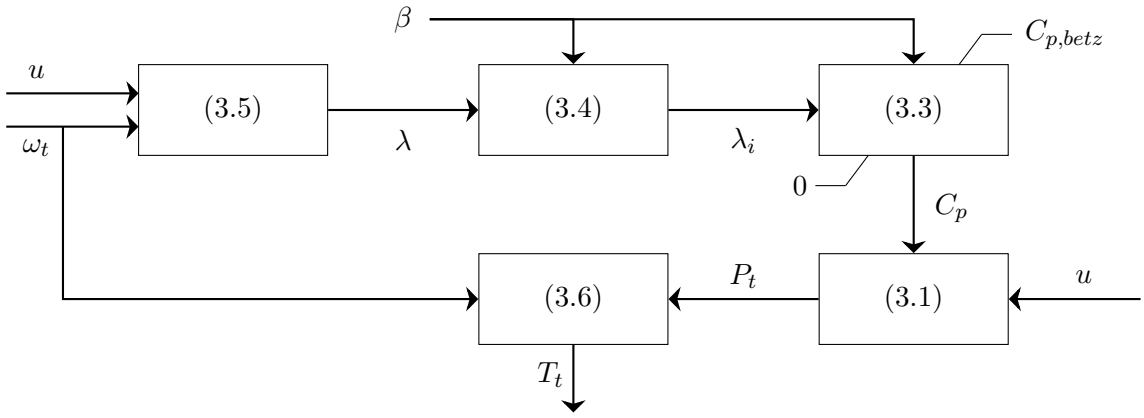

Figure 3.3: Flow diagram summarising rotor power extraction.

Table 3.1: Turbine rotor performance values. Notes can be found in Appendix B.

Parameter	Value	Reference	Parameter	Value	Reference
A_t	0.22	[108]	B_t	116	[108]
C_t	0.4	[108]	D_t	0	[108]
E_t	0	[108]	F_t	5	[108]
G_t	12.5	[108]	H_t	0.08	[108]
K_t	0.035	[108]	λ_{opt}	6.3	Note 1
$C_{p,max}$	0.4832	Note 1	$C_{p,betz}$	0.593	[33]

3.2.2 Drive Train Dynamics

The torque (T_t) extracted from the wind is applied to the drive shaft. As a direct drive turbine was modelled, the drive shaft is connected directly to the generator without a gearbox and the drive train can be modelled as a mechanical mass-spring-damper system which dynamically impacts the resulting mechanical torque (T'_m) applied to the generator.

The higher the order of the mechanical system (number of masses and connections), the more accurately the dynamics will be modelled. However, the higher order the modelling, the more computationally expensive the calculations become, and the higher number of estimated coefficients are required, potentially reducing accuracy. Therefore a compromise must be made. In general, drive train models for direct-drive PMSG turbines are either lumped-mass or 2-mass models. Ideally, a 3-mass model would be used as all fundamental torque oscillations that may interact with the electrical transients can be modelled [33] but no data was freely available for a 3-mass model and therefore a 2-mass model was used, as represented in Figure 3.4. J_t, J_g are the moments of inertia of the turbine and generator respectively, α_t, α_g are the rotational accelerations of the turbine and generator respectively, ω_g is the rotational speed of the generator, θ_t, θ_g are the rotational displacements of the turbine and generator respectively, C_d is the shaft damping coefficient, K is the shaft stiffness and T_e is the electromagnetic torque.

The 2-mass model is described by the matrix of equations of motion (3.7) [110].

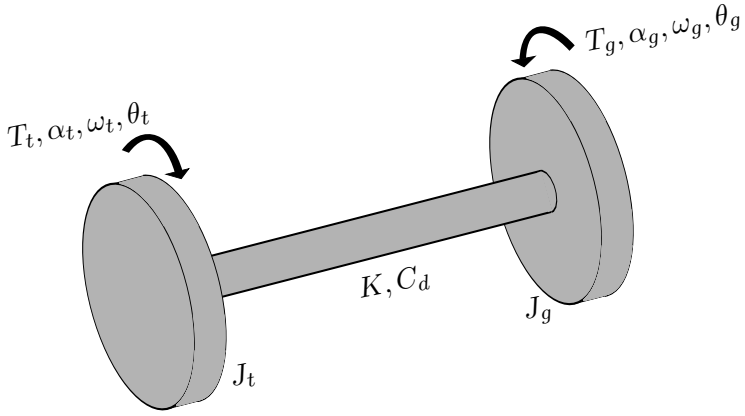

Figure 3.4: 2-mass model of drive train.

$$\begin{Bmatrix} T_t \\ T_e \end{Bmatrix} = \begin{bmatrix} J_t & 0 \\ 0 & J_g \end{bmatrix} \begin{Bmatrix} \alpha_t \\ \alpha_g \end{Bmatrix} + \begin{bmatrix} C_d & -C_d \\ -C_d & C_d \end{bmatrix} \begin{Bmatrix} \omega_t \\ \omega_g \end{Bmatrix} + \begin{bmatrix} K & -K \\ -K & K \end{bmatrix} \begin{Bmatrix} \theta_t \\ \theta_g \end{Bmatrix} \tag{3.7}$$

This matrix can be expanded to provide six equations of motion to be solved numerically.

$$T'_m = (\omega_t - \omega_g)C_d + (\theta_t - \theta_g)K \tag{3.8}$$

$$\alpha_t = \frac{T_t - T'_m}{J_t} \tag{3.9}$$

$$\alpha_g = \frac{T'_m - T_g}{J_g} \tag{3.10}$$

$$\omega_t = \int \alpha_t(t)dt \tag{3.11}$$

$$\omega_g = \int \alpha_g(t)dt \tag{3.12}$$

$$\theta_t = \int \omega_t(t)dt \tag{3.13}$$

$$\theta_g = \int \omega_g(t)dt \tag{3.14}$$

As the drive train model was solved discretely, the integrations were performed discretely in

MATLAB. Figure 3.5 details the block diagram of the drive train dynamics. T_s is the simulation sampling time.

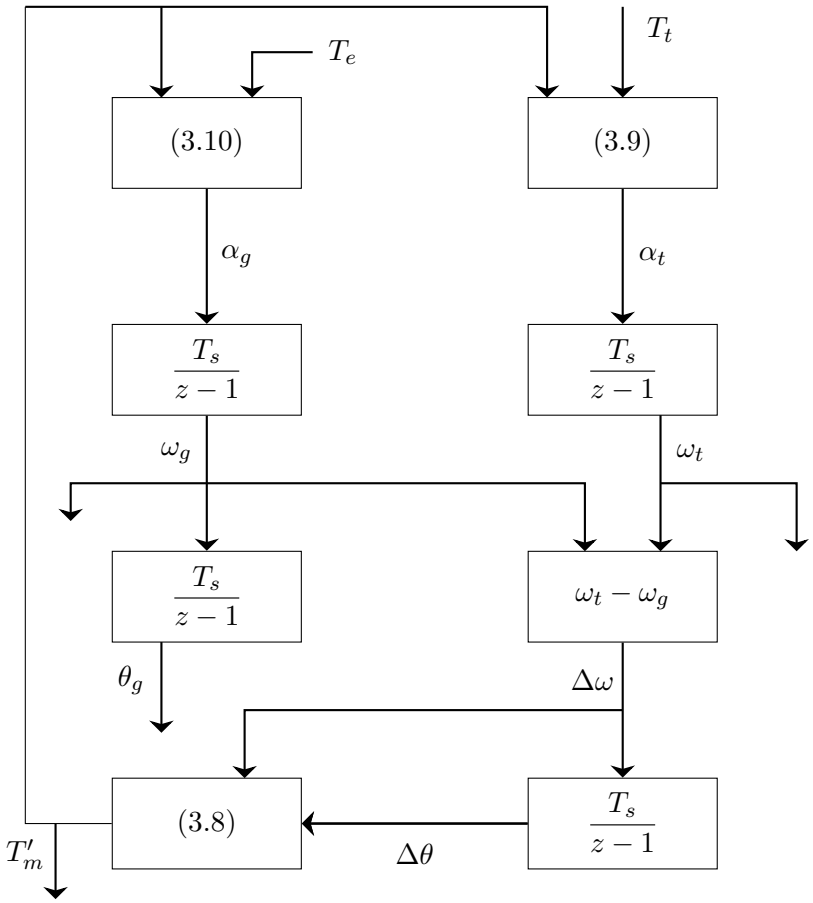

Figure 3.5: Flow diagram summarising drive train dynamics.

3.2.3 Generator

The resulting torque T'_m is applied to the generator. The generator modelled was a non-salient PMSG and was modelled as a 2nd order generator in the $dq0$ reference frame [111]. The mechanical component was modelled with the torque swing equation to simulate the acceleration due to difference between mechanical and electrical torque (3.10). The generator used for the simulation was SIMULINK's inbuilt SimPowerSystems 'permanent magnet synchronous machine (PMSM)'. The generator and drive train dynamics parameters can be found in Table 3.2 and Appendix B. f_{rat} is the turbine rated frequency, $V_{l,rat}$ is the rated line voltage, I_{rat} is the rated current, and T_{rat} rated torque.

Table 3.2: Drive train parameter values. Notes can be found in Appendix B

Parameter	Value	Reference	Parameter	Value	Reference
$P_{t,rat}$	2.0MW	[111]	$\omega_{t,r}$	22.5rpm	[111]
u_{rat}	12.7m/s	Note 1	r	34m	Note 1
ρ	1.225kg/m^3	[33]	J_t	2.92×10^6kg/m^2	[112]
J_g	200kg/m^2	[113]	K	4.0×10^7Nm/rad	[112]
C_d	6.72×10^6Nms/rad	Note 2	p	52	[111]
ϕ	8.24Vs$_{(\text{peak})}$	[111]	r_s	0.821mΩ	[111]
L_d	1.5731mH	[111]	L_q	1.5731mH	[111]
f_{rat}	9.75Hz	[111]	$V_{l,rat}$	690V$_{(\text{rms})}$	[111]
I_{rat}	1867.76A$_{(\text{rms})}$	[111]	T_{rat}	848.826kNm	[111]

3.2.4 Machine-Side Converter

In a typical wind turbine the converter is comprised of a back-to-back rectifier/inverter. The rectifier acts as the MSC and the inverter acts as the GSC. The roles of the MSC and GSC differ depending on control strategy but the MSC typically controls the wind turbine speed for optimum power production whilst the GSC maintains the DC link voltage and controls power extraction to the grid.

Due to turbine speed variation, the MSC experiences a more varied operating profile compared to the fixed frequency GSC. As the thermal loading of the device is linked to the operating profile and a more varied thermal profile is likely to cause more damage that a steady thermal profile, the MSC is consequently of greater interest for reliability evaluation. Therefore, only the MSC is modelled fully and the GSC is replaced with a constant voltage source to maintain the DC link (Section 3.2.5); it was assumed that, as the DC link decouples the machine from the grid and the variations in DC voltage under GSC control would be minimal, there would be no relevant change to the reliability of the MSC. The MSC was modelled as a 2-level IGBT-diode pair active rectifier, as 2-level converters are found in the majority of turbine designs [114] (Figure 3.6). Simulink's inbuilt SimPowerSystems 'Universal Bridge' was used and the 'Power Electronic Device' was set to 'IGBT/ Diodes'.

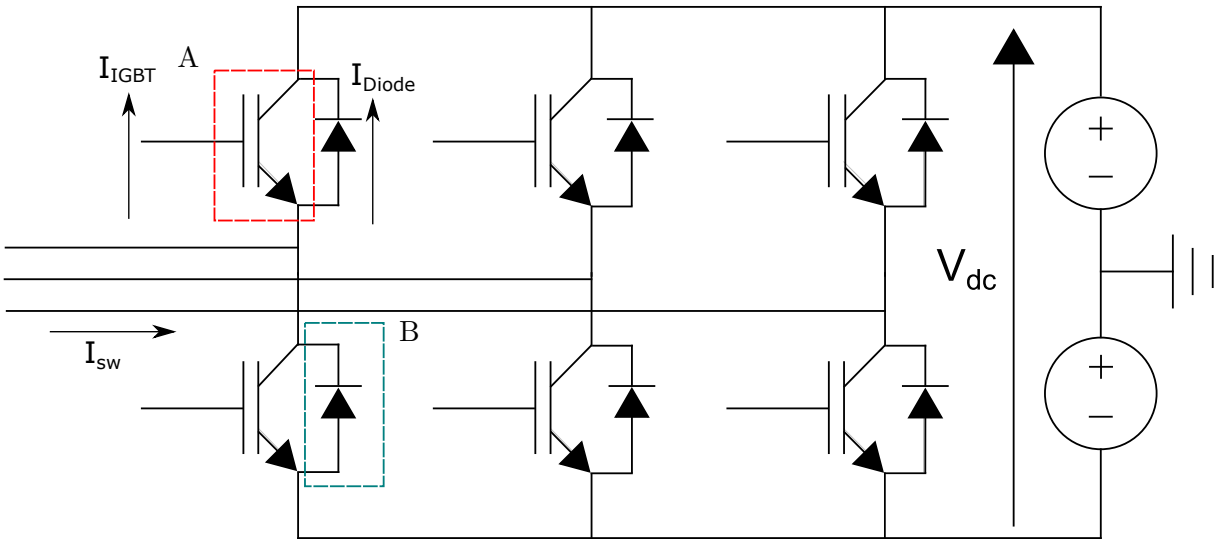

Figure 3.6: 2-Level rectifier schematic with ideal DC link voltage. The red box (A) indicates an IGBT, and the blue box (B) a free-wheeling diode.

The MSC parameters were based on the power modules found in the SEMIKRON SKS B2 100 GD 69/11-MA PB [115]. These stacks have SKiiP 2013 GB172-4DWV3 half-bridge modules [116]. and the parameters used are detailed in Appendix B. The choice of the stacks is explained in Section 3.2.6.

The current output is split between diode and IGBT depending on the direction of the current and can be determined by the sign convention outlined in [117]. This current must also be halved to determine the current throughput of each power module as two parallel stacks are required to provide the power rating for the turbine [114]. Figure 3.7 illustrates the conversion from converter output to device currents. I_{sw2} is the current on one switch from the SIMULINK model. The positive values of I_{sw2} give the I_{IGBT2} and the negative values give the I_{Diode2}. These are then halved to give the current in each stack.

3.2.5 DC link

As discussed in Section 3.2.4 the GSC has been replaced with a fixed voltage supply. Typically for a low voltage GSC (690V) the DC link voltage (V_{DC}) is maintained at anywhere between 1000-1300V [33, 118]. Based on the RE stack detailed in Section 3.2.4 and the PWM strategy chosen in Section 3.2.6, the DC link was set to 1150V (±575V) (Figure 3.6).

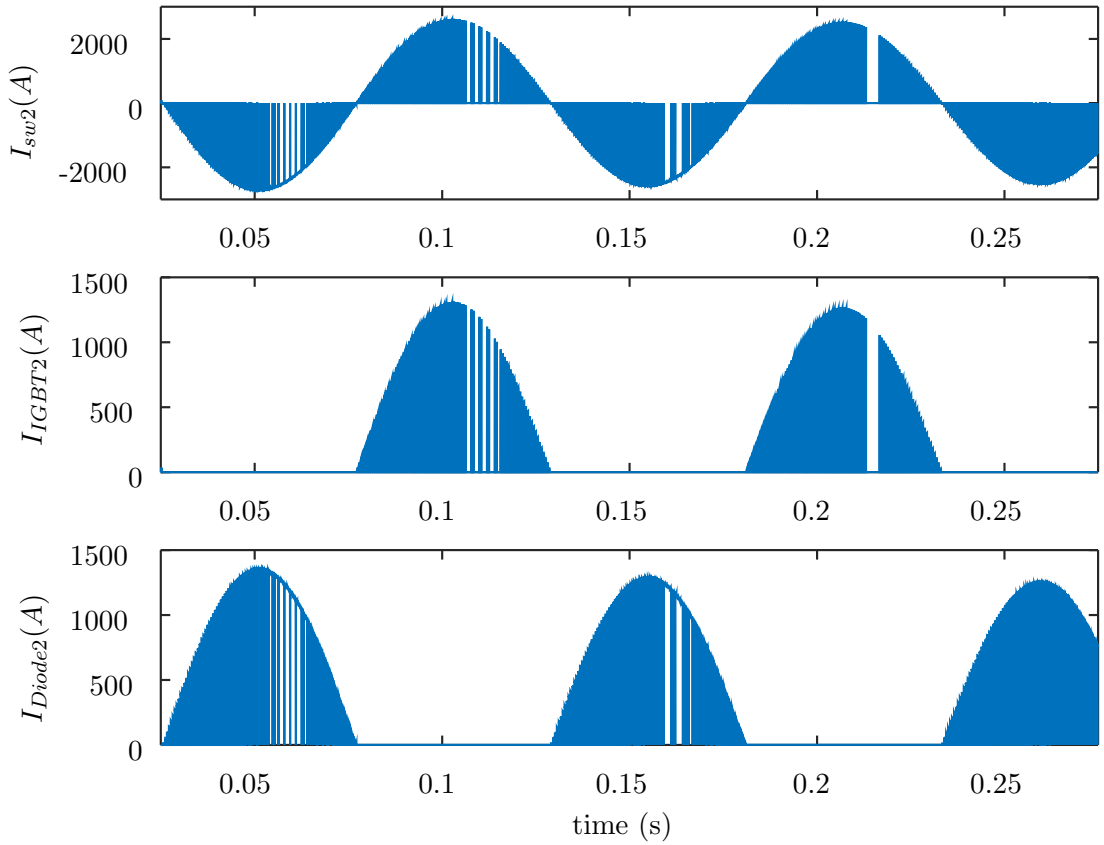

Figure 3.7: Current distribution in power module devices.

3.2.6 Turbine Control

Power extraction is controlled in 2 ways: MPPT below rated speed, and active pitch control above rated speed.

Maximum Power Point Tracking

MPPT is achieved by maintaining $C_{p,max}$ via λ_{opt} (Figure 3.2) when below rated wind speed. The ω_t must be controlled to maintain this λ_{opt} (3.15).

$$\omega_{t,opt}(u) = \frac{u\lambda_{opt}}{r} \tag{3.15}$$

Where $\omega_{t,opt(u)}$ is the optimum turbine rotational speed at a given wind speed.

$\omega_{t,opt}(u)$ is achieved using torque control. By varying T_g, the turbine can accelerate or decelerate (3.10). To calculate the $T_{ref}(u)$, the equation for turbine power (3.1) and torque (3.6) can be used to determine a relationship between $\omega_{t,opt}(u)$ and $T_{ref}(u)$ (3.16-3.18).

$$P_{t,max} = 0.5 C_{p,max} \rho \pi r^2 \left(\frac{r}{\lambda_{opt}} \right)^3 \omega_{t,opt}(u)^3 \tag{3.16}$$

$$K_{mppt} = 0.5 C_{p,max} \rho \pi r^2 \left(\frac{r}{\lambda_{opt}} \right)^3 \tag{3.17}$$

$$T_{ref}(u) = K_{mppt} {\omega_{opt}}^2 \tag{3.18}$$

Where K_{mppt} is a turbine specific constant.

As u is not measured in this control strategy, $\omega_{t,opt}(u)$ is unknown at any given point. Instead T_{ref} is calculated using ω_t (3.19). If $\omega_t \neq \omega_{t,opt}(u)$ then ω_t will continue to change, changing T_{ref} until ω_t reaches steady state.

$$T_{ref} = K_{mppt} {\omega_t}^2 \tag{3.19}$$

T_{ref} is achieved by varying the current demanded of the generator. For this control, the d, q currents ($I_{d,q}$) are used in a $dq0$ control strategy (3.20, 3.21), with $I_{d,q}$ calculated from the stator currents (I_{abc}) via a Park transform.

$$I_{d,ref} = 0 \tag{3.20}$$

$$I_{q,ref} = \frac{4}{3\phi p} T_{ref} \tag{3.21}$$

Where $I_{d,q,ref}$ are the reference d, q currents, p is the number of generator poles, and ϕ is the permanent magnet flux linkage.

$I_{d,ref}$ is maintained at zero as it relates to magnetisation which is not required for a PMSM. Holding the magnetisation current at zero also minimises resistive losses [119].

These currents are achieved by applying a controlled voltage on the generator terminals using the MSC. Again the voltages are processed in the d, q reference frame ($V_{d,q}$). $V_{d,q}$ are determined by using independent proportional-integral (PI) controllers that use the error between $I_{d,q}$ and $I_{d,q,ref}$ to produce $V_{d,q}$ errors. These errors are added to the known generator voltages (impedance and armature voltages) to produce the required terminal voltages for the generator

($V_{d,q,ref}$) [33]. $V_{d,q,ref}$ is converted into the abc reference frame ($V_{abc,r}$) via an inverse Park transform for use by the converter PWM.

Figure 3.8 details the $dq0$-control of the MSC. r_s is the PMSG stator phase resistance, L_d, L_q are the PMSG d, q armature inductances, $\omega_{t,max}$ is the maximum turbine rotational speed (see Section 3.2.6, Controller Interaction), and ω_e is the magnetic field rotational speed which is calculated using (3.22).

$$\omega_e = \frac{p}{2}\omega_g \tag{3.22}$$

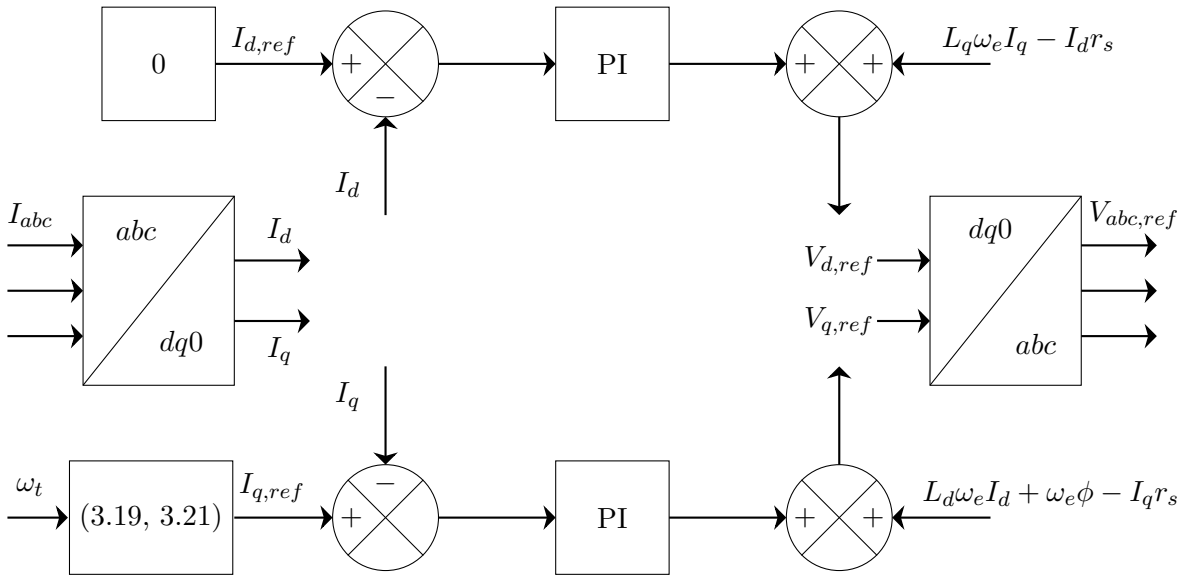

Figure 3.8: Flow diagram of machine-side controller.

The PWM converts the modulated $V_{abc,ref}$ (between -1 and 1) (V_m) into a switching pattern for the IGBTs in order to produce the 3-phase converter output voltage ($V_{c,abc}$). In this case a sine-wave pulse width modulation (SPWM) strategy was chosen and implemented using the 'PWM Generator (2-level)' Simulink block. The carrier mode of operation was set to 'synchronised' to ensure the carrier frequency remained synchronised to the reference signal. The carrier/reference ratio ($R_{c/r}$) can be found in Appendix B.

As SPWM was used, V_m was calculated using (3.23).

$$V_m = \frac{2}{V_{DC}} V_{abc,r} \tag{3.23}$$

Pitch Control

Pitch control limits mechanical power extraction above rated speed by pitching the blades away from the optimum angle, reducing the turbine's C_p (Figure 3.2).

There are a number of control methods available for pitch control [120]. For this work the difference in ω_t and rated ω_t ($\omega_{t,rat}$) was used with a PI controller to produce a β error (β_{err}) (Figure 3.9.a). In reality the $\beta - \omega_t$ relationship is not linear but the approximation was found to control the turbine effectively (Section 3.5).

β_{err} is added to the current β to produce a reference β (β_{ref}) and applied to the pitch actuator (Figure 3.9.b). The pitch actuator is modelled as a 1st order dynamic system as found in [121] with limits on β and the rate of change of β (β_{rate}). These values can be found in Appendix B.

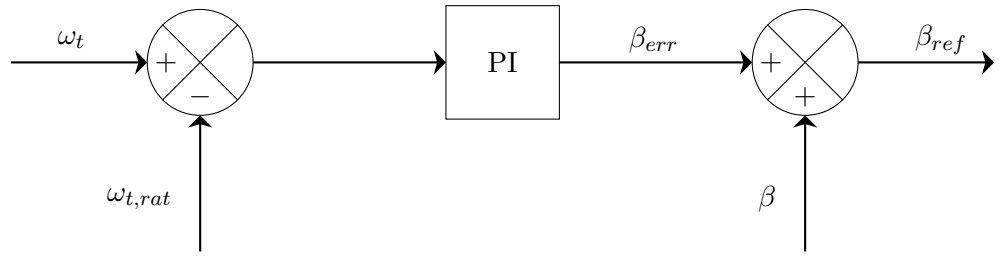

(a)

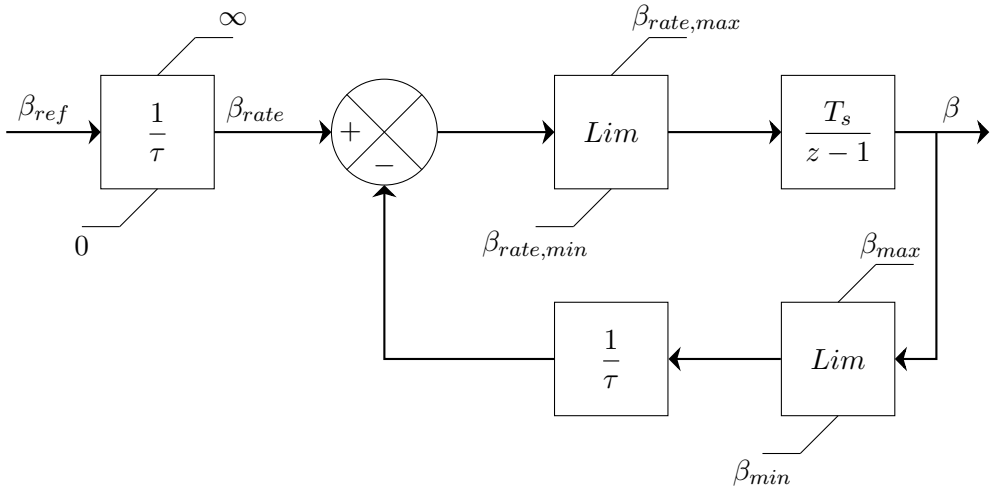

(b)

Figure 3.9: Flow diagram of (a) pitch controller and (b) pitch actuator.

Controller Interaction

For improved turbine control close to the MPPT-rated operating border, the pitch and MSC controllers have overlapping active regions. The pitch controller will continue to operate if the turbine drops below $\omega_{t,rat}$ until β has reached 0°. This avoids undesirable β values at lower

wind speeds. The MSC controller is not constrained to below the rated turbine rotational speed ($\omega_{t,rat}$) but by a higher maximum ($\omega_{t,max}$). This allows the torque controller to deal with sudden increases in wind speed that the pitch controller is too slow to respond to effectively, vastly improving turbine control in the rated region. This control interaction strategy is similar to the strategy outlined in [122].

To allow for this interaction, the MSC power modules have to be rated accordingly. Therefore the MSC was modelled using two parallel SKS B2 100 GD 69/11-MA PB stacks, providing an $I_{out,max}$ of 1000A$_{\text{rms}}$ per stack [115]. This corresponds to a total I_q of 2828A, which was reduced to 2800A to allow for noise and controller overshoot. Using (3.21) and (3.19), this dictates a $\omega_{t,max}$ of 2.43rad/s.

3.2.7 Sensors and Sampling

To emulate a turbine's control regime more accurately, sensors were modelled with sampling rates based on those found in [123]. The I_d, I_q and β measurement signals were sampled directly using zero-order hold (ZOH). ω_t and ω_g sensors used the variation in speed to determine the new speed measurement (ω_{meas}) as outlined in Figure 3.10. τ_ω is the speed sensor time constant.

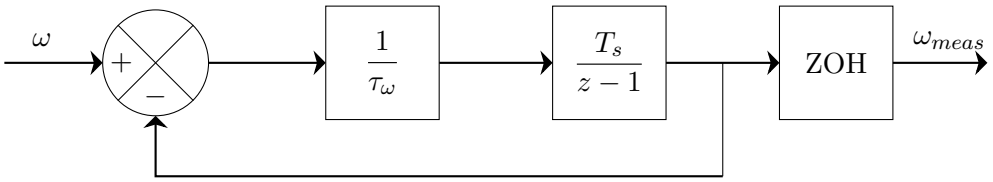

Figure 3.10: Rotational speed sensor model.

The precision of these signals was also reduced using 'Quanitizer' blocks. This emulated the real measurement of the physical system, and remove controller action on insignificant error signals such as, for example, those of order of magnitude of $\times 10^{-14}$. The sampling rates, time constants and quantization levels can be found in Appendix B.

3.2.8 Simulation Configuration

The Simulink simulation is discretized using the Tustin and Backward Euler method with a T_s of 5x10^{-6} s. As the simulation was discretized, purely resistive snubbers were needed to simulate having no snubbers in the 'Universal Bridge' [117]. To do this, the default snubber parameters in the 'Universal Bridge' were used (Appendix B).

This high sampling rate provided a numerical stiffness issue as the sampling time was much

higher than the simulation time (microseconds versus minutes). To mitigate against the potentially high computational cost, the simulations were run concurrently using parallel computing techniques with MATLAB configured to load the SIMULINK model and run it in the workspace, rather than opening the model for each simulation instance. This significantly reduced the time to produce the simulation results.

To tune the PI controllers, due to limitations in the MATLAB software, a simpler model of the drive train was constructed. The PMSG was modelled as found in [111] and the MSC was omitted. SIMULINK's 'Tune' graphical user interface in the PI controllers was used to tune the controllers before the PI parameters were applied to the more complex model. These parameters and the sampling rates, time constants, and quantization levels can be found in Table 3.3 and Appendix B.

Table 3.3: Converter and control parameter values. Notes can be found in Appendix B

Parameter	Value	Reference	Parameter	Value	Reference
V_f	0.95V	[116]	$V_{f,d}$	0.95V	[116]
T_f	0s	Note 3	T_t	0s	Note 3
R_{on}	1.2mΩ	[116]	V_{DC}	1150V	Sec. 3.2.5
R_{snub}	$1\times10^5\Omega$	[117]	C_{snub}	∞F	[117]
$R_{c/r}$	200	Note 4	β_{max}	45°	[123]
β_{min}	45°	[123]	$\beta_{rate,max}$	8°/s	[123]
$\beta_{rate,min}$	-8°/s	[123]	τ	0.5s	[124]
P_p	3.357	Sec. 3.2.8	I_p	0.012	Sec. 3.2.8
P_{id}	-0.148	Sec. 3.2.8	I_{id}	-5.377	Sec. 3.2.8
P_{iq}	-0.155	Sec. 3.2.8	I_{iq}	-2.689	Sec. 3.2.8
β_{samp}	0.00125s	[123]	β_{quant}	0.01	[123]
ω_{samp}	0.00125s	[123]	ω_{quant}	0.001	[123]
I_{samp}	0.00125s	[123]	I_{quant}	0.01	[123]
T_s	5×10^{-6}s	-	$\omega_{t,max}$	2.43rad/s	Sec. 3.2.6
τ_ω	0.01s	[123]	f_{sw}	2kHz	[115]

3.2.9 Drive Train Model Summary

The drive train model consists of the following key features:

- Modelled as a direct-drive 2MW wind turbine.
- Mechanical drive train modelled as a 2-mass model.
- 2nd order non-salient PMSG modelled in the $dq0$ reference frame.
- FRC with MSC based on SEMIKRON RE stacks.
- GSC modelled as an ideal DC link.
- Turbine controlled using ω_t as the reference signal.
- MPPT achieved using $dq0$ vector control.
- MSC switching achieved using SPWM.
- Power limited above rated wind speed using active pitch control.
- MSC and pitch control allowed to interact to improve turbine response.

3.3 DDTRET: Thermal Loading Model

Chapter 2 outlined a number of approaches for determining the thermal loading of the power converter that have been considered in the literature. For this work the focus was on exploring the validity of manufacturers' approach to thermal modelling and therefore the power loss and thermal equivalent circuit approach was used.

The thermal loading model was based primarily on the approach used by SEMIKRON [105], with modifications made in line with the methodology discussed in [125]. The following sections outline the power loss model (Section 3.3.1), the thermal model (Section 3.3.2) and the temperature initialisation procedure (Section 3.3.3).

3.3.1 Power Loss Model

To convert the current throughput into T_j profiles, power losses must be calculated, specifically:

- The IGBT and diode conduction losses.
- The IGBT switching losses and diode reverse recovery losses.

Conduction Losses

The conduction losses are related to the power dissipated from the devices' internal resistance. This is calculated by determining the voltage and current of the device (3.24, 3.25).

$$P_{C,IGBT} = V_{ce} I_c \tag{3.24}$$

$$P_{C,diode} = V_{fd} I_f \tag{3.25}$$

Where $P_{C,IGBT}$ and $P_{C,diode}$ are the IGBT and diode conduction losses respectively, V_{ce} is the IGBT collector-emitter voltage, V_{fd} is the diode forward voltage, and I_f is the diode forward current.

I_c and I_f are the input currents. V_{ce} and V_f are functions of the device T_j, and I_c and I_f respectively. The functions are given in the manufacturer's data sheet [116] for a T_j of 25°C and 125°C. V_{ce} and V_f are calculated by interpolating between the values given at these reference temperatures.

Switching/Reverse Recovery Losses

Switching and reverse recovery losses occur when there is a change in the direction of voltage and current as device response is not instantaneous but occurs over nanoseconds [125]. Nanosecond simulation is impractical for run times longer than a few seconds and the energy loss information given in manufacturer's datasheets is not detailed enough for accurate temporal loss simulation. For example, the energy loss during switch on (E_{on}), and switch off (E_{off}) are not given separately, but reported as a summation of the two (E_{on+off}) [116]. As such, a simplified approach has to be taken.

With the above assumptions, the switching/ reverse recovery losses were found by:

1. Determining the energy losses at low-high switching events. The switching/reverse recovery energy loss is given as a function of input current at two reference V_{DC}'s and is assumed to be linear [116]. The IGBT energy loss is E_{on+off}, whilst the diode energy loss is twice the reverse energy loss (E_{rr}).

2. Calculating the equivalent modulated power losses over the switching cycle using (3.26-3.29) [105].

$$P_{sw}(t : T_{s,th} : (t + T_{p,sw}(t))) = \frac{E_{on+off}(t)}{T_{p,sw}} \tag{3.26}$$

$$P_{rr}(t : T_{s,th} : (t + T_{p,rr}(t))) = \frac{E_{rr}(t)}{T_{p,rr}} \tag{3.27}$$

$$P_{sw,T_j}(t) = (1 + TC_{Esw}(T_{j,IGBT}(t) - T_{ref}))P_{sw}(t) \tag{3.28}$$

$$P_{rr,T_j}(t) = (1 + TC_{Err}(T_{j,diode}(t) - T_{ref}))P_{rr}(t) \tag{3.29}$$

P_{sw} is the IGBT switching power loss, P_{rr} is the diode reverse recovery power loss, t is the time step, $T_{s,th}$ is the thermal sampling time, $T_{p,sw}$ is the IGBT switching time period, $T_{p,rr}$ is the diode reverse recovery time period, P_{sw,T_j}, P_{rr,T_j} are the T_j corrected P_{sw} and P_{rr} respectively, TC_{Esw}, TC_{Err} are the switching loss and reverse recovery temperature coefficients respectively, and T_{ref} is the reference temperature of the energy loss LUTs.

With the conduction and switching/reverse recovery power losses calculated the total power loss for each device can be calculated by summing the power losses at each time step.

3.3.2 Thermal Loss Model

As discussed in Chapter 2, converter thermal modelling is carried out in three ways:

- Thermal equivalent circuits.
- Thermal diffusion equations.
- FEA.

The choice of thermal model is based on data availability and computational efficiency. The thermal equivalent circuits are used when Foster network RC manufacturing data is available as this is the most computationally efficient whilst providing accurate results. Modifications are made to improve the network accuracy further, which often involves converting to a Cauer network. If this data is not available or detailed device analysis is required, thermal diffusion equations or FEA is used. However these methods are computationally expensive. As the

RC network data was available, and detailed analysis of the internal thermal paths was not required,a thermal equivalent circuit was used.

The data given in [105] is for a Foster RC network. This network gives a numerical approximation of the thermal network which means that the calculated temperatures, except T_j and T_a, have no physical meaning. To provide a more accurate half-bridge temperature profile, the Foster thermal resistance ($R_{th,f}$) and time constant (τ_{th}) parameters were converted into RC parameters (3.30) [126], and then converted into Cauer RC parameters using the algorithm available at [127]. This conversion was carried out independently for each IGBT, diode and heat sink. Figure 3.11 gives the half-bridge Cauer RC network.

$$C_{th,f} = \frac{\tau_{th}}{R_{th,f}} \tag{3.30}$$

Where $C_{th,f}$ is the Foster thermal capacitance.

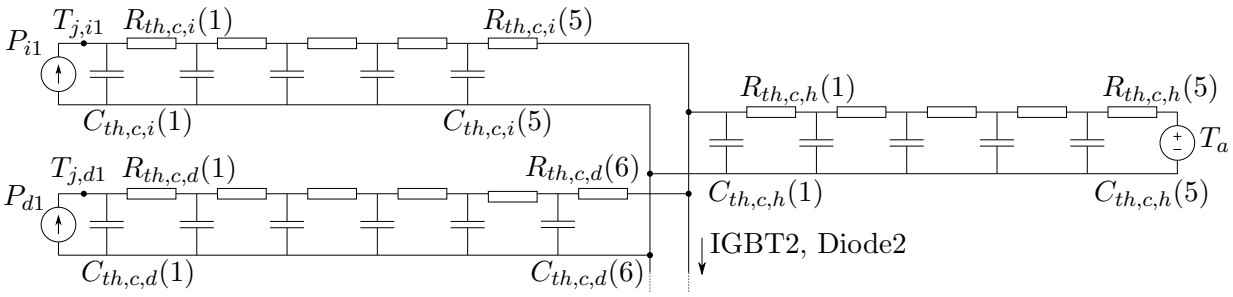

Figure 3.11: Half bridge Cauer RC network (only one IGBT and diode represented here).

P_{i1} is the IGBT power loss, P_{d1} is the diode power loss, $T_{j,i1}$ is IGBT1's junction temperature, $T_{j,d1}$ is diode1's junction temperature, $R_{th,c,i}$ is the IGBT Cauer thermal resistance, $R_{th,c,d}$ is the diode Cauer thermal resistance, $R_{th,c,h}$ is the heatsink Cauer thermal resistance, $C_{th,c,i}$ is the IGBT Cauer thermal capacitance, $C_{th,c,d}$ is the diode Cauer thermal capacitance and $C_{th,c,h}$ is the heatsink Cauer thermal capacitance. The values can be found in Table 3.4 and Appendix B.

Table 3.4: Thermal model parameter values

Parameter	Value	Reference	Parameter	Value	Reference
T_a	40°C	[80]	$R_{th,c,i}(1)$	1.5×10^{-3}K/W	-
$R_{th,c,i}(2)$	7.3×10^{-3}K/W	-	$R_{th,c,i}(3)$	5.9×10^{-3}K/W	-

Continued on next page

Table 3.4 – *Continued from previous page*

Parameter	Value	Reference	Parameter	Value	Reference
$R_{th,c,i}(4)$	2.5×10^{-3}K/W	-	$R_{th,c,i}(5)$	0.37×10^{-3}K/W	-
$C_{th,c,i}(1)$	0.55Ws/K	-	$C_{th,c,i}(2)$	3.61Ws/K	-
$C_{th,c,i}(3)$	35.90Ws/K	-	$C_{th,c,i}(4)$	476.61Ws/K	-
$C_{th,c,i}(5)$	4.81×10^{3}Ws/K	-	$R_{th,c,d}(1)$	2.8×10^{-3}K/W	-
$R_{th,c,d}(2)$	10.2×10^{-3}K/W	-	$R_{th,c,d}(3)$	10.5×10^{-3}K/W	-
$R_{th,c,d}(4)$	11.9×10^{-3}K/W	-	$R_{th,c,d}(5)$	8.6×10^{-3}K/W	-
$R_{th,c,d}(6)$	0.94×10^{-3}K/W	-	$C_{th,c,d}(1)$	0.773Ws/K	-
$C_{th,c,d}(2)$	1.45Ws/K	-	$C_{th,c,d}(3)$	4.90Ws/K	-
$C_{th,c,d}(4)$	36.07Ws/K	-	$C_{th,c,d}(5)$	577.76Ws/K	-
$C_{th,c,d}(6)$	1.60×10^{4}Ws/K	-	$R_{th,c,h}(1)$	0.79×10^{-3}K/W	-
$R_{th,c,h}(2)$	3.1×10^{-3}K/W	-	$R_{th,c,h}(3)$	4.3×10^{-3}K/W	-
$R_{th,c,h}(4)$	0.88×10^{-3}K/W	-	$R_{th,c,h}(5)$	0.14×10^{-3}K/W	-
$C_{th,c,h}(1)$	337.28Ws/K	-	$C_{th,c,h}(2)$	409.76Ws/K	-
$C_{th,c,h}(3)$	$1.37\times^{3}$Ws/K	-	$C_{th,c,h}(4)$	$1.91\times^{4}$Ws/K	-
$C_{th,c,h}(5)$	$1.30\times^{4}$Ws/K	-	$T_{j,ref}$	125°C	-
TC_{Esw}	0.003	[105]	TC_{Err}	0.006	[105]

In this case, T_a is set to 40°C as found in [80] and is the temperature of the cooling fluid. It is assumed that this cooling fluid system is adequately sized to provide a constant temperature at the heat sink surface. This was deemed sufficient for this study, but this could be adapted to consider an imperfect cooling system.

3.3.3 Thermal Model Initialisation

The power losses (P_{loss}) are dependent on T_j and therefore the power loss and thermal sub-systems must be run con-currently. Technically, the current throughput of the devices is also dependent on the power losses and T_j, but it was assumed that this effect would be negligible [125].

Due to the power-thermal inter-dependency, the initialisation of C_{th} temperatures was solved

iteratively. The initial steady-state temperatures are related to the R_{th} only [105], with the temperatures analogous of a voltage drop (temperature) due to a current throughput (power). The steps are as follows:

1. Set initial temperatures for each C_{th} (typically to T_a).
2. Take first 0.5s of input current for each device.
3. Calculate power loss over 0.5s given device T_j.
4. Calculate steady state temperatures using R_{th} only.
5. Update device temperatures.
6. Compare previous and new device temperatures. If the variation is less than 0.001°C then the temperatures are deemed correct as the change will now be insignificant. Otherwise repeat steps 2-6.

This initialisation is dependent on variations in the input current and therefore all tests are carried out with a 5s constant wind speed at the start.

3.4 DDTRET: Lifetime Model

With the T_j profiles calculated using the approach explained in Section 3.3, the impact of operating conditions on power converter remaining useful life can be estimated. As discussed in Chapter 2 there are a number of approaches taken for estimating the impact of temperature on the reliability of the device, but they are all based on fatigue cycles. Therefore, as SEMIKRON specific data is available, and more complex modelling techniques' applicable operating conditions limit their viability, SEMIKRON's cycles-to-failure against mean T_j and ΔT_j for IGBT3 modules was used (Figure 3.12).

With the lifetime data available from data sheets, the total device life used be calculated using the following steps:

1. Break down the T_j data into cycles with mean T_j ($T_{j,mean}$) and ΔT_j. This was carried out using the rainflow counting algorithm available in MATLAB [128].
2. Use cycle data to provide a cycles-to-failure look-up table (LUT) and calculate percentage of total life used per cycle.

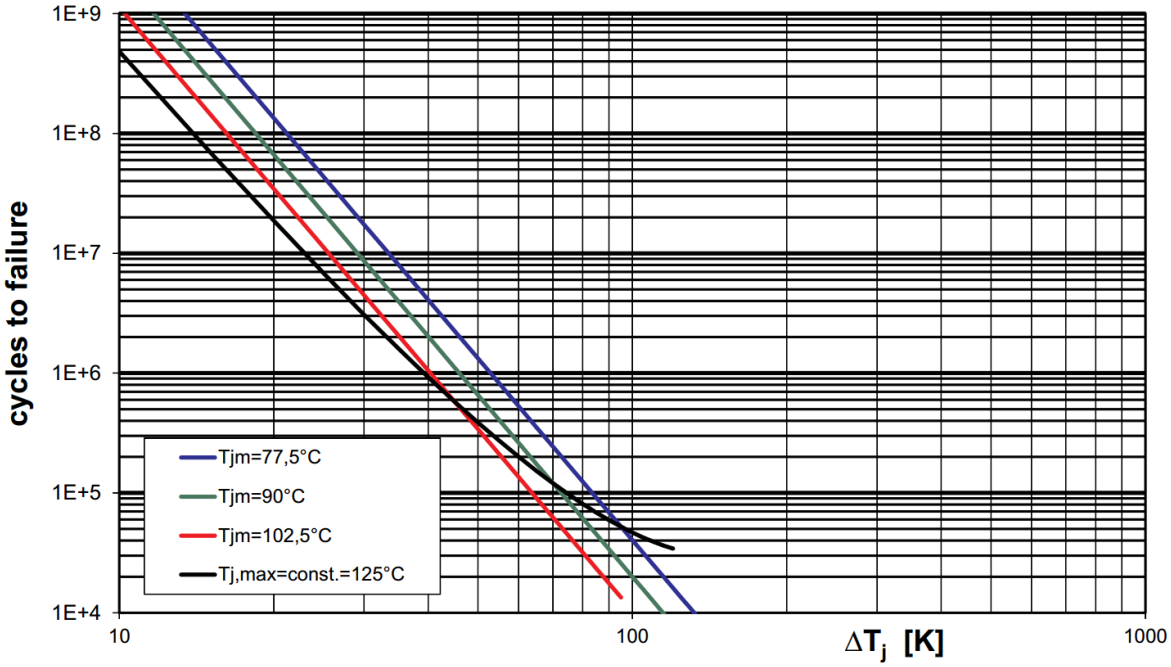

Figure 3.12: SEMIKRON IGBT3 cycles to failure data [105].

3. Sum the percentage of total life used per cycle to produce percentage of total life used due to the given thermal profile.

There has been little discussion in the literature about the minimum ΔT_j range over which damage to the power module occurs; an issue that is briefly outlined in [85]. In general, studies either disregard cycles that have a ΔT_j of less than 30K due to a lack of manufacturer's data, or extrapolate the curves given to cover all temperature swings. SEMIKRON's data reaches as low as 10K (Figure 3.12), but it is unclear if this is based on experimental data or extrapolation of existing data.

Held et al. has attempted to provide an empirical limit to the ΔT_j that will cause damage to the power module by considering the limit for plastic strain to occur in the aluminium of an IGBT [129]. This limit was given as 18K, though in reality the limit may be lower due to the simplified model of the bondwire used in the analysis. The effect of this limitation on life estimation will be explored in Chapter 5.

3.5 DDTRET Drive Train Model Verification

This section outlines the DDTRET electrical response to a range of static and dynamic wind speed conditions to verify that the drive train responds as theoretically expected. The conditions shown are:

- Wind speed reduction in MPPT operating region (Section 3.5.1) to test the wind turbine model under variable speed conditions.
- Wind speed increased from MPPT to rated operating region (Section 3.5.2) to verify that the controller interaction introduced in Section 3.2.6 is operating correctly, and to verify that the pitch controller is stable.

To note, validation of the DDTRET's thermal reponse can be found in Chapter 5.

3.5.1 Wind Speed Reduction in MPPT Operating Region

Figure 3.13 details the turbine response to a ramped reduction in wind speed from 12m/s to 8m/s in the MPPT operating region. The following steps describe the turbine response to this large reduction in wind speed:

1. As the wind speed drops (Fig. 3.13.a, 1.5 to 2s), P_t reduces (Fig. 3.13.b, 1.5 to 2s).
2. As the ω_t response (Fig. 3.13.c) is limited by the drive train dynamics, the reduction in P_t causes a dramatic reduction in T_t (Fig. 3.13.d, 1.5 to 2s).
3. As the turbine control signals are based on the ω_t, T_g only reduces slowly (Fig. 3.13.e) and therefore is greater than T_t, causing turbine rotor deceleration.
4. ω_t subsequently reduces (Fig. 3.13.c), triggering the MSC controller to reduce I_q (Fig. 3.13.h).
5. As I_q reduces, T_g reduces proportionally (Fig. 3.13.e), causing a lower $T_t - T_{ref}$ (Fig. 3.13.d), and therefore a lower α_t (Fig. 3.13.c).
6. When T_t and T_{ref} converge (Fig. 3.13.d, 29s), ω_t remains constant (Fig. 3.13.c, 29s). C_p returns to its maximum value (Fig. 3.13.f, 29s), and P_t increases slightly (Fig. 3.13.b), showing successful MPPT region operation after a large wind speed change.

3.5.2 Wind Speed Ramp from MPPT to Rated Operating Region

Figure 3.5.2 details the turbine response to a ramp in wind speed from 11m/s to 13.5m/s; from the MPPT to rated operating region. The turbine rated wind speed (u_{rat}) is 12.7m/s and $P_{t,r}$ is the rated turbine power. The turbine response is slower than in Section 3.5.1 and is more complex due to controller interaction. The following steps describe the turbine response to this large reduction in wind speed:

1. As the wind speed increases (Fig. 3.5.2.a, 1.5 to 2s), P_t increases (Fig. 3.5.2.b 1.5 to 2s).

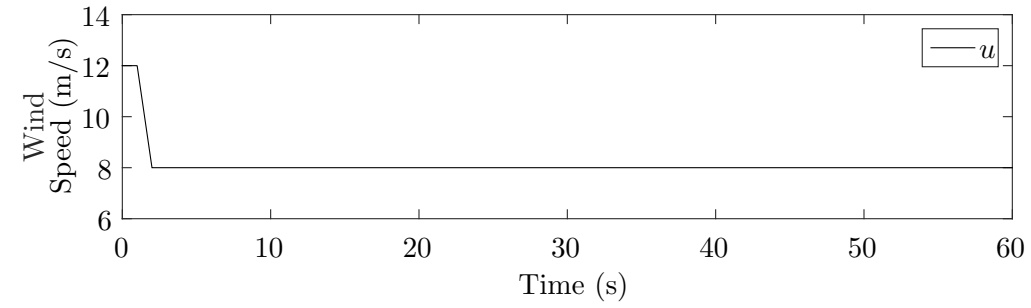
Wind
Speed (m/s)
14
12
10
8
6
0
10
20
30
40
50
60
Time (s)
u

(a)

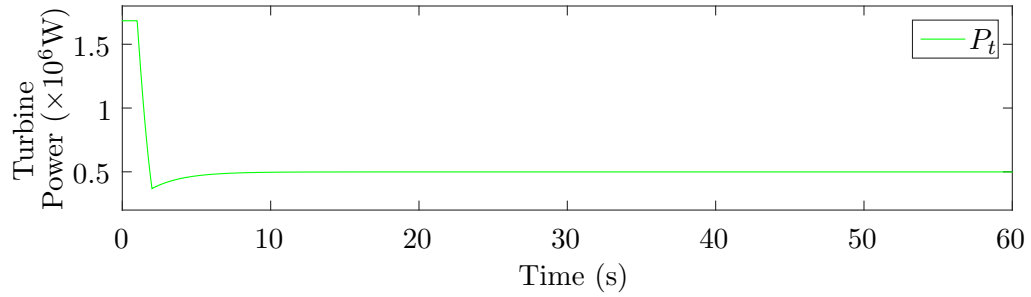
Turbine
Power (×10^6W)
1.5
1
0.5
0
10
20
30
40
50
60
Time (s)
P_t

(b)

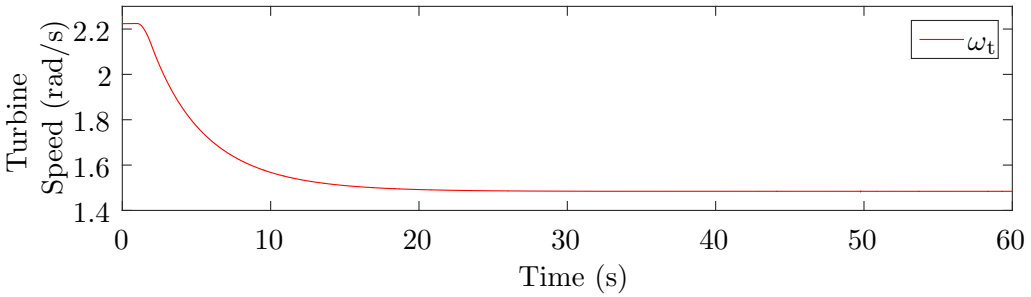
Turbine
Speed (rad/s)
2.2
2
1.8
1.6
1.4
0
10
20
30
40
50
60
Time (s)
ω_t

(c)

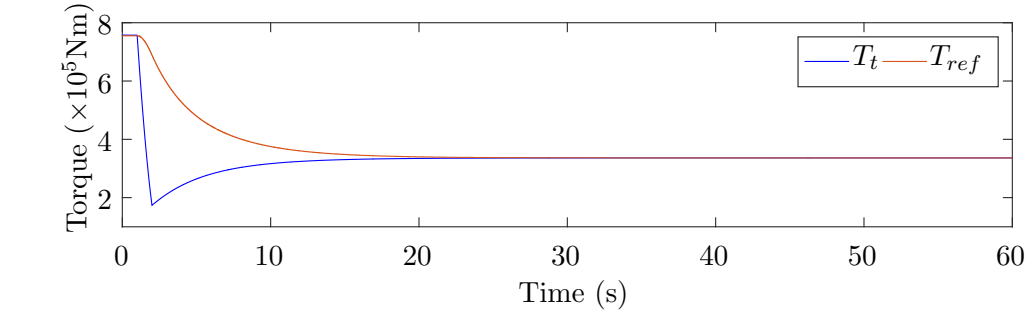
Torque (×10^5Nm)
8
6
4
2
0
10
20
30
40
50
60
Time (s)
T_t
T_ref

(d)

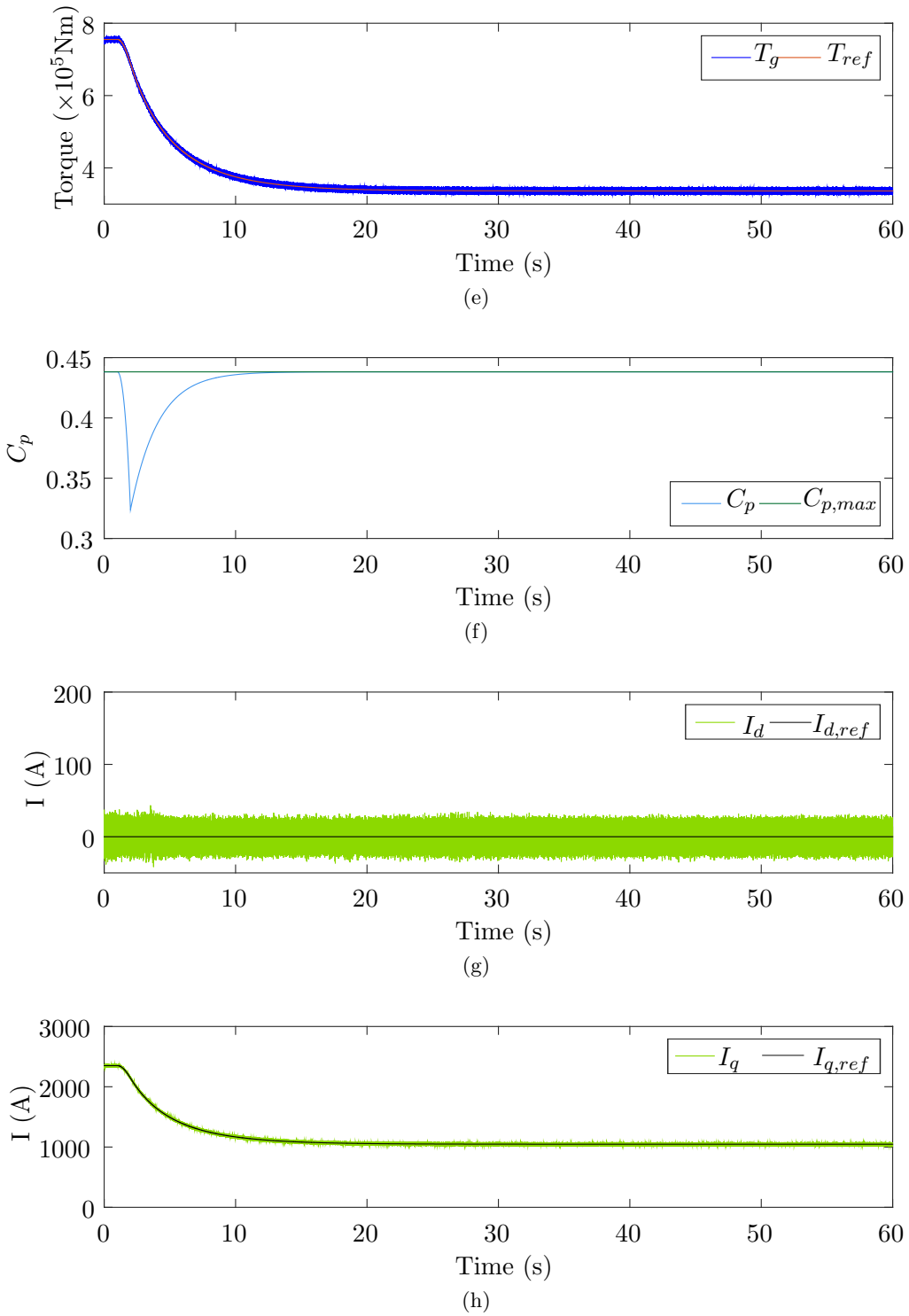

Figure 3.13: Turbine response to reduction in wind speed: (a) wind speed, (b) turbine power, (c) turbine speed, (d) turbine torque, (e) generator torque, (f) C_p and (g, h) generator d, q currents.

2. As the ω_t response (Fig. 3.5.2.c) is limited by the drive train dynamics, the increase P_t causes a dramatic increase in T_t (Fig. 3.5.2.d, 1.5 to 2s).

3. As the turbine control signals are based on ω_t, T_g remains low (Fig. 3.5.2.e) compared to T_t, causing turbine rotor acceleration.

4. ω_t subsequently increases (Fig. 3.5.2.c), triggering the MSC controller to increase I_q (Fig. 3.5.2.h).

5. As I_q increases, T_g increases proportionally (Fig. 3.5.2.e), causing a lower $T_t - T_{ref}$, and therefore a lower $\Delta\omega_t$ (Fig. 3.5.2.c).

6. ω_t exceeds the rated turbine speed ($\omega_{t,rat}$) at approximately 6s (Fig. 3.5.2.c), causing the pitch controller to respond (Fig. 3.5.2.f).

7. Both controllers interact to control the turbine until ω_t exceeds the maximum turbine speed ($\omega_{t,max}$) at approximately 7s (Fig. 3.5.2.c). I_q remains at $I_{q,max}$ (Fig. 3.5.2.h) to support the pitch controller until the controllers reduce ω_t below $\omega_{t,max}$ again.

8. When T_t and T_{ref} converge (Fig. 3.5.2.d, 37s), ω_t remains constant (Fig. 3.5.2.c), β and I_q are constant (Fig. 3.5.2.f,h), and C_p is now at a lower value (Fig. 3.5.2.g). The controllers have returned P_t to 2MW (Fig. 3.5.2.b), showing successful rated region operation after a large wind speed change.

Interaction between the controllers occurs, increasing the complexity of the current experienced by the power module devices (Figure 3.5.2.h) compared to directly deriving the current from the wind speed. I_q reaches 2800A rather than stopping at 2640A, and provides a much longer, and more realistic, variation in current.

The interaction between controllers may be avoided by disabling the MSC controller when the pitch controller is active. However, the response of the turbine would be slower and simulations revealed that in some extreme cases the turbine became marginally stable (continually oscillated around the target ω_t). Therefore controller interaction is necessary for good turbine performance.

3.6 Summary

In a wind turbine, electrical loading is highly variable and is determined by wind speed, the wind turbine configuration and the control strategies. Simplified drive train models found in the literature miss the effects of mechanics on the electrical loading. Therefore, to provide wind turbine representative electrical loading profiles for simulation and experimentation, a highly detailed drive train model and power module thermal model (DDTRET) were constructed that

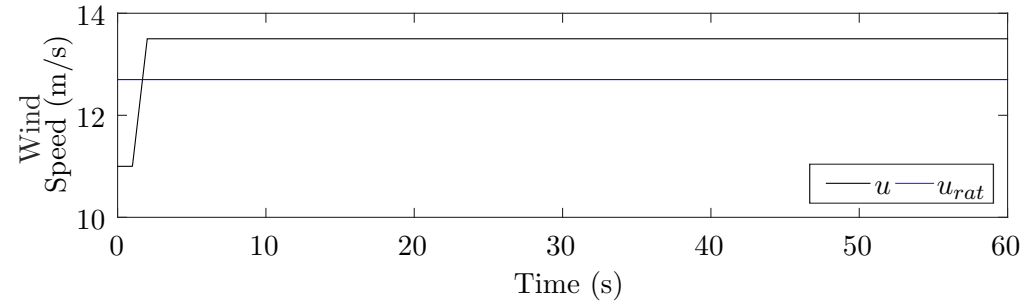
Wind Speed (m/s)
14
12
10
0
10
20
30
40
50
60
Time (s)
u
u_{rat}

(a)

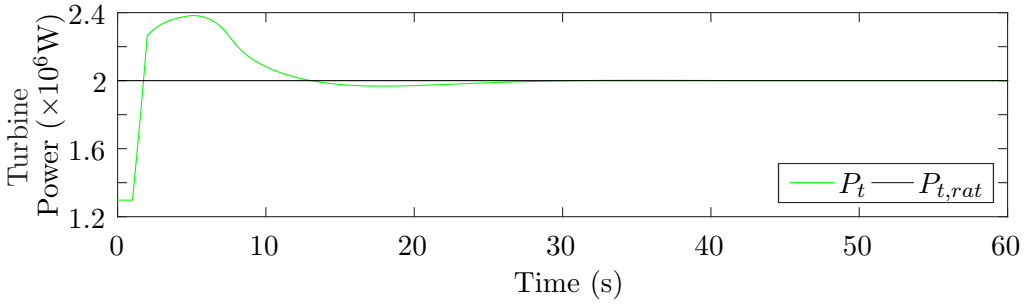
Turbine Power ($\times 10^6$W)
2.4
2
1.6
1.2
0
10
20
30
40
50
60
Time (s)
P_t
$P_{t,rat}$

(b)

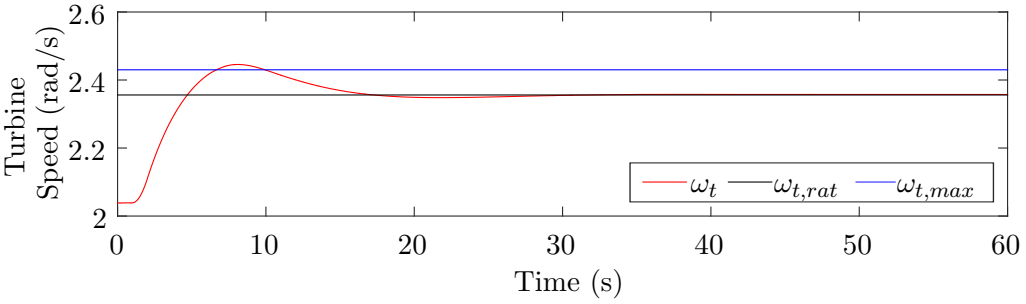
Turbine Speed (rad/s)
2.6
2.4
2.2
2
0
10
20
30
40
50
60
Time (s)
ω_t
$\omega_{t,rat}$
$\omega_{t,max}$

(c)

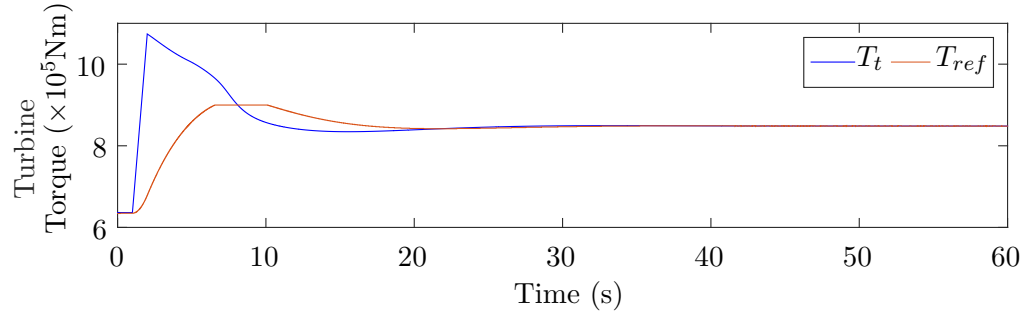
Turbine Torque ($\times 10^5$Nm)
10
8
6
0
10
20
30
40
50
60
Time (s)
T_t
T_{ref}

(d)

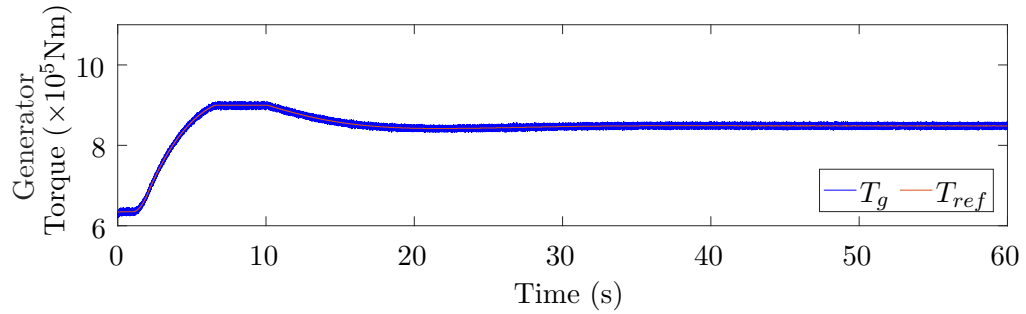
Generator Torque ($\times 10^5$Nm)
10
8
6
0
10
20
30
40
50
60
Time (s)
T_g
T_{ref}

(e)

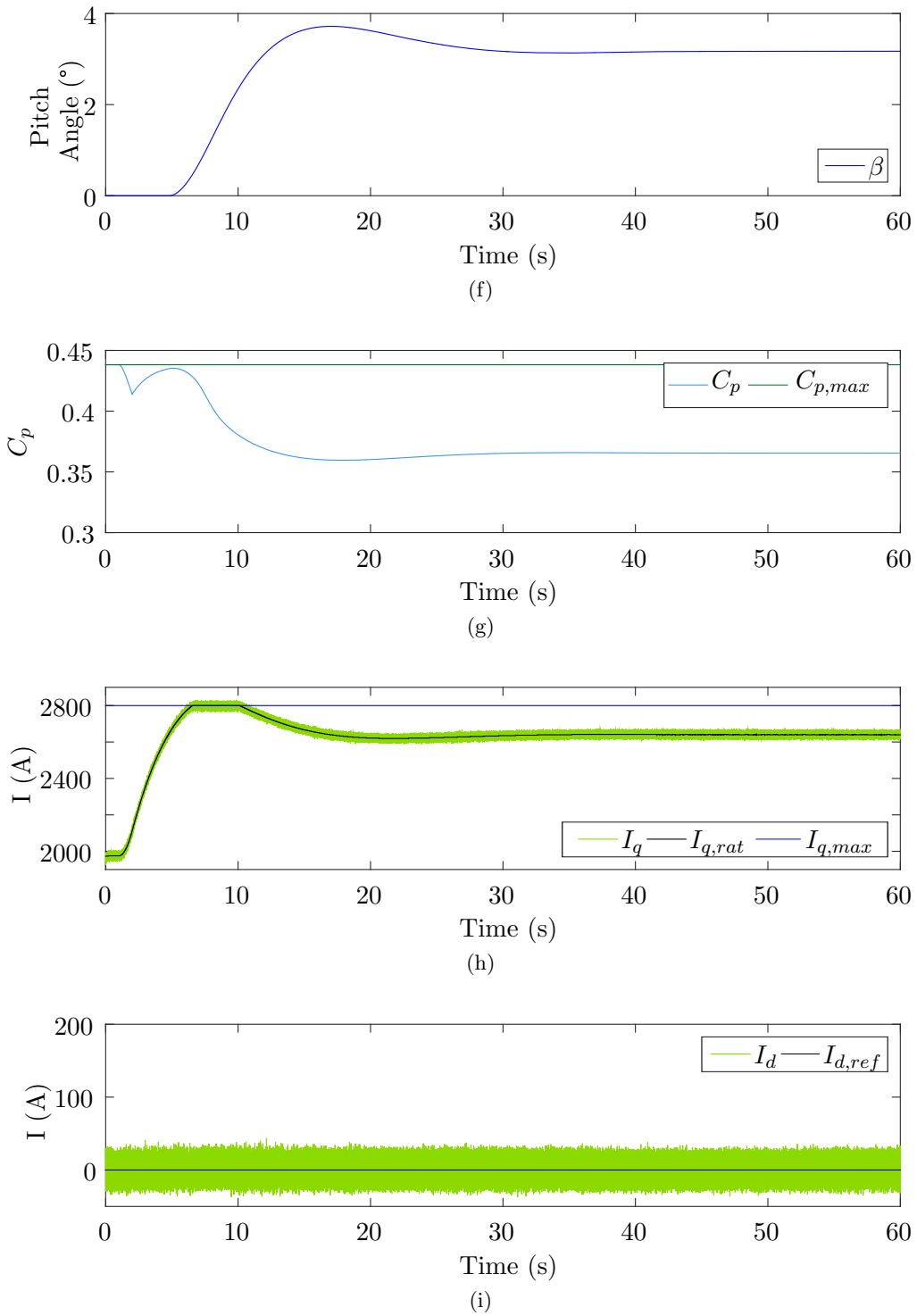

Figure 3.14: Turbine response to wind speed ramp from 11 to 13.5m/s: (a) wind speed, (b) turbine power, (c) turbine speed, (d) turbine torque, (e) generator torque (f) pitch angle, (g) C_p, and (h, i) generator d, q currents.

included key aspects of wind turbine drive trains. Figure 3.15 summarises the whole system model.

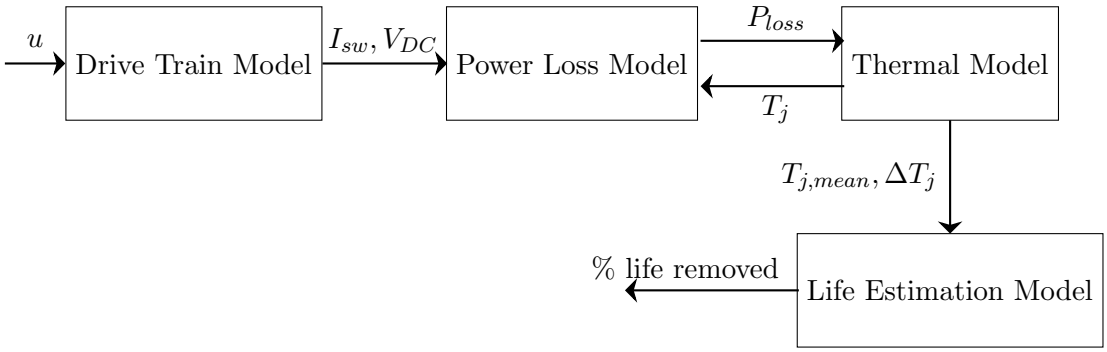

Figure 3.15: Summary of DDTRET.

The DDTRET consists of a 2MW FRC PMSG turbine with MPPT achieved using torque control and rated operation maintained using an active pitch system. There are also detailed models for rotor power extraction, drive train dynamics, generator, MSC, DC link, turbine control and sensors.

The DDTRET's thermal model consists of two key aspects: power loss model and a thermal equivalent circuit. The power loss model considers conduction losses, IGBT switching losses and diode reverse recovery losses. The thermal equivalent circuit uses Cauer RC parameters for a half-bridge module and heat sink. Due to the interdependence between power loss and temperature, the model must be simulated concurrently and the initialisation is performed iteratively.

A lifetime model was outlined based on the cycles-to-failure versus $T_{j,mean}$ and ΔT_j. The cycles from a thermal profile are counted using a rainflow counting algorithm.

Finally, the operation of the drive train model was verified using two wind speed scenarios to show the MSC and pitch control in action, including their interaction. DDTRET successfully responded to the extreme changes in wind speed.

Chapter 4

Experimental Rig Construction

4.1 Introduction

To provide the holistic approach outlined in Chapter 2, the drive train simulation described in Chapter 3 is complimented with an experimental rig to measure the T_j profiles in a laboratory setting. This chapter outlines various temperature measurement approaches and chooses the most suitable for this application (Section 4.2). The chosen measurement approach is then described and calibrated in Section 4.3. Finally, the experimental rig to produce the necessary T_j profiles is detailed and verified in Section 4.4.

4.2 Temperature Measurement Approaches

There are three main categories of temperature measurement: direct contact, estimation through temperature sensitive parameters, and measurement of IR radiation.

4.2.1 Direct Contact Approaches

Direct contact with the measured device can be carried out using a thermocouple or thermistor. A thermocouple relies on two different metals that produce a potential difference between them when heated, whilst a thermistor changes resistance with temperature. As these approaches are based on conduction, they require adhesion to the DUT, and typically have slow response times of hundreds of ms [130]. This makes them unsuitable for high frequency temperature measurements. This is highlighted by their limited use in power converter literature, with only one example of use for temperature monitoring [104], and as a steady state validation tool for other approaches [131].

Thermistors are frequently used to monitor the approximate temperature of the power modules [105], but are typically situated at relatively large distances from the power module devices (15mm, Figure 4.1), making them unsuitable for precise temperature measurement.

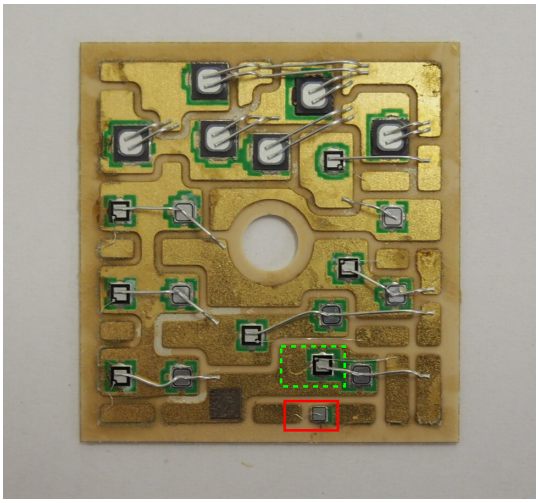

Figure 4.1: Photograph of typical power module device, highlighting the thermistor (red solid box) and the nearest chip (green dashed box).

4.2.2 IR Spectrum

A body will emit IR with a spectral content that is determined by the temperature of the body and the emissivity of the body's surface. This relationship is well documented and can be calculated using Planck's formula for a black body (emissivity (ϵ) of 1) (4.1). Therefore, by measuring the spectral radiance from a body over a specified wavelength range using a photoconductive sensor and correcting for output by the emissivity of the body (as a percentage of the radiance from a black body), the temperature of the body can be measured without physical contact with the body.

$$B_{\lambda_w} = \frac{2hc^2}{{\lambda_w}^5(e^{\frac{hc}{\lambda_w K_B T}} - 1)} \tag{4.1}$$

B_{λ_w} is the spectral radiance in terms of wavelength λ_w, h is the Planck constant, c is the speed of light, and T is the temperature.

IR measurement comes in two main forms; IR cameras and IR sensors. The output of IR cameras are more recognisable by their multi-coloured images, providing an array of temperatures for a surface. Unfortunately IR cameras are often expensive, particularly when fast response times and accurate temperature measurements are required, making them unsuitable for cer-

tain experimental work. As such, IR cameras have been typically been used for validation of other temperature measurement/estimation approaches: thermal sensitive parameter validation experiments [132], validating power converter thermal models [85, 133, 134], and validating the use of IR sensors in certain applications [131].

In contrast, IR sensors are essentially single pixel IR cameras and are subsequently less expensive. They are also able to measure spot temperatures more accurately, making them ideal for use in T_j monitoring in the power module.

Research involving IR sensors for power converter T_j measurements has primarily been concerned with comparison with other temperature measurement approaches to assess their suitability. This includes the favourable comparison of IR sensors with an IR camera, but with a low sample rate of 1S/s due to the averaging processing used [131]. IR sensors could therefore be an effective measurement device for T_j due to the low cost, accuracy and small size.

IR approaches have some disadvantages. Firstly, though requiring no physical contact with the measured device, line of sight is required. This requires modification of the measured device through removal of its protective casing. Furthermore, as the measured radiation is dependent on the emissivity of the device, the sensor must be calibrated for each new device type to compensate for this [135].

As far as the author is aware, there has been limited use of IR sensors in wind turbine applications. IR sensors have been used by Bartram et al. to verify an FEA model of a DFIG power converter [74]. The IR sensor in this application was used to produce both a spatial and temporal temperature mapping of the whole module. The temporal fidelity of the results is relatively low for the required sampling frequency of 4kHz in this research.

4.2.3 Temperature Sensitive Electrical Parameters

Temperature sensitive electrical parameters use measurable device voltages and currents to estimate the temperature of the power module devices. Some examples include the measurement of collector-emitter saturation voltage (V_{ces}), gate-emitter voltage (V_{ge}) and saturation current (I_{css}) [132]. In all cases, a small measurement signal is needed that is independent of the normal operating conditions. Therefore, to be used in a functional environment, the converter control requires complex changes and the measurement signals are susceptible to the noisy converter electromagnetic environment. This makes these measurement approaches impractical [133].

4.2.4 Chosen Approach

With all three of these approaches there are disadvantages, and a compromise must be made when choosing a suitable temperature approach.

Temperature sensitive electrical parameters require complex changes to the converter operation and will therefore not be able to provide wind turbine representative operating conditions during measurement. Whilst this approach is practical for a laboratory setting, it is unlikely that any feasible approach will be created that could be used for live monitoring of wind turbine converter and as such these methods are not considered further in this research.

Direct contact approaches, such as a thermocouple, require direct contact using various adhesives that, during preliminary testing, varied the temperature significantly due to thermal insulation of the device. Coupled with the slow response rates, this approach would never be a practical long term solution for detailed temperature measurement of power modules.

IR, due to its lack of physical contact, fast response times, and lack of modification to the converter operation, make it the most suitable measurement approach. With the need to modify the power module to provide line-of-sight, the relatively low cost and small size of IR sensors have made it a more attractive approach than the use of IR cameras. In particular, their small size means that future development of the technology could, unlike the other approaches, make them suitable for implementation into the converter design for field tests. As such, the IR sensor has been chosen to measure T_j in the power modules.

As IR sensors do not provide a perfect solution for measuring T_j, the rest of this chapter concerns itself with the set-up of the IR sensor, with a focus on providing solutions to three challenges:

- The sensor needs line-of-sight to the measured device in the IR spectrum, but the power modules are typically enclosed in IR-opaque materials.
- The sensor must be calibrated using an external measurement.
- The emissivity of the power module device surfaces is unknown.

4.3 Thermal Measurement: Measurement Set-up

The following section outlines the requirements of the thermal measurement set up of the sensor. The set up is highly dependent on the sensor selected, and therefore the first stage was to

determine the sensor technology used (Section 4.3.1). With the sensor chosen, the required optics and device mounting to focus on the DUT is outlined, alongside the sensor amplification circuitry (Section 4.3.2). Finally, the sensor calibration is outlined in Section 4.3.3.

4.3.1 Infra-red Sensor Selection

When selecting IR sensors for this research there were 4 main considerations:

1. Response time.
2. Spectral range.
3. Detectivity (how well the sensor detects the signal magnitude at a given wavelength).
4. Sensor cost.

As discussed in Section 4.2.2, a black body radiates a spectrum of infra-red light with the distribution and radiance dependent on the temperature of the body. To aid in determining the most suitable sensor for this experiment, the spectra for expected minimum (25°C) and maximum temperatures (125°C) were examined over the relevant IR spectral range for temperature measurement (0.7 - 25μm). This spectrum was then compared to the sensor detectivity over this range.

In general, it was found that sensors with faster response time and higher maximum detectable spectral wavelength were orders of magnitude more expensive. Furthermore, sensors with a wider spectral range also had lower maximum detectivity. After considering a number of options, a compromise between cost, response time, and spectral range was reached by using a PbSe photoconductive sensor from ThorLabs [136] (Figure 4.2). Figure 4.3 highlights the spectral range and relative photo sensitivity (result is given at 15V supply voltage as given in the datasheet; the detectivity of the sensor can be increased by increasing this voltage) in comparison to the body's spectral response.

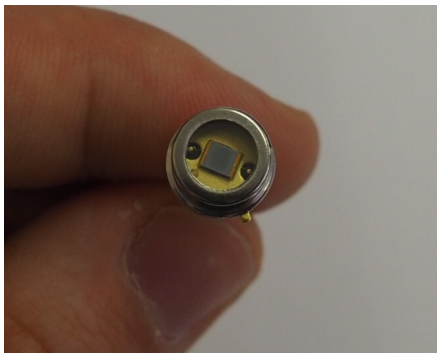

Figure 4.2: Photograph of PbSe photoconductive sensor.

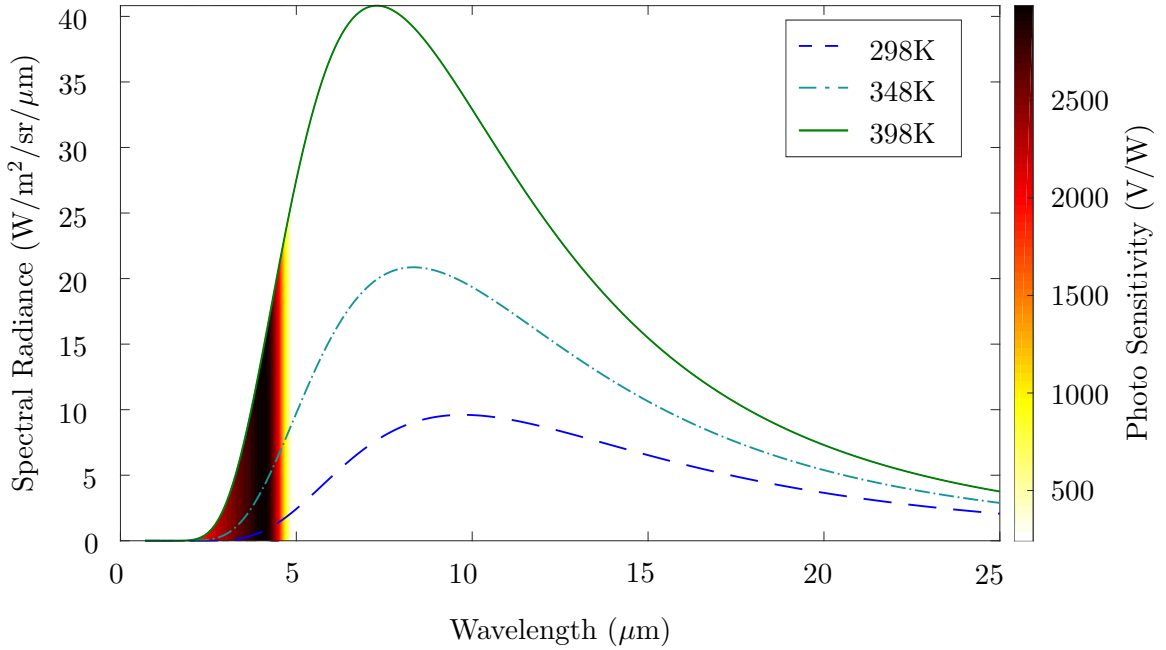

Figure 4.3: Black body radiance compared with the relative photo sensitivity of the PbSe photoconductive sensor.

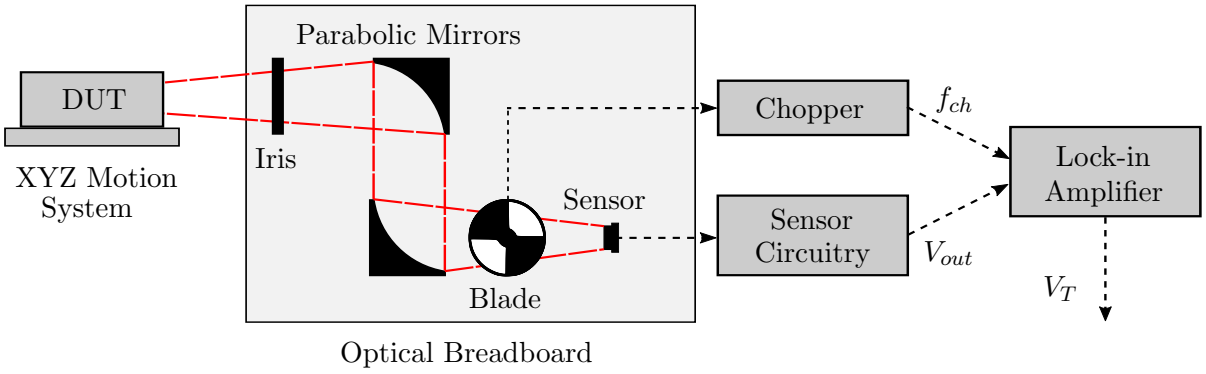

Figure 4.4: Optical set-up. V_T is the temperature dependent voltage output and f_{ch} is the chopping frequency.

4.3.2 Optics and Sensor Circuitry

With the sensor selected, the sensor signal must be captured and processed. Figure 4.4 summarises the optical set-up and Figure 4.5 provides photographs of the equipment. This section outlines the key features of each of the components.

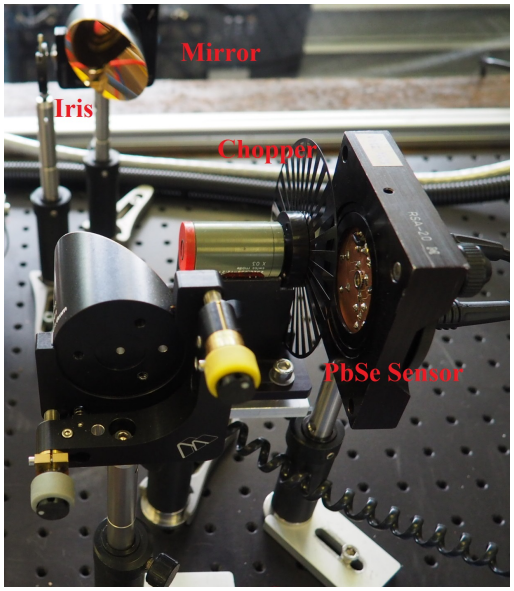

(a)

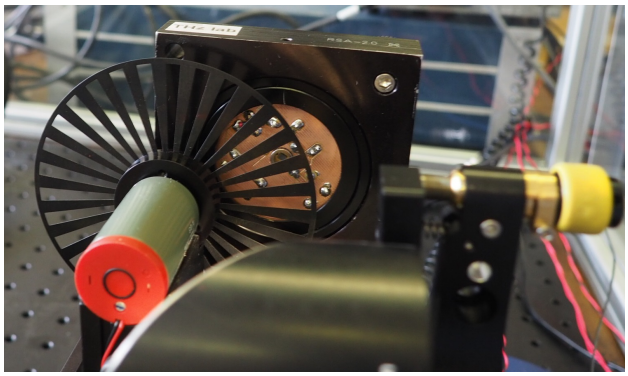

(b)

Figure 4.5: Photographs of optical equipment. (a) Parabolic mirrors and chopper, (b) close up of chopper and mounted IR sensor.

XYZ Motion System

The high sensitivity of the sensor to changes in IR meant that the DUT had to be precisely positioned. To achieve this precision an XYZ motion system was installed with 0.01mm precision in all 3 axes. The DUT was mounted to the Z-axis motion panel.

Mirrors and Iris

As a body radiates IR omni-directionally, it was crucial to focus the IR onto the sensor to provide the strongest possible signal. Therefore, two 4-inch parabolic mirrors were used. An iris was added to aid in aligning to ensure no other sources of IR were being measured (Figure 4.5).

Sensor Circuitry and Amplification

Figure 4.6 provides a schematic diagram of the sensor circuitry. Two capacitor types were used to smooth the incoming DC voltage, and the 50Ω resistor acts as the bias resistor as per the IR sensor's manufacturing specifications.

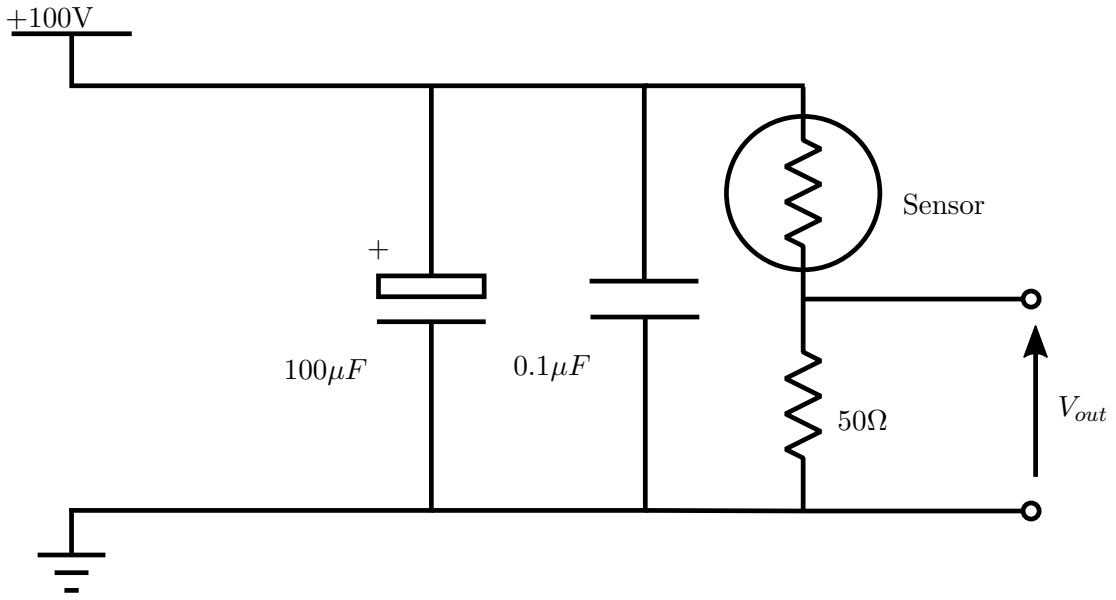

Figure 4.6: Sensor circuit diagram.

Photo-conductive sensors have a large DC bias from the sensor supply that masks any voltage change due to the dark resistance so it is necessary to pulse the incident radiation to generate an AC signal and remove the impact of this DC bias from the output voltage. This was done using an optical chopper, where a blade with open segments is spun at a given frequency in the path of the incident IR radiation As the chopping frequency is known, ΔV_{out} due to the change in dark resistance can be detected and amplified using a lock-in amplifier searching at the set chopping frequency. Higher chopping frequencies provide higher signal-to-noise ratios [136]. Subsequently, a 3.5kHz chopping frequency was used as this was the highest the available equipment would allow without interference from the second harmonic of the DUT switching frequency (which is 4kHz, See Section 4.4.4).

4.3.3 Sensor set-up Verification and Calibration

As the IR sensor used in the research was not pre-calibrated and some modifications were made to the device to improve its emissivity, it was important to verify the effect of these changes and then calibrate the sensor. This section verifies the improvements made with the addition

of white-out fluid and impact of the silicon gel. The sensor is then calibrated and the noise patterns found in the sensor analysed.

Emissivity Improvement

Power module components typically have an emissivity (ϵ) of much less than 1. Therefore, the IR radiation will be much lower than the theoretical maximum. To maximise the radiation, the ϵ was increased to 0.95-0.96 using a white-out fluid [135] painted onto the surface of the DUT using a delicate brush. White-out fluid also has a short curing time, making it ideal for laboratory use. There is also a silicon gel isolating gel that covers the device that will not transmit 100% of this IR radiation. Therefore this silicon gel was removed from the surface of the DUT.

To verify the white-out fluid's impact and the silicon gel's impact on emissivity, a device with a similar material composition and surface area to the DUT was tested: two parallel 20Ω surface-mount resistors. The surface-mount resistors were mounted on a small PCB using lead-free solder (lead solder failed when the surface temperature reached around 100°C). The PCB was mounted on a polyurethane model board block to ensure that the mounting material did not act as a heat-sink. The test resistor set-up is shown in Figure 4.7.

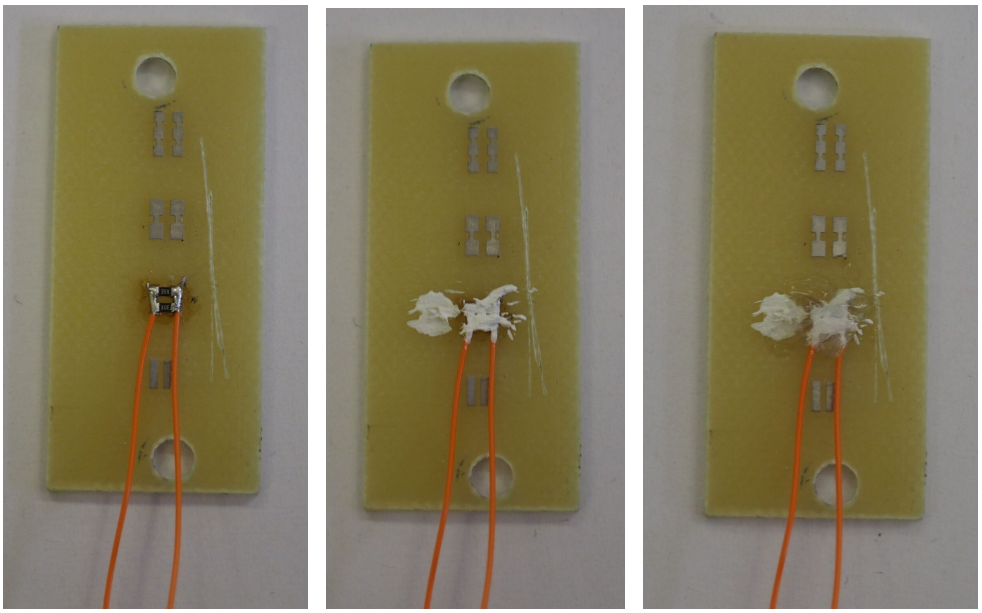

(a) (b) (c)

Figure 4.7: Photographs of surface mount resistor (a) uncovered, (b) with white-out fluid and (c) with white-out fluid and electrically insulating silicon gel.

A known voltage was applied to the uncovered resistors using a constant voltage source until

a steady state temperature was reached. The subsequent sensor signal strength was recorded for one second at a sampling frequency of 300Hz, and averaged to give the steady state result. The experiment was repeated with the resistors covered in the white-out fluid and the signal strength compared with the uncovered results (Table 4.1).

Material	Relative Signal Strength
Bare device	100%
White-out fluid	244%
White-out fluid + silicon gel	141%

Table 4.1: Relative IR signal strength when measuring surface mounted resistors with various covering materials at constant voltage.

Table 4.1 reveals that the white-out fluid caused a significant improvement in the emissivity, and therefore signal strength (2.44 times stronger), from the DUT. This not only provides a baseline for calibration by having constant emissivity, but also improves the signal strength significantly.

Effect of Silicon Gel on Emissivity

Much like the white-out fluid, the silicon isolation gel described in Section 4.4.5 will have an effect on the IR signal strength. However, the silicon gel reduces both the emissivity and the transmittance. To measure the effect of silicon gel, the device set up and experiment from the previous section was repeated, but with silicon gel applied to the surface mount resistor. Figure 4.7.c shows the device with silicon gel applied and Table 4.1 shows the impact of the silicon gel on the signal strength.

Table 4.1 reveals that the silicon gel had a significant reduction (42%) on the signal strength when compared to the white-out only case. Therefore, for the laboratory environment, the silicon gel was removed from the DUT to improve the strength of the IR signal. The gel removal is discussed in further detail in Section 4.4.5.

Sensor Calibration

To calibrate the sensor for use on the DUT, the surface-mount resistor set-up described above was used with white-out fluid applied to its surface. Originally, a K-type thermocouple was

attached to the surface of the resistors to provide a reference temperature. However, it was found to be impractical as the adhesive heat-shrink used to attach the thermocouple to the device significantly changed the device's thermal properties. Instead, a FLIR C2 IR camera was used.

To produce a calibration curve, a range of known voltages from a constant voltage source were applied to the resistors, and images of the device were taken when the temperature reached steady state. The resistors were then placed on the XYZ table and the same voltages were applied to the resistors. The corresponding signal strength was recorded over one second and collated with the temperatures measured by the IR camera to produce a calibration curve. Table 4.2 provides the lock-in amplifier and DC bias settings used for this calibration curve while Figure 4.8 shows the resultant calibration curve. Figure 4.9 provides example thermal image of the resistors during a particular test. The calibration curve equation is detailed in (4.2).

Parameter	Value
DC bias voltage	100V
Amplifier time constant	30ms
Amplifier sensitivity	2μV

Table 4.2: DC bias and amplifier parameters for calibration.

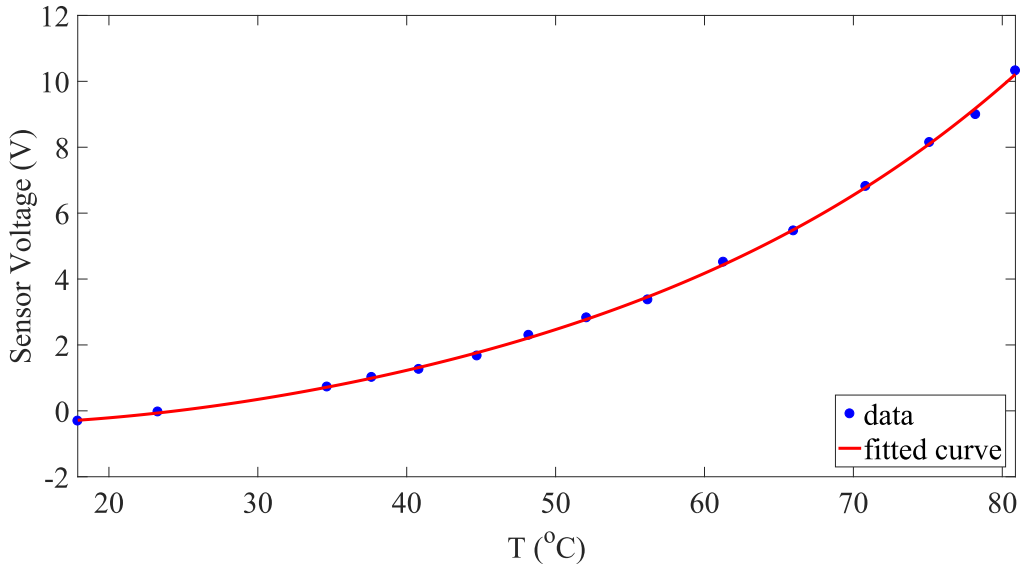

Figure 4.8: Calibration curve for IR sensor. The R^2 value is 0.9999.

$$S_V = 3.922 \times 10^{-7}T^4 - 6.261 \times 10^{-5}T^3 + 0.00547T^2 - 0.1315T + 1.086 \tag{4.2}$$

S_V is the sensor voltage.

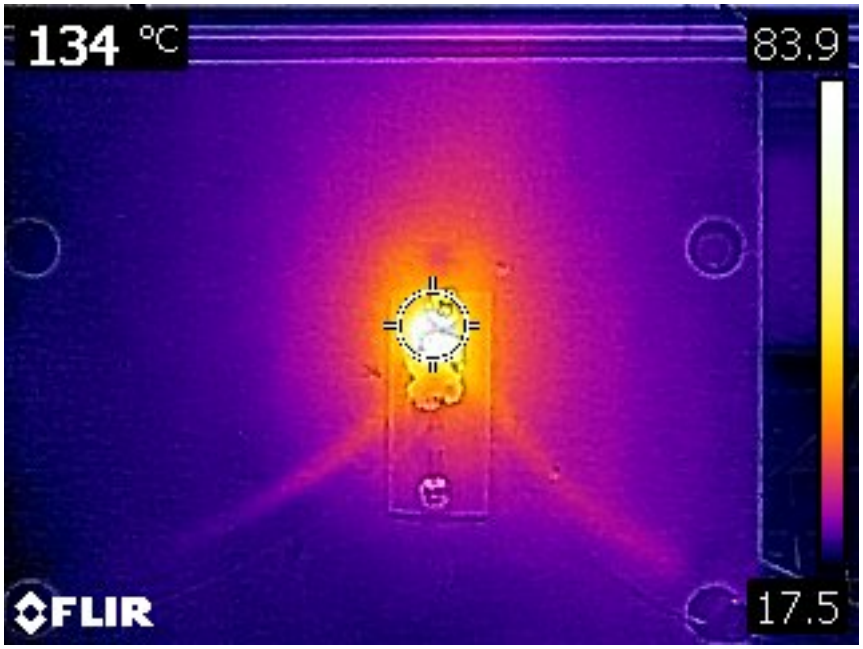

Figure 4.9: Thermal image of surface mount resistor during calibration.

IR Sensor Noise Patterns

One of the limitations of IR sensors is their small signal magnitude meaning that the output signal after filtering and amplification is still susceptible to noise. To understand how this noise may affect the temperature measurements, the standard deviation was calculated for the data sets used for calibration and plotted against the signal mean (Figure 4.10.a). The signal-to-noise ratio (SNR) was also estimated using (4.3) and plotted against the signal mean (Figure 4.10.b).

$$SNR = \frac{\mu_v}{\sigma_v} \tag{4.3}$$

μ_v is the signal mean, and σ_v is the signal standard deviation.

The standard deviation of the signal had little correlation with the size of the signal and remains within the same order of magnitude. As such, in general the SNR increased with increasing signal mean. This result means that the sensor provided more precise temperature measurements at higher temperatures. This is important as the higher temperature range is where the most damage is expected to occur.

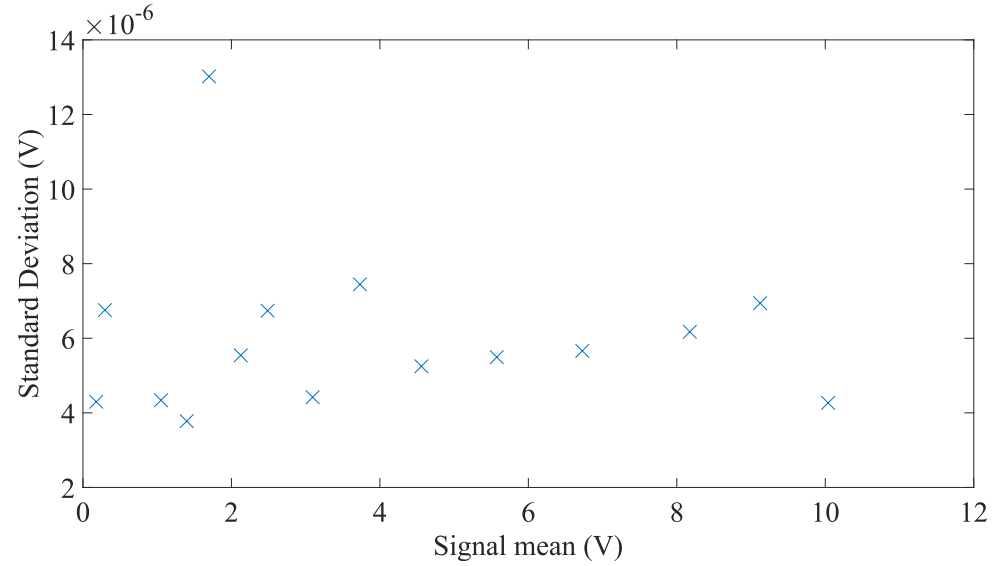

(a)

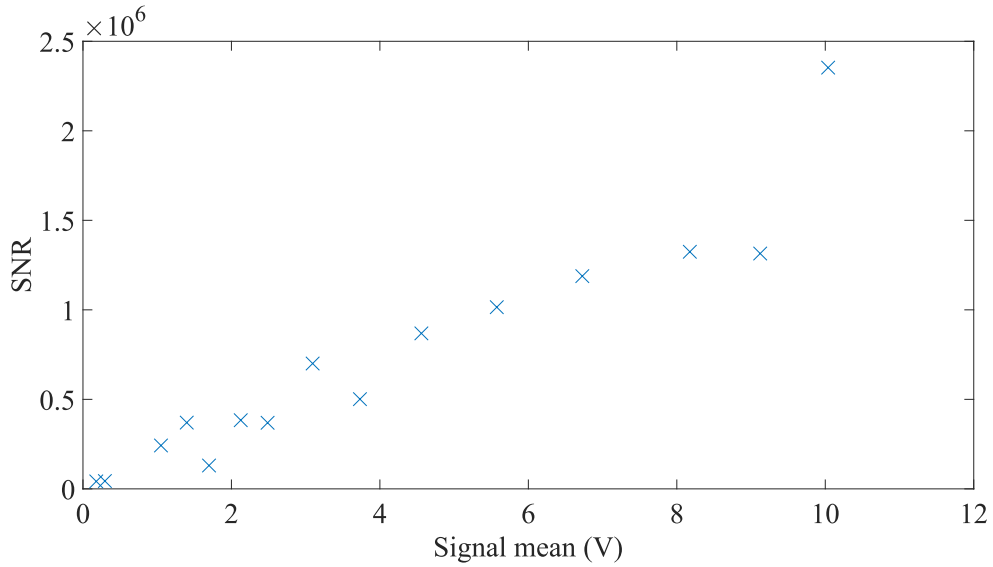

(b)

Figure 4.10: Signal mean value against (a) standard deviation and (b) SNR.

4.4 Thermal Measurement: Electrical Design

To determine the efficacy of the IR sensor for T_j measurement, an experimental rig that has similar aspects to the power converter in a wind turbine has been constructed. The DUT has then been modified to allow line-of-sight in the IR spectrum for the IR sensor.

This section outlines the key aspects of this rig, including power module selection (Section 4.4.1), DC link set up (Section 4.4.2), the devices used to vary the current throughput (Section 4.4.3), how the device is controlled (Section 4.4.4), and how the device and is modified

to allow for IR measurement (Section 4.4.5). The system is then verified in Section 4.4.7. The full experimental rig design is outlined in Figure 4.11.

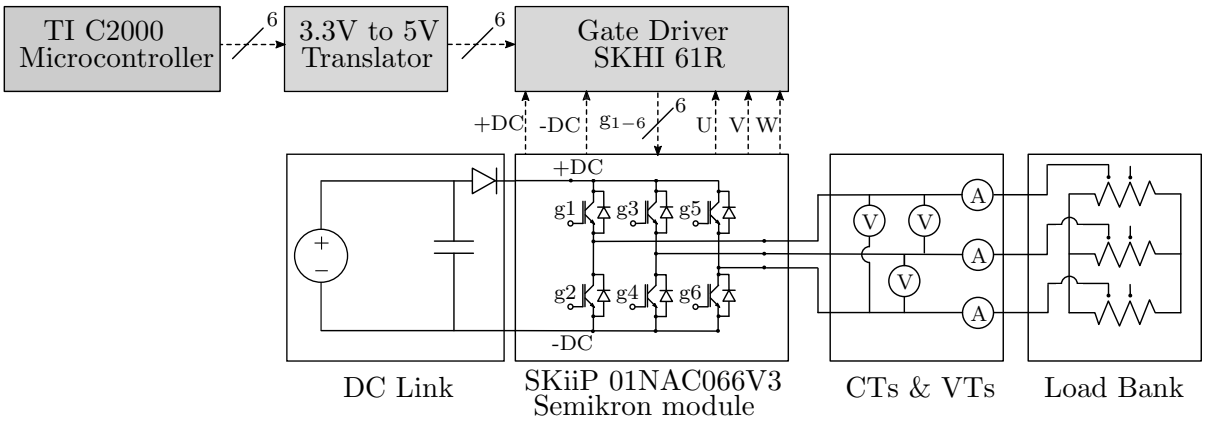

Figure 4.11: Electrical circuit diagram.

4.4.1 Power Module Selection

In the model in Chapter 3, two parallel SEMIKRON SKSB2100GD69/11-MAPB stacks were used. These stacks contained the SKiiP2013GB172-4DWV3 half-bridge SKiiP module for each leg in the stacks. Ideally these modules would be the DUT but this was impractical due to the indicative cost, and current and voltage rating (1000A$_{nom}$ and 1700V_{ces}) of these SKiiP modules. A lower rated DUT power module was required to operate within the available laboratory infrastructure.

The lower rated power module selected was the SEMIKRON 01NAC066V3 MiniSKiiP module [137]. This module has a much lower current and voltage rating (6A$_{nom}$ and 600V_{ces}) and much lower unit cost whilst still using the Trench3 IGBT technology found in the larger device, allowing for practical but realistic laboratory testing. The module contains a 3-phase passive rectifier and active inverter but can be reconfigured to only use the active inverter. Figure 4.12 shows the module with case on and off.

The key limitation of using the 01NAC066V3 module is that the packaging technology differs from the SKiiP2013 module: the SKiiP2013 uses SKiNTER technology which replaces solder with cold welded silver between direct copper bond (DCB) and chip [138]. However, according to expert advice, this increases the lifetime of the device but does not change the fundamental failure modes, meaning that the 01NAC066V3 module was suitable for emulation of the large modules found in MW-scale turbines.

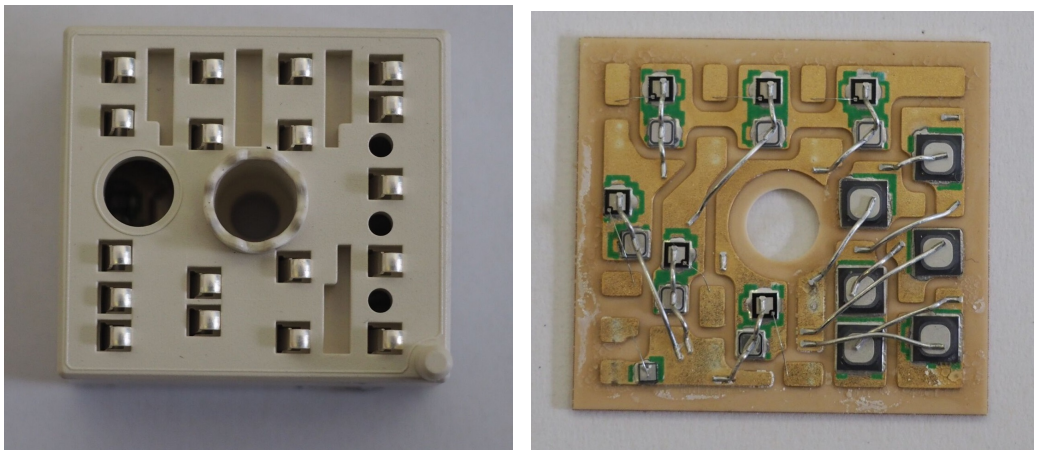

(a) (b)

Figure 4.12: Photographs of the SEMIKRON 01NAC066V3 MiniSKiiP module (a) with case, and (b) without case and with silicon gel removed.

4.4.2 DC Link Voltage

As the DUT collector-emitter saturation voltage (V_{ces}) is lower than that of the MW-scale power modules, the DC link voltage must be scaled accordingly. (4.4) can be applied to determine the equivalent DC link voltage. The values are given in Table 4.3.

$$V_{DC,e} = \frac{V_{ces,e}}{V_{ces,f}} V_{DC,f} \tag{4.4}$$

$V_{DC,e}$ and $V_{DC,f}$ are the experimental and full-scale DC link voltage respectively, and $V_{ces,e}$ and $V_{ces,f}$ are the experimental and full-scale power module collector-emitter saturation voltage respectively.

Parameter	Value
$V_{ces,e}$	600V
$V_{ces,f}$	1700V
$V_{DC,e}$	406V
$V_{DC,f}$	1150V

Table 4.3: Power module voltage parameters.

A switch mode power supply with an output capacitor was used to emulate this DC link (Figure 4.11). Unfortunately, due to equipment limitations the DC link voltage could only be

set to a maximum of 300V but this was deemed reasonable as it was assumed that the current throughput would have the greater impact on thermal loading.

4.4.3 Load Bank

A resistor bank was used to provide a range of operating conditions for this experimental rig. The resistor bank had a number of discrete resistance values (Figure 4.13), limiting the possible loading on the device to 0-5A.

Figure 4.13: Photograph of resistor bank.

4.4.4 System Control

To invert the DC link voltage, the six IGBTs were switched using SPWM at a frequency of 2kHz. The SPWM was generated using a Texas instruments micro-controller interfaced with MATLAB/Simulink to allow the use of in-built function blocks. The voltage was controlled in an open loop configuration with the required voltage set in software and uploaded to the micro-controller.

The IGBTs require a -9V (open switch) and +15V (closed switch) supply so a SKHI61R driver [139] was used. This driver also provided opto-couples to protect the control circuitry. As this driver required 5V input signals from the control circuitry and the micro-controller only generates 3.3V, a voltage-level translator was implemented with a buffer to reduce overheating of the translator due to excess current draw.

4.4.5 Device Access and Connection

One of the main challenges with the chosen temperature measuring approach is the need to have visual access to the IGBTs and diodes. As shown in Figure 4.12, the device comes with a plastic case that uses sprung metallic legs to connect to the device, and the devices are coated in an insulating silicon gel to avoid flash-over. Ideally, the case would be removed and the metallic legs replicated in the laboratory environment whilst still having visual access to ensure consistency with normal operating conditions. However, for simplicity the connections were replaced with direct solder joints.

This direct soldering technique required the silicon gel to be removed by placing the whole device (with case) in a dodecylbenzenesulfonic acid bath for 24-48 hours. This removed the silicon gel, and the case floated to the top of the bath. Due to the toxicity of the acid, the device was then cleaned with isopropanol and dried with nitrogen. The connections were then soldered to the device, and the device secured to a heat-sink with a screw and thermal paste.

Originally, the silicon gel was not reapplied and a metal screw was used to secure the device to the heat-sink. However, preliminary testing led to instantaneous catastrophic failure across the DC link due to flash-over between wires and the screw (Figure 4.14). To prevent this reoccurring the insulating silicon gel was reapplied, and the metal screw replaced with a nylon one. The final device set up is shown in Figure 4.15.

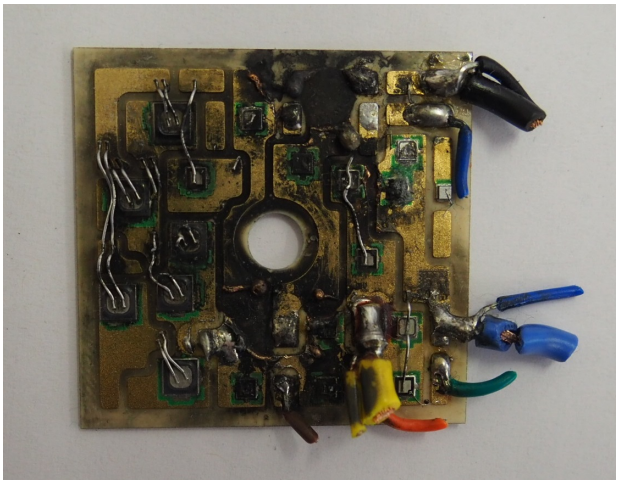

Figure 4.14: Photograph of device after catastrophic failure.

As the device was opened up and a high voltage DC link had exposed connections, the whole experiment was encased in a polycarbonate case to ensure the users' safety. Whilst this would

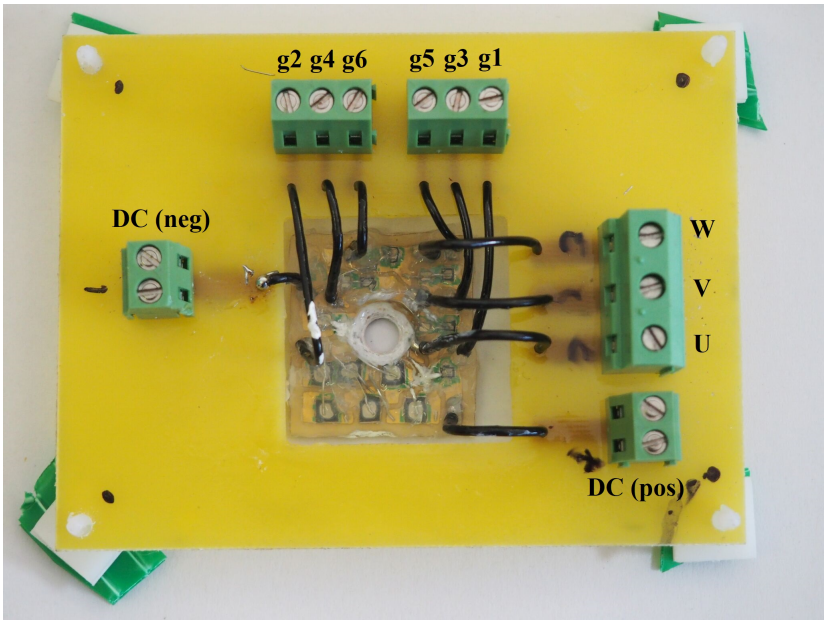

Figure 4.15: Photograph of final device set-up.

reduce the air circulation to the device, the case was sufficiently large to ensure that the internal ambient temperature would not be raised.

4.4.6 Noise Reduction

Due to the high frequency noise generated by the switching, there were a number of issues with interference on both the gate driver and the temperature measurement output. To mitigate these experimental noise issues the following steps were made:

- Isolated grounding for power circuitry, control circuitry and measurement circuitry.
- Metallic shielding for control circuitry.
- Load bank placed a large distance from the rest of the experiment.
- Power cables and gate driver cables kept perpendicular.
- Power circuitry grounding used braiding.

4.4.7 System Verification

To determine whether the experimental rig was producing equivalent voltage and current profiles with those of the simulations in Chapter 3, the experimental rig (Figure 4.11) was modelled and simulated in Simulink. The same conditions were then applied to both the model and the experimental rig and the voltage and current waveforms compared.

The simulated and experimental voltage waveforms were compared at 300V with a 32Ω star connected resistive load with a desired output frequency of 1Hz (Figure 4.16). Unsurprisingly, the simulated 3 phase voltage output is significantly cleaner (Figure 4.16.a) than that of the experimental rig (Figure 4.16.b) as the simulation assumes that the IGBTs are perfect switches. In contrast, the real IGBTs are imperfect and produce short voltage transients when switching. However, both produce very similar magnitude waveforms and Figures 4.16.d,e reveal that individual voltage changes are consistent between simulation and experiment. When a 400Hz filter is applied to the waveform in Figure 4.16.c, the resulting waveform shows that a 3-phase 1Hz sinusoidal waveform was successfully produced.

A similar pattern was found with the voltage at 250V with the same load and desired output frequencies. Figure 4.17.a,b shows the simulation and experimental phase current respectively. Again, the current is noisier in the experimental data due to the effect of switching noise. The 4 levels in the current would suggest that the 2-level converter is producing 4 levels. However, this is simply due to the summation of 2 phases on each phase in a purely resistive circuit with no neutral; if a neutral is added to the centre of the star load in the simulation the current produced has 2 levels. A 400Hz filter was added to the experimental data to remove switching effects to reveal that a 1Hz current sinusoidal waveform was successfully produced.

4.5 Summary

In this chapter the temperature measurement approaches in the literature were critiqued and the IR sensor approach was deemed the most appropriate method due to its high response time, lack of physical contact, and low cost. The subsequent thermal measurement experimental design for this research was outlined, including the optics required, the modifications made to allow for more accurate temperature measurement, and the calibration of the chosen IR sensor.

To provide a realistic testing environment for the temperature measurement approach and allow for comparison with the simulation results, a simplified experimental rig with a 3-phase power converter was constructed. This rig included a scaled down Semikron power module with the same IGBT technology as the power modules used in Chapter 3. This rig included a resistive load, open loop switching control, and the modifications to the power module required for accurate temperature measurement. The electrical system was verified against a simulated system.

The next chapter uses the experimental approach outlined in this chapter, alongside the simulation work in Chapter 3, to explore the impact of wind turbine conditions on the thermal profile and reliability of the power module devices.

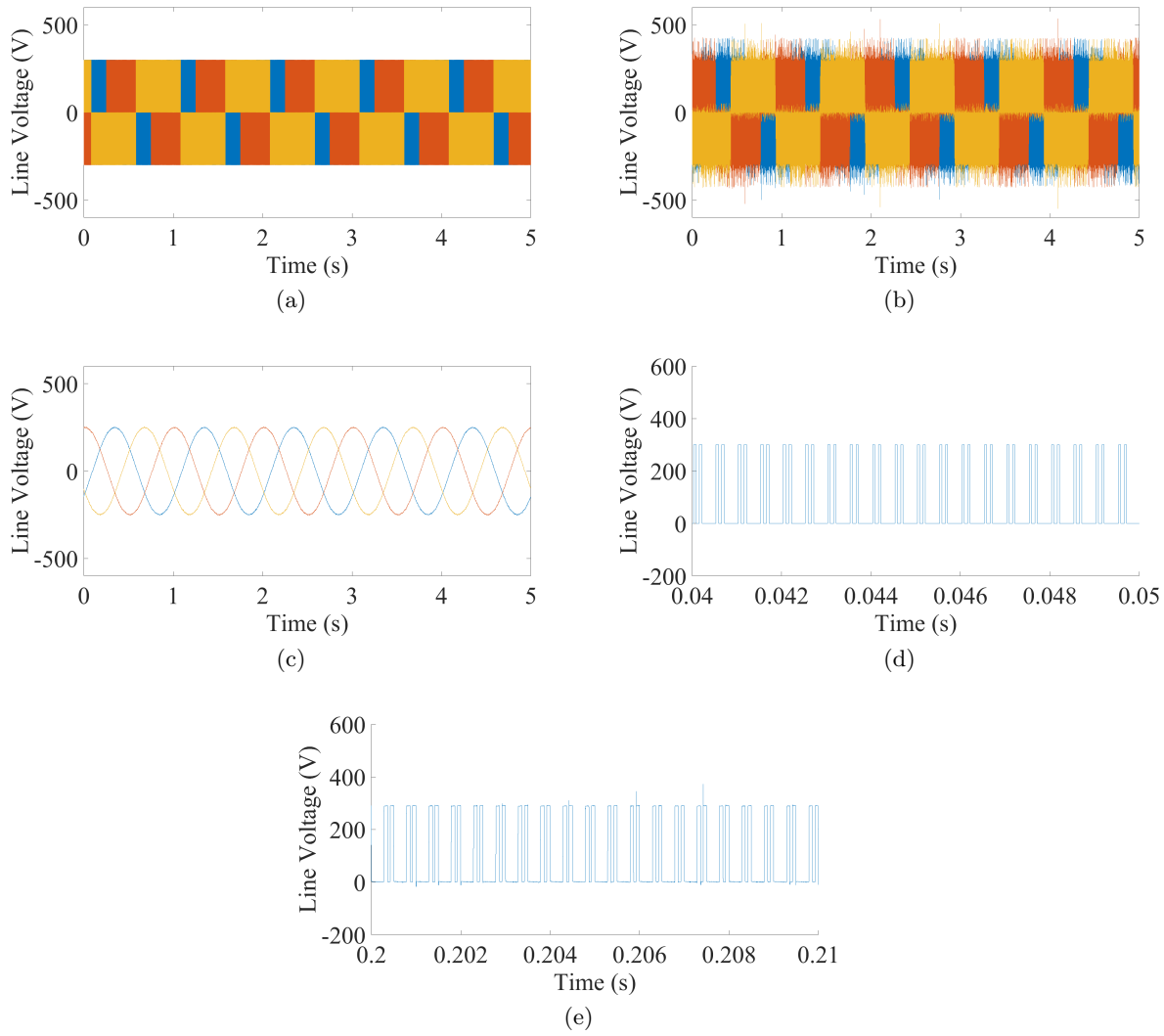

Figure 4.16: Verification of 3-phase voltage output: (a) simulated voltage, (b) measured voltage, (c) filtered measured voltage, (d) zoomed-in simulated voltage, (e) zoomed-in experimental voltage.

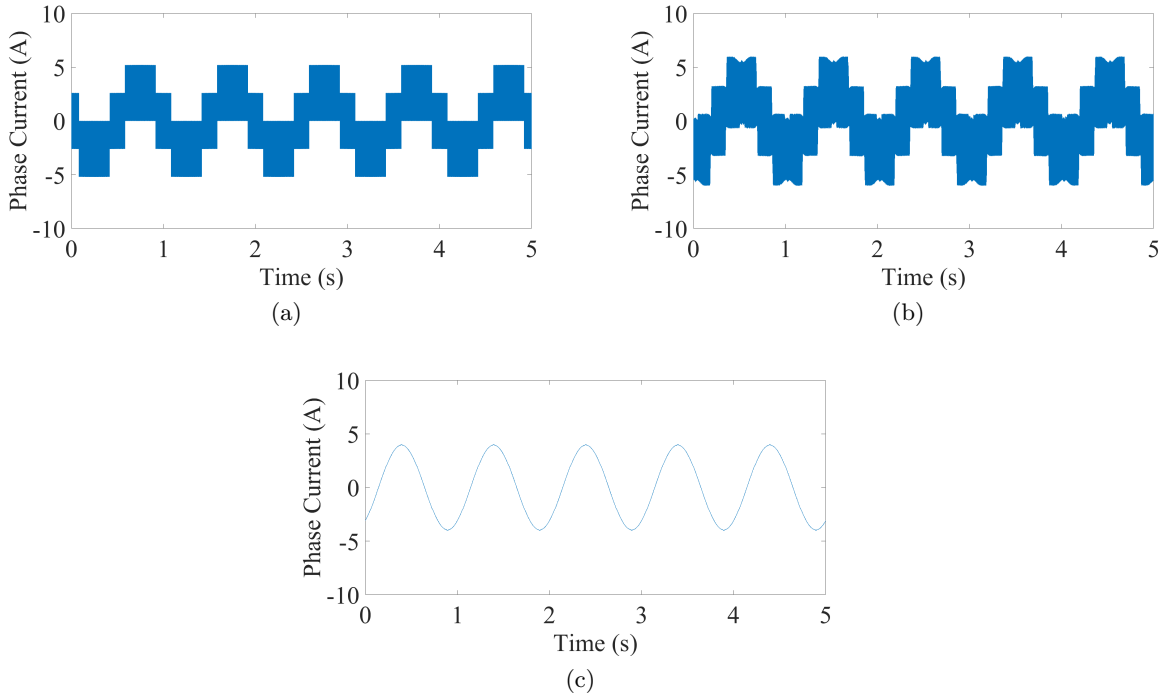

Figure 4.17: Verification of current output: (a) simulated current, (b) measured current, (c) filtered measured current.

Chapter 5

Simulation and Experimental Results

5.1 Introduction

With the drive train model and experimental rig construction detailed in chapters 3 and 4 respectively, this chapter uses these foundations to answer the following three research questions:

- Which wind speed operating conditions theoretically cause the greatest thermal loading to the power modules in the power converter? (RQ1)
- Can the junction temperature be measured in order to prove the simulation models cost effectively? (RQ2)
- What can be learnt by comparing the results of wind turbine simulations with those of the experimental rig? (RQ4)

This chapter is split into three main sections. Firstly the individual T_j cycles produced by the DDTRET are validated against manufacturer data (Section 5.2.1), and then analysed to examine their potential impact on the T_j reached during operation (Section 5.2.2).

Secondly, constant wind speed loading conditions are applied to both DDTRET and the experimental rig. The experimental rig from Chapter 4 verifies the presence of temperature variations due to the fundamental current frequency (Section 5.3.1). With the temperature variation verified, the DDTRET is used to explore the impact of different wind speeds on the thermal profile (Section 5.3.2) and the results are compared to those in [88] (Section 5.3.3). The constant wind speed conditions are then applied to the experimental rig and compared to the simulation results (Section 5.3.3), including verifying the importance of including heat sink parameters (Section 5.3.5).

Thirdly, variable wind speed conditions are analysed through the DDTRET. The impact of the drive train model mechanical properties are examined to determine their necessity for providing accurate converter loading simulation (Section 5.4.1). Finally, the wind speed data sampling frequency required for accurate representation of the real loading in the power converter is determined (Section 5.4.3).

5.2 Simulated Individual T_j Cycles

Firstly, to begin answering RQ1, the T_j cycles due to AC current and device switching are examined as these are the building blocks for the rest of the thermal profiles. To this end, the individual T_j cycles are validated against the plots produced in the manufacturer's handbook (Section 5.2.1). The potential impact due to the unique features of the simulated T_j cycles for both high and low wind speeds for the IGBTs and diodes is then evaluated (Section 5.2.2).

5.2.1 Validation against Manufacturer Data

To validate the individual T_j cycle shape, a constant wind speed of 12.7m/s (drive frequency of 9.75Hz) was simulated using the DDTRET, the diode T_j for an individual cycle recorded, and was compared alongside an example given by the manufacturer found in [105] which shows how the T_j profile should change with frequency (Figure 5.1).

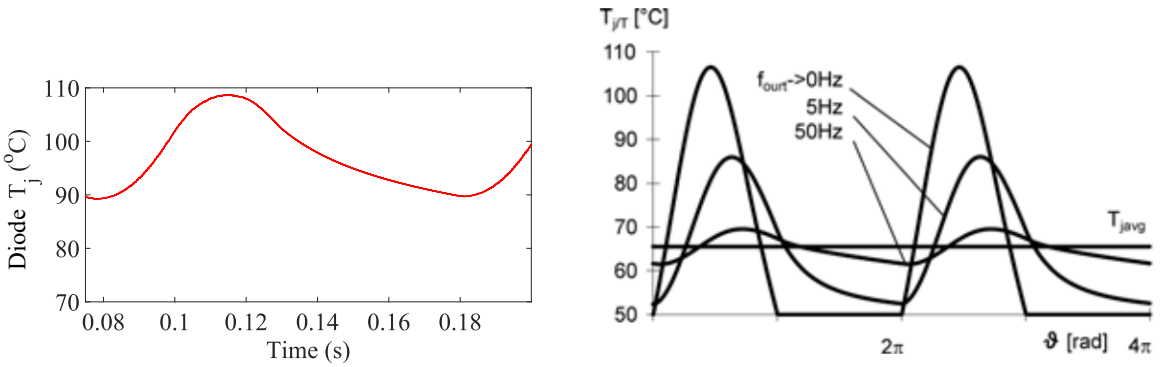

Figure 5.1: Individual T_j response to constant wind speed of 12.7m/s for (a) diode and (b) manufacturer's handbook data.

The T_j profile shape for the diode (Figure 5.1.a) is comparable with the expected response from the manufacturer's handbook (Figure 5.1.b). It should be noted that the manufacturer's data considers only the average power loss of the switching cycle, rather than individual switching events. This simulation output can therefore show higher frequency temperature variation than

revealed in the manufacturer's data which may reveal interesting temperature variations due to irregular device switching patterns.

5.2.2 T_j Cycle Results and Discussion

The current and temperature profiles over individual power cycles were examined to explore the impact of device switching on T_j at both constant high (12.7m/s, 9.75Hz drive frequency) and low wind speed (4m/s, 3.1Hz drive frequency) at turbine steady state. Figure 5.2 compares the diode and IGBT current and T_j profiles at constant wind speeds of 4m/s and 12.7m/s.

T_j variation due to device switching becomes apparent in the IGBT (Figure 5.2.f) as shown by the highly irregular T_j pattern near the profile peak. This can be attributed to the converter being connected to a PMSG, with the reactance causing the current to be out-of-phase with the voltage, and therefore the switching cycles are not distributed symmetrically over the input current, with a period of low voltage (Figure 5.2.e). The low voltage means the IGBT has a smaller duty cycle. Where there is infrequent current due to a low duty cycle (Figure 5.2.e), T_j varies more (Figure 5.2.f). This reduces the maximum T_j reached by the IGBT. As this replicates the real system, it would be expected that this would also occur in the wind turbine power modules.

This effect is not seen in the diode as the current not flowing through the IGBT must pass through the diode, creating a near continuous current throughput (Figure 5.2.g) and therefore a smooth T_j response (Figure 5.2.h).

The opposite is true at low wind speeds. The IGBT current becomes more uniform (Figure 5.2.a), whilst the diode current becomes less uniform (Figure 5.2.c). As such, the T_j noise significantly reduces for the IGBT at 4m/s (Figure 5.2.b) compared to the profile at 12.7m/s, whilst the T_j noise increases slightly for the diode when moving from 4m/s to 12.7m/s (Figure 5.2.d).

The changes in frequency, current and subsequent switching frequency all have a significant impact on the magnitude and shape of the individual T_j cycles, particularly for the IGBT at high wind speeds. This could mean that the traditional approaches of averaging could be producing incorrect estimations of the temperature profiles and subsequently inaccurate estimations of the damage done to the power modules.

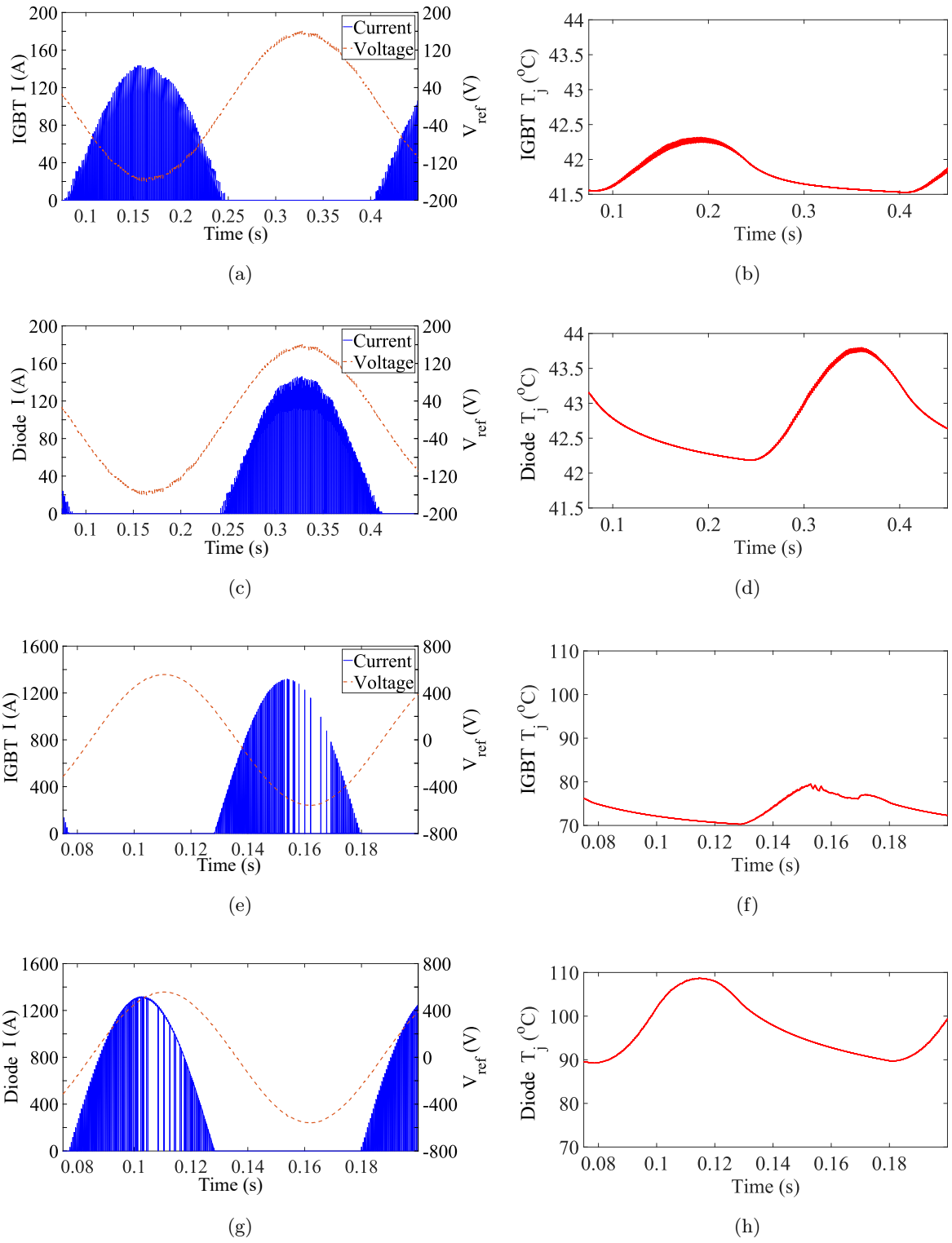

Figure 5.2: Device current and T_j response to switching events at 4m/s and 12.7m/s wind speed inputs: (a,b) IGBT at 4m/s, (c,d) diode at 4m/s, (e,f) IGBT at 12.7m/s, (g,h) diode at 12.7m/s.

5.3 Constant Wind Speeds

The previous section has attempted to provide validation of the individual T_j cycles against manufacturer data. The thermal profiles are now simulated and emulated experimentally for constant wind speeds to determine the following contributions to RQ4:

- Is it possible to measure a temperature variation due to the current cycling to confirm that current swings cause a quantifiable temperature variation?
- How do frequency and current affect the magnitude of ΔT_j?
- Can the requirement for a heat sink for accurate temperature measurement be confirmed?

Firstly, the experimental rig outlined in Chapter 4 is used to confirm that temperature variations occur due to the fundamental frequency current swings (Section 5.3.1). Secondly, the DDTRET was subjected to five constant wind speed profiles between cut-in (4m/s) and rated (12.7m/s) wind speeds for 60s. The results are analysed, with a focus on the impact of the 18K plastic deformation limit, as discussed in Chapter 3, on which wind speeds should be considered as damaging to the wind turbine (Section 5.3.2). Thirdly, the results are validated and compared to the results in [88] to determine important factors that should be considered to provide accurate wind turbine thermal profiles (Section 5.3.3). Fourthly, the constant wind speed profiles are emulated in the experimental rig from Chapter 4 and compared to the simulation results (Section 5.3.3). Finally, the impact of including heat sink parameters on the temperature profiles is examined (Section 5.3.5).

5.3.1 Constant Power, Varying Frequency

To confirm that a DUT ΔT_j was detectable experimentally the DUT was electrically loaded to provide the maximum ΔT_j possible and the PbSe sensor used to measure the surface of one IGBT. The current was set to the maximum available from the DC source (5A), at the maximum voltage (300V with a m of 1) and the fundamental AC output frequency was set to 1Hz to allow for the maximum possible time for the device to heat up and cool down during current cycles.

For this test, the device was operated until the heat sink reached thermal equilibrium (measured using a K-type thermocouple). Once at thermal equilibrium the sensor voltage was recorded over 50s with a sampling frequency of 300Hz and amplifier time constant of 10ms. The sensor voltage was then converted to temperature using the calibration curve in Figure 4.8. The resulting temperature profile is displayed in Figure 5.3.a.

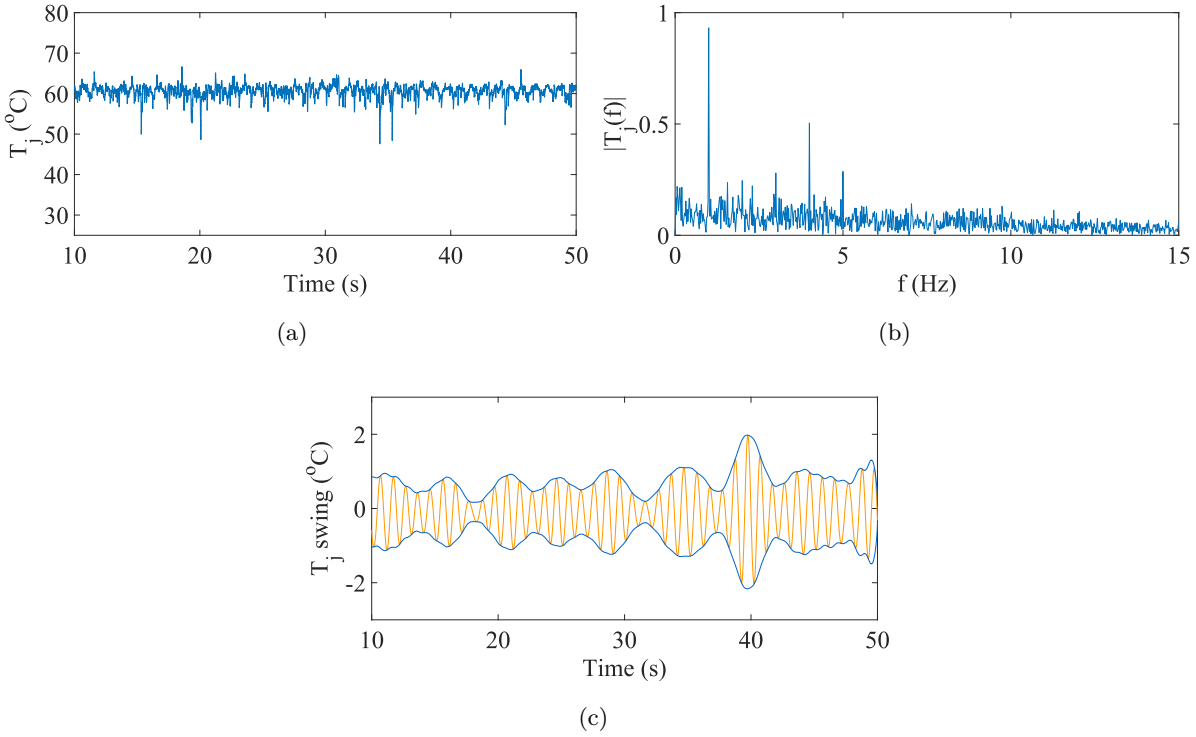

Figure 5.3: Steady state DUT temperature at 300V, 5A and 1Hz fundamental frequency: (a) temporal temperature profile, (b) frequency spectrum, and (c) filtered ΔT_j.

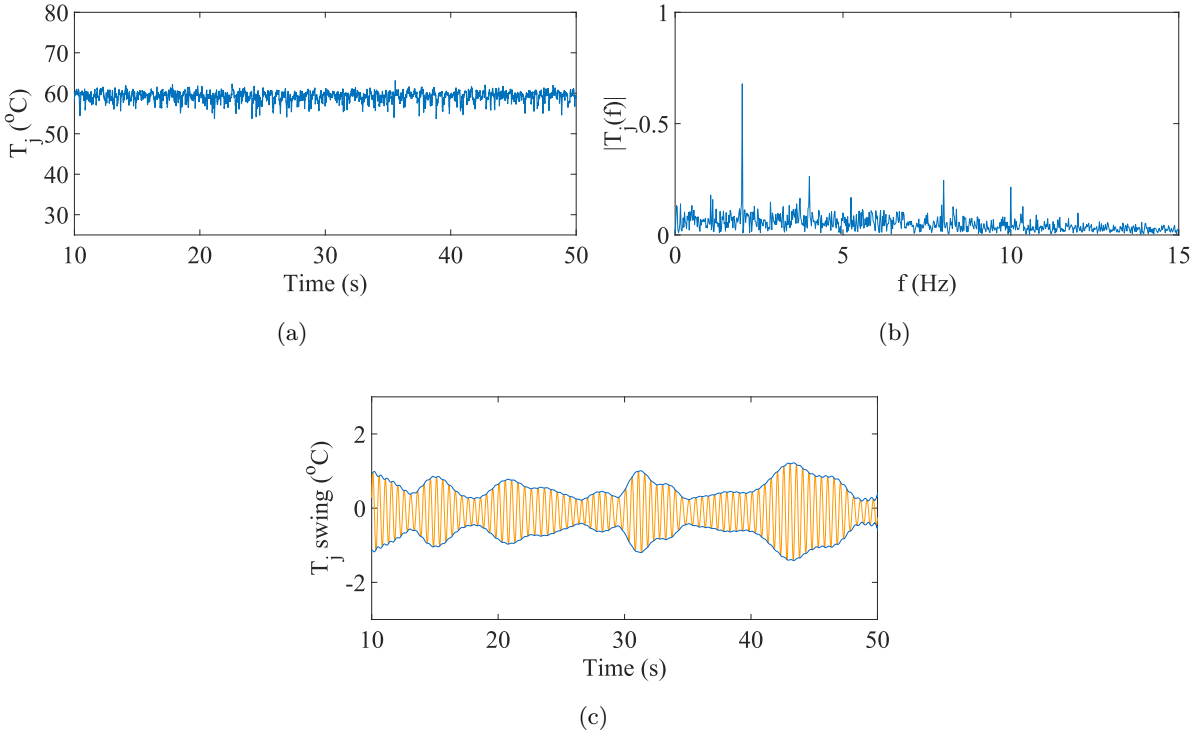

Figure 5.4: Steady state DUT temperature at 300V, 5A and 2Hz fundamental frequency: (a) temporal temperature profile, (b) frequency spectrum, and (c) filtered ΔT_j.

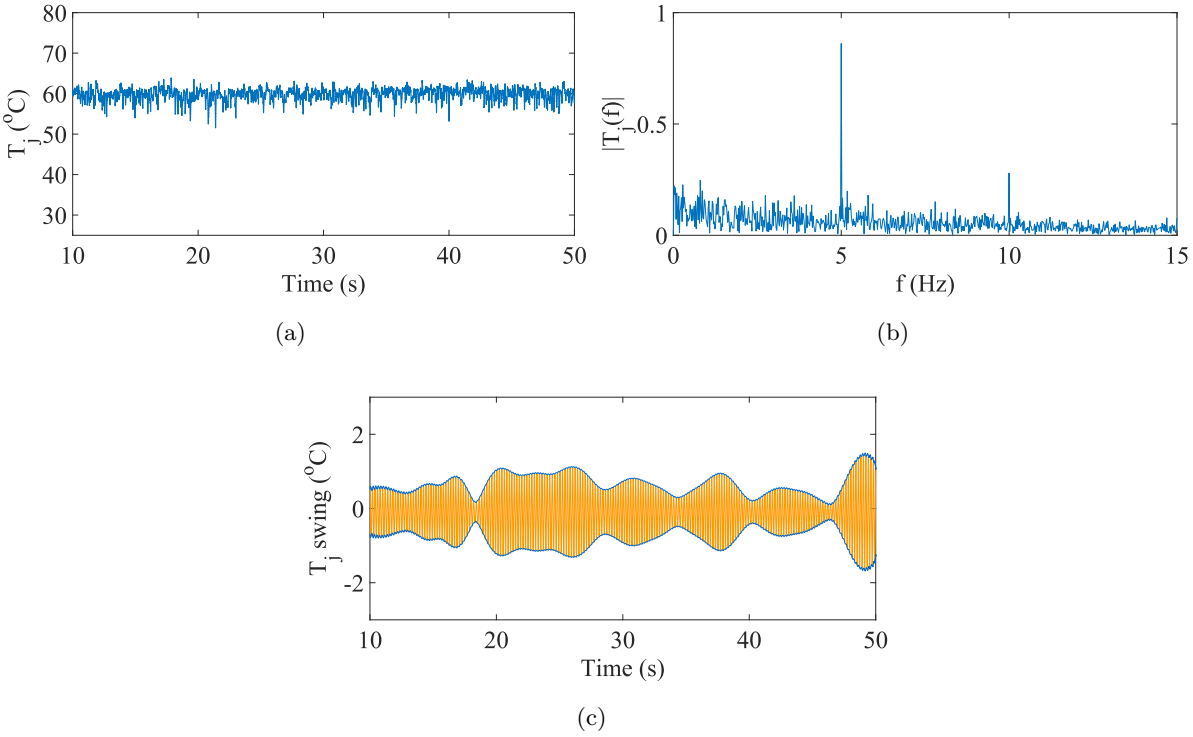

Figure 5.5: Steady state DUT temperature at 300V, 5A and 5Hz fundamental frequency: (a) temporal temperature profile, (b) frequency spectrum, and (c) filtered ΔT_j.

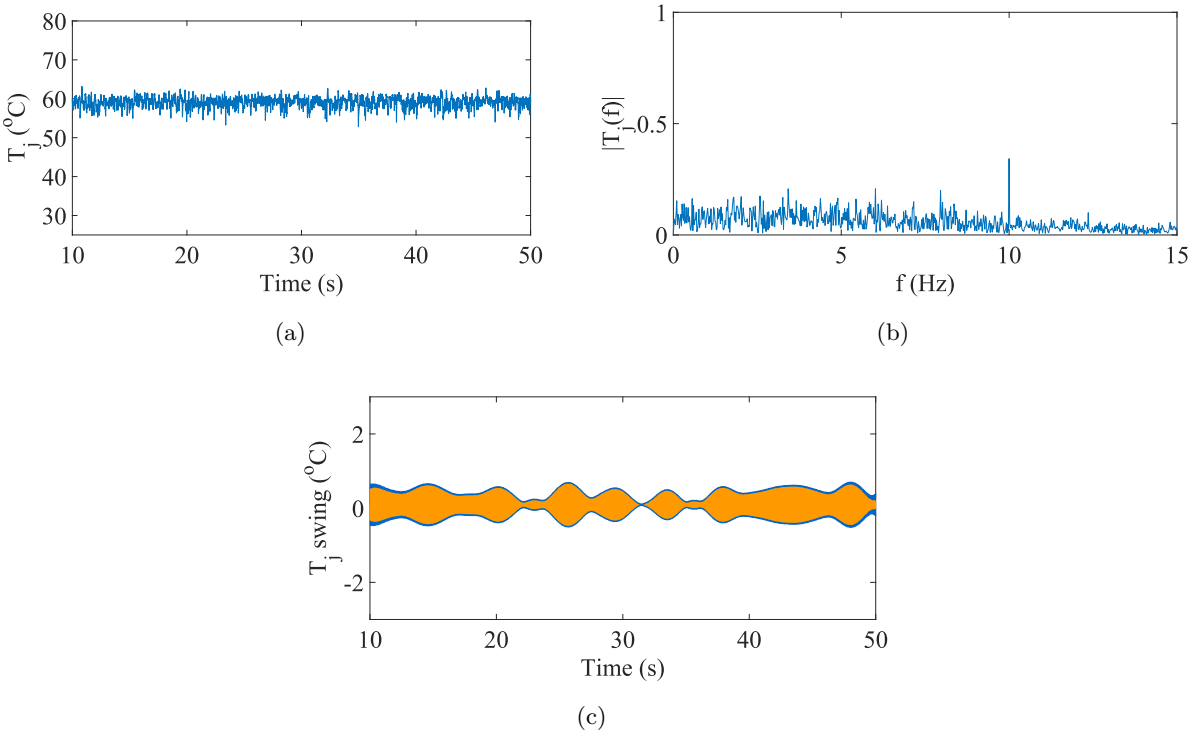

Figure 5.6: Steady state DUT temperature at 300V, 5A and 10Hz fundamental frequency: (a) temporal temperature profile, (b) frequency spectrum, and (c) filtered ΔT_j.

The resulting temperature trace clearly shows that the device is reaching a significant mean temperature of 60.5°C. The frequency spectrum reveals a very distinct peak at 1Hz, showing that there is a detectable ΔT_j at 1Hz (Figure 5.3.b).

With a narrow band pass filter, ΔT_j can be observed in the time domain (Figure 5.3.c). Most of the swing profile is around 2°C, with a peak of 4°C. There is therefore a confirmed ΔT_j caused by the current variations.

The test was repeated at 2Hz (Figure 5.4), 5Hz (Figure 5.5) and 10Hz (Figure 5.6) to see if the fundamental frequency had any impact on ΔT_j. Interestingly, as the fundamental frequency increases, the peak remains relatively consistent on the frequency spectrum until 10Hz where it drops considerably (Figures 5.3-5.6.b). This reduction at 10Hz was thought to be due to the high frequency not allowing the DUT to reach thermal equilibrium within a cycle, however further investigation found that the lock-in amplifier's low pass filter, despite being set to a cut-off frequency of 15.9Hz, was attenuating the signal. A repeat test at a higher cut-off frequency of 53.1Hz produced a much higher magnitude peak which was comparable to the other frequencies, but the temperature profile measured became prohibitively noisy for ongoing use. Therefore the 10ms time constant was kept and the attenuation at higher frequencies was deemed an acceptable compromise. There is also issue with the fundamental peak magnitude on the 2Hz frequency spectrum being lower than that of 5Hz and 1Hz. This is suspected to be a product of the short test cycle and use of one repeat. Therefore, future testing is required with a larger number of repeats per frequency and a larger number of frequencies tested.

What these results did show is that the device had sufficient time to reach thermal equilibrium between current cycles regardless of the testing frequency. This was faster than the 0.03Hz found in the simulations (Section 5.4.3), which is understandable as the experimental device is significantly smaller and therefore has a much lower thermal inertia.

Figures 5.3-5.6.c reveal that the temperature variation measured due to the current was not consistent as found in Section 5.2.2, but varies with lower frequency components. It is hypothesised that this is a product of the optical chopper introducing errors in the measurement signal that manifest as lower frequency variations in the output temperature as the variation was observed with no temperature source. However, further testing of the temperature measurement system with a known, oscillating temperature source would be required to confirm this.

This testing regime has determined that there are DUT ΔT_j caused by the oscillating current,

confirming the general trend detailed in Section 5.2.2. The frequency spectrum has revealed that the approach has produced distinctive peaks at the relevant frequencies, and the peak magnitudes have been consistent for all frequencies tested.

5.3.2 Constant Wind Speed Simulation Results

With the presence of temperature peaks at the fundamental frequencies confirmed, this section explores the simulated temperature profiles at different constant wind speed profiles. Figure 5.7 shows the thermal response to constant WSTS for one IGBT and diode in the power converter from cut-in to rated wind speed from DDTRET. The T_a is 40°C as found in [80].

It can be observed from Figure 5.7 that the mean T_j increases non-linearly as wind speed increases due to the cubic relationship between wind speed and power. The ΔT_j also increases due to the higher power loss per cycle, and the ΔT_j frequency increases due to the higher generator rotational speed.

The diode T_j and ΔT_j (Figure 5.7.b) are consistently higher than the IGBT (Figure 5.7.a). This is due to the higher power losses experienced by the diodes and the higher R_{th} of the diodes. The higher diode R_{th} (K/W) means that for every watt of heat loss, the diode experiences a greater rise in temperature than the IGBT. This is then coupled with the greater power losses due to the more continuous current flow through the diode, causing the higher T_j and ΔT_j. This was also found for the MSC devices in [88] and suggests that the diode is more vulnerable to thermal cycling with both higher mean T_j and ΔT_j.

The diode exceeds the 18K threshold outlined in Chapter 3 when at 12m/s. Therefore, whenever the turbine is operating above 12m/s, plastic deformation would occur and a proportion of the device useful life consumed. To determine how frequently this could occur, the 01/07/2005 to 30/06/2006 10 minute average SCADA WSTS at the Egmond Aan Zee wind farm in the Netherlands [140] was used as a case study. The histogram of this wind speed data is displayed in Figure 5.8.

Using the data outlined in Figure 5.8, the total time at above 12m/s was computed and the number of 18K+ cycles per year estimated by multiplying the frequency of the current at 12m/s (9.2Hz) with the number of seconds at 12m/s or above. The cost to remaining life was then calculated using the cycles to failure data introduced in Chapter 3, assuming all ΔT_j above 12m/s are 18K. Note that these results using the 18K are for demonstration purposes rather than providing a definitive estimation of converter lifetime.

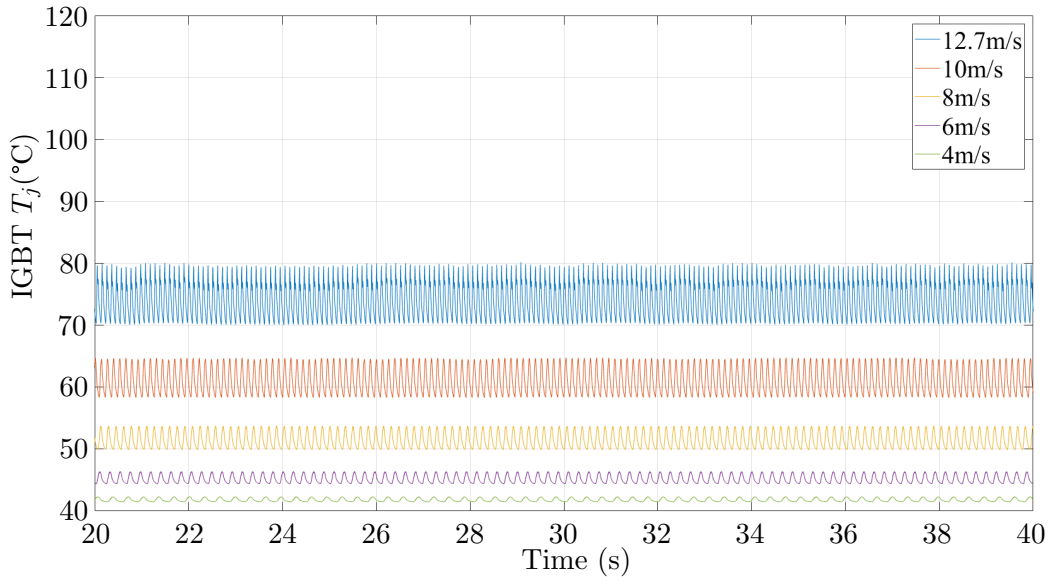

(a)

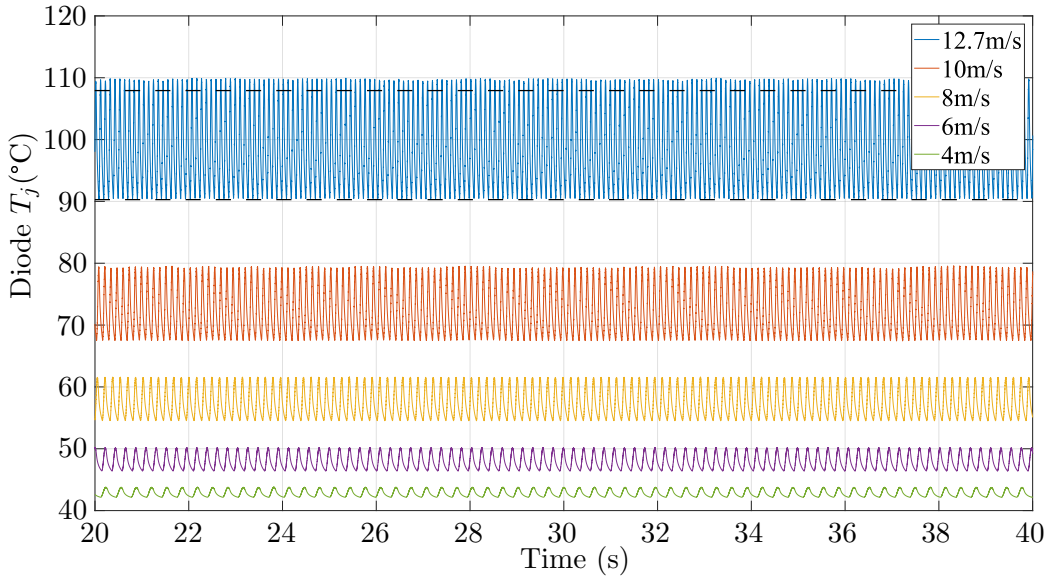

(b)

Figure 5.7: T_j response to constant wind speeds over 20 seconds for (a) IGBT and (b) Diode. The dashed line indicates the 18K threshold discussed in Chapter 3.

In this case study, the turbine was operating in the damaging conditions 20.1% of the year. Using the cycles-to-failure curve, this would represent an annual cost to life of approximately 11.8%. Assuming this was a representative annual wind speed profile and there is no other downtime, the power module would be expected to fail due to power cycling after 8.5 years. This is a reasonable first approximation based on the design life of a typical wind turbine of

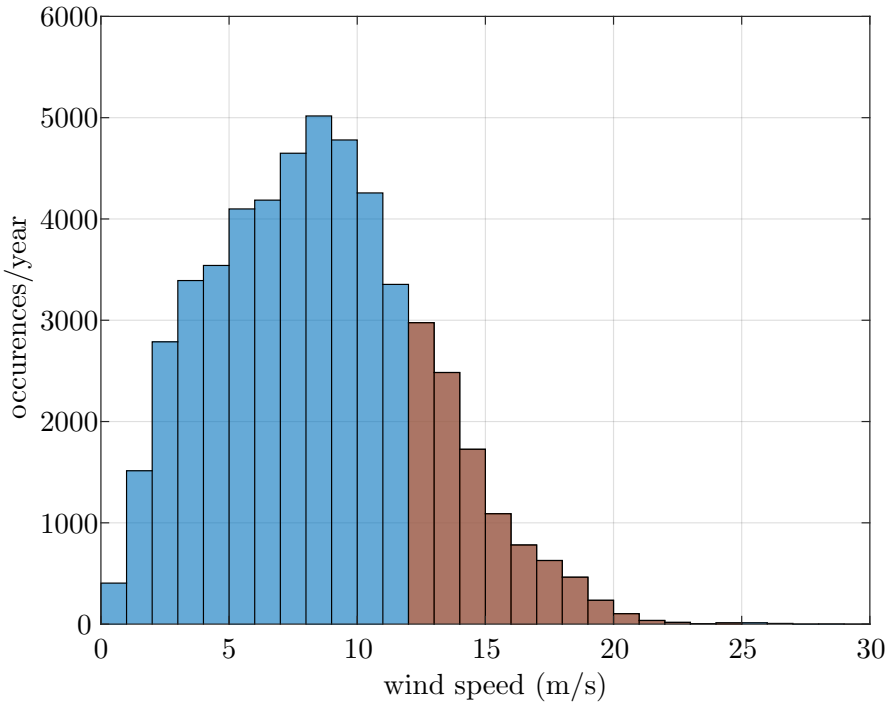

Figure 5.8: Histogram of number of 10 minute SCADA data points for each wind speed during a typical year at a wind farm. Red bars indicate when the turbine is operating at 12m/s or above.

20-25 years and the result of 5-7 years minimum lifetime in [97]. Indeed, 8.5 years would be an overestimation of the lifetime of the device as the ΔT_j rises up to 20.7K and the frequency up to 9.75Hz for rated conditions.

In contrast, the often assumed minimum plastic deformation threshold of 40K would yield an infinite lifetime for the device. Even a threshold of 21K would provide an infinite lifetime when solely considering SCADA data for wind speed, whilst a threshold of 15K would reduce the wind speed threshold for damage to approximately 11m/s. Therefore, determining the appropriate threshold is paramount for accurate life estimation of the power modules due to thermal cycling as lifetime calculations are so dependent on it. Furthermore, if this threshold was calculated, the power converter design itself could be optimised to avoid plastic deformation at the lowest possible cost.

To note, there were no tests carried out to determine the impacts due to increased power and increased frequency independently. In order to determine their independent effect on the junction temperature further testing with fixed power with varying frequency, and fixed frequency with varying power, would be required.

5.3.3 Validation against Comparable Study

The results in Figure 5.7 for the 2MW simulation were compared to the 1.55MW turbine in [88] (Figure 5.9); it is assumed the scaled power ratings would have limited impact on the thermal loading as the converter rating would also be scaled leading to comparable T_j profiles for a given wind speed. However, whilst it was found that the ΔT_j for both IGBTs and diodes was comparable at 8.5m/s and 12m/s, the mean T_j for 12m/s was approximately 10°C higher in this study than in [88], despite T_a being 10°C lower. This is in part is due to the lack of R_{th} value for the heat-sink in [88]. At steady state conditions this will create a higher case temperature T_c and therefore higher mean T_j. The mean T_j change from 12m/s to 8.5m/s is also much lower in [88] (6°C for the IGBT and 17°C for the diode) than for the results in Figure 5.7 (19°C for the IGBT and 35°C for the diode). This suggests that the MSC in this work is more susceptible to T_j rises due to the higher R_{th} values in the devices. This highlights 3 key conclusions:

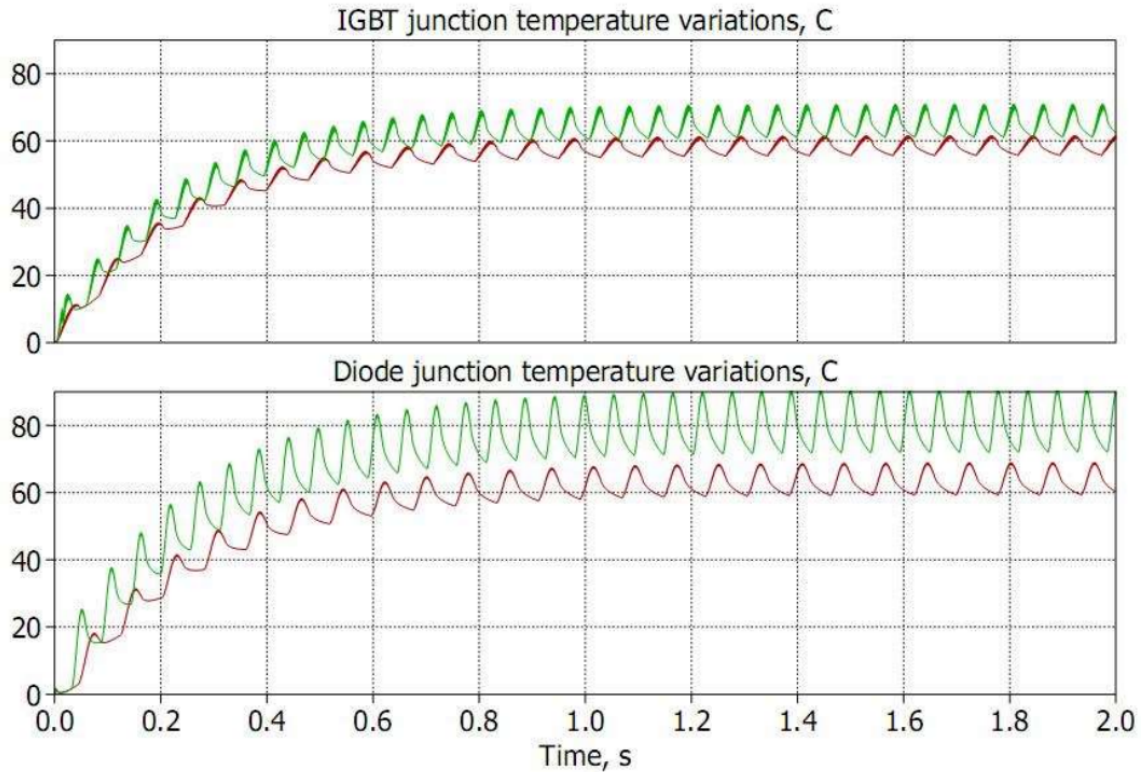

Figure 5.9: Thermal response results from [88]. The red lines indicate a wind speed of 8.5m/s and the green lines indicate a wind speed of 12m/s.

- The ΔT_j magnitude for IGBTs and diodes is consistent with that found in [88], but there is greater variation in mean T_j between wind speeds in this study due to the power modules' differing thermal properties which would lead to more extreme loading on the

power module devices.

- The value of T_a can have a large impact on the mean T_j value as shown by the disparity between this study and the results in [88].
- The inclusion of the heat-sink thermal parameters in the model causes a significant increase in the mean T_j by up to 30°C.

5.3.4 Replication of Wind Turbine Conditions

One of the key tests to perform was the replication of the conditions applied to the DDTRET in Section 5.3.2 in an experimental setting. The 12.7m/s conditions could not be replicated as the DC source did not have the current or voltage capacity required (5A instead of 6A, and 300V instead of 406V). The load bank's discrete resistances also meant that an exact match of voltage and current was impossible, and the modulation index, m, would have to change to accommodate the different maximum voltages available. Therefore the current was given priority and the voltage varied to compensate as all the losses are driven by the collector current. The simulation parameters and their physical test equivalents are given in Table 5.1. m_f is the full scale modulation index, m_e is the experimental modulation index, $I_{c,f}$ is the full scale IGBT collector current, $I_{c,e}$ is the experimental IGBT collector current, and R_L is the load resistance. $I_{c,e}$ was calculated by using the ratio between rated $I_{c,e}$ and rated $I_{c,f}$ (6/2800), and m_e was set so that the scaled equivalent AC voltage matched the full scale AC voltage output.

Wind Speed	Frequency	$V_{DC,f}$	$V_{DC,e}$	m_f	m_e	$I_{c,f}$	$I_{c,e}$	R_L
4m/s	**3.1Hz**	1150V	**300V**	0.28	**0.57**	323	**0.56**	**150Ω**
6m/s	**4.6Hz**	1150V	**300V**	0.42	**0.67**	483	**1.26**	**80Ω**
8m/s	**6.1Hz**	1150V	**300V**	0.55	**0.79**	633	**2.24**	**52Ω**
10m/s	**7.7Hz**	1150V	**300V**	0.72	**0.93**	828	**3.50**	**40Ω**

Table 5.1: Experimental test parameters and values for four wind speeds.

The results of the tests are summarised in Figure 5.10. The rise in mean temperature with wind speed confirms the increase found in Section 5.3. This is as the overall device power losses increase with increased power throughput of the device. However, unlike in Figure 5.7 where the ΔT_j increased with increasing wind speed, in this case ΔT_j actually reduced. This cannot be

explained by an increasing fundamental frequency reducing the time to heat up between cycles as Section 5.3.1 highlighted that the frequency had little to no effect on the magnitude of the ΔT_j. Therefore, the only remaining factor untested was the impact of m on ΔT_j.

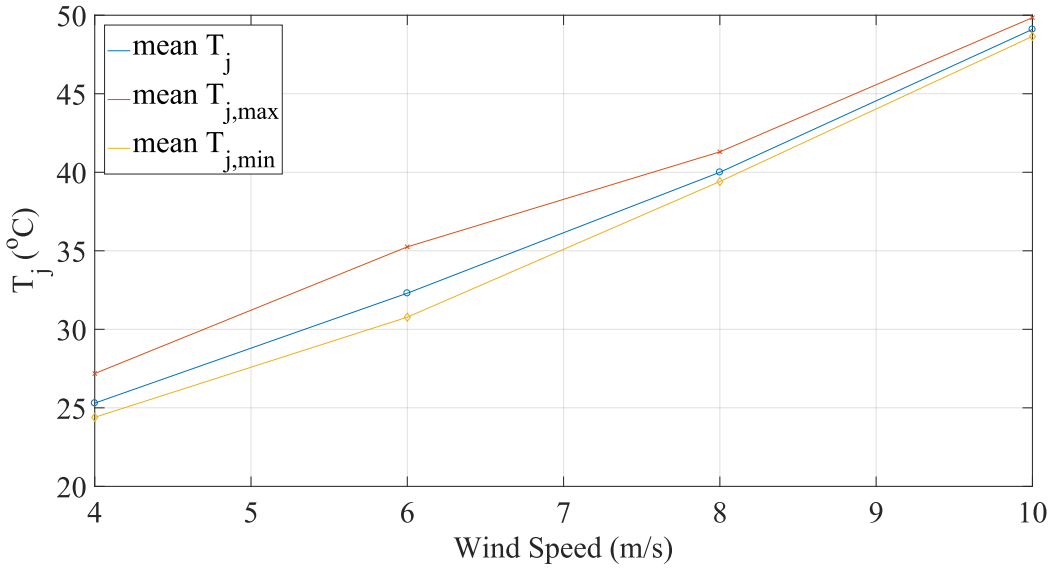

Figure 5.10: Mean T_j values for equivalent wind speed tests.

To test the impact of the m, two further tests were conducted. The first involved applying a 300V DC link with a 32Ω load and modifying m to 0.57 to produce an I_c current of 2.7A. The second test returned the m to 1 and changed the load to 80Ω to also produce a current of 2.7A. This was also compared to the 1Hz fundamental frequency ΔT_j in Section 5.3.1. The results are detailed in Figure 5.11.

Figure 5.11.c reveals that the ΔT_j is larger for a smaller m than the ΔT_j resulting from a higher m (Figure 5.11.b), and is even higher than the ΔT_j arising from the highest current test (Figure 5.11.a). This is despite the mean temperatures for the results in Figures 5.11.b,c both being 47°C, whilst the mean temperature for the result in Figure 5.11.a is higher at 60.5°C. Therefore, a higher mean current produces a higher mean temperature, but a lower m produces a higher ΔT_j.

At first glance, this seems counter-intuitive and seemingly disproves the results in Section 5.3. However, this result can be explained by the use of a resistive load in the experimental rig. Despite an average I_c of 2.7A reducing the overall power losses experienced by the device, the instantaneous I_c at switching is still 5A when the load is at 32Ω. What is unclear at present is why when m is reduced, there is a higher ΔT_j around the mean. This requires further

experimentation. In contrast, the inductive load in the simulations acts as a low pass filter, smoothing the current throughput, in effect creating a current throughput similar to that of the 80Ω resistive load which does provide a lower ΔT_j as found in the simulations.

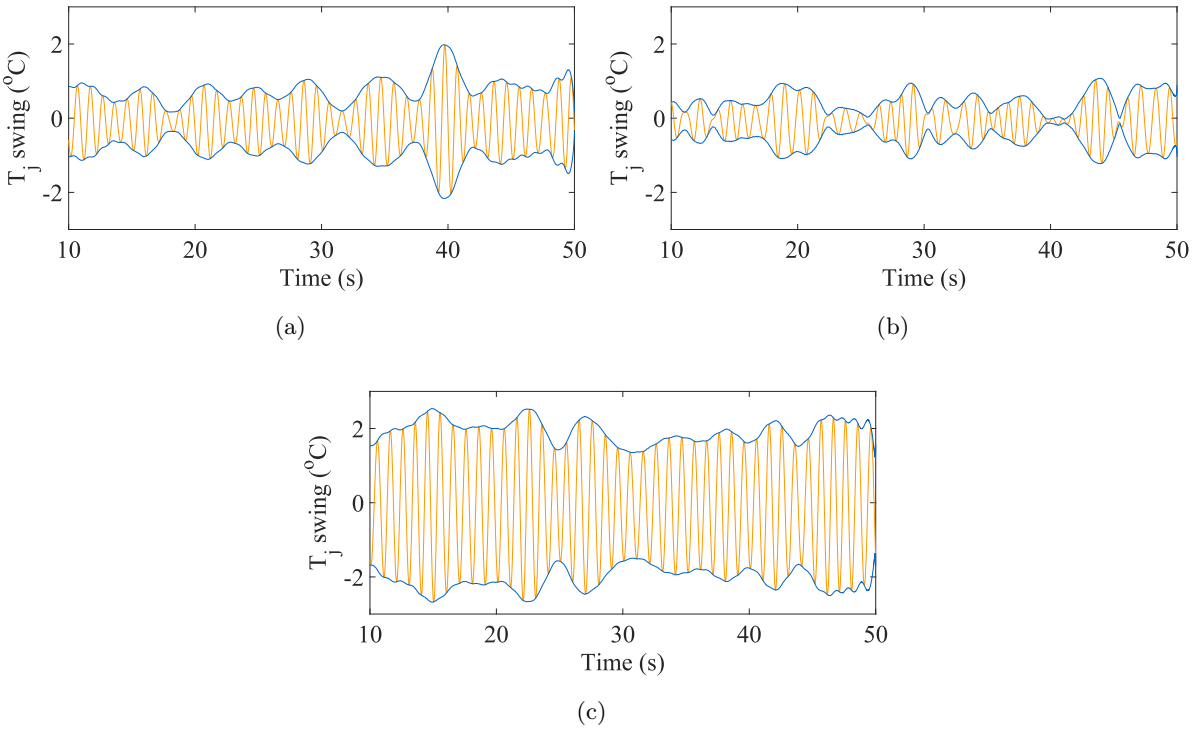

Figure 5.11: Filtered 1Hz ΔT_j for (a) 300V DC link, 32Ω resistive load a with m of 1, (b) 300V, 80Ω and a m of 1, and (c) 300V, 32Ω and a m of 0.57.

These results therefore validate that the mean temperature will increase with increasing wind speed in a PMSG wind power module as shown by the increasing mean temperature with current, and highlights the importance of providing an equivalent reactive load to emulate the wind turbine power module conditions in future testing as the resistive load produces an opposite ΔT_j trend to the expected response with a reactive load.

5.3.5 Impact of Heatsink

As discussed in Section 5.3.3, comparison of simulation results with a comparative study revealed the difference including heat sink parameters made to the calculated temperature profile. To validate the inclusion of heat sink parameters, the temperature was monitored from cold start for 25 minutes for the test regimes outlined in Table 5.1 at 300Hz. A five second moving average filter was then applied to each temperature result to highlight the mean temperature trend at each equivalent wind speed by removing the ΔT_j resulting from the current cycling (Figure 5.12).

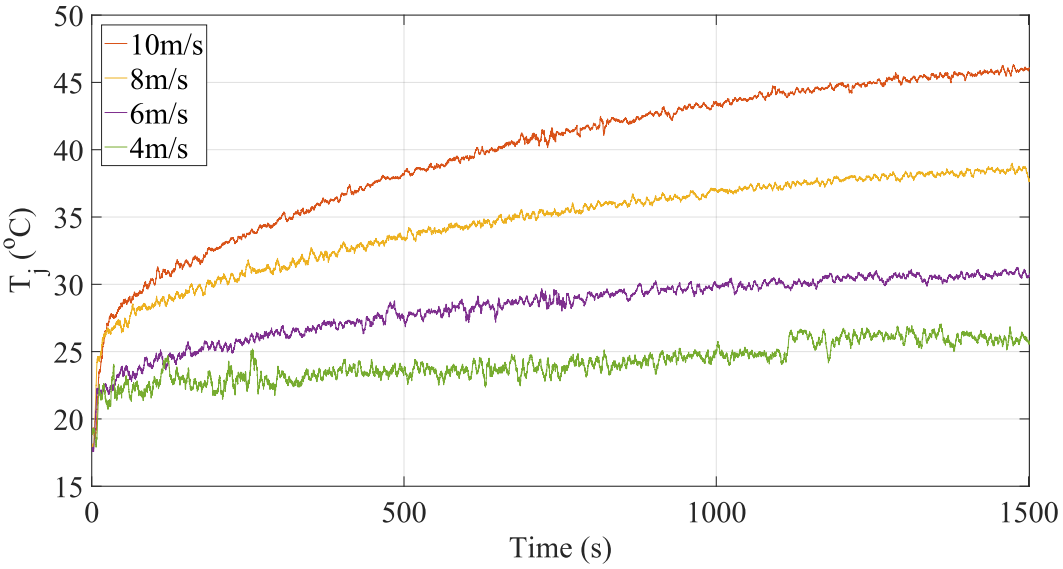

Figure 5.12: Moving average heat up curves of DUT under various equivalent wind speed conditions.

Comparing Figure 5.12 to Figure 5.9, it is clear that the heat sink causes the temperature rise to take orders of magnitude longer than without. Whilst the time taken may be an overestimation due to the small size of the DUT meaning the thermal separation from junction to heat sink is smaller than in a larger device, it is unlikely that this would reduce the heat up time from 1000s of seconds to fractions of a second. Indeed DDTRET also takes a significant amount of time to reach steady state. Therefore, it can be concluded that the heat sink parameters must be included in any thermal modelling of the power converter for accurate thermal simulation for both peak temperature (Section 5.3.3) and thermal time constant.

5.4 Simulated Synthetic Wind Speed Inputs

In Section 5.3.2 the example of SCADA data was used to represent how often a turbine may be in a damaging operating state. Whilst this can provide a rough estimate, SCADA data can mask much of the wind speed variation and therefore the full range of T_j cycles. This section analyses the impact of using SCADA data on the resultant T_j profile and estimated cost to life in more detail. It is also determined whether it is necessary to simulate higher frequency current cycles in order to provide accurate T_j simulation (Section 5.4.2). Following this, the required minimum frequency wind speed data for satisfactory simulation of T_j profiles is determined (Section 5.4.3). This is with the aim of answering RQ1.

5.4.1 Drive Train Response to Turbulent Wind Profile

Figure 5.13 details the current response of one IGBT in the MSC to a synthetic turbulent wind speed input for 60s. The wind speed was simulated using the normal turbulence model equation (5.1) [141] with a mean hub wind speed (V_{hub}) of 8m/s and turbulence intensity (I_{ref}) of 0.12. The wind speeds were produced for each second and the intermediate wind speeds linearly interpolated.

$$\sigma_1 = I_{ref}(0.75V_{hub} + 5.6) \tag{5.1}$$

where σ_1 is the turbulence standard deviation.

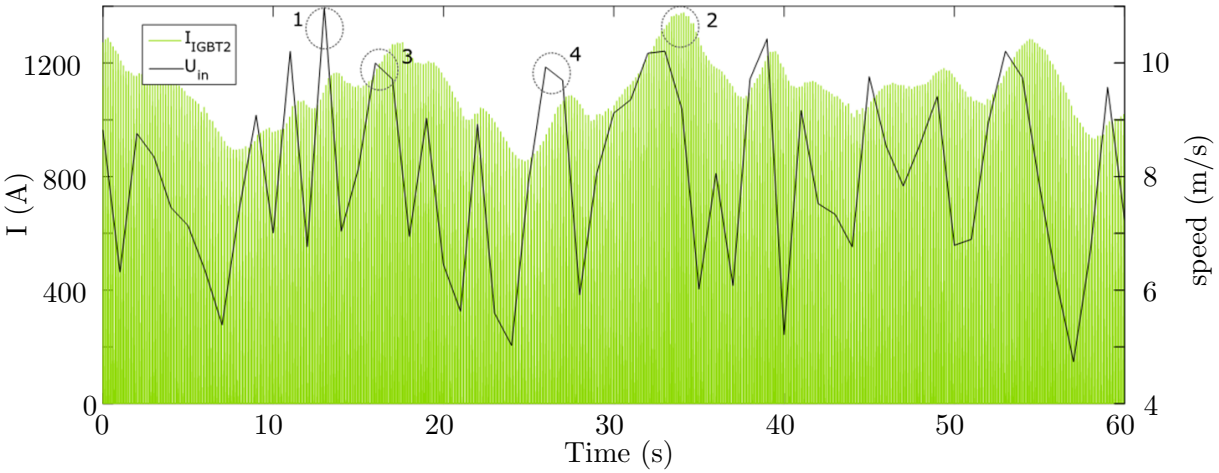

Figure 5.13: IGBT current response to turbulent wind speed.

Figure 5.13 demonstrates three important characteristics that are specific to wind turbine power converters:

- There are delays between the peaks in wind speed and peaks in current as the drive train dynamics introduces a time-delayed response to the changing wind speed through inertia.
- The highest wind speed |1| does not correspond to the highest current |2|. As the wind does not remain at |1|, the wind does not have the power to speed up the turbine sufficiently to reach optimum operating conditions. In contrast the lower but sustained wind speed before |2| allows the turbine get closer to the optimum operating point.
- The wind speeds |3| and |4| are similar, but give different current responses. The current at |3| is higher as the wind speed prior to this peak is higher than the wind speeds before |4|. The wind speed history is just as important as the present wind speed in determining the current throughput of the converter.

The turbulent wind speed has highlighted that the current in the converter cannot be directly

derived from the present wind speed, and the dynamics of the drive train and the wind speed history must be considered. It can therefore be inferred that it is impossible to get accurate reliability from lower time resolution wind data such as SCADA as vital wind speed information is lost.

5.4.2 Analysis of using Low Frequency Wind Speed Data

As the use of low frequency average wind speed data is a popular choice for reliability analysis, it was deemed crucial to analyse the impact of this data on the life estimation of the power converter. Two wind speed profiles were analysed and compared. The first is a step change in wind speed from 12.7m/s to 10m/s, before returning to 12.7m/s (Figure 5.14.a) to represent SCADA data. The second profile has the same average wind speeds, but with 'turbulence' added of amplitude ±0.5m/s and a frequency of 0.05Hz to represent a low frequency, low magnitude wind speed oscillation (Figure 5.14.d). The resulting temperature profiles are considered as both a directly derived single temperature at each wind speed, and with the resulting T_j profile from the current cycling.

Temperatures Derived From SCADA

The first step was to determine the impact of using mean, or maximum and minimum T_j values on the estimated cost to life for the profile in Figure 5.14.a. The wind speed profile was applied to the DDTRET and the mean, maximum and minimum T_j values were extracted. These T_j profiles were applied to the cycles-to-failure data (Chapter 3) to calculate the life cost during this 20 minute period. For meaningful comparison, the indicative expected lifetime was estimated by extrapolating the 20 minute period until the end-of-life would be reached. The results of this analysis can be found in Table 5.2.

Device	T_j used	ΔT_j (° C)	mean T_j (° C)	life cost (%)	Expected life (yrs)
IGBT	mean-mean	12.87	67.13	-	-
IGBT	max-min	21.85	69.23	7.38×10^{-7}	5156.06
Diode	mean-mean	26.33	85.56	4.66×10^{-6}	816.56
Diode	max-min	42.48	88.69	6.19×10^{-5}	61.47

Table 5.2: Estimated device lifetime based on 10 minute wind data.

Firstly, Table 5.2 reveals that there is a significant increase in ΔT_j between the mean-mean profile and max-min profile. Interestingly, there is also a slight increase in the mean T_j which can

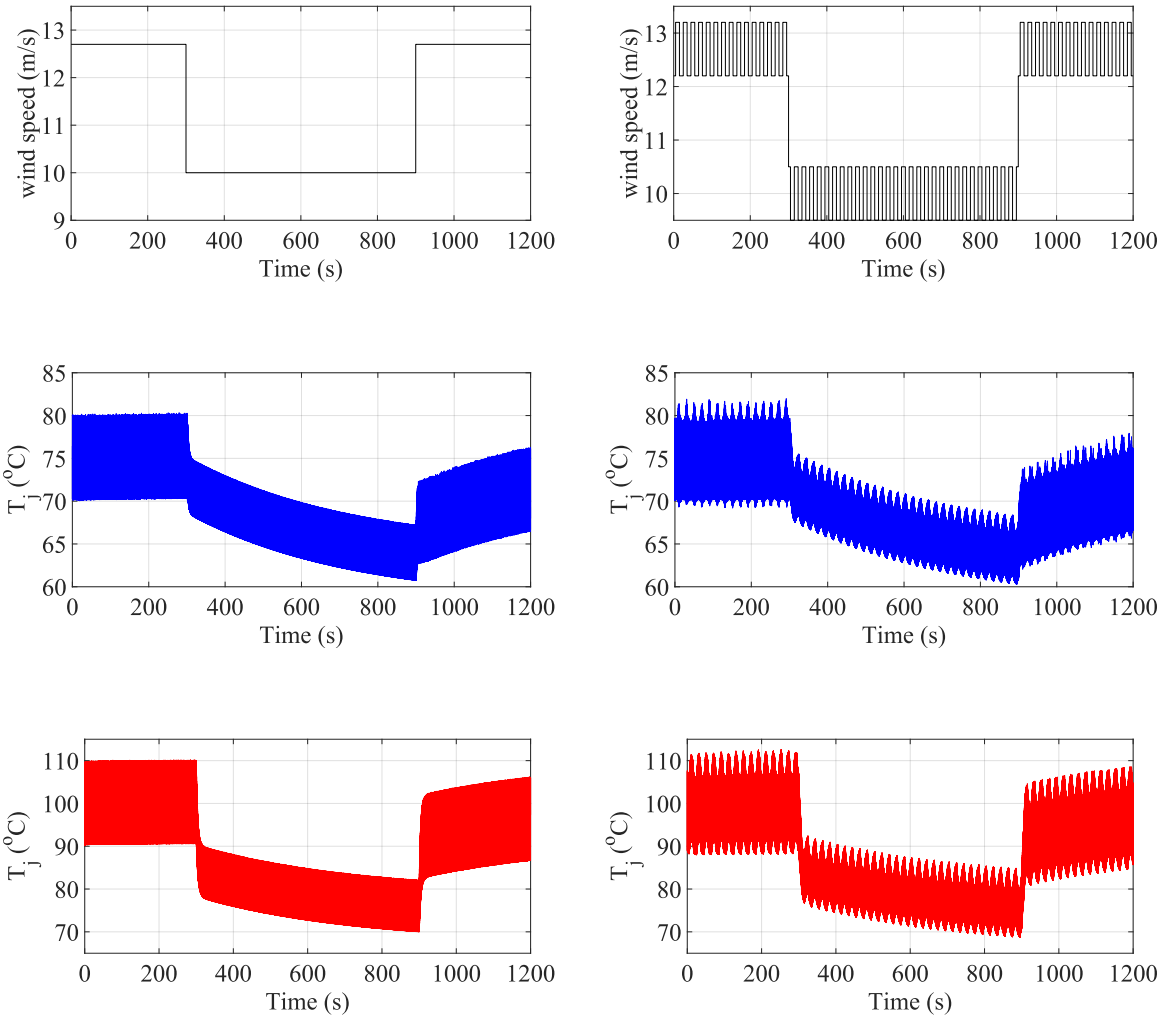

Figure 5.14: T_j Response of (b,e) IGBT and (c,f) diode to varying wind speed inputs (a,d).

be attributed to the non-linear increase in temperature with wind speed; the maximum-mean ΔT_j is larger than the mean-minimum ΔT_j, providing a higher overall mean value.

Secondly, the expected life of the devices decreases significantly from the mean-mean data to the max-min data. This can be attributed primarily to the increase in ΔT_j, with a small contribution from the increase in mean T_j. Indeed, IGBT device ΔT_j increases from below the 18K theoretical plastic deformation limit described in Chapter 3, so the device does not see any damage, to above this 18K limit.

Finally, the indicative expected life of the devices is unrealistically high; even the lowest expected lifetime is three times the design life of a typical wind turbine, and the studies discussed in Chapter 2 show that this cannot be the case. These results reveal that the use of single tem-

perature points for long time periods, such as in [82], is simply unrealistic due to the extremely high estimated life times produced by the approach. To further condemn this approach, the results in [82] were replicated and it was discovered that the rainflow counting algorithm had been incorrectly applied to the T_j profiles; the expected lifetimes were reported in hundreds of years, but were in fact in the thousands of years. They therefore provide little useful information for wind turbine converter reliability improvement.

Current Cycling Temperatures

The use of SCADA representative temperatures has been shown to be inadequate for lifetime estimation of power modules. Therefore, the impact of introducing current cycling data from the drive train operation superimposed onto the SCADA wind speed profile has been explored. For this analysis, the results are compared to the mean T_j results from Table 5.2 (Table 5.3).

T_j Source	Device	SKiiP3 Life Cost (%)	Expected Life (yrs)
SCADA mean-mean	IGBT	-	-
DDTRET	IGBT	3.9266×10^{-7}	9690.76
SCADA mean-mean	Diode	4.66×10^{-6}	816.56
DDTRET	Diode	1.0157×10^{-2}	0.375

Table 5.3: Estimated Device lifetime based on wind speed inputs in Figure 5.14 with current cycling considered.

The current cycles added to the Figure 5.14.a profile have introduced IGBT T_j cycles above the 18K threshold, moving the life expectancy from infinite to very high. However, these cycles only occur when moving between wind speed levels as the ΔT_j at 12.7m/s is still too low to cause plastic deformation according to the 18K limit (Figure 5.7.a). In contrast, the diode's expected life has reduced dramatically to a few months as the current cycles lead to cycles above the 18K. Whilst this is only indicative, it reveals that even short periods at high wind speeds can do significant damage to the diodes.

Addition of Turbulence

The impact of using current cycles in lifetime analysis was expanded by introducing turbulence (Figure 5.14). The results of the life expectancy calculations for both non-turbulent and turbulent wind speed profiles are outlined in Table 5.4.

It would be expected that the more varied wind speed profile would cause higher damage.

U Input	Device	SKiiP3 Life Cost (%)	Expected Life (yrs)
Non-Turbulent	IGBT	2.2836×10^{-7}	16663.05
Turbulent	IGBT	3.9266×10^{-7}	9690.76
Non-Turbulent	Diode	1.0581×10^{-2}	0.360
Turbulent	Diode	1.0157×10^{-2}	0.375

Table 5.4: Estimated Device lifetime comparison between SCADA representative temperatures and current cycling temperatures for non-turbulence wind speed input.

From Table 5.4 it is clear that this is the case for the IGBT, though is due to the transition ΔT_j becoming more extreme and therefore more damaging. However, the diode T_j profile becomes slightly less damaging. This is due to the T_j and ΔT_j cycle distribution shown by the rainflow counting data (Figure 5.15). Whilst there are some cycles with a higher mean T_j due to the higher wind speeds for the more turbulent wind profile (Figure 5.15.b) when compared to the 2000+ cycles for the non-turbulent results (Figure 5.15.a), on average the mean T_j for many of the cycles has actually reduced (Figure 5.15.b). Furthermore, the lower wind speeds have also introduced more lower ΔT_j cycling that actually drop below the 18K threshold, providing 4.4% fewer damaging cycles over the same period (Figure 5.15.b). Combined, these two effects reduced the impact on the converter lifetime for the diode when moving from the non-turbulent to turbulent wind speed profile. As a reminder, these lifetimes are for illustrative purposes as the wind turbine would not remain in the wind speed state indefinitely as assumed by the lifetime calculation.

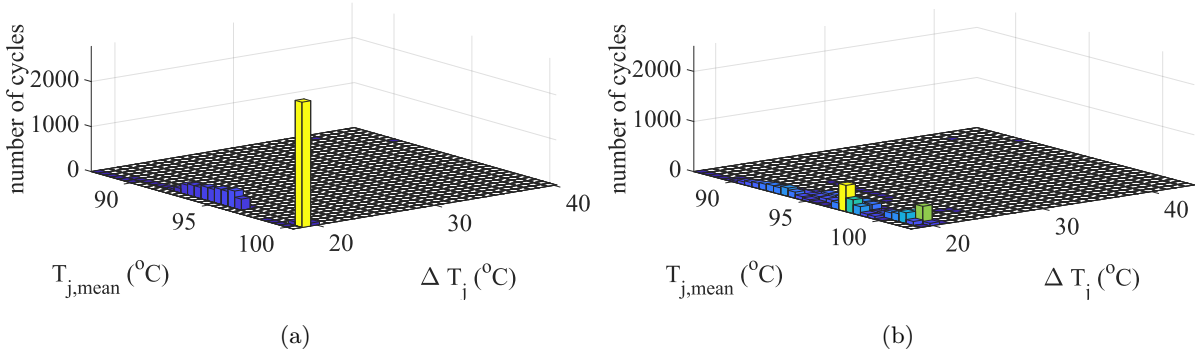

Figure 5.15: Cycle count of T_j for (a) Figure 5.14.e. and (b) Figure 5.14.f.

What these results reveal is that SCADA representative temperatures cannot provide an accurate estimation of life for the power converter. A rough estimate can be achieved by if

current cycling data is applied through the DDTRET, but a much more accurate result can be provided if detailed wind speed profiles are applied to the DDTRET. The importance of this more detailed wind speed profile is shown by the reduced lifetime estimation for the IGBT when turbulence is introduced, but an increased lifetime estimation for the diode.

5.4.3 Wind Speed Data Temporal Fidelity

Section 5.4.2 discovered that the use of SCADA wind speed data is limited for providing accurate lifetime estimation of the wind turbine power converter as it oversimplifies the loading profile. However, the analysis did not determine the wind speed data frequency required to provide sufficient quality temperature profiles for converter lifetime analysis.

To address this, experiments have been constructed which use synthetic WSTS to isolate potential wind speed characteristics and determine their impact on thermal loading. Square waves have been used to represent sudden changes in wind speed, which was validated against high frequency wind speed data (Figure 5.16).

The tests are conducted over 65s or 125s of wind speed data, with the first 5s carried out at constant wind speed to minimise the impact of variations in the input current due to the initialisation procedure (Chapter 3). For the square wave tests this constant wind speed represents the average power wind speed, which is slightly higher than the average wind speed. The model time step is also much smaller than the test period to ensure it does not influence the results; 5×10^{-6}s for the drive train.

The power module T_j response to square wave WSTS is detailed to understand what might be masked by using SCADA data in lifetime and ΔT_j calculations. For comparison the maximum ΔT_j over the simulation period (max ΔT_j) has been plotted for square gust amplitudes of 1 and 2m/s, for varying frequencies and mean wind speeds, for both IGBT and diode (Figure 5.17).

In general, the higher the frequency of wind speed variation, the lower ΔT_j becomes. This is as the turbine inertia acts as a low-pass filter, restricting the high frequency wind speed variation being transmitted as current variation. Indeed, wind speed variations with frequency greater than 0.25Hz lead to a minimal increase in ΔT_j compared to the constant wind speed case (0Hz). Therefore, reasonable approximations of T_j profiles can be made (within 1°C) with 0.25Hz wind speed data. Furthermore, these results imply that lower turbulence wind farm sites, such as offshore, have more damaging thermal profiles in the converter than higher turbulence onshore sites. There are exceptions to this trend. ΔT_j becomes relatively consistent below 0.03Hz. This

is because the turbine has time to respond to the change of wind speed and reaches its steady operating state. The turbine is then at this steady state condition long enough for T_j to reach its maximum before the wind speed reduces. The same will also be true for the minimum T_j. Therefore gust frequencies of 0.03Hz and below provide the maximum ΔT_j.

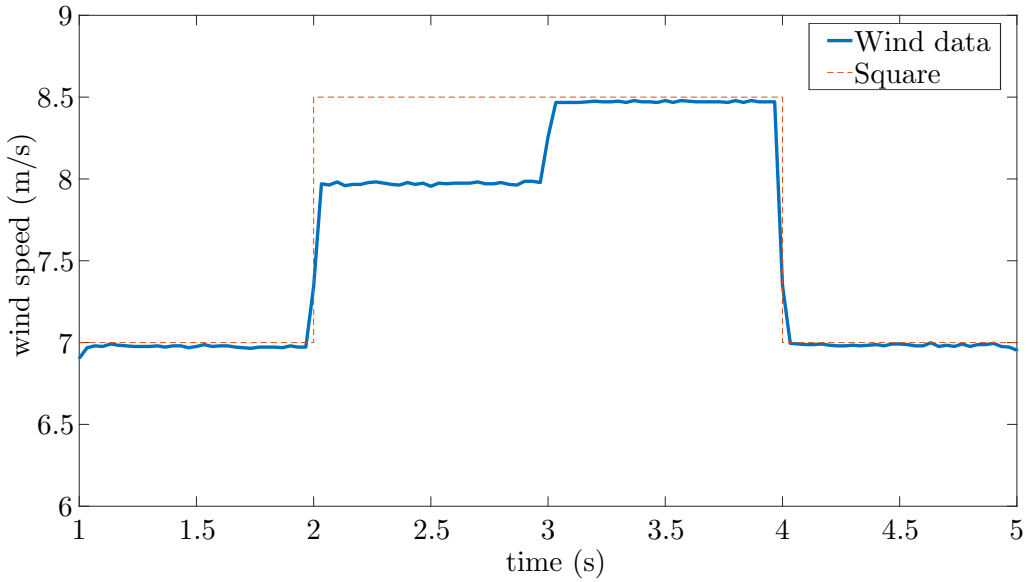

Figure 5.16: Example of square wind speed gust and square wave representation used for this analysis.

These results agree with the previous section that the use of one wind speed data point for a long time period e.g. 10 minute SCADA data, 3-hourly data found in [82], or the use of a wind speed distribution as in [79, 80], can mask a large amount of information and will underestimate the T_j variation significantly; in Figure 5.17.d the diode ΔT_j at U_m of 12m/s increases by up to 59%, taking it beyond the plastic deformation limit. Therefore these results agree with the conclusions in [77] that higher frequency wind speed data is required for accurate T_j profile estimation, and it is suggested that a minimum WSTS sampling frequency of 0.25Hz is required, though it is recognised that this will not always be available/practical. This, however, would reduce the amount data required for studies such as in [77, 84, 85, 88] where higher frequency WSTS is currently used. The results at higher U_m also indicate that the unique operating conditions of wind turbines may have a significant effect on the T_j profile experienced by the power converter, and therefore the lack of drive train dynamic modelling, such as inertia, in [74, 80, 86] will change the T_j profiles significantly.

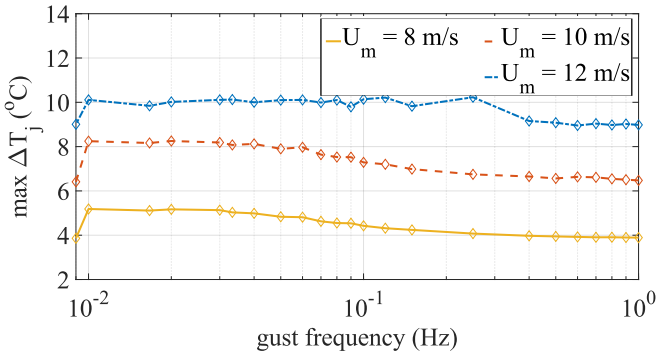

(a) IGBT, ΔU of 1m/s

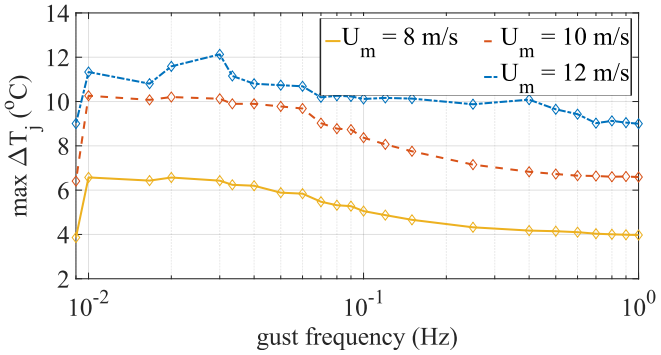

(b) IGBT, ΔU of 2m/s

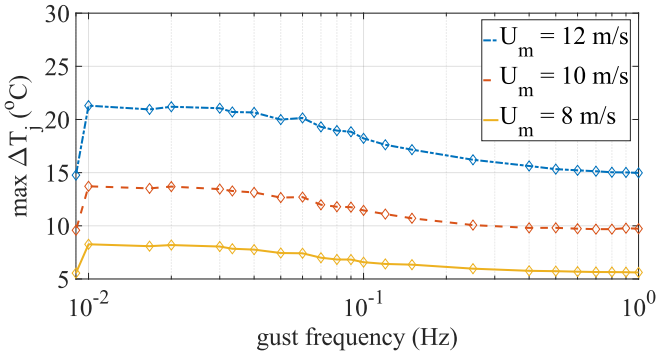

(c) Diode, ΔU of 1m/s

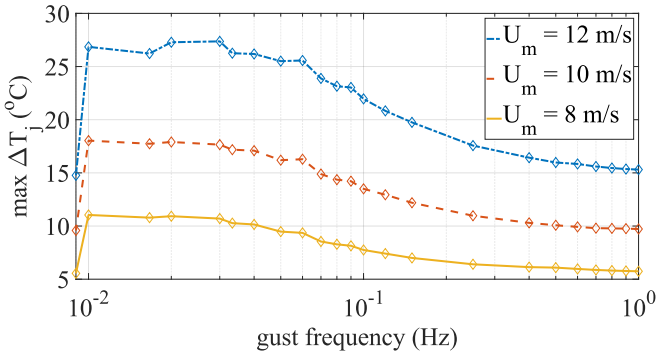

(d) Diode, ΔU of 2m/s

Figure 5.17: max ΔT_j over varying mean wind speeds (U_m) and square gust frequencies for (a) IGBT for ΔU of 1m/s, (b) IGBT for ΔU of 2m/s, (c) diode for ΔU of 1m/s and (d) diode for ΔU of 2m/s.

5.5 Summary

This chapter has used the drive train model and experimental set up outlined in this thesis to analyse wind turbine power converter reliability with a holistic approach. From this holistic approach, the following conclusions have been made:

- The turbulent wind speed has highlighted the need to also consider the wind speed history in deriving the current throughput. Therefore the power module current throughput is complex and cannot be directly derived from the current wind speed but requires a drive train model.
- At high wind speeds and the resulting high frequency sine wave output the switching pattern of the IGBT causes intermittent T_j profiles.
- The diodes experience greater thermal loading than the IGBTs in all comparative cases as a result of their thermal properties and current throughput.
- A comparison with another study and experimental tests showed that the inclusion of heat sink thermal parameters and ambient temperature are important for providing accurate T_j profiles.
- The lower the frequency of wind speed variation, the higher ΔT_j becomes, implying that low turbulence sites such as offshore have greater thermal variation, and therefore damage, in the converter.
- For the first time, the minimum wind speed data frequency for accurate converter thermal simulation has been determined. Wind speed variations with frequency greater than 0.25Hz have a small increase in ΔT_j and therefore reasonable approximations of T_j profiles can be made with 0.25Hz wind speed data. Wind speed data at lower frequencies allow simulations to overlook damaging temperature variations.
- At high wind speeds the ΔT_j exceeded the theoretical plastic deformation limit. With a typical wind speed profile the lifetime of the device was estimated at 8.5 years.
- Experimental tests confirmed that the PbSe sensor is able to measure ΔT_j at the current fundamental frequencies.
- A replication of the wind speed conditions in the laboratory environment showed the same pattern for increasing mean temperature with increasing wind speed.
- Interesting ΔT_j results highlighted the need to accurately replicate the reactive load found in a real wind turbine in a laboratory setting.

Chapter 6

Ongoing Research Projects

6.1 Introduction

With all research there are always paths untravelled, alleys unexplored and detours made and this project is no exception. This chapter briefly outlines the spin-off activities from this project that are avenues of ongoing investigation. This research is split into two main categories: experimental emulation of wind turbine operating conditions (Section 6.2), and power converter condition monitoring (Section 6.3).

6.2 Wind Turbine Laboratory Emulation

Research from this thesis has highlighted the need for more advanced, larger-scale testing of devices. In response ANECTO, a power electronics testing company, have supported an ongoing research project, proposed by the author, to construct a rig to emulate wind turbine operating conditions applied to power converter in a laboratory environment. This rig is heavily reliant on the research carried out in Chapter 4, using much of the same equipment and control. This research aims to tackle further some key limitations of present converter reliability research that have begun to be addressed in this thesis:

1. Present device manufacturers design their power modules conservatively based on perceived worst case operating conditions, however [46] has shown that failure rates remain high. By providing a test bench whereby converters are able to be tested under realistic conditions, the power module design may be optimised, reducing the cost of the power modules significantly. Furthermore, understanding the loading conditions that cause the greatest damage may reveal that present design methodologies are not accounting for the

truly worst case scenarios.

2. Data used for lifetime estimation could be significantly improved using realistic loading profiles when compared to fixed cycling testing. This will pave the way for more realistic lifetime estimations, allow for improved prognosis of device end-of-life and increase the possibility of utilising reactive maintenance. This will significantly reduce wind turbine O&M costs and subsequently LCoE.

3. Wind turbine specific power cycling can be combined with testing under controlled atmospheric conditions to replicate power cycling in the harsh marine environment. This can include replicating the impacts of humidity and ambient temperature on device reliability, and testing potential solutions with a high level of confidence of their practical application in the field.

The test bench also aims to test a $600V_{ces}$, 30A MiniSKiiP 15AC066V1 power module [142] to examine the impact of scaling factors on the temperature results as compared to the 6A device used in Chapter 4. This rig is based on the test bench in Chapter 5, with some changes implemented to extend the operational range for more realistic, industrial-scale testing as outlined in the next section.

6.2.1 Emulation Concept

Figure 6.1 details the circuit diagram for the wind turbine emulation rig.

There are a number of modifications to the test bench outlined in Chapter 4:

- The direction of current has been reversed so that the DUT is set up as an active rectifier (MSC).
- To emulate a wind turbine drive train and generator, an AC-AC converter and inductor bank have been added.
- The load in Figure 6.1.a have been replaced with a DC link for regeneration.
- The control has been significantly expanded to allow for closed loop control of the AC-AC converter and DUT to emulate wind turbine conditions more closely. Much of this control is based on the DDTRET (Chapter 3).

Generator Emulation

Typically, a wind turbine generator is emulated using a motor-generator set, with the motor representing the turbine torque from the mechanical drive train. Whilst this unquestionably

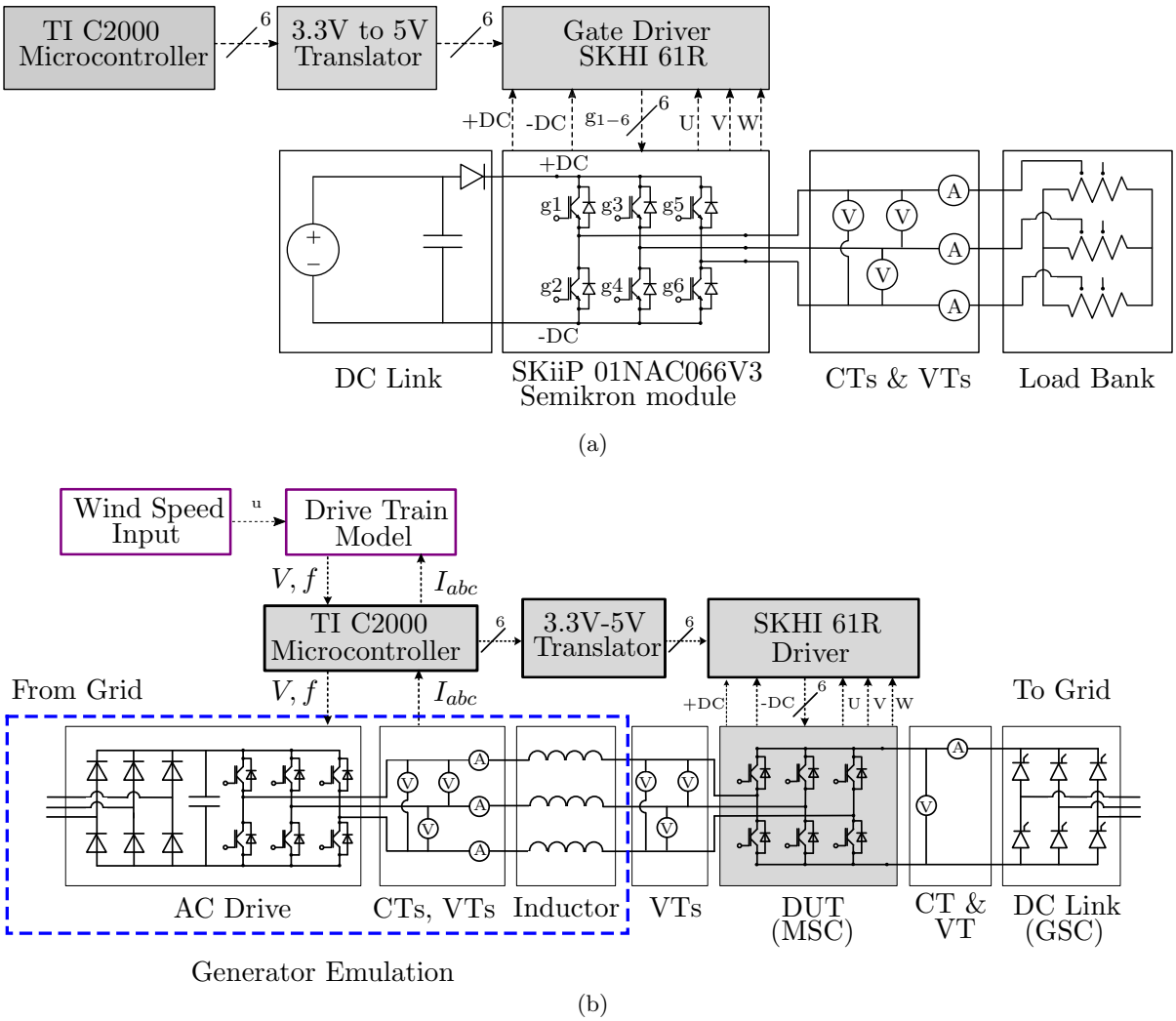

Figure 6.1: Comparison of (a) circuit diagram from rig used in this thesis and (b) circuit diagram of wind turbine drive train emulation rig.

provides an accurate emulation of generator output, there is little flexibility to examine the impact of varying machine parameters on converter loading without purchasing a new generator each time. Furthermore, scaling down the full-scale machine parameters could require costly bespoke generator design and construction to ensure that the generator parameters are scaled appropriately. These factors potentially make this approach impractical.

In response, the generator emulation outlined in Figure 6.1 is designed to provide test bench flexibility with minimal modification costs. In this case, the generator emulation is based on the per-phase equivalent circuit diagram of a synchronous generator (Figure 6.2). E_a is the armature voltage, X_s is the synchronous internal reactance, R_s is the synchronous internal resistance, and E_c is the converter voltage.

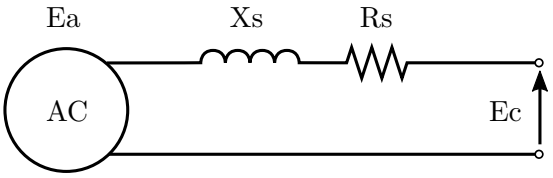

Figure 6.2: Synchronous machine per-phase equivalent circuit diagram.

The AC-AC converter in Figure 6.1 emulates the armature voltage of the generator by providing a voltage-frequency ratio that is determined by the machine being emulated. The internal impedance is replicated using a variable inductor bank. A change in generator parameters can be made by modifying this voltage-frequency ratio and the impedance on the lines, providing the required flexibility lacking in previous approaches. Furthermore, this approach will allow for any range of drive train parameters to be emulated by changing the software used to control the converter, with no mechanical modifications required. This facilitates the testing of other drive drain topologies outside the wind industry, such as in electric vehicles.

Regeneration

The consumption of tens of amps at hundreds of volts for sustained periods of time is demanding on research budgets and does not aid in providing sustainable research into a sustainable technology. As such, it was decided that any power throughput of the device should not be dumped into a load bank, but fed back into the grid. This regeneration is achieved using a controllable DC link connected to the grid (Figure 6.1). This will become even more critical when testing at wind turbine power levels.

Control

There are two main sub-systems to the test bench control: input control to emulate wind turbine operating conditions, and DUT control.

For turbine emulation, the control variables are the AC-AC converter voltage and frequency. Variable values are determined using the drive train model developed in Chapter 3. Wind turbine conditions can then be emulated by feeding the software with the required wind speed profiles so that the turbine generator response and subsequent voltage and frequency can be calculated. For the software to ensure stability, the feedback loop will be closed using a measured current signal as found in the original drive train model.

As a Texas instruments controller will be implemented, as in the test bench outlined in

Chapter 4, the DDTRET Simulink control blocks can be ported onto the controller with no fundamental changes required. This will ensure that the control in the simulation work will be comparable to that used in the test bench.

6.3 Power Converter Condition Monitoring

The knowledge gained during the project has opened up other opportunities for power converter research, particularly power converter condition monitoring. These opportunities have branched from two main sources: the drive train model and the converter set-up.

The drive train model has subsequently been modified by other researchers for a number of wind turbine condition monitoring based scoping studies. The most significant contribution has been the addition of a medium speed gearbox and GSC to allow for the exploration of using readily available converter signals to detect faults in the gearbox and characterise potentially damaging gust profiles. Details of this study, co-authored by this thesis' author, can be found in [143]. Other studies have included the addition of start-up and shut-down procedures, and multi-level converter modules and their respective impacts on turbine reliability.

The converter set-up has also provided opportunities for experimental work into condition monitoring of the converter itself. This has used a number of the control techniques developed in this project to provide cycling conditions for converters whilst measuring potential damage, with damage emulated through artificially overheating the device.

It in envisaged that this condition monitoring work will be combined with the reliability work outlined in this thesis to produce a centre of excellence for wind turbine power converter reliability and condition monitoring at Durham University.

6.4 Further DDTRET Testing

There is a range of testing that can be carried out utilising the DDTRET which would aid in furthering knowledge of power converter thermal loading in wind turbines.

Firstly, despite efforts to accurately scale between simulation and experimental models during set up, at present the simulation and experimental set up provide temperature results that are difficult to correlate. This could be rectified by producing a simulation that is at the same scale as the experimental work for direct comparison and further development. This simulation could also produce data that could be used to validate the larger scale model. This was not carried out, in part, due to the lack of thermal capacitance data available for the DUT, but now the

experimental component of DDTRET is set up this thermal capacitance could now be measured directly.

Secondly, whilst the impact of increasing wind speed was simulated using DDTRET, it was impossible to distinguish to what extent different drive train characteristics affect the temperature profile of the power converter. There is scope to provide parameter sensitivity studies to determine the independent impact of various aspects of the current trace. An example of this would be to maintain the power levels but vary the driving frequency to see if the frequency affected the ability of the device to reach thermal equilibrium, and how this affected the number of thermal cycles in a period. The results of this type of study would aid in the selection of operating frequencies for large scale wind turbines that could extend the life of the power converter.

Finally, one of the key questions that arose from this research was the fact that there is much inherent disagreement on the ΔT_j that will instigate damage to the devices. Consensus on this value would provide a much improved understanding on the failure mechanisms found in wind turbines and provide improved ability to optimise converter designs for the wind environment. This test bench can now provide a platform to explore this important ΔT_j threshold.

6.5 Summary

This chapter has outlined a number of avenues of research that have branched out from the work outlined in this thesis. This ongoing research includes the construction of an experimental rig to emulate the converter operating conditions in a wind turbine in a laboratory environment. This emulation utilises a novel approach to providing the current cycles to the converter.

Other work includes the expansion of the drive train model for use in condition monitoring, particularly using readily available converter signals to monitor the drive train's performance, and provided the basis for experimental studies into direct power converter condition monitoring.

Chapter 7

Conclusions

An analysis of several wind farm failure data has revealed that the power converter, particularly in permanent magnet synchronous generator wind turbines, is a reliability critical system. As such, the power converter has been identified as requiring further investigation to determine the cause of failure to reduce wind turbines' levelised cost of energy.

A critique of the literature that determine the reliability of the power converter in the wind turbine/wind farm concluded that physics-of-failure models as the most promising approach for providing useful information to wind farm operators on how the operation of wind turbines impacts the reliability of the power converter. The limitations of the present research approaches have been outlined, including the present lack of a holistic approach for power converter reliability analysis specific to wind turbine power converters, and the disparity between experimental and in-field testing results. In response a holistic approach to wind turbine power converter reliability research was proposed which considered realistic operating conditions of the wind turbine being emulated in a laboratory environment.

This holistic approach included simulation work in the form of a drive train model and power converter thermal model, packaged as the DDTRET. The drive train model consisted of a 2MW fully rated converter permanent magnet synchronous generator turbine with maximum power point tracking achieved using torque control and rated operation maintained using an active pitch system. The power module thermal model consists of two key aspects: a power loss model and a thermal equivalent circuit. A lifetime model was outlined based on the cycles-to-failure versus mean junction temperature and junction temperature swing. The cycles from a thermal profile are counted using a rainflow counting algorithm.

An experimental rig has been designed and implemented for temperature measurement validation to allow for thermal monitoring of the device under test. An infra-red sensor approach was deemed the most appropriate method for this research which has not been used for this type of work before. The subsequent thermal measurement experimental design for this research was outlined, including the optics required and the calibration of the chosen lead selenide infra-red sensor. For a realistic testing environment a simplified experimental rig with a 3-phase power converter was constructed. This rig included a scaled down Semikron power module, resistive load, open loop switching control, and the modifications to the power module required for accurate temperature measurement. The electrical system was verified against a simulated system.

This DDTRET and experimental set up was used to analyse wind turbine power converter reliability with a holistic approach. This analysis highlighted some key considerations for future reliability analysis of power converters:

- The wind turbine power module current throughput is complex and cannot be directly derived from the present wind speed, therefore requiring implementation of DDTRET to ensure accuracy.
- At high wind speeds the switching pattern of the IGBT causes intermittent junction temperature profiles.
- The diodes experience greater thermal loading than the IGBTs in all comparative cases.
- Inclusion of heat sink thermal parameters and ambient temperature are important for providing accurate junction temperature profiles.
- The lower the frequency of wind speed variation, the higher junction temperature swing becomes, implying that low turbulence sites such as offshore have greater thermal variation, and therefore damage, in the converter.
- For the first time, the minimum wind speed data frequency for accurate converter thermal simulation has been determined. Reasonable approximations of junction temperature profiles can be made with a minimum of 0.25Hz sampled wind speed data.
- At high wind speeds the junction temperature swing exceeded the theoretical plastic deformation limit. With a typical wind speed profile the lifetime of the device was estimated at 8.5 years.
- Experimental tests confirmed that the lead selenide (PbSe) sensor is able to measure junction temperature swing at the current fundamental frequency.

- Experimental tests showed that the frequency had no impact on the maximum junction temperature swing reached during a current cycle but did change the number of cycles experienced.
- Laboratory testing showed the same pattern for increasing mean temperature with increasing wind speed as the simulation work.
- Interesting junction temperature swing results highlighted the need to accurately replicate the reactive load found in a real wind turbine in a laboratory setting.

A number of avenues of research have branched out from the work outlined in this thesis. This ongoing research includes the construction of an experimental rig to emulate the converter operating conditions in a wind turbine in a laboratory environment which would not be possible without the experimental work carried out here. This emulation utilises a novel approach to providing the current cycles to the converter. Other work includes the expansion of the drive train model for use in condition monitoring studies, particularly using readily available converter signals to monitor the drive train's performance, and provided the basis for experimental studies into direct power converter condition monitoring.

References

[1] BBC, "Why the falling cost of light matters," 2014. [online]. Available at: http://www.bbc.co.uk/news/business-38650976.

[2] Extreme Energy Initiative, "Defining 'extreme energy'," 2017. [online]. Available at: http://extremeenergy.org/2013/07/25/defining-extreme-energy-a-process-not-a-category/.

[3] e.on, "The energy trilemma," 2017. [online]. Available at: https://www.eonenergy.com/for-your-business/large-energy-users/manage-energy/energy-efficiency/decentralised-energy-experts/The-energy-trilemma.

[4] BBC, "Russia's gas fight with ukraine," 2017. [online]. Available at: http://www.bbc.co.uk/news/world-europe-29521564.

[5] BBC, "Fracking at preston new road: Cuadrilla's work begins for shale gas extraction," 2017. [online]. Available at: http://www.bbc.co.uk/news/uk-england-lancashire-38520562.

[6] Royal College of Physicians, "Every breath we take: the lifelong impact of air pollution," 2016. [online]. Available at: https://www.rcplondon.ac.uk/projects/outputs/every-breath-we-take-lifelong-impact-air-pollution.

[7] IPCC, "Ipcc: Summary for policymakers," 2017. [online]. Available at: http://www.ipcc.ch/pdf/assessment-report/ar5/wg1/WG1AR5_SPM _FINAL.pdf.

[8] D. J. MacKay, "Sustainable energy–without the hot air," *UIT Cambridge, England*, 2009.

[9] EU, "Climate action," 2012. [online]. Available at: http://ec.europa.eu/clima/about-us/mission/index_en.htm.

[10] J. Radcliffe, "The future role for energy storage in the uk main report," tech. rep., The Energy Research Partnershop, 2011.

[11] P. Taylor, R. Bolton, D. Stone, X.-P. Zhang, C. Martin, and P. Upham, "Pathways for energy storage in the uk," Tech. Rep. 007, 2012.

[12] Inside Energy, "The numbers behind our clean power plan video," 2017. [online]. Available at: http://insideenergy.org/2016/09/26/the-numbers-behind-our-clean-power-plan-video-or-lightning-bolts-and-the-saturn-v-rocket/.

[13] K. Rohrig and B. Lange, "Improving security of power system operation applying dg production forecasting tools," in *2008 IEEE Power and Energy Society General Meeting - Conversion and Delivery of Electrical Energy in the 21st Century*, pp. 1–6, 2008.

[14] DECC, "Contracts for difference (cfd) allocation round one outcome," 2015.

[15] IRENA, "Renewable power generation costs in 2014," 2017. [online]. Available at: https://www.irena.org/DocumentDownloads/Publications/IRENA_RE_Power_Costs_2014_report.pdf.

[16] S. S. Gjerde and T. Undeland, "Power conversion system for transformer-less offshore wind turbine," in *Proceedings of the 2011-14th European Conference on Power Electronics and Applications (EPE 2011)*, pp. 1–10, 2011.

[17] M. Boettcher and F. W. Fuchs, "Power electronic converters in wind energy systems - considerations of reliability and strategies for increasing availability," in *Proceedings of the 2011-14th European Conference on Power Electronics and Applications (EPE 2011)*, pp. 1–10, 2011.

[18] M. Nandigam and S. K. Dhali, "Optimal design of an offshore wind farm layout," in *International Symposium on Power Electronics, Electrical Drives, Automation and Motion, SPEEDAM 2008*, pp. 1470–1474, 2008.

[19] S. S. Gjerde and T. M. Undeland, "The best suitable multilevel converters for offshore wind power generators without transformers," in *2010 International Power Electronics Conference (IPEC)*, pp. 2398–2404, 2010.

[20] H. Ergun, D. Van Hertem, and R. Belmans, "Transmission system topology optimization for large-scale offshore wind integration," *IEEE Transactions on Sustainable Energy*, vol. 3, pp. 908–917, 2012.

[21] A. Zervos, C. Kjaer, and S. Clifford, "Pure power: Wind scenarios up to 2030," 2008. [online]. Available at: http://www.ewea.org/fileadmin/ewea_documents/documents/publications/reports/purepower.pdf.

[22] Crown Estate, "Round 3 offshore wind site selection at national and project levels, the crown estate," 2012. [online]. Available at: http://www.thecrownestate.co.uk/media/310531/round_3_offshore_wind_site_selection_at_national_and_project_levels.pdf.

[23] E. Davey, "Record investments of 40 billion in renewable electricity to bring green jobs and growth to the uk," 2013. [online]. Available at: https://www.gov.uk/government/news/record-investments-of-40-billion-in-renewable-electricity-to-bring-green-jobs-and-growth-to-the-uk.

[24] S. S. Gjerde and T. M. Undeland, "Fault tolerance of a 10 mw, 100 kv transformerless offshore wind turbine concept with a modular converter system," in *2012 15th International Power Electronics and Motion Control Conference (EPE/PEMC)*, pp. LS7c.3–1–LS7c.3–8, 2012.

[25] D. W. Elliott, S. J. Finney, and C. Booth, "Single converter interface for a cluster of offshore wind turbines," in *IET Conference on Renewable Power Generation (RPG 2011)*, pp. 1–6, 2011.

[26] Crown Estate, "A guide to uk offshore wind operations and maintenance," 2013. [online]. Available at: https://www.thecrownestate.co.uk/media/5419/ei-km-in-om-om-062013-guide-to-uk-offshore-wind-operations-and-maintenance.pdf.

[27] W. Musial and B. Ram, "Large-scale offshore wind power in the united states: Assessment of opportunities and barriers," 2010. [online]. Available at: http://www.nrel.gov/docs/fy10osti/40745.pdf.

[28] S. Bala, J. Pan, D. Das, O. Apeldoorn, and S. Ebner, "Lowering failure rates and improving serviceability in offshore wind conversion-collection systems," in *2012 IEEE Power Electronics and Machines in Wind Applications (PEMWA)*, pp. 1–7, 2012.

[29] J. Chivite-Zabalza, I. Larrazabal, I. Zubimendi, S. Aurtenetxea, and M. Zabaleta, "Multi-megawatt wind turbine converter configurations suitable for off-shore applications, combining 3-l npc pebbs," in *2013 IEEE Energy Conversion Congress and Exposition (ECCE)*, pp. 2635–2640, 2013.

[30] J. Birk and B. Andresen, "Parallel-connected converters for optimizing efficiency, reliability and grid harmonics in a wind turbine," in *2007 European Conference on Power Electronics and Applications*, pp. 1–7, 2007.

[31] D. Jovcic and J. V. Milanovic, "Offshore wind farm based on variable frequency mini-grids with multiterminal dc interconnection," in *The 8th IEE International Conference on AC and DC Power Transmission, 2006. ACDC 2006*, pp. 215–219, 2006.

[32] T. M. Iversen, S. S. Gjerde, and T. Undeland, "Multilevel converters for a 10 mw, 100 kv transformer-less offshore wind generator system," in *2013 15th European Conference on Power Electronics and Applications (EPE)*, pp. 1–10, 2013.

[33] O. Anaya-Lara, N. Jenkins, J. Ekanayake, P. Cartwright, and M. Hughes, *Wind energy generation: modelling and control*. John Wiley & Sons, 2011.

[34] K. Ma, M. Liserre, and F. Blaabjerg, "Reactive power influence on the thermal cycling of multi-mw wind power inverter," in *2012 Twenty-Seventh Annual IEEE Applied Power Electronics Conference and Exposition (APEC)*, pp. 262–269, 2012.

[35] M. A. Parker and O. Anaya-Lara, "Cost and losses associated with offshore wind farm collection networks which centralise the turbine power electronic converters," *IET Renewable Power Generation*, vol. 7, pp. 390–400, 2013.

[36] M. Spring, P. Davies, G. Gaal, and M. Sepulveda, "Top 30 chart for wind turbine failure mechanisms," in *EWEA Annual Event*, 2015.

[37] H. Wang, K. Ma, and F. Blaabjerg, "Design for reliability of power electronic systems," in *IECON 2012 - 38th Annual Conference on IEEE Industrial Electronics Society*, pp. 33–44, 2012.

[38] G. Van Bussel and M. Zaaijer, "Reliability, availability and maintenance aspects of large-scale offshore wind farms, a concepts study," in *Proceedings of MAREC 2001*, 2001.

[39] A. Sannino, H. Breder, and E. K. Nielsen, "Reliability of collection grids for large offshore wind parks," in *Probabilistic Methods Applied to Power Systems, PMAPS 2006*, pp. 1–6, 2006.

[40] E. Spahić, A. Underbrink, V. Buchert, J. Hanson, I. Jeromin, and G. Balzer, "Reliability model of large offshore wind farms," in *2009 IEEE Bucharest Power Tech Conference*, pp. 1–6, 2009.

[41] A. Underbrink, J. Hanson, A. Osterholt, and W. Zimmermann, "Probabilistic reliability calculations for the grid connection of an offshore wind farm," in *9th International Conference on Probabilistic Methods Applied to Power Systems*, pp. 1–5, 2006.

[42] F. Spinato, P. J. Tavner, G. J. W. van Bussel, and E. Koutoulakos, "Reliability of wind turbine subassemblies," *IET Renewable Power Generation*, vol. 3, pp. 387–401, 2009.

[43] J. Ribrant and L. M. Bertling, "Survey of failures in wind power systems with focus on swedish wind power plants during 1997-2005," *IEEE Transactions on Energy Conversion*, vol. 22, pp. 167–173, 2007.

[44] P. Tavner, "Introduction to wind turbines and their reliability & availability, scada & monitoring." Presentation, 2011.

[45] J. Carroll, A. McDonald, O. Barrera Martin, D. McMillan, and R. Bakhshi, "Offshore wind turbine sub-assembly failure rates through time," in *EWEA Annual Event*, 2015.

[46] J. Carroll, A. McDonald, and D. McMillan, "Reliability comparison of wind turbines with dfig and pmg drive trains," *IEEE Transactions on Energy Conversion*, vol. 30, no. 2, pp. 663–670, 2015.

[47] M. Shafiee, M. Patriksson, A.-B. Strömberg, and L. Bertling, "A redundancy optimization model applied to offshore wind turbine power converters," in *2013 IEEE Grenoble PowerTech*, pp. 1–6, 2013.

[48] K. Xie, Z. Jiang, and W. Li, "Effect of wind speed on wind turbine power converter reliability," *IEEE Transactions on Energy Conversion*, vol. 27, pp. 96–104, 2012.

[49] P. Lyding, S. Faulstich, B. Hahn, and P. Tavner, "Reliability of the electrical parts of wind energy systems - a statistical evaluation of practical experiences," in *EPE Wind Energy Chapter Symposium*, 2010.

[50] E. Wolfgang, "Examples for failures in power electronics systems," in *ECPE tutorial on reliability of power electronic systems, Nuremberg, Germany*, 2007.

[51] S. Yang, A. Bryant, P. Mawby, D. Xiang, L. Ran, and P. Tavner, "An industry-based survey of reliability in power electronic converters," *IEEE Transactions on Industry Applications*, vol. 47, no. 3, pp. 1441–1451, 2011.

[52] K. Abdennadher, P. Venet, G. Rojat, J.-M. Retif, and C. Rosset, "A real-time predictive-maintenance system of aluminum electrolytic capacitors used in uninterrupted power supplies," *IEEE Transactions on Industry Applications*, vol. 46, no. 4, pp. 1644–1652, 2010.

[53] G. M. Buiatti, J. A. Martin-Ramos, A. M. Amaral, P. Dworakowski, and A. J. Marques Cardoso, "Condition monitoring of metallized polypropylene film capacitors in railway power trains," *IEEE Transactions on Instrumentation and Measurement*, vol. 58, no. 10, pp. 3796–3805, 2009.

[54] F. Perisse, *Etude et analyse des modes de défaillances des condensateurs électrolytiques à l'aluminium et des thyristors, appliquées au système de protection du LHC (Large Hadron Collider)*. PhD thesis, Université Claude Bernard-Lyon I, 2003.

[55] C. Busca, R. Teodorescu, F. Blaabjerg, S. Munk-Nielsen, L. Helle, T. Abeyasekera, and P. Rodriguez, "An overview of the reliability prediction related aspects of high power igbts in wind power applications," *Microelectronics Reliability*, vol. 51, no. 9, pp. 1903–1907, 2011.

[56] S. Yang, D. Xiang, A. Bryant, P. Mawby, L. Ran, and P. Tavner, "Condition monitoring for device reliability in power electronic converters: A review," *IEEE Transactions on Power Electronics*, vol. 25, pp. 2734–2752, 2010.

[57] A. Sannino, H. Breder, and E. K. Nielsen, "Reliability of collection grids for large offshore wind parks," in *International Conference on Probabilistic Methods Applied to Power Systems, 2006. PMAPS 2006.*, pp. 1–6, IEEE, 2006.

[58] X. Liu and S. Islam, "Reliability issues of offshore wind farm topology," in *Proceedings of the 10th International Conference on Probabilistic Methods Applied to Power Systems, 2008. PMAPS '08*, pp. 1–5, 2008.

[59] A. Karyotakis, *On the optimisation of operation and maintenance strategies for offshore wind farms*. PhD thesis, UCL (University College London), 2011.

[60] B. Kazemtabrizi, C. Crabtree, and S. Hogg, "Reliability evaluation of new offshore wind farm electrical grid connection topologies," in *ASME Turbo Expo 2013: Turbine Technical Conference and Exposition*, pp. 1–10, American Society of Mechanical Engineers, 2013.

[61] H. Arabian-Hoseynabadi, H. Oraee, and P. J. Tavner, "Wind turbine productivity considering electrical subassembly reliability," *Renewable Energy*, vol. 35, pp. 190–197, 2010.

[62] P. J. Tavner, G. J. W. Van Bussel, and F. Spinato, "Machine and converter reliabilities in wind turbines," in *The 3rd IET International Conference on Power Electronics, Machines and Drives*, pp. 127–130, 2006.

[63] T. Zhang and A. Zain, "Modular converter system reliability & performance analysis in design," in *2010 2nd IEEE International Symposium on Power Electronics for Distributed Generation Systems (PEDG)*, pp. 252–258, 2010.

[64] S. Li, "Reliability models for dfigs considering topology change under different control strategies and components data change under adverse operation environments," *Renewable Energy*, vol. 57, pp. 144–150, 2013.

[65] A. Seebregts, L. Rademakers, and B. van den Horn, "Reliability analysis in wind turbine engineering," *Microelectronics Reliability*, vol. 35, no. 910, pp. 1285 – 1307, 1995.

[66] G. J. Herbert, S. Iniyan, and R. Goic, "Performance, reliability and failure analysis of wind farm in a developing country," *Renewable Energy*, vol. 35, no. 12, pp. 2739 – 2751, 2010.

[67] P. Zhu, Y. Liu, R. Robert, and X. Hao, "Offshore wind converter reliability evaluation," in *2011 IEEE 8th International Conference on Power Electronics and ECCE Asia (ICPE & ECCE)*, pp. 966–971, 2011.

[68] H. Li, H. Ji, Y. Li, S. Liu, D. Yang, X. Qin, and L. Ran, "Reliability evaluation model of wind power converter system considering variable wind profiles," in *2014 IEEE Energy Conversion Congress and Exposition (ECCE)*, pp. 3051–3058, IEEE, 2014.

[69] M. Pecht and W.-C. Kang, "A critique of mil-hdbk-217e reliability prediction methods," *IEEE Transactions on Reliability*, vol. 37, no. 5, pp. 453–457, 1988.

[70] D. Hirschmann, D. Tissen, S. Schroder, and R. W. De Doncker, "Reliability prediction for inverters in hybrid electrical vehicles," *IEEE Transactions on Power Electronics*, vol. 22, no. 6, pp. 2511–2517, 2007.

[71] H. Wang, K. Ma, and F. Blaabjerg, "Design for reliability of power electronic systems," in *IECON 2012-38th Annual Conference on IEEE Industrial Electronics Society*, pp. 33–44, IEEE, 2012.

[72] A. Goel and R. J. Graves, "Electronic system reliability: collating prediction models," *IEEE Transactions on Device and Materials Reliability*, vol. 6, no. 2, pp. 258–265, 2006.

[73] M. Arifujjaman, M. Iqbal, and J. Quaicoe, "Reliability analysis of grid connected small wind turbine power electronics," *Applied Energy*, vol. 86, no. 9, pp. 1617–1623, 2009.

[74] M. Bartram, J. Von Bloh, and R. W. De Doncker, "Doubly-fed-machines in wind-turbine systems: Is this application limiting the lifetime of igbt-frequency-converters?," in *IEEE 35th Annual Power Electronics Specialists Conference, 2004. PESC 04. 2004*, vol. 4, pp. 2583–2587, IEEE, 2004.

[75] T. Lei, M. Barnes, and A. C. Smith, "Thermal cycling evaluation for dfig wind turbine power converter based on joint modelling," in *2013 IEEE Energy Conversion Congress and Exposition (ECCE)*, pp. 3845–3851, IEEE, 2013.

[76] R. Pittini, S. D'Arco, M. Hernes, and A. Petterteig, "Thermal stress analysis of igbt modules in vscs for pmsg in large offshore wind energy conversion systems," in *Proceedings of the 2011-14th European Conference on Power Electronics and Applications (EPE 2011)*, pp. 1–10, IEEE, 2011.

[77] A. Isidori, F. M. Rossi, and F. Blaabjerg, "Thermal loading and reliability of 10 mw multilevel wind power converter at different wind roughness classes," in *2012 IEEE Energy Conversion Congress and Exposition (ECCE)*, pp. 2172–2179, IEEE, 2012.

[78] L. Wei, R. J. Kerkman, R. A. Lukaszewski, H. Lu, and Z. Yuan, "Analysis of igbt power cycling capabilities used in doubly fed induction generator wind power system," *IEEE Transactions on Industry Applications*, vol. 47, no. 4, pp. 1794–1801, 2011.

[79] D. Zhou, F. Blaabjerg, T. Franke, M. Tonnes, and M. Lau, "Reliability and energy loss in full-scale wind power converter considering grid codes and wind classes," in *2014 IEEE Energy Conversion Congress and Exposition (ECCE)*, pp. 3067–3074, IEEE, 2014.

[80] F. Fuchs and A. Mertens, "Steady state lifetime estimation of the power semiconductors in the rotor side converter of a 2 mw dfig wind turbine via power cycling capability analysis," in *Proceedings of the 2011-14th European Conference on Power Electronics and Applications (EPE 2011)*, pp. 1–8, IEEE, 2011.

[81] O. S. Senturk, S. Munk-Nielsen, R. Teodorescu, L. Helle, and P. Rodriguez, "Electro-thermal modeling for junction temperature cycling-based lifetime prediction of a press-pack igbt 3l-npc-vsc applied to large wind turbines," in *2011 IEEE Energy Conversion Congress and Exposition (ECCE)*, pp. 568–575, IEEE, 2011.

[82] E. Kostandyan and K. Ma, "Reliability estimation with uncertainties consideration for high power igbts in 2.3 mw wind turbine converter system," *Microelectronics Reliability*, vol. 52, no. 9, pp. 2403–2408, 2012.

[83] E. E. Kostandyan and J. Sorensen, "Reliability assessment of igbt modules modeled as systems with correlated components," in *2013 Proceedings-Annual Reliability and Maintainability Symposium (RAMS)*, pp. 1–6, IEEE, 2013.

[84] M. Musallam and C. M. Johnson, "Impact of different control schemes on the life consumption of power electronic modules for variable speed wind turbines," in *Proceedings of the 2011-14th European Conference on Power Electronics and Applications (EPE 2011)*, pp. 1–9, IEEE, 2011.

[85] K. Ma, M. Liserre, F. Blaabjerg, and T. Kerekes, "Thermal loading and lifetime estimation for power device considering mission profiles in wind power converter," *IEEE Transactions on Power Electronics*, no. 99, 2014.

[86] D. Weiss and H.-G. Eckel, "Fundamental frequency and mission profile wearout of igbt in dfig converters for windpower," in *2013 15th European Conference on Power Electronics and Applications (EPE)*, pp. 1–6, IEEE, 2013.

[87] D. Weiss and H.-G. Eckel, "Comparison of the power cycling stress of igbt in dfig and full size converter for windenergy applications," in *2014 16th European Conference on Power Electronics and Applications (EPE'14-ECCE Europe)*, pp. 1–9, IEEE, 2014.

[88] E. Baygildina, P. Peltoniemi, O. Pyrhonen, K. Ma, and F. Blaabjerg, "Thermal loading of wind power converter considering dynamics of wind speed," in *IECON 2013-39th Annual Conference of the IEEE Industrial Electronics Society*, pp. 1362–1367, IEEE, 2013.

[89] C. Busca, R. Teodorescu, F. Blaabjerg, L. Helle, and T. Abeyasekera, "Dynamic thermal modelling and analysis of press-pack igbts both at component-level and chip-level," in *IECON 2013-39th Annual Conference of the IEEE Industrial Electronics Society*, pp. 677–682, IEEE, 2013.

[90] K. Ma, F. Blaabjerg, and M. Liserre, "Electro-thermal model of power semiconductors dedicated for both case and junction temperature estimation," in *Proc. of PCIM*, pp. 1042–1046, 2013.

[91] M. Musallam and C. M. Johnson, "Real-time compact thermal models for health management of power electronics," *IEEE Transactions on Power Electronics*, vol. 25, no. 6, pp. 1416–1425, 2010.

[92] E. E. Kostandyan and J. D. Sørensen, "Physics of failure as a basis for solder elements reliability assessment in wind turbines," *Reliability Engineering & System Safety*, vol. 108, pp. 100–107, 2012.

[93] C. Yin, H. Lu, M. Musallam, C. Bailey, and C. Johnson, "A physics-of-failure based prognostic method for power modules," in *10th Electronics Packaging Technology Conference, 2008. EPTC 2008.*, pp. 1190–1195, IEEE, 2008.

[94] M. Musallam, C. M. Johnson, C. Yin, H. Lu, and C. Bailey, "Real-time life expectancy estimation in power modules," in *2nd Electronics System-Integration Technology Conference, 2008. ESTC 2008.*, pp. 231–236, IEEE, 2008.

[95] D. N. Dinesh Chamund, "Igbt module reliability: Application note," 2010. [online]. Available at: http://www.dynexpowersemiconductors.com/media//d/n/dnx_an5945.pdf.

[96] M. Bartram, *IGBT-Umrichtersysteme fuer Windkraftanlagen: Analyse der Zyklenbelastung, Modellbildung, Optimierung und Lebensdauervorhersage.* PhD thesis, ISEA, RWTH Aachen, 2005.

[97] K. Fischer, T. Stalin, H. Ramberg, T. Thiringer, J. Wenske, and R. Karlsson, "Investigation of converter failure in wind turbines: a pre study," 2012. [online]. Available at: http://www.elforsk.se/Global/Vindforsk/Rapporter

[98] S. Beczkowski, P. Ghimre, A. R. de Vega, S. Munk-Nielsen, B. Rannestad, and P. Thogersen, "Online vce measurement method for wear-out monitoring of high power igbt modules," in *2013 15th European Conference onPower Electronics and Applications (EPE)*, pp. 1–7, IEEE, 2013.

[99] P. Ghimire, K. B. Pedersen, A. R. d. Vega, B. Rannestad, S. Munk-Nielsen, and P. B. Thogersen, "A real time measurement of junction temperature variation in high power igbt modules for wind power converter application," in *2014 8th International Conference on Integrated Power Systems (CIPS)*, pp. 1–6, VDE, 2014.

[100] J. Due, S. Munk-Nielsen, and R. Nielsen, "Lifetime investigation of high power igbt modules," in *Proceedings of the 2011-14th European Conference on Power Electronics and Applications (EPE 2011)*, pp. 1–8, IEEE, 2011.

[101] A. R. de Vega, P. Ghimire, K. B. Pedersen, I. Trintis, S. Beczckowski, S. Munk-Nielsen, B. Rannestad, and P. Thogersen, "Test setup for accelerated test of high power igbt modules with online monitoring of v_{ce} and v_f voltage during converter operation," in *2014 International Power Electronics Conference (IPEC-Hiroshima 2014-ECCE-ASIA)*, pp. 2547–2553, IEEE, 2014.

[102] L. Helle, O. S. Senturk, and R. Teodorescu, "Special tests for the power electronic converters of wind turbine generators," in *2011 IEEE Power and Energy Society General Meeting*, pp. 1–4, IEEE, 2011.

[103] R. Wu, L. Smirnova, F. Iannuzzo, H. Wang, and F. Blaabjerg, "Investigation on the short-circuit behavior of an aged igbt module through a 6 ka/1.1 kv non-destructive testing equipment," in *Proceedings of 40th Annual Conference of the IEEE Industrial Electronics Society (IECON)*, pp. 3367–3373, 2014.

[104] D. Wagenitz, A. Westerholz, E. Erdmann, A. Hambrecht, and S. Dieckerhoff, "Power cycling test bench for igbt power modules used in wind applications," in *Proceedings of the 2011-14th European Conference on Power Electronics and Applications (EPE 2011)*, pp. 1–10, IEEE, 2011.

[105] A. Wintrich, U. Nicolai, W. Tursky, and T. Reimann, "Application manual power semiconductors," 2015. [online]. Available at: https://www.semikron.com/dl/service-support/downloads/download/semikron-application-manual-power-semiconductors-english-en-2015.

[106] T. Burton, D. Sharpe, N. Jenkins, and E. Bossanyi, *Wind energy handbook*. John Wiley & Sons, 2001.

[107] H. Siegfried, *Grid integration of wind energy conversion systems*. John Wiley & Sons, 1998.

[108] J. Slootweg, H. Polinder, and W. Kling, "Dynamic modelling of a wind turbine with doubly fed induction generator," in *Power Engineering Society Summer Meeting*, vol. 1, pp. 644–649, 2001.

[109] A. Betz, *Introduction to the theory of flow machines*. Pergamon Press, 1966.

[110] S. S. Rao and F. F. Yap, *Mechanical vibrations*, vol. 4. Addison-Wesley New York, 1995.

[111] B. Wu, Y. Lang, N. Zargari, and S. Kouro, *Power conversion and control of wind energy systems*. John Wiley & Sons, 2011.

[112] V. Akhmatov, *Analysis of dynamic behaviour of electric power systems with large amount of wind power*. PhD thesis, Technical University of Denmark, 2003.

[113] J.-B. Sim, K.-C. Kim, R.-W. Son, and J.-K. Oh, "Ride-through of pmsg wind power system under the distorted and unbalanced grid voltage dips," *Journal of Electrical Engineering & Technology*, vol. 7, no. 6, pp. 898–904, 2012.

[114] SEMIKRON, "Optimised converter for solar and wind," 2014. [online]. Available at: http://www.semikron.com/dl/service-support/downloads/download/semikron-flyer-semistackre-2014-04-08.

[115] SEMIKRON, "Sks b2 100 gd 69/11 - ma pb datasheet," 2013. [online]. Available at: http://www.semikron.com/dl/service-support/downloads/download/semikron-datasheet-sks-b2-100-gd-69-11-ma-pb-08800565.

[116] SEMIKRON, "Skiip 2013 gb172-4dw v3 datasheet," 2014. [online]. Available at: http://www.semikron.com/dl/service-support/downloads/download/semikron-datasheet-skiip-2013-gb172-4dw-v3-20451248.

[117] MathWorks, "Universal bridge," 2015. [online]. Available at: http://uk.mathworks.com/help/physmod/sps/powersys/ref/universalbridge.html.

[118] SEMIKRON, "Semistack re datasheets," 2015. [online]. Available at: http://https://www.semikron.com/products/product-lines/semistack-re.html.

[119] M. Chinchilla, S. Arnaltes, and J. C. Burgos, "Control of permanent-magnet generators applied to variable-speed wind-energy systems connected to the grid," *IEEE Transactions on Energy Conversion*, vol. 21, no. 1, pp. 130–135, 2006.

[120] J. Zhang, M. Cheng, Z. Chen, and X. Fu, "Pitch angle control for variable speed wind turbines," in *Third International Conference on Electric Utility Deregulation and Restructuring and Power Technologies.*, pp. 2691–2696, 2008.

[121] F. D. Bianchi, H. De Battista, and R. J. Mantz, *Wind turbine control systems: principles, modelling and gain scheduling design*. Springer Science & Business Media, 2006.

[122] A. D. Hansen, P. Sørensen, F. Iov, and F. Blaabjerg, "Control of variable speed wind turbines with doubly-fed induction generators," *Wind Engineering*, vol. 28, no. 4, pp. 411–432, 2004.

[123] W. Leithead and B. Connor, "Control of variable speed wind turbines: dynamic models," *International Journal of Control*, vol. 73, no. 13, pp. 1173–1188, 2000.

[124] F. M. Gonzalez-Longatt, P. Wall, and V. Terzija, "A simplified model for dynamic behavior of permanent magnet synchronous generator for direct drive wind turbines," in *IEEE Trondheim PowerTech*, pp. 1–7, 2011.

[125] P. Wyllie, *Electrothermal Modelling for Doubly Fed Induction Generator Converter Reliability in Wind Power*. PhD thesis, Durham University, 2014.

[126] NXP, "An11261: Using rc thermal models: Application note," 2014. [online]. Available at: http://www.nxp.com/ documents/application_note/AN11261.pdf.

[127] K. Shailesh, "Convert foster network to cauer," 2014. [online]. Available at: http://uk.mathworks.com/matlabcentral/fileexchange/46348-convert-foster-network-to-cauer/content//fostercauer.m.

[128] A. Nieslony, "Rainflow counting algorithm," 2003. [online]. Available at: http://uk.mathworks.com/matlabcentral/fileexchange/3026-rainflow-counting-algorithm.

[129] M. Held, P. Jacob, G. Nicoletti, P. Scacco, and M.-H. Poech, "Fast power cycling test of igbt modules in traction application," in *Proceedings of Second International Conference on Power Electronics and Drive Systems*, pp. 425–430, IEEE, 1997.

[130] RS, "Rs pro k type thermocouple glass fibre 2m 0.3mm diameter -50°c +750°c," 2017. [online]. Available at: http://uk.rs-online.com/web/p/products/6212170/.

[131] A. Eriksen, D. Osinski, and D. R. Hjelme, "Evaluation of thermal imaging system and thermal radiation detector for real-time condition monitoring of high power frequency converters," *Advances in Manufacturing*, vol. 2, no. 1, pp. 88–94, 2014.

[132] L. Dupont, Y. Avenas, and P.-O. Jeannin, "Comparison of junction temperature evaluations in a power igbt module using an ir camera and three thermosensitive electrical parameters," *IEEE Transactions on Industry Applications*, vol. 49, no. 4, pp. 1599–1608, 2013.

[133] Y. Avenas and L. Dupont, "Evaluation of igbt thermo-sensitive electrical parameters under different dissipation conditions–comparison with infrared measurements," *Microelectronics Reliability*, vol. 52, no. 11, pp. 2617–2626, 2012.

[134] T. Bruckner and S. Bernet, "Estimation and measurement of junction temperatures in a three-level voltage source converter," in *Fourtieth IAS Annual Meeting*, pp. 106–114, IEEE, 2005.

[135] FLIR, "Use low-cost materials to increase target emissivity," 2017. [online]. Available at: http://www.flir.com/science/blog/details/?ID=71556.

[136] Thorlabs, "Fdpse2x2 lead selenide photoconductor user guide," 2017. [online]. Available at: https://www.thorlabs.com/drawings/c7b0c7db2ebcb5c-75C9AC04-5056-2306-D929B1EBB3AF0DB5/FDPSE2X2-Manual.pdf.

[137] SEMIKRON, "Skiip 11nab066v1 datasheet," 2006. [online]. Available at: http://www.semikron.com/dl/service-support/downloads/download/semikron-datasheet-skiip-11nab066v1-25230580.

[138] SEMIKRON, "Skinter technology," 2015. [online]. Available at: http://www.semikron.com/innovation-technology/construction-and-connection-technology/skinter-technology.html.

[139] SEMIKRON, "Skhi61r semidriver," 2007. [online]. Available at: http://shop.semikron.com/out/media/ds/SEMIKRON_DataSheet_SKHI_61_R_L6100061.pdf.

[140] Noordzeewind, "Noordzeewind: Reports and data," 2017. [online]. Available at: http://www.noordzeewind.nl/en/knowledge/reportsdata/.

[141] IEC, "Iec 61400-1: Wind turbines part 1: Design requirements," *International Electrotechnical Commission*, 2005.

[142] SEMIKRON, "Skiip 01nac066v3," 2017. [online]. Available at: https://www.semikron.com/dl/service-support/downloads/download/semikron-datasheet-skiip-01nac066v3-25232340/.

[143] C. Rieg, C. Smith, and C. Crabtree, "Monitoring wind turbine loading using power converter signals," in *Journal of Physics: Conference Series*, vol. 749, p. 012018, IOP Publishing, 2016.

Appendices

Appendix A

Journal and Conference Papers

This appendix includes a selection of the journal and conference papers produced during the research project. This includes a conference paper detailing the wind speed profile work conducted that was not included in the main body of this thesis. The papers are as follows:

1. C. Smith, C. Crabtree, and P. Matthews, "Impact of wind conditions on thermal loading of PMSG wind turbine power converters," in IET Power Electronics eFirst, 2017.

2. C. Smith, C. Crabtree, and P. Matthews, "Impact of wind conditions on thermal loading of PMSG wind turbine power converter," in 10th International IET PEMD conference, Glasgow, 2016.

3. C. Smith, G. Wadge, C. Crabtree, and P. Matthews, "Characterisation of Electrical Loading Experienced by a Nacelle Power Converter," in EWEA Annual Event, Paris, 2015.

4. C. Smith, C. Crabtree, and P. Matthews, "Evaluation of Synthetic Wind Speed Time Series for Reliability Analysis of Offshore Wind Farms," in EWEA Annual Event, Paris, 2015.

IET Power Electronics

Research Article

IET Journals
The Institution of Engineering and Technology

Impact of wind conditions on thermal loading of PMSG wind turbine power converters

ISSN 1755-4535
Received on 7th October 2016
Revised 12th April 2017
Accepted on 24th May 2017
doi: 10.1049/iet-pel.2016.0802
www.ietdl.org

Christopher J. Smith[1], Christopher J. Crabtree[1] ✉, Peter C. Matthews[1]

[1]*School of Engineering and Computing Sciences, Durham University, South Road, Durham, UK*

✉ *E-mail: c.j.crabtree@durham.ac.uk*

Abstract: Power converter reliability is critical for permanent magnet synchronous generator (PMSG) wind turbines. Converter failures are linked to power module thermal loading but studies often neglect turbine dynamics, control and the impact of wind speed sampling rate on lifetime estimation. This study addresses this using a 2 MW direct-drive PMSG wind turbine model with a two-level converter, and simulating junction temperatures (T_j) using a power module thermal equivalent circuit under various synthetic wind speed conditions. These synthetic wind conditions include constant and square wave profiles representing stable and gusty wind conditions. Responses to square wave wind speeds showed that the lower the gust frequency, the higher ΔT_j becomes, demonstrating that low turbulence sites have greater thermal variation in the converter. In contrast, wind speed variations with frequencies >0.25 Hz deliver only small increases in ΔT_j. It is concluded that reasonable approximations of T_j profiles can be made with 0.25 Hz wind speed data, but that lower data rate wind measurements miss essential, damaging characteristics.

1 Introduction

To meet EU renewable energy targets for 2020 and beyond, the levelised cost of energy (LCoE) of offshore wind must be reduced to below £100/MWh [1]. Operation and maintenance (O&M) accounts for ∼30% of the LCoE [2]. A key aspect of O&M is turbine sub-system reliability. By understanding which components have the greatest impact on downtime and power production, O&M resources can be focused to minimise turbine disruption and reduce the LCoE of offshore wind.

1.1 Wind turbine power converter reliability

Numerous studies have explored the reliability of wind turbine sub-systems using operational data. Carroll *et al.* [3] examined a large dataset for offshore wind turbines with mixed turbine technology to determine the main causes of failure and concluded that power converters had a typical failure rate of ∼0.2 failures/turbine/year, much lower than the highest failure rate of > 1 failure/turbine/year for pitch systems. However, a more focused study on turbine type [4] found that the failure rate of fully-rated converters (FRC) in permanent magnet synchronous generator (PMSG) turbines was 0.593 failures/turbine/year compared with 0.106 failures/turbine/year for partially-rated converters in doubly fed induction generator turbines. This suggests that the unique operating conditions of PMSG-FRCs are causing higher failure rates. Furthermore, Spring *et al.* [5] examined large wind turbine datasets and used expert knowledge to determine the impact of component failure to turbine downtime, compiling a top 30 list of failure sources. It was concluded that power converters were the highest source of turbine downtime, with their failure modes occupying the top 15 positions. Converter reliability must, therefore, be examined with a focus on the FRC in PMSG turbines.

Of the failures outlined in [4], power module failure is the failure mode for nearly all major converter repairs. Traditionally, power module failure has been linked to power module thermal loading, where the variation of temperature in the insulated gate bipolar transistors (IGBT) and diode cases causes fatigue through expansion and contraction between package layers (Fig. 1*a*). The temperature used for reference is the virtual junction temperature, ($\Delta T_{j,IGBT}$, $\Delta T_{j,diode}$), which is a virtual representation of the chip p–n junction temperature (Fig. 1*b*).

1.2 Power converter reliability studies

This approach has been applied in a number of studies to explore the expected reliability of power converters in wind turbines [7–16]. However, these studies often have limitations. Some studies neglect the impact of wind turbine dynamics and control, so wind speed inputs are directly converted into a T_j [7–9], which will deviate significantly from the true T_j profile in the converter. The use of wind speed distributions [8, 10] and large time steps, e.g. 3-hourly [11] neglects the impact of wind speed history, which has been shown to have a large impact on the current loading, and subsequently, the thermal loading of the converter [17]. For example, the use of supervisory control and advisory data acquisition (SCADA) data may only provide a mean and maximum wind speed over a 10 min period, which may hide a large amount of variation that is causing damage to the converter.

Some studies have included both realistic wind speed profiles and drive train models [12–15]. However, only two have studied a PMSG wind turbine [14, 15], and these two studies disagree whether high-frequency wind speed events impact the thermal loading of the converter significantly. There is therefore a need for a detailed study into the impact of operating conditions on power converter reliability to help inform how the turbine should be operated in order to extend its life and reduce the LCoE.

1.3 Research contributions

These limitations mean that operational profiles and failure data may not be representative of converter operation in the field, and there is no consensus on the required wind speed data frequency for accurate thermal simulation. This paper addresses these limitations by identifying the temporal fidelity over which wind events (such as gusts) cause the highest thermal variation. The minimum wind speed sampling frequency that will still provide accurate thermal profile simulation can then be determined. The impact of modelling assumptions on the estimated T_j profiles is also explored. These results will provide guidance for future simulation and experimental studies to improve converter reliability analysis accuracy, with an aim of improving best practice in both academia and industry.

To simulate these thermal loading profiles, a drive train model (Section 2.1), power loss model (Section 2.2), thermal model (Section 2.3), and wind inputs (Section 2.4) are required. The

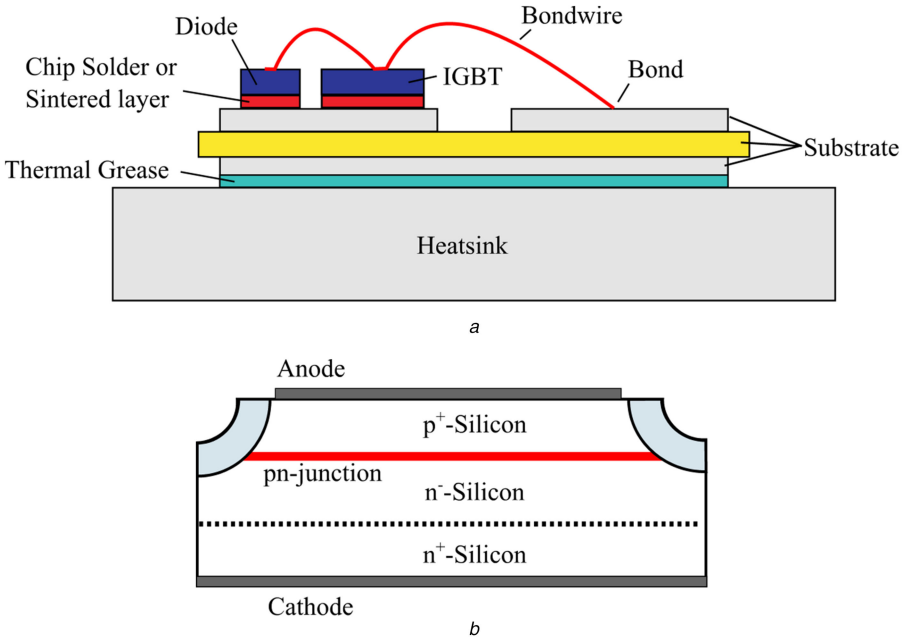

Fig. 1 *Chip layout and packaging for typical power module devices. Figures adapted from [6]*
(a) Typical IGBT power module packaging with no base plate. Areas of fatigue include the bondwire, the bondwire bonds, and the chip solder/sintered layer, ***(b)*** Internal structure of a typical p–n diode chip showing the location of the p–n junction used as the virtual reference point for $T_{j,diode}$

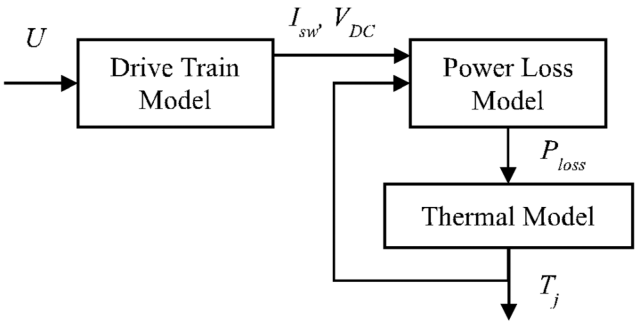

Fig. 2 *Summary of drive train and converter thermal model*

impacts of temporal fidelity and modelling assumptions were explored through an analysis of individual T_j cycles (Section 3.1), comparison of constant wind speed results with a comparable study (Sections 3.2 and 3.3) and analysis of the converter response to synthetic wind speed time series (WSTS) (Section 3.4). A summary of the main findings is given in Section 4.

2 Approach

First, an approach to identifying the thermal loading of a wind turbine power converter was developed as follows:

- Modelling of a wind turbine drive train to provide the current throughput of the converter.
- Modelling of the resultant power losses in the converter due to the current throughput.
- Modelling the power module thermal processes in response to the power losses.
- Simulation of power module thermal response to selected wind speed inputs.

Fig. 2 illustrates the full-system model. U is the incoming wind speed, I_{sw} is the converter switch current, V_{DC} is the DC link voltage, and P_{loss} is the power module device switching losses.

This section outlines the details of each of the sub-systems.

2.1 Drive train model

The drive train model developed for this work was a 2 MW FRC-PMSG, direct-drive turbine. The model was split into five sub-systems: rotor power extraction, drive train dynamics, generator, machine-side converter (MSC), and turbine control. Fig. 3 provides a summary of the drive train model. T_t is the turbine torque extracted from the wind, T_m is the mechanical torque resulting from the shaft stiffness and damping, T_g is the electromagnetic torque, ω_t is the turbine rotational speed, ω_g is the generator rotational speed, β is the pitch angle, β_{ref} is the reference pitch angle, I_{abc} is the generator output current, $V_{t,abc}$ is the generator terminal voltage applied by the MSC, and $V_{ref,abc}$ is the reference MSC output voltages.

This section outlines the core aspects of each sub-system. Detailed descriptions can be found in [17, 18].

2.1.1 Turbine power extraction: T_t from the wind is calculated using the following equation:

$$T_t = \frac{0.5 C_p \rho \pi r^2 U^3}{\omega_t} \tag{1}$$

C_p is the power coefficient, ρ is air density, and r is the turbine radius.

C_p depends on the tip speed ratio (λ) and β. The C_p, λ, and β relationship is turbine specific but it is typical to use a numerical approximation (2) and (3) [19], with λ calculated using (4)

$$\frac{1}{\lambda_i} = \frac{1}{\lambda + H_t \beta} - \frac{K_t}{\beta^3 + 1} \tag{2}$$

$$C_p = A_t \left(\frac{B_t}{\lambda_i} - C_t \beta - D_t \beta^{E_t} - F_t \right) e^{(-G_t/\lambda_i)} \tag{3}$$

$$\lambda = \frac{\omega_t r}{U} \tag{4}$$

A_t to F_t and K_t are turbine specific constants. The values used can be found in the Appendix.

2.1.2 Drive train dynamics: T_t is applied to the drive shaft. The drive train can be modelled as a mechanical mass-spring-damper system which dynamically impacts the T_m applied to the generator.

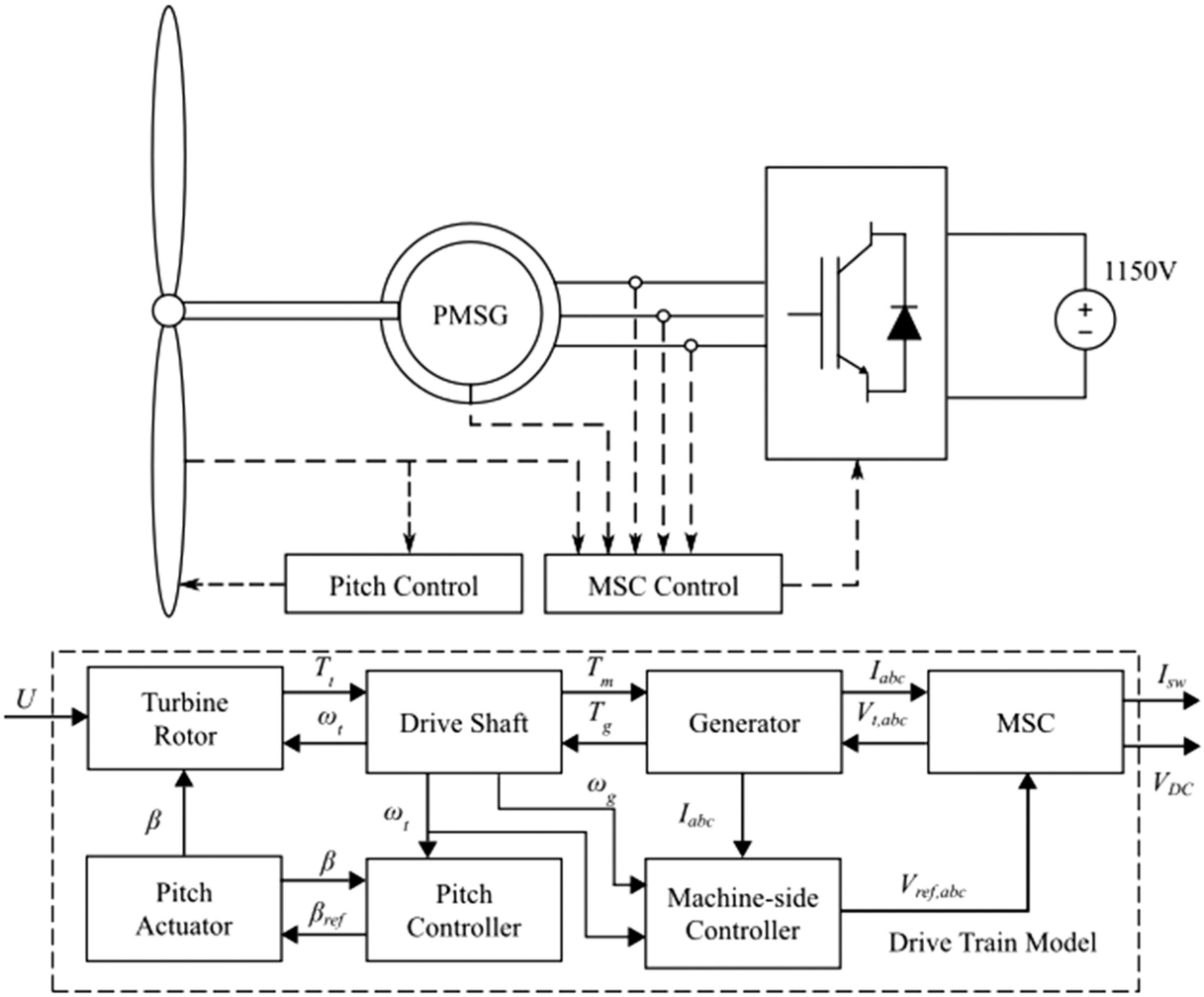

Fig. 3 *Drive train model summary*

The drive train was modelled as a two-mass system, rather than a lumped-mass system, to include the dynamic effects of shaft stiffness and damping. The two-mass system is defined by the following equation [20]:

$$\begin{bmatrix} J_{\mathrm{t}} & 0 \\ 0 & J_{\mathrm{g}} \end{bmatrix} \begin{Bmatrix} \alpha_{\mathrm{t}} \\ \alpha_{\mathrm{g}} \end{Bmatrix} + \begin{bmatrix} C_{\mathrm{d}} & -C_{\mathrm{d}} \\ -C_{\mathrm{d}} & C_{\mathrm{d}} \end{bmatrix} \begin{Bmatrix} \omega_{\mathrm{t}} \\ \omega_{\mathrm{g}} \end{Bmatrix} + \begin{bmatrix} K & -K \\ K & -K \end{bmatrix} \begin{Bmatrix} \theta_{\mathrm{t}} \\ \theta_{\mathrm{g}} \end{Bmatrix} = \begin{Bmatrix} T_{\mathrm{t}} \\ T_{\mathrm{g}} \end{Bmatrix} \quad (5)$$

J_{t}, J_{g} are the moments of inertia of the turbine and generator, respectively, θ_{t}, θ_{g} are the rotational displacements of the turbine and generator, respectively, C_{d} is the shaft damping coefficient, K is the shaft stiffness, and α_{t}, α_{g} are the rotational accelerations of the turbine and generator, respectively. The expanded matrix can be solved numerically, with T_{m} calculated using the following equation:

$$T_{\mathrm{m}} = \left(\omega_{\mathrm{t}} - \omega_{\mathrm{g}}\right) C_{\mathrm{d}} + \left(\theta_{\mathrm{t}} - \theta_{\mathrm{g}}\right) K \quad (6)$$

2.1.3 Generator: The generator model used is a second-order non-salient PMSG in the $dq0$ reference frame [21] with a current rating of 1868 $\mathrm{A_{rms}}$. The mechanical component was modelled with the torque swing equation. The generator parameters can be found in the Appendix.

2.1.4 MSC: In a typical wind turbine, the converter is comprised of an MSC and grid-side converter (GSC). The role of the MSC and GSC differs depending on control strategy but the MSC typically controls the speed of the wind turbine for optimum power production whilst the GSC controls power export to maintain the DC-link voltage.

Due to the turbine's variable speed operation for maximum power extraction, the MSC experiences a more varied operating profile compared with the GSC, which operates at fixed frequency. The MSC is consequently of greater interest for reliability analysis. Here, only the MSC is modelled while the GSC is replaced with a constant voltage source of 1150 $\mathrm{V_{DC}}$ (± 575 $\mathrm{V_{DC}}$).

The MSC parameters were based on the power modules found in the SEMIKRON SKSB2100GD69/11-MAPB stacks [22]. These stacks have a maximum DC voltage of 1200 V and a maximum current of 1000 $\mathrm{A_{rms}}$. The stacks use SKiiP2013GB172-4DWV3 half-bridge integrated power modules [23].

The voltage output of the MSC is determined by $V_{abc,\mathrm{ref}}$ from the machine-side controller (Section 2.1.5). Pulse width modulation (PWM) converts the modulated $V_{abc,\mathrm{ref}}$ (V_{m}) into a switching pattern for the IGBTs in order to produce the three-phase converter output voltage ($V_{\mathrm{c},abc}$). Space vector PWM was chosen and therefore V_{m} was calculated using the following equation:

$$V_{\mathrm{m}} = \frac{\sqrt{3}}{V_{\mathrm{DC}}} V_{abc,\mathrm{ref}} \quad (7)$$

The current through the devices is split between diode and IGBT depending on the current polarity. Since two parallel stacks are required to reach the current rating of the turbine (Section 2.1.3), this current is split equally between stacks [24].

2.1.5 Turbine control: Power extraction is controlled in two ways depending on operating region. Maximum power point tracking (MPPT) is used for below rated speed, while active pitch control is used above rated speed to limit power.

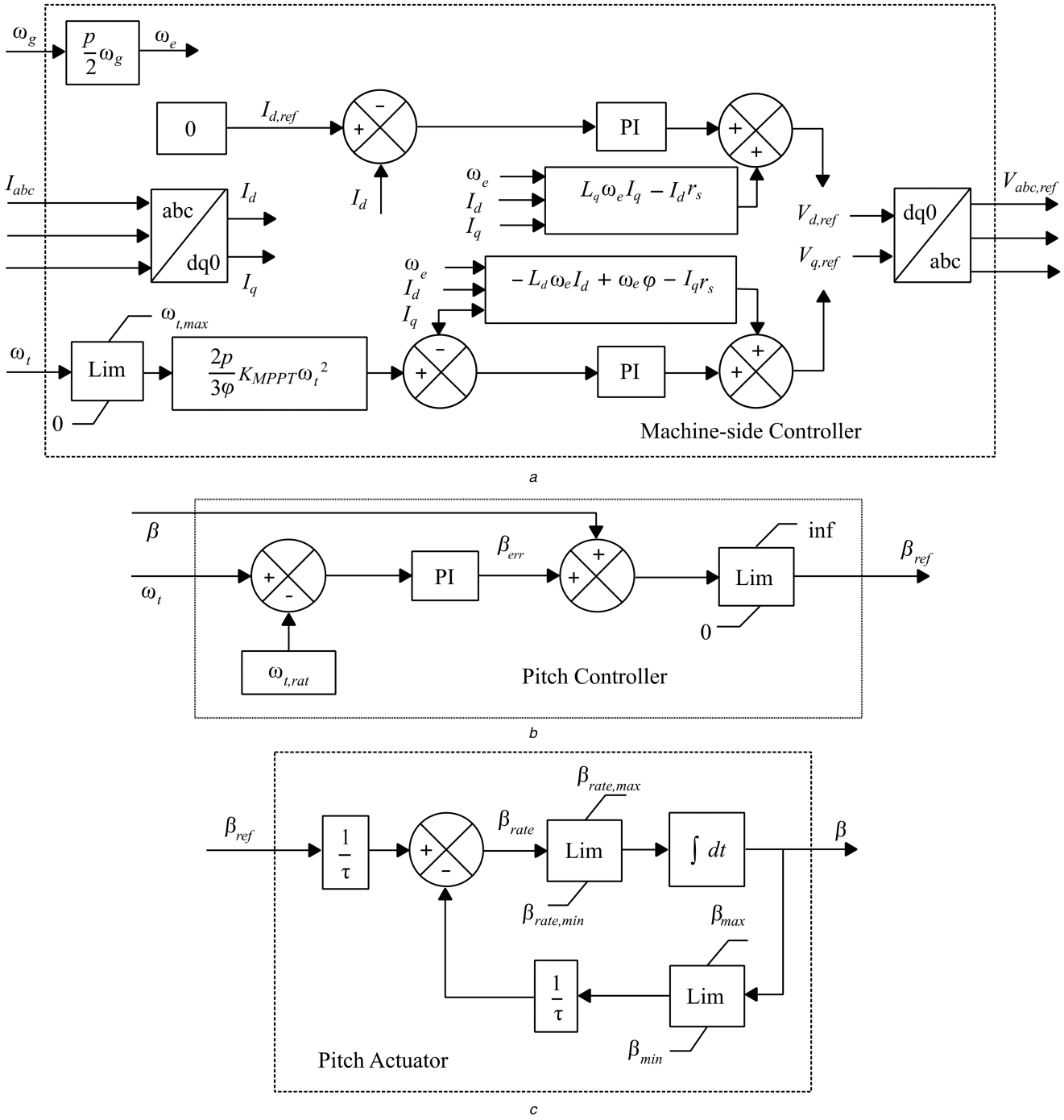

Fig. 4 *Schematics of*
(a) Machine side controller, ***(b)*** Pitch controller, ***(c)*** Pitch actuator

For MPPT, C_p must be maximised ($C_{p,max}$). By controlling ω_t, the optimum λ can be maintained (λ_{opt}) when below rated wind speed

$$\omega_{t,opt(u)} = \frac{U\lambda_{opt}}{r} \tag{8}$$

$\omega_{t,opt(u)}$ is the optimum turbine rotational speed at a given wind speed.

As U is not measured in this control strategy, $\omega_{t,opt}$ is unknown. Instead ω_t is varied until the turbine reaches steady state, which occurs when $\omega_t = \omega_{t,opt}$. ω_t is varied via T_g, which is carried out using direct-quadrature-zero current (I_{dq0}) control applied to the MSC. Fig. 4*a* illustrates the machine-side control algorithm. $V_{d,q}$ are the d,q reference frame voltages, $V_{d,q,ref}$ are the required d,q terminal voltages, $I_{d,q,ref}$ are the reference $I_{d,q}$, r_s is the PMSG stator phase resistance, $L_{d,q}$ are the PMSG d,q armature inductances, φ is the permanent magnet flux linkage, K_{MPPT} is a turbine specific constant, $\omega_{t,max}$ is the maximum turbine rotational speed considered by the controller, and ω_e is the magnetic field rotational speed, which is related to ω_g via the generator pole pairs.

To determine the required generator currents, ω_t is related to the required T_g (T_{ref}) via the turbine power curve using a turbine specific constant K_{MPPT} (9) and (10). The reference I_q is calculated using a known relationship between I_q and T_g in the generator (11). I_d is maintained at 0 A [25]. These currents are achieved by applying a controlled voltage on the generator terminals using the MSC

$$T_{ref} = K_{MPPT}\omega_t^2 \tag{9}$$

$$K_{\mathrm{MPPT}} = 0.5 C_{p,\max} \rho \pi r^2 \left(\frac{r}{\lambda_{\mathrm{opt}}} \right)^3 \tag{10}$$

$$I_{q,\mathrm{ref}} = \frac{2p}{3\varphi} T_{\mathrm{ref}} \tag{11}$$

To note, the machine-side controller is not constrained by the rated turbine rotational speed ($\omega_{\mathrm{t,rat}}$) but by a higher maximum ($\omega_{\mathrm{t,max}}$). This allows the machine-side controller to deal with sudden increases in wind speed for which the pitch controller is too slow to respond effectively. This provides a similar controller interaction to [26].

Pitch control limits power extraction when above rated wind speed by pitching the blades away from the optimum angle, reducing the turbine's C_{p}.

There are a number of pitch control methods available [27]. For this work, the difference in ω_{t} and rated ω_{t} ($\omega_{\mathrm{t,rat}}$) is used to produce a β error (β_{err}) (Fig. 4*b*). β_{err} is added to the current β to produce a reference β (β_{ref}) and applied to the pitch actuator (Fig. 4*c*). The pitch actuator is modelled as a first-order dynamic system [28] with limits on β and the rate of change of β (β_{rate}). These values can be found in the Appendix.

2.1.6 Drive train model summary: The drive train model consists of the following key features:

- Modelled as a direct-drive 2 MW PMSG wind turbine to align with modern turbine technology with sufficient data for modelling.
- Mechanical drive train modelled as a two-mass model to capture the critical dynamics of a wind turbine drive train.
- FRC with MSC based on SEMIKRON Renewable Energy stacks to provide realistic converter parameters.
- GSC modelled as an ideal DC link to isolate impacts of wind on the MSC.
- Turbine controlled using ω_{t} as the reference signal, with both MPPT and active pitch control as in the majority of modern wind turbines.

2.2 Converter power loss model

To convert the current throughput into T_{j} profiles, power losses must be calculated, specifically:

- The IGBT and diode conduction losses.
- The IGBT switching losses and diode reverse recovery (RR) losses.

The conduction and switching losses are summed for each device. The power loss model used is based on [29, 30].

2.2.1 Conduction losses: Conduction losses depend on device internal resistance so are calculated using the device voltage and current

$$P_{\mathrm{C,IGBT}} = V_{\mathrm{ce}} I_{\mathrm{c}} \tag{12}$$

$$P_{\mathrm{C,diode}} = V_{\mathrm{f}} I_{\mathrm{f}} \tag{13}$$

$P_{\mathrm{C,IGBT}}$ and $P_{\mathrm{C,diode}}$ are the IGBT and diode conduction losses, respectively, V_{ce} is the IGBT collector–emitter voltage, V_{f} is the diode forward voltage, I_{c} is the IGBT collector current, and I_{f} is the diode forward current.

I_{c} and I_{f} are the input currents. V_{ce} and V_{f} are functions of I_{c} and I_{f}, respectively, and the device T_{j}. The functions are given in the manufacturer's data sheet [23] for a T_{j} of 25 and 125°C. V_{ce} and V_{f} are calculated by interpolating between the values given at these reference temperatures.

2.2.2 Switching/RR losses: Switching and RR losses occur when there is a change in direction of voltage and current. Device response is not instantaneous but occurs over nanoseconds [29]. Nanosecond simulation is impractical for run times longer than a few seconds and the energy loss information given in manufacturer's datasheets is not detailed enough for accurate temporal loss simulation. For example, the energy loss during switch on (E_{on}) and switch off (E_{off}) are not given separately, but reported as a summation of the two ($E_{\mathrm{on+off}}$) [23]. As such, a simplified approach has to be taken.

It has been assumed that the energy loss is given by the conditions at the first low-high (L-H) switching instance. The energy is modulated over the switching cycle (between L-H and the next L-H) to provide a constant switching power loss. This was deemed acceptable as the device thermal time constants (µs-ms) will dominate the thermal profile [29].

With the above assumptions, the switching/RR losses were found by

(i) Determining the energy losses at L-H switching events. The switching/RR energy loss is given as a function of input current at two reference V_{DC} [23] and is assumed to be linear. The IGBT energy loss is $E_{\mathrm{on+off}}$, whilst the diode energy loss is twice the reverse energy loss (E_{rr}).

(ii) Calculating the equivalent modulated power losses over the switching cycle using the following equations [30]:

$$P_{\mathrm{sw}}\left(t : T_{\mathrm{s,th}} : \left(t + T_{\mathrm{p,sw}}(t)\right)\right) = \frac{E_{\mathrm{on+off}}(t)}{T_{\mathrm{p,sw}}(t)} \tag{14}$$

$$P_{\mathrm{rr}}\left(t : T_{\mathrm{s,th}} : \left(t + T_{\mathrm{p,rr}}(t)\right)\right) = \frac{E_{\mathrm{rr}}(t)}{T_{\mathrm{p,rr}}(t)} \tag{15}$$

$$P_{\mathrm{sw},T_{\mathrm{j}}}(t) = \left(1 + TC_{E\mathrm{sw}}\left(T_{\mathrm{j,IGBT}}(t) - T_{\mathrm{ref}}\right)\right) P_{\mathrm{sw}}(t) \tag{16}$$

$$P_{\mathrm{rr},T_{\mathrm{j}}}(t) = \left(1 + TC_{E\mathrm{rr}}\left(T_{\mathrm{j,diode}}(t) - T_{\mathrm{ref}}\right)\right) P_{\mathrm{rr}}(t) \tag{17}$$

P_{sw} is the IGBT switching power loss, P_{rr} is the diode RR power loss, t is the time step, $T_{\mathrm{s,th}}$ is the thermal sampling time, $T_{\mathrm{p,sw}}$ is the IGBT switching time period, $T_{\mathrm{p,rr}}$ is the diode RR time period, $P_{\mathrm{sw},Tj}$, $P_{\mathrm{rr},Tj}$ are the T_{j} corrected P_{sw} and P_{rr}, respectively, $\mathrm{TC}_{E\mathrm{sw}}$, $\mathrm{TC}_{E\mathrm{rr}}$ are the switching loss and RR temperature coefficients, respectively, and T_{ref} is the reference temperature of the energy loss look-up tables (LUTs).

2.3 Thermal loss model

Converter thermal modelling can be carried out in three ways:

- Thermal equivalent circuits using resistor–capacitor (RC) networks [8, 10–12, 14–16].
- Thermal diffusion equations [13].
- Finite-element analysis [7].

As the RC network data was readily available, a common practice approach of thermal equivalent circuit modelling was used.

The data given in [23] is for a Foster RC network. To provide a more accurate half-bridge temperature profile the Foster thermal resistance ($R_{\mathrm{th,f}}$) and time constant (τ) parameters were converted into RC parameters [31], and then converted into Cauer RC parameters to provide a more realistic thermal profile throughout the device [32]. Fig. 5 gives the half-bridge Cauer RC network. The parameters are available in the Appendix.

The power losses (P_{loss}) are dependent on T_{j} and therefore the power loss and thermal sub-systems must be run concurrently. Due to the power-thermal inter-dependency, the initialisation of C_{th} temperatures was solved iteratively. The steady-state temperatures are related to the R_{th} only [30]. Therefore, initial temperatures were

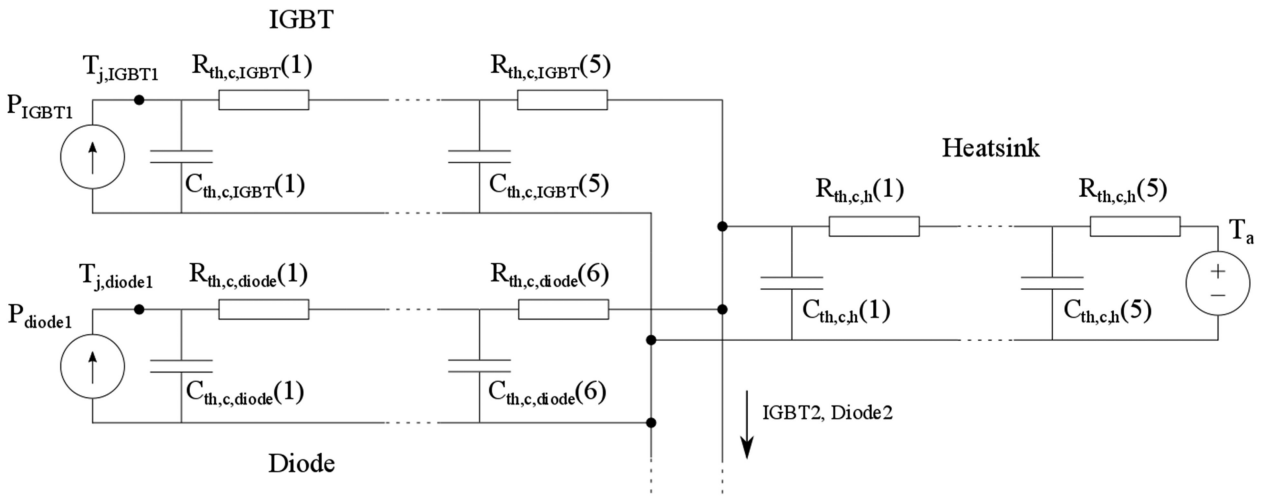

Fig. 5 *Half-bridge Cauer RC network (one IGBT and diode represented). P_{IGBT1} is the IGBT power loss, P_{diode1} is the diode power loss, $R_{th,c}$ is the Cauer thermal resistance, and $C_{th,c}$ is the Cauer thermal capacitance*

set throughout the device, and then the power losses and temperatures were iteratively updated until steady state was reached.

2.4 Wind speed inputs

Wind speed and converter current throughput are partly decoupled by the drive train inertia and control [17]. As such, it can be challenging to determine which characteristics of a WSTS have the largest impact on thermal loading.

To address this, experiments have been constructed which use synthetic WSTS to isolate potential wind speed characteristics and determine their impact on thermal loading. Square waves have been used to represent sudden changes in wind speed, which was validated against high-frequency wind speed data. The tests are carried out over 65 s, with the first 5 s carried out at constant wind speed to minimise the impact of variations in the input current. For the square wave tests this constant wind speed represents the average power wind speed, which is slightly higher than the average wind speed. The model time step is also much smaller than the test period to ensure it does not influence the results; 5×10^{-6}s for the drive train, and 5×10^{-5}s for the thermal simulation.

2.5 Summary

To summarise, a Simulink model of a wind turbine drive train and power converter thermal network has been constructed. This allows for any wind speed profile to be entered and the corresponding power module thermal profiles be produced.

3 Results and discussion

This section outlines the analysis performed on T_j profiles produced in response to constant and square wave WSTS.

3.1 Individual T_j cycles

The power loss and temperature profiles over individual power cycles were examined. Fig. 6 compares the diode and IGBT current T_j profiles at a constant 12.7 m/s. The T_j profile for the diode (Fig. 6*d*) is comparable with the expected response found in Fig. 5.2.13 in the manufacturer's handbook [30], although it should be noted that the manufacturer's data considers only the average power loss of the switching cycle, rather than individual switching events. This simulation output can show higher frequency temperature variation than revealed in the manufacturer's data.

This higher frequency temperature variation becomes most apparent in the IGBT (Fig. 6*c*), particularly in the first half of the current cycle. This can be attributed to the converter being connected to a PMSG. The PMSG reactance causes the current to be out-of-phase with the voltage, and therefore the switching cycles are not distributed symmetrically over the input current, with a period of low voltage (Fig. 6*a*). The low voltage means the IGBT has a smaller duty cycle. Where there is infrequent current due to a low duty cycle (Fig. 6*a*), T_j varies more (Fig. 6*c*). This effect is not seen in the diode as the current not flowing through the IGBT must pass through the diode, creating a near continuous current throughput (Fig. 6*b*) and therefore a smooth T_j response (Fig. 6*d*).

3.2 Constant wind speeds

Fig. 7 shows the thermal response to constant WSTS for an IGBT and diode with an ambient temperature (T_a) of 40°C [8]. The mean T_j increases non-linearly as wind speed increases due to the cubic relationship between wind speed and power. The ΔT_j also increases due to the higher power loss per cycle, and the ΔT_j frequency increases due to the higher generator rotational speed.

The diode temperatures T_j and ΔT_j (Fig. 7*b*) are consistently higher than the IGBT (Fig. 7*a*). This is due to the higher power losses experienced by the diodes and the higher R_{th} of the diodes. The higher diode R_{th} (K/W) means that for every watt of heat loss, the diode experiences a greater rise in temperature than the IGBT. This is then coupled with the greater power losses due to the more continuous current flow through the diode (Section 3.1), causing the higher T_j and ΔT_j. This was also found for the MSC devices in [14] and suggests that the diode is more vulnerable to thermal cycling, with both higher mean T_j and ΔT_j.

3.3 Study comparison

The results in Figs. 7*a* and *b* were compared with the 1.55 MW turbine in [14] (Fig. 7*c*); it is assumed the scaled power ratings would have limited impact on the thermal loading as the converter rating would also be scaled, leading to comparable T_j profiles for a given wind speed. However, whilst it was found that the ΔT_j for both IGBTs and diodes was comparable at a given wind speed, the mean T_j for a given wind speed was higher in this study than in [14], despite T_a being 10°C lower. This is in part is due to the lack of R_{th} value for the heatsink in [14]. At steady-state conditions this will create a higher case temperature (T_c) and therefore higher mean T_j. The mean T_j change from 12 to 8.5 m/s is also much lower in [14]. This suggests that the MSC in this work is more susceptible to T_j rises due to the higher R_{th} values in the devices. This highlights three key conclusions that must be made.

- The ΔT_j magnitude for IGBT and diodes is consistent with those found in [14], but there is greater variation in mean T_j between wind speeds in this study.

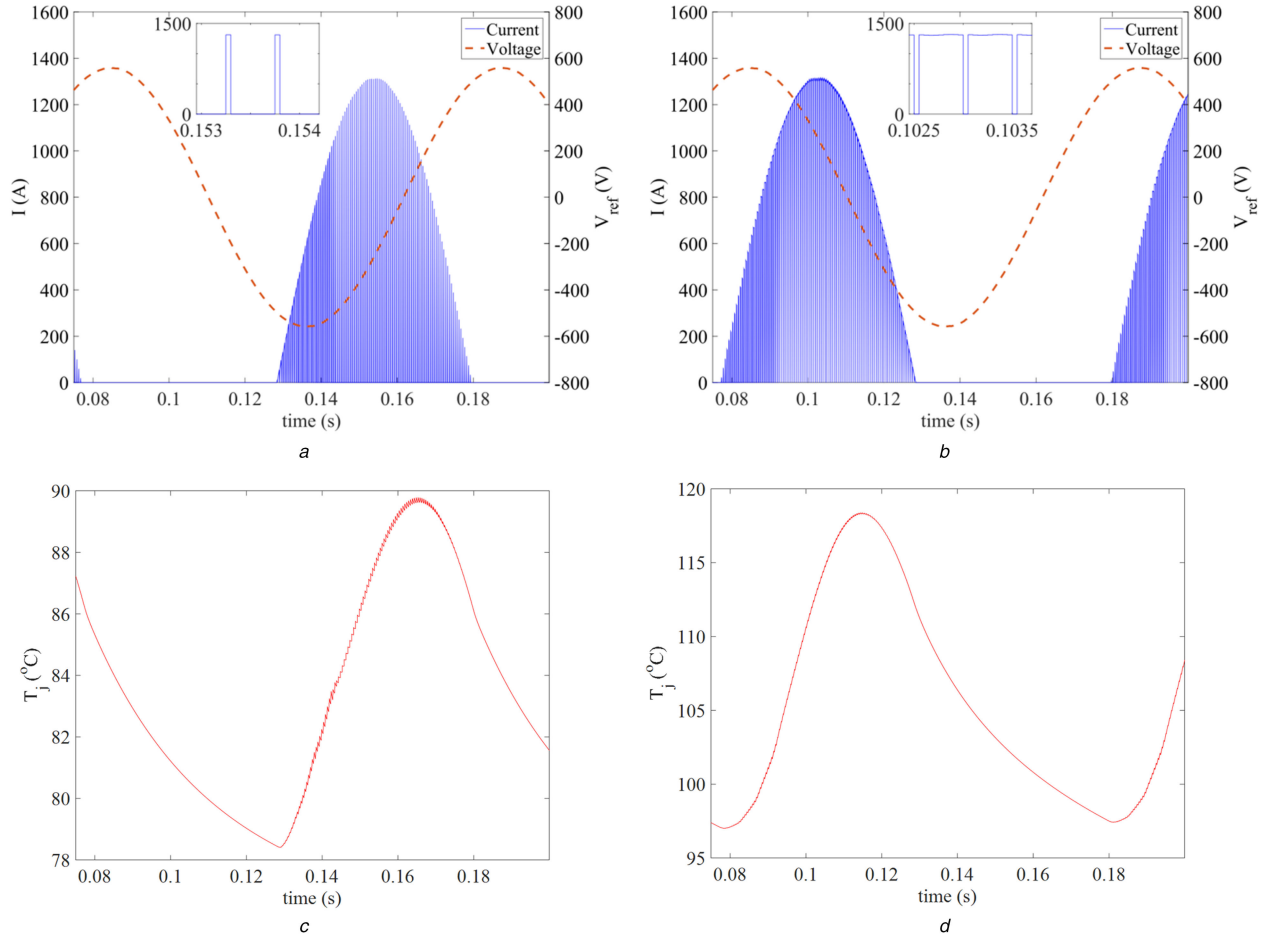

Fig. 6 *Cycle view of*
(a) IGBT current with the current waveform peak magnified, ***(b)*** Diode current with the current waveform peak magnified, ***(c)*** IGBT T_j, ***(d)*** Diode T_j at a constant 12.7 m/s

- The value of T_a can have a large impact on the mean T_j value.
- The inclusion of the heatsink thermal parameters in the model causes a significant increase in the mean T_j.

3.4 Response to varying wind speed input

The T_j response of the power module to a range of square wave WSTS is detailed to understand what might be masked by using SCADA data in lifetime/temperature swing calculations. For comparison, the maximum T_j swing over the simulation period (max ΔT_j) have been plotted for square gust amplitudes of 1 and 2 m/s, for varying frequencies and mean wind speeds, for both IGBT and diode (Fig. 8).

In general, the higher the frequency of wind speed variation, the lower ΔT_j becomes. This is as the turbine inertia acts as a low-pass filter, restricting the high-frequency wind speed variation being transmitted as current variation. Indeed, wind speed variations with frequency >0.25 Hz lead to a minimal increase in ΔT_j compared with the constant wind speed case (0 Hz). Therefore, reasonable approximations of T_j profiles can be made (within 1°C) with 0.25 Hz wind speed data. Furthermore, these results imply that lower turbulence wind farm sites, such as offshore, have more damaging thermal profiles in the converter than higher turbulence onshore sites.

There are exceptions to this trend. ΔT_j becomes relatively consistent below 0.03 Hz. This is because the turbine has time to respond to the change of wind speed and reaches its steady operating state. The turbine is then at this steady-state condition long enough for T_j to reach its maximum before the wind speed reduces. Lower frequencies will increase the number of times that the maximum T_j is reached during a particular gust, but will not affect the maximum T_j. The same will also be true for the minimum T_j. Therefore, gust frequencies of 0.03 Hz and below provide the maximum ΔT_j.

These results show that the use of one wind speed data point for a long time period, e.g. 10 min SCADA data, 3 hourly data found in [11], or the use of a wind speed distribution in [8, 10], can mask a large amount of information and will underestimate the T_j variation significantly; in Fig. 8*d* the diode ΔT_j at U_m of 12 m/s increases by up to 71%. Therefore, these results agree with the conclusions in [15] that higher frequency wind speed data is required for accurate T_j profile estimation, and it is suggested that a minimum WSTS frequency of 0.25 Hz is required, though it is recognised that this will not always be available/practical. This, however, would reduce the amount of data required for studies such as in [12–15]. The results at higher U_m also indicate that the unique operating conditions may have a significant effect on the T_j profile experienced by the power converter, and therefore the lack of drive train dynamic modelling in [7–9] will change the T_j profiles significantly.

4 Conclusions

The power converter is reliability critical for FRC-PMSG wind turbines. Converter failures are typically linked to the thermal loading of the power module. This paper models the converter thermal loading when the turbine is subjected to various synthetic WSTS to explore and demonstrate the impact of the frequency of wind speed variation on power converter thermal loading.

The thermal simulation has three main parts: a PMSG drive train model, a converter power loss model based on conduction and switching/RR, and a thermal equivalent circuit model. Both constant and square wave WSTS were tested to replicate real wind characteristics. From the results, it can be concluded that:

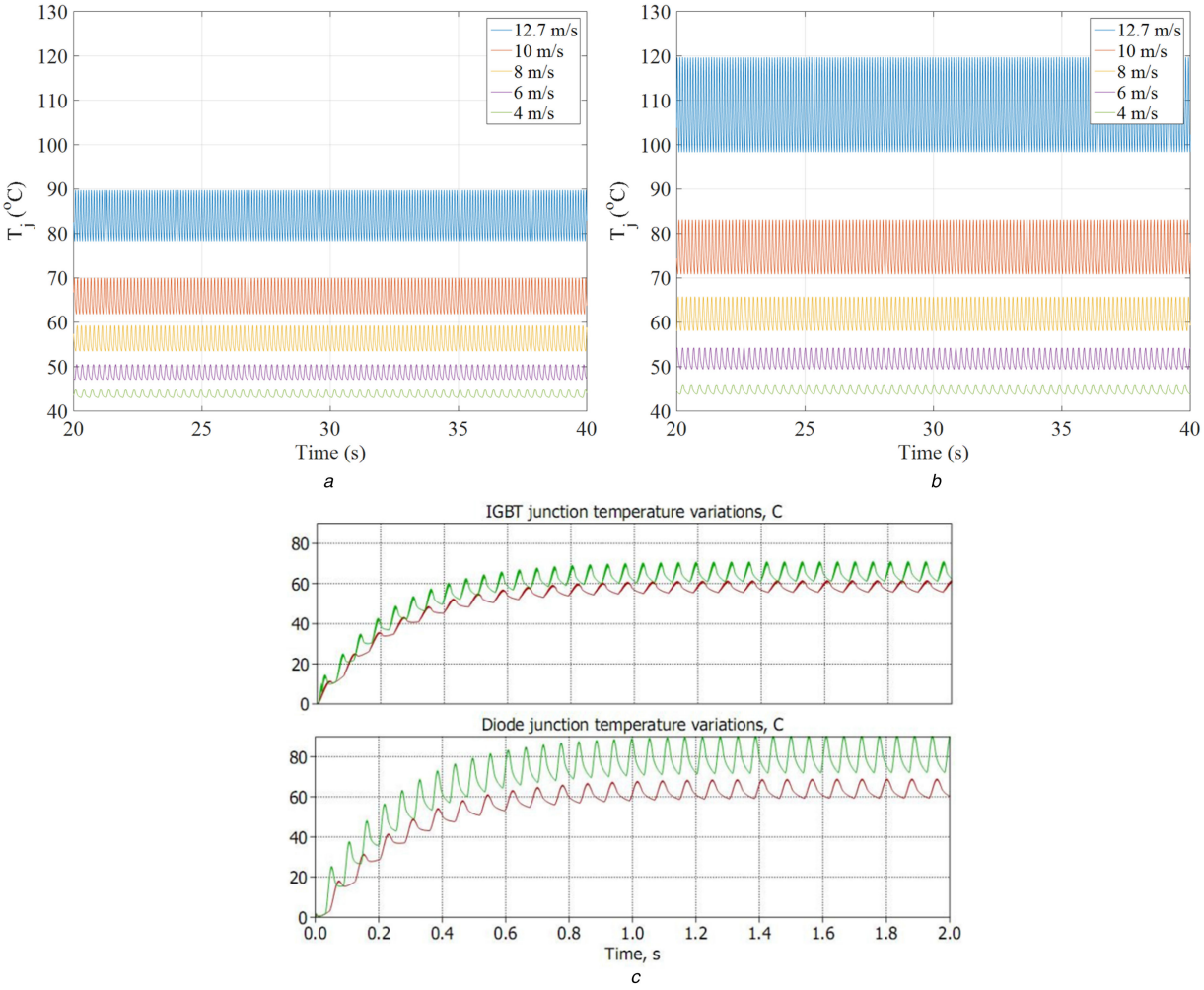

Fig. 7 *T_j response to constant wind speeds in the MPPT region for*
(a) IGBT, ***(b)*** Diode, ***(c)*** Results found in [14] for a 12 m/s input

- At high wind speeds the switching pattern of the IGBT causes intermittent T_j profiles.
- The diodes experience greater thermal loading than the IGBTs in all comparative cases.
- A comparison with another study showed that the inclusion of heat sink thermal parameters and ambient temperature are important for providing accurate T_j profiles.
- The lower the frequency of wind speed variation, the higher ΔT_j becomes, implying that low turbulence sites such as offshore have greater thermal variation, and therefore damage, in the converter.
- For the first time, the minimum wind speed data frequency for accurate converter thermal simulation has been determined. Wind speed variations with frequency >0.25 Hz have a small increase in ΔT_j and therefore reasonable approximations of T_j profiles can be made with 0.25 Hz wind speed data. Wind speed data at lower frequencies allow simulations to overlook damaging temperature variations.

5 Acknowledgments

This work was supported by the EPSRC SUPERGEN Wind project (grant number EP/L014106/1).

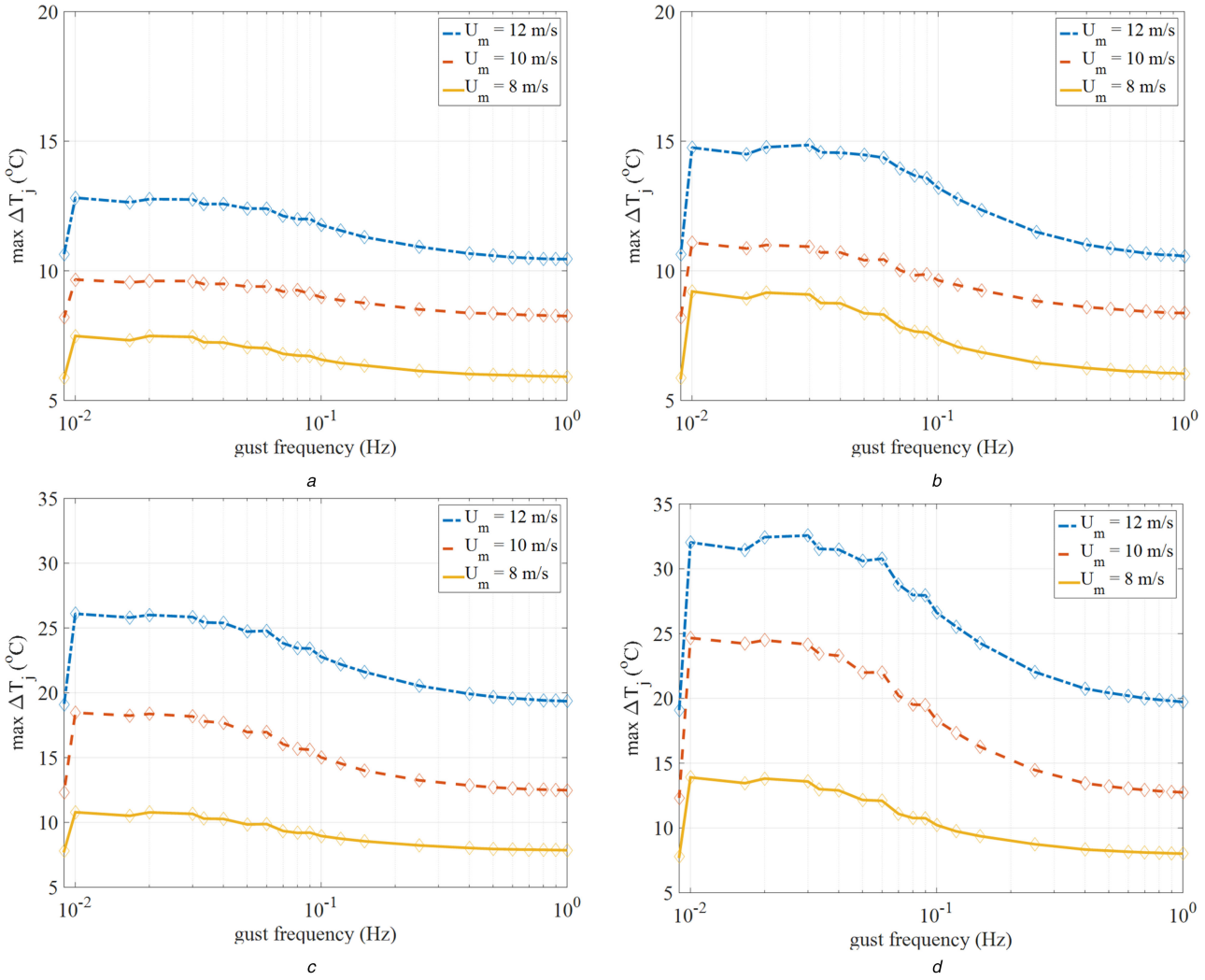

Fig. 8 *Max ΔT_j over varying mean wind speeds (U_m) and square gust frequencies for*
(a) IGBT for ΔU of 1 m/s, ***(b)*** IGBT for ΔU of 2 m/s, ***(c)*** Diode for ΔU of 1 m/s, ***(d)*** Diode for ΔU of 2 m/s

6 References

[1] 'Offshore Wind Cost Reduction, Pathways Study. Available at http://www.thecrownestate.co.uk/media/5493/ei-offshore-wind-cost-reduction-pathways-study.pdf, accessed 19 July 2016

[2] 'Large-Scale Offshore Wind Power in the United States: Assessment of Opportunities and Barriers'. Available at http://www.nrel.gov/docs/fy10osti/40745.pdf, accessed 19 July 2016

[3] Carroll, J., McDonald, A., McMillan, D.: 'Failure rate, repair time and unscheduled O&M cost analysis of offshore wind turbines', *Wind Energy*, 2015, **19**, (6), pp. 1107–1119

[4] Carroll, J., McDonald, A., McMillan, D.: 'Reliability comparison of wind turbines with DFIG and PMG drive trains', *IEEE Trans. Energy Convers.*, 2015, **30**, (2), pp. 663–670

[5] Spring, M., Davies, P., Gaal, G., *et al.*: 'Top 30 Chart for wind turbine failure mechanisms'. EWEA Annual Event, Paris, France, November 2015

[6] 'Application Manual Power Semiconductors'. Available at https://www.semikron.com/dl/service-support/downloads/download/semikron-application-manual-power-semiconductors-english-en-2015, accessed 8 September 2016

[7] Bartram, M., De Doncker, R.: 'Doubly-fed-machines in wind-turbine systems: is this application limiting the lifetime of IGBT-frequency-converters?'. IEEE PESC, Aachen, Germany, June 2004, pp. 2583–2587

[8] Fuchs, F., Mertens, A.: 'Steady state lifetime estimation of the power semiconductors in the rotor side converter of a 2 MW DFIG wind turbine via power cycling capability analysis'. EPE, Birmingham, UK, August 2011

[9] Weiss, D., Eckel, H.: 'Fundamental frequency and mission profile wearout of IGBT in DFIG converters for windpower'. EPE, Lille, France, September 2013

[10] Zhou, D., Blaaberg, F., Franke, T., *et al.*: 'Reliability and energy loss in full-scale wind power converter considering grid codes and wind classes'. IEEE ECCE, Pittsburgh, USA, September 2014, pp. 3067–3074

[11] Kostandyan, E., Ma, K.: 'Reliability estimation with uncertainties consideration for high power IGBTs in 2.3 MW wind turbine converter system', *Microelectron. Reliab.*, 2012, **52**, (9), pp. 2403–2408

[12] Ma, K., Liserre, M., Blaabjerg, F., *et al.*: 'Thermal loading and lifetime estimation for power device considering mission profiles in wind power converter', *IEEE Trans. Power Electron.*, 2015, **30**, (2), pp. 590–602

[13] Mussallam, M., Johnson, C.: 'Impact of different control schemes on the life consumption of power electronic modules for variable speed wind turbines'. EPE, Birmingham, UK, August 2011

[14] Baygildina, E., Peltoniemi, P., Pyrhönen, O., *et al.*: 'Thermal loading of wind power converter considering dynamics of wind speed'. IEEE IECON, Vienna, Austria, November 2013, pp. 1362–1367

[15] Isidoril, A., Rossi, F., Blaaberg, F., *et al.*: 'Thermal loading and reliability of 10-MW multilevel wind power converter at different wind roughness classes', *IEEE Trans. Ind. Appl.*, 2014, **50**, (1), pp. 484–494

[16] Senturk, O., Munk-Nielsen, S., Teodorescu, R., *et al.*: 'Electro-thermal modeling for junction temperature cycling-based lifetime prediction of a press-pack IGBT 3L-NPC-VSC applied to large wind turbines'. IEEE ECCE, Phoenix, USA, September 2011, pp. 568–575

[17] Smith, C., Wadge, G., Crabtree, C., *et al.*: 'Characterisation of electrical loading experienced by a nacelle power converter'. EWEA Annual Event, Paris, France, November 2015

[18] Smith, C., Crabtree, C., Matthews, : 'Impact of wind conditions on thermal loading of PMSG wind turbine power converter'. IET PEMD, Glasgow, UK, April 2016

[19] Heier, S.: '*Grid integration of wind energy: onshore and offshore conversion systems*' (John Wiley & Sons, 2014, 3rd edn.)

[20] Rao, S., Yap, F.: '*Mechanical vibrations*' (Addison-Wesley, 1995)

[21] Wu, B., Lang, Y., Kouro, S.: '*Power conversion and control of wind energy systems*' (John Wiley & Sons, 2011)

[22] 'SKS B2 100 GD 69/11 - MA PB Datasheet'. Available at http://www.semikron.com/dl/service-support/downloads/download/semikron-datasheet-sks-b2-100-gd-69-11-ma-pb-08800565, accessed 7 December 2015

[23] 'SKiiP 2013 GB172-4DW V3 Datasheet'. Available at http://www.semikron.com/dl/service-support/downloads/download/semikron-datasheet-skiip-2013-gb172-4dw-v3-20451248, Accessed 8 December 2015

[24] 'Optimised Converter for Solar and Wind'. Available at http://www.semikron.com/dl/service-support/downloads/download/semikron-flyer-semistackre-2014-04-08, accessed 14 September 2015

[25] Anaya-Lara, O., Jenkins, N., Ekanayake, J., *et al.*: '*Wind energy generation: modelling and control*' (John Wiley & Sons, 2009)

[26] Hansen, A., Sorensen, P., Iov, F., *et al.*: 'Control of variable speed wind turbines with doubly-fed induction generators', *Wind Eng.*, 2004, **28**, pp. 411–432

[27] Zhang, J., Cheng, M., Chen, Z., *et al.*: 'Pitch angle control for variable speed wind turbines'. DPRT, Nanjuing, China, April 2008, pp. 2691–2696
[28] Bianchi, F., De Battista, H., Mantz, R.: '*Wind turbine control systems: principles, modelling and gain scheduling design*' (Springer Science & Business Media, 2006)
[29] Wyllie, P.: 'Electrothermal modelling for doubly fed induction generator converter reliability in wind power'. Durham University thesis, 2014
[30] Wintrich, A., Nicolai, U., Tursky, W., *et al.*: 'Application manual power semiconductors' (SEMIKRON International GmBH, 2015)
[31] 'AN11261: Using RC Thermal Models: Application note'. Available at http://www.nxp.com/documents/application_note/AN11261.pdf, accessed 9 December 2015
[32] 'Convert Foster Network to Cauer'. Available at http://uk.mathworks.com/matlabcentral/fileexchange/46348-convert-foster-network-to-cauer/content//fostercauer.m, accessed 9 December 2015
[33] Slootweg, J., Polinder, H., Kling, W.: 'Dynamic modelling of a wind turbine with doubly fed induction generator'. PESSM, Canada, July 2001, pp. 644–649
[34] Akhmatov, V.: 'Analysis of dynamic behaviour of electric power systems with large amount of wind power'. Technical University of Denmark thesis, 2003
[35] Sim, J., Kim, K., Son, R., *et al.*: 'Ride-through of PMSG wind power system under the distorted and unbalanced grid voltage dips', *J. Electr. Eng. Technol.*, 2012, **7**, (6), pp. 898–904
[36] Leithead, W., Connor, B.: 'Control of variable speed wind turbines: dynamic models', *Int. J. Control.*, 2000, **73**, (13), pp. 1173–1188
[37] Gonzalez-Longatt, F., Wall, P., Terzija, V.: 'A simplified model for dynamic behavior of permanent magnet synchronous generator for direct drive wind turbines'. IEEE PES PowerTech, Trondheim, June 2011, pp. 1–7

7 Appendix

$P_{t,rat}$ is the rated turbine power, f_{rat} is the rated frequency, U_{rat} is the rated wind speed, $V_{l,rat}$ is the rated line voltage, I_{rat} is the rated current, T_{rat} is the rated torque, V_f is the IGBT forward voltage, V_{fd} is the diode forward voltage, $T_{f,t}$ is the IGBT fall time and tail time, respectively, R_{on} is the IGBT on-state slope resistance, $P_{p,id,iq}$ are the proportional gains for the pitch, I_d, and I_q controllers, respectively, $I_{p,id,iq}$ are the integral gains for the pitch, I_d, and I_q controllers, respectively, and f_{sw} is the switching frequency (see Table 1).

Table 1a *Continued*

Parameter	Value	Reference
A_t	0.22	[33]
B_t	116	[33]
C_t	0.4	[33]
D_t	0	[33]
E_t	0	[33]
F_t	5	[33]
G_t	12.5	[33]
H_t	0.08	[33]
K_t	0.035	[33]
$P_{t,rat}$	2.0 MW	[21]
$\omega_{t,rat}$	22.5 rpm	[21]
f_{rat}	9.75 Hz	[21]
λ_{opt}	6.3	—
$C_{p,max}$	0.438	—
U_{rat}	12.7 m/s	—
r	34 m	—
ρ	1.225 kg/m^3	[25]
J_t	2.92×10^6 kg/m^2	[34]
J_g	200 kg/m^2	[35]
K	4.0×10^7 Nm/rad	[34]
C_d	6.72×10^6 Nms/rad	—
$V_{l,rat}$	690 $V_{(rms)}$	[21]
$I_{,rat}$	1867.76 $A_{(rms)}$	[21]
T_{rat}	848.826 kNm	[21]
R_s	8.21×10^{-4} Ω	[23]
L_d	1.5731 mH	[23]
p	52	[23]
φ	8.24 Vs (peak)	[23]
V_f	0.95 V	[23]
V_{fd}	1.9 V	[23]
R_{on}	0.925 mΩ	[23]
V_{DC}	1150 V	—
β_{max}	45°	[36]
β_{min}	0°	[36]
$\beta_{rate,max}$	8°/s	[36]
$\beta_{rate,min}$	−8°/s	[36]
τ	0.5 s	[37]
P_p	3.357	—
I_p	0.012	—

Table 1b *Drive train parameters*

Parameter	Value	Reference
P_{id}	−0.148	—
I_{id}	−5.377	—
P_{iq}	−0.155	—
I_{iq}	−2.689	—
f_{sw}	2 kHz	[22]
$R_{th,c,IGBT}(1)$	1.5×10^{-3} K/W	—
$R_{th,c,IGBT}(2)$	7.3×10^{-3} K/W	—
$R_{th,c,IGBT}(3)$	5.9×10^{-3} K/W	—
$R_{th,c,IGBT}(4)$	2.5×10^{-3} K/W	—
$R_{th,c,IGBT}(5)$	0.37×10^{-3} K/W	—
$C_{th,c,IGBT}(1)$	0.55 Ws/K	—
$C_{th,c,IGBT}(2)$	3.61 Ws/K	—
$C_{th,c,IGBT}(3)$	35.90 Ws/K	—
$C_{h,c,IGBT}(4)$	476.61 Ws/K	—
$C_{h,c,IGBT}(5)$	4.81×10^3 Ws/K	—
$R_{th,c,diode}(1)$	2.8×10^{-3} K/W	—
$R_{th,c,diode}(2)$	10.2×10^{-3} K/W	—
$R_{th,c,diode}(3)$	10.5×10^{-3} K/W	—
$R_{th,c,diode}(4)$	11.9×10^{-3} K/W	—
$R_{th,c,diode}(5)$	8.6×10^{-3} K/W	—
$R_{th,c,diode}(6)$	0.94×10^{-3} K/W	—
$C_{th,c,diode}(1)$	0.773 Ws/K	—
$C_{th,c,diode}(2)$	1.45 Ws/K	—
$C_{th,c,diode}(3)$	4.90 Ws/K	—
$C_{th,c,diode}(4)$	36.07 Ws/K	—
$C_{th,c,diode}(5)$	577.76 Ws/K	—
$C_{th,c,diode}(6)$	1.60×10^4 Ws/K	—
$R_{th,c,h}(1)$	0.79×10^{-3} K/W	—
$R_{th,c,h}(2)$	3.1×10^{-3} K/W	—
$R_{th,c,h}(3)$	4.3×10^{-3} K/W	—
$R_{th,c,h}(4)$	0.88×10^{-3} K/W	—
$R_{th,c,h}(5)$	0.14×10^{-3} K/W	—
$C_{th,c,h}(1)$	337.28 Ws/K	—
$C_{th,c,h}(2)$	409.76Ws/K	—
$C_{th,c,h}(3)$	1.37×10^3 Ws/K	—
$C_{h,c,h}(4)$	1.91×10^4 Ws/K	—
$C_{h,c,h}(5)$	1.30×10^4 Ws/K	—
TC_{Esw}	0.003	[30]
TC_{Err}	0.006	[30]
T_{ref}	125°C	—

Impact of wind conditions on thermal loading of PMSG wind turbine power converters

C J Smith*, C J Crabtree*, P C Matthews*

**School of Engineering and Computing Sciences, Durham University, United Kingdom, c.j.smith2@dur.ac.uk, c.j.crabtree@dur.ac.uk, p.c.matthews@dur.ac.uk*

Keywords: Power converter, thermal loading, reliability.

Abstract

Power converter reliability is critical for permanent magnet synchronous generator (PMSG) wind turbines. Converter failures are commonly linked to the power module thermal loading. This paper models the expected converter thermal loading when the turbine is subjected to various synthetic wind speed conditions, including constant and square wave profiles. It was found that the model performed as expected compared to manufacturer's data and the diodes had greater thermal loading than the insulated-gate bipolar transistors (IGBTs). The preliminary results from synthetic square wave wind speed time series (WSTS) suggest that wind events with a period >5s are critical to the device thermal loading.

1 Introduction

To meet EU renewable energy targets for 2020 and beyond, the Levelised Cost of Energy (LCoE) of offshore wind needs to be reduced to below £100/MWh [1]. Operation and maintenance (O&M) accounts for approximately 30% of the LCoE [2]. A key aspect of O&M is the reliability of the turbine sub-systems. By understanding which components' reliability has the greatest impact on downtime and power production, O&M resources can be focused to minimise turbine disruption and reduce offshore wind's LCoE.

A number of studies have explored the reliability of wind turbine sub-systems. [3] examined a large dataset for offshore wind turbines with varying turbine technology to determine the main causes of failure and concluded that the power converter had a typical failure rate of ~0.2 failures/turbine/year (f/t/y), which was much lower than the highest failure rate of >1 f/t/y for the pitch system. However, a more focused study on turbine type [4] found that the failure rate of fully-rated converters (FRC) in permanent magnet synchronous generator (PMSG) turbines was 0.593 f/t/y compared to the 0.106 f/t/y for doubly fed induction generator (DFIG) turbines. Furthermore, [5] examined large datasets of wind turbines and consulted expert knowledge to produce a top 30 list of turbine failure modes and concluded that the power converter was the highest risk component to turbine reliability. The reliability of the converter must therefore be examined with a focus on the FRC in PMSG turbines.

Of the failures outlined in [4], power module failure is the failure mode for nearly all major converter repairs. Traditionally, this power module failure has been linked to power module thermal loading, where the variation of junction temperature in the insulated gate bipolar transistors ($\Delta T_{j,IGBT}$) and diodes ($\Delta T_{j,diode}$) causes fatigue through expansion and contraction of current carrying components. This is analogous to fatigue in mechanical engineering.

This approach has been applied in a number of studies to explore the expected reliability of power converters in wind turbines [6-15]. However these studies often have limitations:

- Neglect the impact of turbine response by using simplified wind turbine models and/or wind speed inputs.
- Limited scope of failure data. Cycles-to-failure is derived from manufacturer or experimental data which consider only fixed magnitude ΔT_j, implying a fixed input current.
- Limited validation approaches. Experimental work is often carried out at constant input conditions.

These limitations mean that the operational profiles and failure data are not representative of how a converter operates in the field. In response these research questions were formed.

1. Are the thermal loading profiles generated in the power modules verifiable for complex input profiles?
2. Which operating conditions cause the greatest thermal loading to the power modules and does this correspond to the greatest damage?
3. Is the use of manufacturing cycles-to-failure data a valid approach for converter lifetime estimation under complex loading conditions such as operation in a wind turbine?

This paper concentrates on providing the benchmark for the 3 questions by modelling the expected thermal loading and finding the wind conditions which theoretically cause the greatest damage to the converter.

The paper is organised as follows. Section 2 outlines the approach for producing the thermal loading profiles, including a drive train model (Section 2.1), power loss model (Section 2.2), thermal model (Section 2.3) and wind inputs (Section 2.4). Section 3 outlines the thermal loading results from simulations and Section 4 concludes the work.

2 Approach

To determine the thermal loading of a wind turbine power converter the following procedure was followed:

1. Model a wind turbine drive train to provide the current throughput of the converter.
2. Model the resultant power losses in the converter due to the current throughput.
3. Model the power module thermal processes in response to the power losses.
4. Simulation of power module thermal response to a variety of wind speed inputs.

This section outlines the details of each step.

2.1 Drive Train Model

To ensure an accurate current throughput is provided the turbine dynamics need to be considered. A drive train model has been constructed previously for this purpose [16]. The following summarises the model's key details.

- Modelled as a direct-drive 2MW wind turbine.
- Mechanical drive train modelled as a 2-mass model.
- 2nd order non-salient PMSG.
- FRC based on SEMIKRON RE stacks.
- Grid-side converter (GSC) modelled as an ideal DC link.
- Maximum power point tracking (MPPT) achieved using *dq0* vector control.
- Active pitch control.

Updates have been made to the turbine control for this paper:

1. The reference pitch angle (β_{ref}) is limited to positive values to avoid an issue in the actuator system integration delaying the pitch actuator.

2. The torque controller is no longer constrained by the rated turbine rotational speed ($\omega_{t,rat}$) but by a higher maximum ($\omega_{t,max}$). This allows the torque controller to deal with sudden increases in wind speed that the pitch controller is too slow to respond to effectively. This provides a similar controller interaction as found in [17].

Figure 1.b, d shows an improved pitch control response. This updated control requires a higher converter maximum current throughput ($I_{out,max}$) compared to in [16] (Figure 1.c, e). Therefore the MSC was replaced with two parallel SKSB2100GD69/11-MAPB stacks, providing an $I_{out,max}$ of 1000 A_{rms} per stack [18]. This corresponds to a total I_q of 2828 A, which was reduced to 2800 A to allow for noise and controller overshoot This dictates a $\omega_{t,max}$ of 2.43 rad/s.

The new stacks meant the half-bridge modules used were changed to SKiiP 2013GB172-4DWV3 modules [19]. This made little difference to the drive train parameters except the collector-emitter resistance (R_{on}) was reduced to 0.925 mΩ.

To summarise, a 2MW PMSG wind turbine with a FRC model was used from a previous work [16] with improvements to the turbine control and MSC data used.

2.2 Converter Power Loss Model

To convert the current throughput into power module T_j profiles the power module component power losses much be calculated. This section outlines the power loss model used.

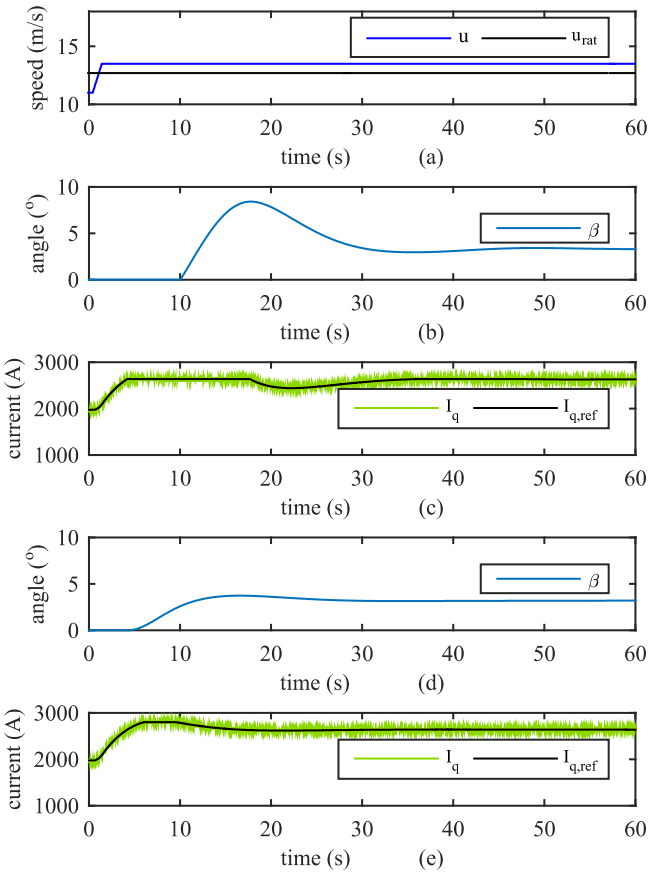

Figure 1: Turbine control update. (b) and (c) are the pitch and I_q response in [16] to a given wind speed input (a). (d) and (e) are the updated pitch and I_q response.

The electrical loss models used in the literature consider losses in IGBTs and diodes. This includes the conduction losses of IGBTs and diodes, the switching losses of the IGBT and the reverse recovery (RR) losses of the diodes [7-10, 20].

The power loss model used is based on the models in [20, 21]. The power losses were calculated as follows:

1. The current throughput of each device is simulated.
2. The IGBT and diode conduction losses are calculated.
3. The IGBT switching losses and diode RR losses are calculated.
4. The conduction and switching losses are summed for each device and fed to the thermal model.

Conduction Losses

The conduction losses are related to the power dissipated from the devices' internal resistance. This is calculated by determining the voltage and current of the device (1, 2).

$$P_{C,IGBT} = V_{ce}\, I_c \quad (1)$$

$$P_{C,diode} = V_f\, I_f \quad (2)$$

Where $P_{C,IGBT}$ and $P_{C,diode}$ are the IGBT and diode conduction losses respectively, V_{ce} is the IGBT collector-emitter voltage, V_f is the diode forward voltage, I_c is the IGBT collector current, and I_f is the diode forward current.

I_c and I_f are the input currents. V_{ce} and V_f are functions of I_c and I_f respectively, and the device T_j. The functions are given in the manufacturer's data sheet [19] for a T_j of 25°C and 125°C. Look-up tables (LUT) have been produced to determine the V_c, and V_f for each time step for these reference T_j. The T_j from the previous time step is used to provide the actual V by linearly interpolating between the reference Vs.

Switching/RR Losses

Switching and RR losses occur when there is a change in direction of voltage and current as these changes are not instantaneous. This occurs in a period of hundreds of nanoseconds [20] so the model fidelity has to be considered.

Simulating over nanoseconds is impractical for times longer than a few seconds. Energy loss information given in manufacturer's datasheets is also not detailed enough for accurate temporal loss simulation. For example, the IGBT energy loss is a total energy loss for both on and off switching events (E_{on+off}) [19]. Splitting this energy equally would not be valid as revealed in other datasheets [22]. This limited information means a simplified approach has to be taken.

It has therefore been assumed that the energy loss is given by the conditions at the first low-high (L-H) switching instance. The energy is modulated over the switching cycle (between L-H and the next L-H) to provide a constant switching power loss. This was deemed acceptable as the device thermal time constants will dominate the thermal profile.

The switching/RR losses are calculated as follows:

1. Determine when the device input changes from L-H.
2. Determine the time period between L-H switching events (T_p). If this time period was found to be greater than a threshold ($T_{p,max}$) the device was deemed to be switched off for a long time and the T_p set to $1/f_{sw,ref,}$ where $f_{sw,ref}$ is the maximum switching frequency of the converter.
3. Determine the energy losses at L-H switching events. The switching/RR energy loss is given as a function of input current at two reference DC voltages (V_{DC}) [19]. Therefore a LUT was constructed for both reference V_{DC}'s and the input current used to determine the corresponding energy loss. The actual V_{DC} is then used to linearly interpolate between these two reference values. For the IGBT this energy loss is the E_{on+off}, whilst the diode energy loss is twice the RR energy loss (E_{rr}).
4. The equivalent modulated power losses over the switching cycle are calculated using (3, 4).

$$P_{sw}(t{:}T_{s,th}{:}\,(t + T_{p,sw}(t))) = \frac{E_{on+off}(t)}{T_{p,sw}(t)} \quad (3)$$

$$P_{rr}(t{:}T_{s,th}{:}(t + T_{p,rr}(t))) = \frac{E_{rr}(t)}{T_{p,rr}(t)} \quad (4)$$

Where P_{sw} is the IGBT switching power loss, P_{rr} is the diode RR power loss, t is the time step, $T_{s,th}$ is the thermal sampling time ($5x10^{-5}$ s), $T_{p,sw}$ is the IGBT switching time period and $T_{p,rr}$ is the diode RR time period.

5. The switching/RR losses are also T_j dependent, with the relationship determined as in (5, 6) [21].

$$P_{sw,T_j}(t) = \left(1 + TC_{Esw}\left(T_{j,IGBT}(t) - T_{ref}\right)\right) P_{sw}(t) \quad (5)$$

$$P_{rr,T_j}(t) = \left(1 + TC_{Err}\left(T_{j,diode}(t) - T_{ref}\right)\right) P_{rr}(t) \quad (6)$$

Where $P_{sw,Tj}$, $P_{rr,Tj}$ are the T_j corrected P_{sw} and P_{rr} respectively, TC_{Esw} TC_{Err} are the switching loss and RR temperature coefficients respectively, and T_{ref} is the reference temperature of the energy loss LUTs.

With the conduction and switching/RR power losses calculated the total power loss can be calculated.

2.3 Thermal Loss Model

Converter thermal modelling is carried out in three ways:

- Thermal equivalent circuits [7-9, 11-14].
- Thermal diffusion equations [10].
- Finite Element Analysis (FEA) [6].

The choice of thermal model is based on data availability and computational efficiency. The thermal equivalent circuits are used when Foster network resistor-capacitor (RC) manufacturing data is available. Modifications are made to improve the network accuracy, which often involves converting to a Cauer network. If this data is not available or detailed device analysis is required, thermal diffusion equations or FEA is used. However these methods are computationally expensive. As the RC network data was available a thermal equivalent circuit was used.

The data given in [19] is for a Foster RC network. This network gives a numerical approximation of the thermal network which means that the calculated temperatures, except T_j and the ambient temperature (T_a), have no physical meaning. To provide a more accurate half-bridge temperature profile the Foster thermal resistance ($R_{th,f}$) and time constant (τ) parameters were converted into RC parameters (7) [23], and then converted into Cauer RC parameters using the algorithm available at [24]. This conversion was carried out independently for each IGBT, diode and heat sink. Figure 2 gives the half-bridge Cauer RC network.

$$C_{th,f} = \frac{\tau}{R_{th,f}} \quad (7)$$

Where $C_{th,f}$ is the Foster thermal capacitance.

Wind Speed Inputs

Wind speed and converter current throughput are decoupled by the turbine inertia and control [16]. As such, determining which characteristics of a wind speed time series (WSTS) have the largest impact on thermal loading is challenging.

To address this, experiments have been constructed which use synthetic WSTS to isolate potential wind speed characteristics and determine their impact on thermal loading. Square waves have been used to represent sudden changes in wind speed. Figure 3 shows an example synthetic WSTS. The constant wind speed at the start is for initialisation (Section 2.5).

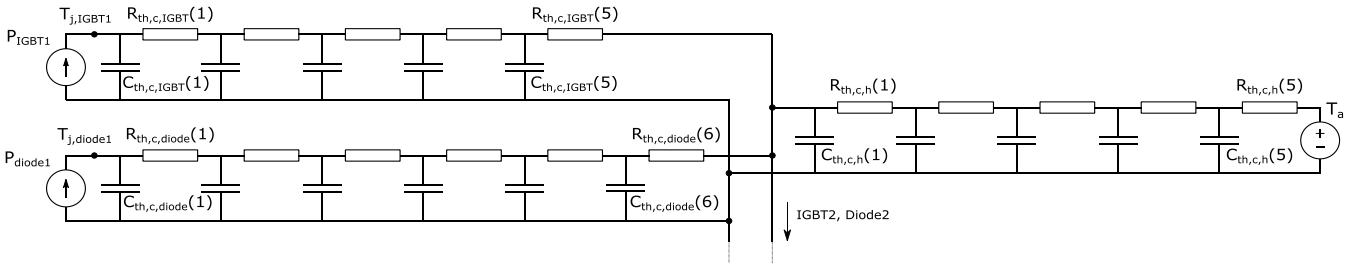

Figure 2: Half bridge Cauer RC network (only one IGBT and diode represented here). P_{IGBT1} is the IGBT power loss, P_{diode1} is the diode power loss, $R_{th,c}$ is the Cauer thermal resistance, $C_{th,c}$ is the Cauer thermal capacitance, and $_h$ is the heat sink.

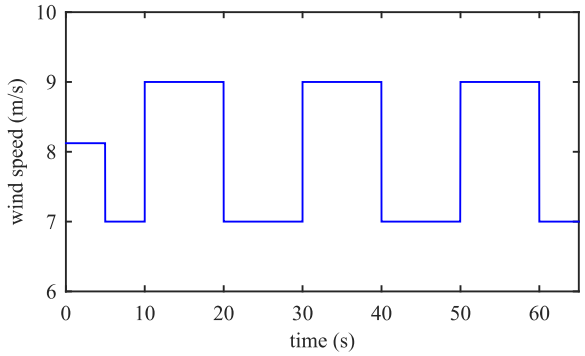

Figure 3: 7-9 m/s, 20s period square wave.

2.4 Overall system

Figure 4 summarises the whole system model.

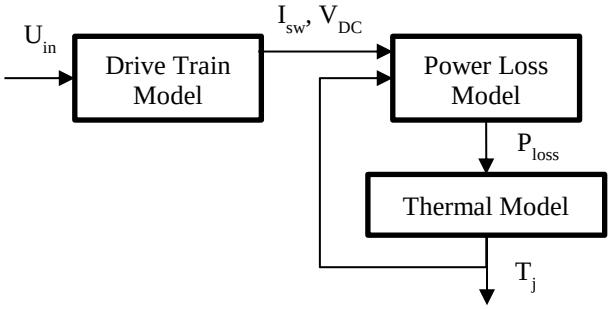

Figure 4: Turbine-converter thermal loading model.

The power losses (P_{loss}) are dependent on T_j and therefore the power loss and thermal sub-systems must be run concurrently. Technically the current throughput of the devices is also related to the power losses and T_j, but it was assumed that this effect would be negligible [20].

Due to the power-thermal inter-dependency the initialisation of C_{th} temperatures was solved iteratively. The steady-state temperatures are related to the R_{th} only [21], with the temperatures analogous of a voltage drop (temperature) due to a current throughput (power). The steps are as follows:

1. Set initial temperatures for each C_{th} (typically to T_a).
2. Take first 0.5s of input current for each device.
3. Calculate power loss over 0.5s given device T_j.
4. Calculate steady state temperatures using R_{th} only.
5. Update device temperatures.
6. Compare previous and new device temperatures. If the variation is less than 0.001°C then the temperatures are deemed correct. Otherwise repeat steps 2-6.

This initialisation is subject to variations in the input current and therefore all tests are carried out with a 5s constant wind speed at the start (Figure 3). For the square wave tests this constant wind speed represents the average power wind speed, which is slightly higher than the average wind speed due to the cubic relationship between wind speed and power.

To summarise, a computer model of a wind turbine drive train and power converter thermal network has been constructed. This allows for any wind speed profile to be entered and the corresponding power module thermal profiles be produced.

3 Results and Discussion

This section outlines the analysis performed on T_j profiles produced in response to constant and square wave WSTS.

3.1 Constant Wind Speeds

Figure 5 shows the thermal response to constant WSTS for IGBT1 and Diode1 with a T_a of 25°C. As expected, the mean T_j increases non-linearly as wind speed increases due to the cubic relationship between wind speed and power. The ΔT_j also increases with increased wind speed due to the higher power loss per cycle, and the ΔT_j frequency increases due to the higher generator rotational speed. Interestingly the diode T_j and ΔT_j (5.a) are consistently higher than the IGBT (5.b). This is due to the higher power losses experienced by the diodes. This was also found for the MSC devices in [11].

The results in Figure 5 were compared to those in [11]. It was found that the T_j and ΔT_j for 12 m/s were similar for both IGBT and diode. However, this similar T_j is misleading as the T_a was 25°C higher in [11]. This suggests that the MSC in this work is more susceptible to T_j rises due to the higher R_{th} values in the devices and heatsink. This is supported by the T_j change from 12 m/s to 8.5 m/s being much lower in [11] than in Figure 5. It also highlights the need to consider T_a.

Figure 6 zooms in on one power loss and T_j cycle. The T_j profile is comparable with the expected response found in Figure 5.2.13 in the manufacturer's handbook [21].

In summary, the devices' T_j response to various constant wind speeds performed as expected, and the diode had a more aggressive thermal response. The individual T_j cycles were consistent with manufacturer's data. This MSC was deemed to be more susceptible to T_j variation than the one in [11] and this difference highlighted the need for an accurate T_a value.

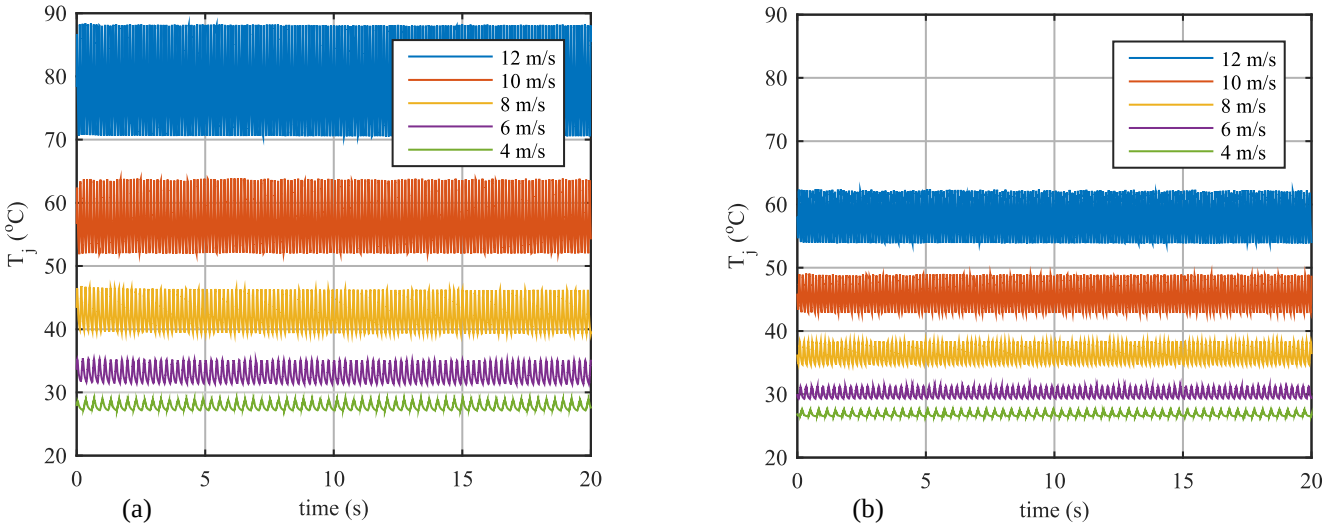

Figure 5: T_j response to constant wind speeds in the MPPT region for (a) Diode1 and (b) IGBT1.

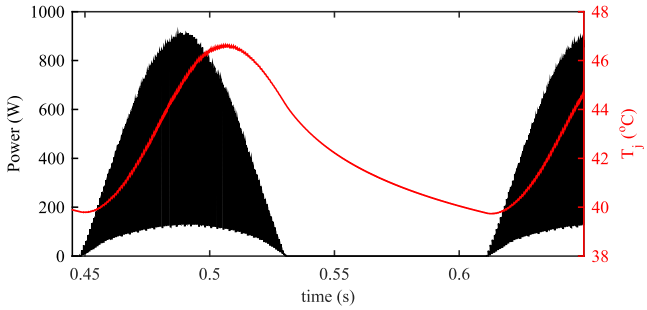

Figure 6: One power loss and T_j cycle for Diode1 at 8m/s.

3.2 Response to Varying Wind Speed input

The T_j response of IGBT1 to a range of square wave WSTS is detailed. For comparison the mean, maximum and minimum T_j ($T_{j,mean}$, $T_{j,max}$, $T_{j,min}$) have been plotted for wave amplitudes of 1 and 2 m/s for varying time periods and mean wind speeds (Figure 7). There are 4 main conclusions from these results:

1. The constant wind speed generally has a lower T_j than the square waves. This is due to the average power being higher than the mean wind speed (U_m) power. Therefore the average wind power must be considered.
2. $T_{j,mean}$ is constant for the square waves for a given U_m.
3. At low time periods (0.5-5s) the temperature range (ΔT) is similar to the constant case (Figure 7). This would suggest that wind speed variations in this period could be neglected for life time estimation, though this assumption needs experimental validation.
4. Between a 5-10s period ΔT becomes significant (Figure 7), particularly for a wave amplitude of 2 m/s (Figure 7.b). This was more pronounced for Diode1. Therefore variations in wind speed over this period cannot be neglected when determining device thermal loading.

4 Conclusions

The wind turbine power converter is reliability critical for FRC-PMSG turbines. Converter failures are traditionally linked to the thermal loading of the power module. This paper

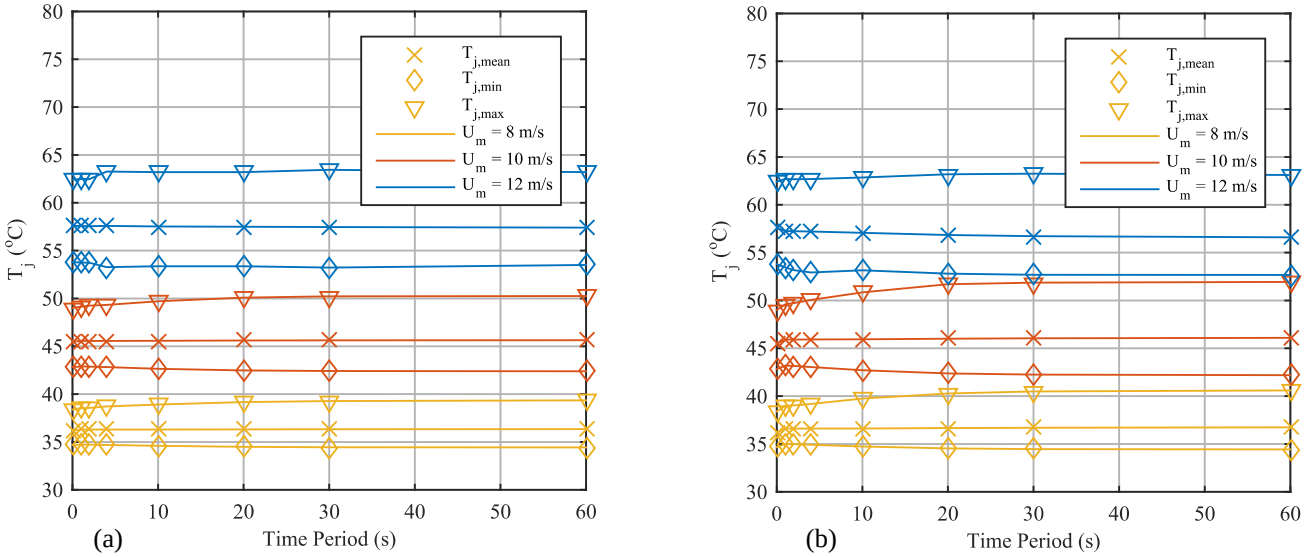

Figure 7: T_j response to square wave WSTS with varying time period, U_m and wave amplitude of (a) 1m/s, (b) 2m/s.

models the expected converter thermal loading when the turbine is subjected to various synthetic WSTS to explore the impact of wind conditions on power converter fatigue.

The thermal simulation has 3 main parts: a PMSG drive train model; a converter power loss model based on conduction and switching/RR; and a Cauer RC thermal equivalent circuit model. Both constant and square wave WSTS were tested and compared to manufacturing data and results in [11]. It was found that the model performed as expected compared to manufacturer's data. The diodes had greater thermal loading than the IGBTs, and this converter had higher mean T_j than in [11]. These preliminary results suggest that wind events of period >5s are critical to device thermal loading.

Future work will provide estimation of theoretical failure times and the most damaging wind speeds to the converter. The results will also be validated using an experimental rig.

References

[1] E. Davey and A. Nimmo. "Offshore Wind Cost Reduction, Pathways Study", (2012). Accessed [07/10/2015]. Available from: http://www.thecrownestate.co.uk/energy-and-infrastructure/offshore-wind-energy/working-with-us/strategic-workstreams/cost-reduction-study/.

[2] W. Musial and B. Ram. "Large-Scale Offshore Wind Power in the United States: Assessment of Opportunities and Barriers", (2010). Accessed [07/10/2015]. Available from: http://www.nrel.gov/docs/fy10osti/40745.pdf.

[3] J. Carroll, A. McDonald, and D. McMillan. "Failure rate, repair time and unscheduled O&M cost analysis of offshore wind turbines", *Wind Energy*. (2015).

[4] J. Carroll, A. McDonald, and D. McMillan. "Reliability Comparison of Wind Turbines With DFIG and PMG Drive Trains", *IEEE Transactions on Energy Conversion*. **30**(2), pp. 663. (2015).

[5] M. Spring, et al. "Top 30 Chart for wind turbine failure mechanisms", *EWEA Annual Event*, (2015).

[6] M. Bartram and R.W. De Doncker. "Doubly-fed-machines in wind-turbine systems: is this application limiting the lifetime of IGBT-frequency-converters?", *IEEE 35th Annual Power Electronics Specialists Conference*, (2004).

[7] K. Ma, et al. "Thermal loading and lifetime estimation for power device considering mission profiles in wind power converter", *IEEE Transactions on Power Electronics*. **30**(2), pp. 590-602. (2015).

[8] D. Zhou, et al. "Reliability and energy loss in full-scale wind power converter considering grid codes and wind classes", *IEEE Energy Conversion Congress and Exposition*, (2014).

[9] O.S. Senturk, et al. "Electro-thermal modeling for junction temperature cycling-based lifetime prediction of a press-pack IGBT 3L-NPC-VSC applied to large wind turbines", *IEEE Energy Conversion Congress and Exposition*, (2011).

[10] M. Musallam and C.M. Johnson. "Impact of different control schemes on the life consumption of power electronic modules for variable speed wind turbines", *14th European Conference on Power Electronics and Applications* (2011).

[11] E. Baygildina, et al. "Thermal loading of wind power converter considering dynamics of wind speed", *39th Annual Conference of the IEEE Industrial Electronics Society*, (2013).

[12] A. Isidoril, et al. "Thermal loading and reliability of 10-MW multilevel wind power converter at different wind roughness classes", *IEEE Transactions on Industry Applications*. **50**(1), pp. 484-494. (2014).

[13] F. Fuchs and A. Mertens. "Steady state lifetime estimation of the power semiconductors in the rotor side converter of a 2 MW DFIG wind turbine via power cycling capability analysis", *14th European Conference on Power Electronics and Applications*, (2011).

[14] E. Kostandyan and K. Ma. "Reliability estimation with uncertainties consideration for high power IGBTs in 2.3 MW wind turbine converter system", *Microelectronics reliability*. **52**(9), pp. 2403-2408. (2012).

[15] D. Weiss and H.-G. Eckel. "Fundamental frequency and mission profile wearout of IGBT in DFIG converters for windpower", *15th European Conference on Power Electronics and Applications*, (2013).

[16] C.J. Smith, et al. "Characterisation of Electrical Loading Experienced by a Wind Turbine Power Converter", *EWEA Annual Event* (2015).

[17] A. Hansen, et al. "Control of variable speed wind turbines with doubly-fed induction generators", *Wind Engineering*. **28**(4), pp. 411-432. (2004).

[18] SEMIKRON. "SKS B2 100 GD 69/11 - MA PB Datasheet", (2013). Accessed [07/12/2015]. Available from: http://www.semikron.com/dl/service-support/downloads/download/semikron-datasheet-sks-b2-100-gd-69-11-ma-pb-08800565.

[19] SEMIKRON. "SKiiP 2013 GB172-4DW V3 Datasheet", (2014). Accessed [08/12/2015]. Available from: http://www.semikron.com/dl/service-support/downloads/download/semikron-datasheet-skiip-2013-gb172-4dw-v3-20451248.

[20] P. Wyllie, *Electrothermal Modelling for Doubly Fed Induction Generator Converter Reliability in Wind Power*. Durham University Thesis. (2014).

[21] A. Wintrich, et al, *Application Manual Power Semiconductors*. 2011, Ilmenau, Germany: ISLE Verlag.

[22] SEMIKRON. "SKiiP 11NAB066V1 Datasheet", (2006). Accessed [18/12/2015]. Available from: http://www.semikron.com/dl/service-support/downloads/download/semikron-datasheet-skiip-11nab066v1-25230580.

[23] NXP. "AN11261: Using RC Thermal Models: Application note", (2014). Accessed [09/12/2015]. Available from: http://www.nxp.com/documents/application_note/AN11261.pdf.

[24] K.R. Shailesh. "Convert Foster Network to Cauer", (2014). Accessed [09/12/2015]. Available from: http://uk.mathworks.com/matlabcentral/fileexchange/46348-convert-foster-network-to-cauer/content//fostercauer.m.

Characterisation of Electrical Loading Experienced by a Nacelle Power Converter

C.J. Smith[a], G.N. Wadge[a], C.J. Crabtree[a], P.C. Matthews[a]

[a]Energy Group, School of Engineering and Computing Sciences, Durham University

I. Abstract

The reliability of fully rated converters (FRC) in permanent magnet synchronous generator (PMSG) wind turbines is critical. A drive train model has been constructed to simulate the current throughput of the power modules in the FRC in response to a variety of isolated wind speed conditions and simulated wind speed profiles to explore potentially damaging operating conditions.

The drive train model is based on a 2MW, PMSG, direct-drive, FRC wind turbine. The mechanical drive train is modelled as a 2-mass model. The machine-side converter (MSC) was parameterised using a Semikron converter. The turbine was controlled via maximum power point tracking (MPPT) and active pitch control.

The results revealed that the turbine inertia and control decoupled the wind and current profiles. Pitch control overshoot leads to long term current variation even when operating at above rated wind speed. Therefore the wind speed cannot be used to directly derive the MSC currents. Instead the detailed wind turbine drive train model presented is required for MSC current simulation.

With this current response, detailed simulation and analysis of the MSC thermal loading is possible. The turbine can now be emulated in an experimental rig using an AC power supply to provide realistic operating conditions.

Keywords – Power Converter Reliability, Power Module Current, Drive Train Model, Simulation

II. Introduction

To meet EU renewable energy targets for 2020 and beyond, the Levelised Cost of Energy (LCoE) of offshore wind needs to be reduced to below £100/MWh [1]. Operation and maintenance (O&M) costs account for around 30% of the LCoE [2] and therefore research has focused on understanding the reliability of components and their impact on the LCoE.

In the past turbine topologies have been modified in response to poor reliability. A number of onshore turbine failure datasets have been examined [3] to find the components causing wind turbine failure. It is broadly accepted that generator and mechanical subsystem failures have led to the longest downtimes. In response turbine manufacturers have introduced direct-drive topologies or simplified the gearbox to improve reliability.

Wind turbine drive trains have also introduced more power electronic devices to allow for variable speed operation for improved energy capture. However these devices have a large number of sensitive components which has led to a concern that these devices will lead to poorer reliability.

[4] examined a large dataset for offshore wind turbines with varying turbine technology to determine the main causes of failure and concluded that the power converter had a typical failure rate of ~0.2 failures/turbine/year (f/t/y) over the turbine population, much lower than components such as the pitch system (~1.1 f/t/y). However this study did not distinguish between turbine technology and the extent power converters are used.

A more focused study on turbine type [5] found that the failure rate of fully-rated converters (FRC) in permanent magnet synchronous generator (PMSG) turbines was 0.593 f/t/y compared to the 0.106 f/t/y for doubly fed induction generator (DFIG) turbines. This FRC failure rate is three times higher than the rest of the turbine population. Of these failures, power modules are the failure mode for nearly all major converter repairs. FRC reliability is critical for PMSG turbines, with power module failure the most critical failure mode.

The reduction in reliability when moving to offshore has been noted as a key concern. This is due to the increased repair times and cost to repair over onshore turbines [6]. Onshore, the converter reliability has been largely ignored as it is relatively easy to repair or replace compared to many of the mechanical components. However, with reduced accessibility, a converter failure offshore is much more critical to the overall performance of the turbine [7]. A small failure in the converter in bad weather could lead to a logistical delay of up to half a year in extreme circumstances [8]. This issue of reduced reliability offshore leads to loss in power generation and a loss of revenue [9], increasing the LCoE.

With power converters becoming increasingly important for turbine reliability, researchers have attempted to predict converter lifetime. Typically this has been carried out using cycles-to-failure against insulated gate bipolar transistor (IGBT) junction temperature swing (ΔT_j) manufacturing data [10]. ΔT_j is calculated by converting power throughput of converters into T_j of IGBT chips using thermal impedance networks. With this T_j data, cycles-to-failure data is used to compute end-of-life.

However, whilst power module failure modes are well understood, manufacturing cycle data is often produced at fixed frequency and magnitude ΔT_j [5]. This is not representative of how a converter is operated in the turbine [10]. Therefore harmful operating conditions may have their impact on reliability omitted.

To address this, an experimental rig is being designed which will apply the power converter under turbine operating conditions. The experiments will focus on extreme operating conditions. Understanding these harmful operating conditions may highlight turbine operations that should be avoided to improve reliability, and provide information on the failure characteristics of power converters for improved maintenance strategies. The rig will also provide opportunities for condition monitoring research.

Prior to this experimental work the potentially harmful operating conditions need to be characterised. This paper outlines a computer simulation of a turbine drive train that is used to meet the following objectives:

- To provide a wind turbine drive train model for characterisation of electrical signals that are experienced by the MSC at different operating points on the power curve.
- To provide data for parameterisation of an experimental rig to test the reliability of MSC under various operating regimes.
- To simulate the electrical signals produced by the generator so an AC power supply can be used in the experimental rig.

The paper is organised as follows. Section III outlines the details of the drive train model constructed, Section IV details the drive train and converter response to various isolated and turbulent wind conditions, and Section V concludes the paper.

III. Drive Train Modelling

The drive train model needs to be relevant to the modern wind turbine industry. As discussed in Section II, the FRC of the PMSG is proving to be reliability critical and therefore is chosen for study. The state-of-the-art offshore wind turbines being constructed are now reaching 5-6 MW. However, there is not enough data freely available to be able to simulate this size in appropriate detail. Therefore a 2MW PMSG-FRC drive train was modelled.

The drive train model can be split into 7 sub-systems; rotor power extraction, drive train dynamics, generator, machine-side converter (MSC), DC link, turbine control and simulation details. This section details the key features of the model.

a. Rotor Power Extraction

The turbine power, P_t, is calculated as follows:

$$P_t = 0.5 C_p \rho \pi r^2 u^3 \quad (1)$$

Where C_p is the coefficient of performance, ρ is air density (kg/m^3), r is the rotor radius (m), and u is the wind speed (m/s).

C_p depends on the tip-speed ratio (λ) of the turbine and the blade pitch angle (β). The C_p, λ and β relationship is turbine specific but it is typical to use a numerical approximation (2, 3).

$$C_p = A_t\left(\frac{B_t}{\lambda_i} - C_t\beta - D_t\beta^{E_t} - F_t\right)e^{\frac{-G_t}{\lambda_i}} \quad (2)$$

$$\frac{1}{\lambda_i} = \frac{1}{\lambda + H_t\beta} - \frac{K_t}{\beta^3 + 1} \quad (3)$$

Where A_t - F_t, K_t are turbine specific constants.

The C_p has been plotted for an example turbine in Figure 1. The parameters are available in Table A in Appendix A.

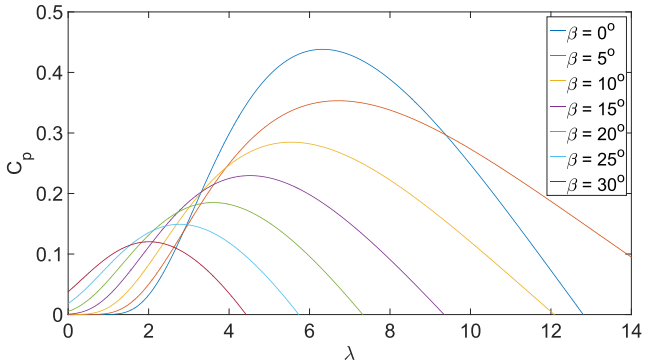

Figure 1: Example C_p-λ curves for turbine rotor with varying β.

λ is the ratio between turbine rotational speed (ω_t) and u and is calculated using (4).

$$\lambda = \frac{\omega_t r}{u} \quad (4)$$

The resultant turbine torque (T_t) is calculated using (5).

$$T_t = \frac{P_t}{\omega_t} \quad (5)$$

Figure 1 summarises the rotor power extraction model.

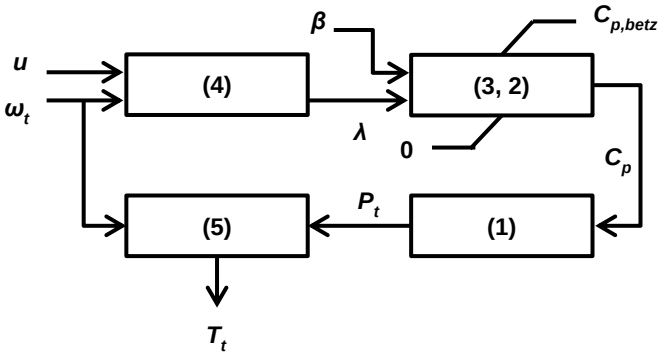

Figure 1: Summary of rotor power extraction model.

b. Drive Train Dynamics

The T_t extracted from the wind is applied to the drive shaft. As a direct drive turbine was modelled the drive shaft is connected directly to the generator without a gearbox. The drive train can be modelled as a mechanical mass-spring-damper system which dynamically impacts the resulting mechanical torque (T_m) applied to the generator.

Ideally the higher the order of the mechanical system (number of masses and connections), the more accurately the dynamics will be modelled. However, the higher order the modelling, the more computationally expensive the calculations become. Therefore a compromise must be made. In general, drive train models for direct-drive PMSG turbines come in either lumped-mass or 2-mass models. A 3-mass model would be preferred as all fundamental torque oscillations that may interact with the electrical transients can be modelled [12] but no data was found and therefore a 2-mass model was used, as represented in Figure 3.

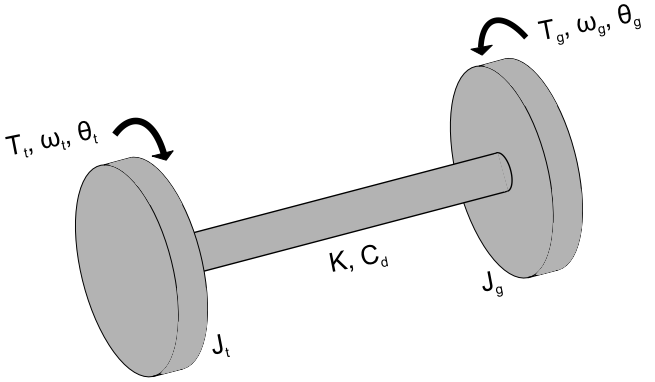

Figure 3: 2-mass model of wind turbine drive train.

J_t, J_g are the moments of inertia of the turbine and generator respectively (kgm^2), ω_g is the rotational speed of the generator (rad/s), Θ_t, Θ_g are the rotational displacements of the turbine and generator respectively (rad), C_d is the shaft damping coefficient (Nms/rad), K is the shaft stiffness (Nm/rad) and T_g is the electromagnetic torque (Nm).

The 2-mass model is described by the following matrix of equations of motion (1.7) [13].

$$\begin{bmatrix} J_t & 0 \\ 0 & J_g \end{bmatrix} \begin{Bmatrix} \alpha_t \\ \alpha_g \end{Bmatrix} + \begin{bmatrix} C_d & -C_d \\ -C_d & C_d \end{bmatrix} \begin{Bmatrix} \omega_t \\ \omega_g \end{Bmatrix} + \begin{bmatrix} K & -K \\ K & -K \end{bmatrix} \begin{Bmatrix} \theta_t \\ \theta_g \end{Bmatrix} = \begin{Bmatrix} T_t \\ T_g \end{Bmatrix} \quad (6)$$

Where α_t, α_g are the rotational accelerations of the turbine and generator respectively (rad/s^2). This matrix can be expanded to provide a number of equations of motion to be solved numerically (7-11).

$$T'_m = (\omega_t - \omega_g)C_d + (\theta_t - \theta_g)K \quad (7)$$

$$\alpha_t = \frac{T_t - T'_m}{J_t} \quad (8)$$

$$\alpha_g = \frac{T'_m - T_g}{J_g} \quad (9)$$

$$\omega = \int \alpha(t)dt \quad (10)$$

$$\theta = \int \omega(t)dt \quad (11)$$

Where T'_m is the resultant torque from the shaft damping and shaft stiffness (Nm).

As the drive train model was solved discretely, the integrations were performed discretely. Figure 4 details the block diagram of the drive train dynamics.

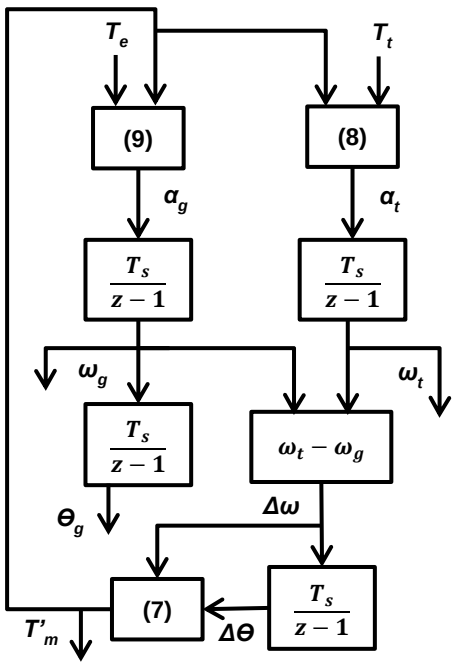

Figure 4: Block diagram of drive train dynamics. T_s is the sample time (s).

c. Generator

The generator used was a non-salient PMSG and was modelled as a 2nd order generator in the *dq0* reference frame [12]. The mechanical component was modelled with the torque swing equation to simulate the acceleration due to difference between mechanical and electrical torque (9).

The generator used for the simulation was Simulink's inbuilt *SimPowerSystems* 'permanent magnet synchronous machine (PMSM)'. The generator parameters can be found in Appendix A.

d. MSC

In a typical wind turbine the converter is comprised of a back-to-back rectifier/inverter. The rectifier acts as the MSC and the inverter acts as the grid-side converter (GSC). The role of the MSC and GSC differs depending on control strategy but the MSC typically controls the speed of the wind turbine for optimum power production whilst the GSC maintains the DC link voltage and controls power extraction to the grid.

Due to turbine speed variation the MSC experiences a more varied operating profile compared to the fixed frequency GSC. The MSC is consequently of greater interest for reliability analysis. Therefore, only the MSC is modelled fully and the GSC is replaced with a constant voltage source to maintain the DC link (Section III.e).

The MSC was modelled as a 2-level IGBT-diode pair active rectifier. Simulink's inbuilt *SimPowerSystems 'Universal Bridge'* was used and the *'Power Electronic Device'* was set to *'IGBT/ Diodes'*.

The MSC parameters were based on the power modules found in the SEMIKRON SKSB1090GD69/11-MAPB stacks [14]. These stacks have SKiiP1513GB172-3DWV3 half-bridge modules and their data can be found in [15]. The parameters used are detailed in Appendix A.

The current across the devices is taken from the *'Universal Bridge'* module. This current output is split across diode and IGBT and can be determined by the sign convention outlined in [16]. This current must also be halved to determine the current throughput of each power module as 2 parallel stacks are required to provide the power rating for the turbine [17]. Figure 5 outlines the conversion from converter output to device currents. I_{sw2} is the current on one switch from the Simulink model. The positive values of I_{sw2} give the current on the IGBT (I_{IGBT2}) and the negative values give the diode current (I_{Diode2}). These are then halved to give the current in each stack.

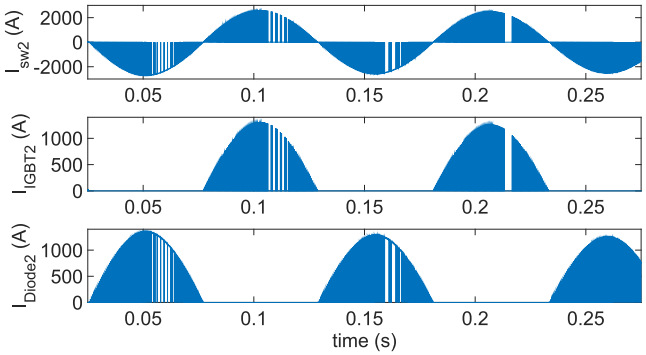

Figure 5: Current output from converter.

To summarise, the MSC of the drive train is modelled as a 2-level IGBT rectifier using Simulink's *'Universal Bridge'* module. The MSC is based on 2 parallel SEMIKRON RE stacks with the model parameters taken from the SKiiP1513GB172-3DWV3 half-bridge.

e. DC Link

As discussed in Section III.d the GSC has been replaced with a fixed voltage supply. Typically for a low voltage PSMG (~690V) the DC link voltage (V_{dc}) is maintained at anywhere between 1000-1300V [12, 18]. Based on the RE stack detailed in Section III.d and the PWM strategy chosen in Section III.f, the DC-link was set to 1150V_{dc} (±575V_{dc}).

f. Turbine Control

Power extraction is controlled in 2 ways; maximum power point tracking (MPPT) for below rated speed, and active pitch control for above rated speed.

MPPT

MPPT is achieved by maintaining C_p at its maximum ($C_{p,max}$) via the an optimum λ (λ_{opt}) (peak in Figure 1) when below rated wind speed. The ω_t must be controlled to maintain this λ_{opt} (12).

$$\omega_{t,opt(u)} = \frac{u\lambda_{opt}}{r} \qquad (12)$$

Where $\omega_{t,opt(u)}$ is the optimum turbine rotational speed at a given wind speed (rad/s).

$\omega_{t,opt(u)}$ is achieved using torque control. By varying the T_g, the turbine can accelerate or decelerate (9). To calculate the torque required at a given wind speed ($T_{ref(u)}$), the equation for turbine power (1) and torque (5) can be used to determine a relationship between $\omega_{t,opt(u)}$ and $T_{ref(u)}$ (13-15).

$$P_{t,max} = 0.5C_{p,max}\rho\pi r^2\left(\frac{r}{\lambda_{opt}}\right)^3{\omega_{t,opt(u)}}^3 \qquad (13)$$

$$K_{MPPT} = 0.5C_{p,max}\rho\pi r^2\left(\frac{r}{\lambda_{opt}}\right)^3 \qquad (14)$$

$$T_{ref(u)} = K_{MPPT}\omega_{t,opt(u)}{}^2 \quad (15)$$

Where K_{MPPT} *is a* turbine specific constant (kgm^2).

As u is not measured in this control strategy, $\omega_{t,opt}$ is unknown at any given point. Instead T_{ref} is calculated using ω_t (16). If $\omega_t \neq \omega_{t,opt}$ then ω_t will continue to change, changing T_{ref} until steady state is reached.

$$T_{ref} = K_{MPPT}\omega_t{}^2 \quad (16)$$

This T_{ref} is achieved by varying the current demanded of the generator. For this control the *d,q* currents ($I_{d,q}$) are used in a *dq0* control strategy (17, 18), with the $I_{d,q}$ calculated from the stator currents (I_{abc}) via a Park transform.

$$I_{d,ref} = 0 \quad (17)$$

$$I_{q,ref} = \frac{2p}{3\varphi}T_{ref} \quad (18)$$

Where $I_{d,qref}$ are the reference *d,q* currents (A), p is the number of generator poles, and φ is the permanent magnet flux linkage (Vs).

$I_{d,ref}$ is maintained at zero as it relates to magnetisation which is not required for a PMSG machine. Holding the magnetisation current at zero also minimises resistive losses [19].

These currents are achieved by applying a controlled voltage on the generator terminals using the MSC. Again the voltages are processed in the *d,q* reference frame ($V_{d,q}$). $V_{d,q}$ are determined by using independent Proportional-Integral (PI) controllers that use the error between $I_{d,q}$ and $I_{d,q,ref}$ to produce $V_{d,q}$ errors. These errors are added to the known generator voltages (impedance and armature voltages) to produce the required terminal voltages for the generator ($V_{d,q,ref}$) [12]. $V_{d,q,ref}$ is converted into the *abc* reference frame ($V_{abc,ref}$) via an inverse Park transform for use by the converter pulse width modulation strategy (PWM). Figure 6 details the *dq0*-control of the MSC.

r_s is the PMSG stator phase resistance (Ω), $L_{d,q}$ are the PMSG *d,q* armature inductances (H), and ω_e is the magnetic field rotational speed (rad/s) which calculated using (19).

$$\omega_e = \frac{p}{2}\omega_g \quad (19)$$

Where *p/2* is the number of pole pairs in the generator.

The PWM converts the modulated $V_{abc,ref}$ (between -1 and 1) (V_m) into a switching pattern for the IGBTs in order to produce the 3-phase converter output voltage ($V_{c,abc}$). In this case a sine-wave PWM (SPWM) strategy was chosen and implemented using the '*PWM Generator (2-level)*' Simulink block. The carrier mode of operation was set to '*synchronised*' to ensure the carrier frequency remained synchronised to reference signal. The carrier/reference ratio ($R_{c/r}$) can be found in Appendix A.

As the SPWM was used, V_m was calculated using (20).

$$V_m = \frac{2}{V_{dc}}V_{abc,ref} \quad (20)$$

To summarise, MPPT was achieved by using torque control via *dq0* vector control of the MSC. SPWM was used to convert the reference voltage signals into switching signals for the IGBTs.

Pitch Control

Pitch control limits power extraction by pitching the blades away from the optimum angle, reducing the turbine's C_p (Figure 1). This pitching occurs above the rated wind speed.

There are a number of control methods available for pitch control [20]. For this work the difference in ω_t and rated ω_t ($\omega_{t,rat}$) was used with a PI-controller to produce a β error (β_{err}) (Figure 7.a). In reality the β-ω_t relationship is not linear but the approximation was found to be adequate for turbine control.

β_{err} is added to the current β to produce a reference β (β_{ref}) and applied to the pitch actuator (Figure 7.b). The pitch actuator is modelled as a 1st order dynamic

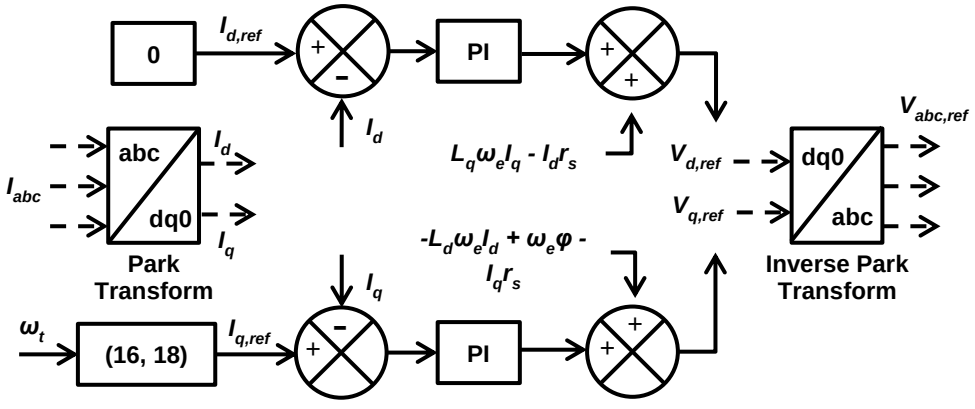

Figure 6: Schematic of machine-side controller.

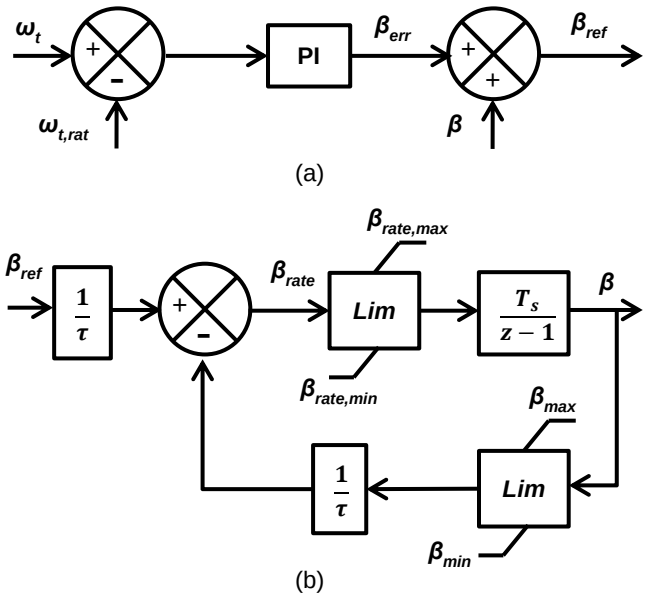

Figure 7: (a) Pitch controller and (b) pitch actuator block diagrams. τ is the actuator time constant (s).

system as found in [21] with limits on β and the rate of change of β (β_{rate}). These values can be found in Appendix A.

g. Simulation Configuration

The Simulink simulation is discretized using the Tustin and Backward Euler method with a T_s of $5x10^{-6}$s. As the simulation was discretized purely resistive snubbers were needed to simulate having no snubbers in the '*Universal Bridge*' [22]. To do this, the default snubber parameters in the *'Universal Bridge'* were used (Appendix A).

To tune the PI controllers a simpler model of the drive train was constructed. The PMSG was modelled as found in [23] and the MSC was omitted. Simulink's '*Tune*' graphical user interface in the PI controllers was used to tune the controllers before the PI parameters were applied to the more complex model. These parameters can be found in Appendix A.

h. Drive Train Model Summary

The drive train model consists of the following key features:

- Modelled as a direct-drive 2MW wind turbine.
- Mechanical drive train modelled as a 2-mass model.
- 2nd order non-salient PMSG modelled in the *dq0* reference frame
- FRC with MSC based on SEMIKRON RE stacks.
- GSC modelled as an ideal DC link.
- Turbine controlled using ω_t as the reference signal.
- MPPT achieved using *dq0* vector control.
- MSC switching achieved using SPWM.
- Power limited above rated wind speed using active pitch control and a 1st order dynamic system actuator model.

IV. Results

This section outlines the drive train model response to a reduction in wind speed in the MPPT operating region (Section IV.a), a ramp up in wind speed from MPPT to rated operation (Section IV.b), and a

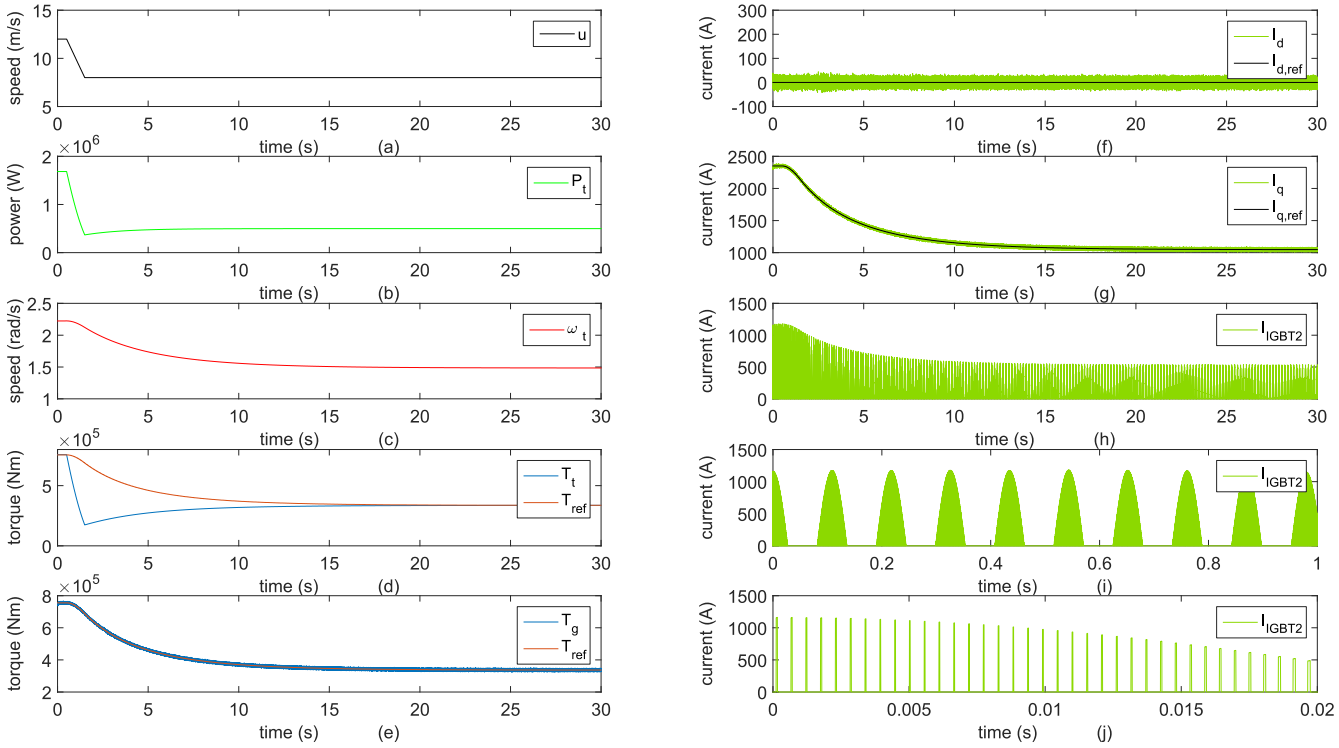

Figure 8: Turbine Response to reduction in wind speed: (a) wind speed, (b) turbine power, (c) turbine speed, (d) turbine torque, (e) generator torque, (f, g) generator *d,q* current and (h-j) IGBT current.

turbulent wind speed input (Section IV.c).

a. Wind Speed Reduction in MPPT Operating Region

Figure 8 details the turbine response to a reduction in wind speed from 12m/s to 8m/s in the MPPT operating region. Figure 8.d-g shows that the turbine model successfully responds to the variation in wind speed.

This turbine response is dictated by the change in ω_t (Figure 8.c). As the ω_t is influenced by the turbine inertia the turbine response is much smoother than the sudden change in wind speed (ω_t reaches steady state ~22s after the wind speed event has finished).

The I_q response follows the ω_t response very closely with negligible overshoot (Figure 8.g) and I_d remains at approximately 0A (Figure 8.f). The negligible overshoot on the I_q response can be attributed to the slow turbine response leading to small I_q errors over time. Furthermore, by following the ω_t response, the current throughput is smoothed and maintains a higher current than if the current was directly derived from the wind speed. Therefore, these results indicate that the drive train dynamics cannot be neglected when determining the current throughput of the converter.

There is noise on both I_d and I_q signals (Figure 8 f,g) due to the harmonics generated by the MSC. This noise is small (~1.9% of rated peak current) but further investigation is required into their impact on ΔT_j before the noise can be deemed negligible.

Figure 8.h-j shows the complexity of the current throughput of the power modules in the MSC. The current varies significantly at various frequencies due to the current demanded of the generator (h), the direction of the current (i), and the switching pattern of the IGBTs (j). This large amount of complexity could not be directly derived from the present wind speed.

The turbine responds successfully to this reduction in wind speed in the MPPT region. The I_q response is dictated by the ω_t response indicating that the drive train dynamics cannot be neglected. The current noise due to harmonics is small, but further investigation is required to determine if it can be neglected. The current in the power modules is complex and cannot be directly derived from the current wind speed.

b. Wind Speed Ramp from MPPT to Rated Operating Region

Figure 9 details the turbine response to a ramp in wind speed from 11m/s to 13.5m/s; from the MPPT to rated operating region. The turbine rated wind speed (u_{rat}) is 12.7m/s. After the disturbance the turbine successfully reaches steady state at the rated turbine power ($P_{t,rat}$) (b) and $\omega_{t,rat}$ (c).

The turbine response is slower than in Section IV.a and is more complex. Figure 9.d shows that the turbine initially starts in the torque control region until $\omega_{t,rat}$ is reached, where T_{ref} remains constant and the pitch controller takes over (Figure 9.e). However due to pitch controller overshoot the ω_t drops below rated again, activating the torque control again. Therefore interaction between the controllers occurs and the current on the device has increased variation (Figure

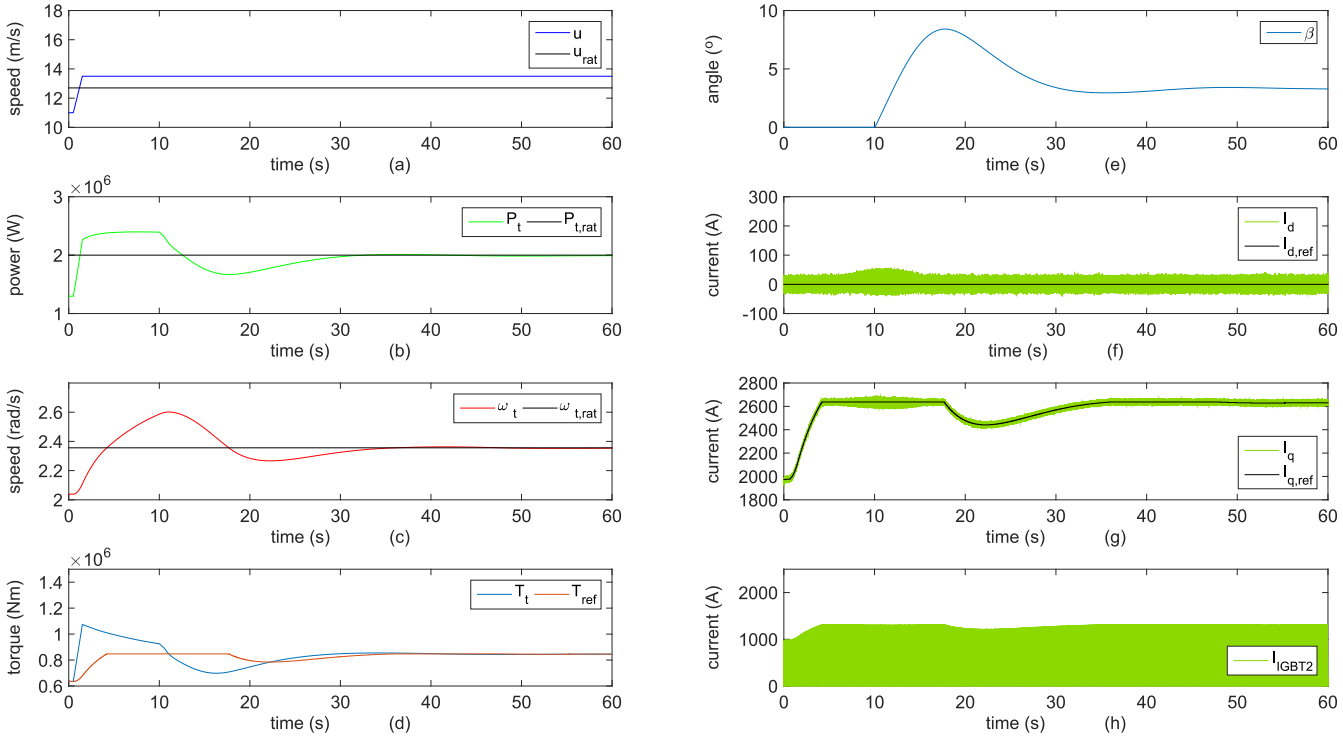

Figure 9: Turbine response to wind speed ramp from 11 to 13.5m/s: (a) wind speed, (b) turbine power, (c) turbine speed, (d) turbine torque, (e) pitch angle, (f, g) generator d,q current and (h) IGBT current.

9.h). This may increase ΔT_j, affecting device lifetime.

The interaction between controllers may be avoided by disabling the torque controller when the pitch controller is active, but the response of the turbine would be slower as ω_t would decrease even further.

Figures 9.f,g show an increase in noise in the $I_{d,q}$ currents and occurs when the ω_t is higher than rated. This noise increase is due to the increasing ω_g, causing changes in the generator voltage which must be matched by the converter output voltage Whether this impacts converter lifetime needs further investigation with thermal modelling and physical testing but it does indicate an increase in converter current loading due to the pitch controller response.

The turbine responds successfully in both MPPT and rated operating regions. The pitch controller overshoot causes interaction between the controllers and potentially increases the thermal loading on the converter power modules. The increased ω_t also increases the noise on the current signals.

c. Turbulent Wind Speed Profile

Figure 10 details the current response of one IGBT in the MSC to a turbulent wind speed input of 60s. The wind speed was simulated using the normal turbulence model (21) [24] with a mean hub wind speed (V_{hub}) of 8m/s and turbulence intensity (I_{ref}) of 0.12. The wind speeds were produced for each second and the intermediate wind speeds linearly interpolated.

$$\sigma_1 = I_{ref}(0.75V_{hub} + 5.6) \qquad (20)$$

Where σ_1 is the turbulence standard deviation.

There a number of points to highlight from Figure 10:

- There are delays in the peaks in wind speed and peaks in current, but the response appears much faster than in Figure 8. This is as the turbine cannot reach its maximum operating condition as the wind speed changes too quickly. If the wind speed remained at the same wind speed for longer the currents would be higher.
- The highest wind speed |1| does not correspond to the highest current |2|. As the wind does not remain at |1|, the wind does not have the power to speed up the turbine sufficiently to reach optimum operating conditions. In contrast the lower but sustained wind speed before |2| allows the turbine get closer to the optimum operating point.
- The wind speeds |3| and |4| are similar, but give different current responses. The current at |3| is higher as the wind speed prior to this peak is higher than the wind speeds before |4|. The wind speed history is just as important as the present wind speed in determining the current throughput of the converter.

The turbulent wind speed has highlighted that the current in the converter cannot be directly derived from the present wind speed, and the dynamics of the drive train and the wind speed history must be considered.

d. Summary

The turbine responded successfully to both isolated wind speed scenarios. The turbine response is dominated by the response in ω_t which is limited by the drive train dynamics. This aspect smooths the current response of the turbine compared to if the current was derived directly from the wind speed. The current was also affected by noise from the MSC which was exasperated by the rise in ω_t above rated. The pitch controller overshoot causes interaction between the controllers and potentially increases the thermal loading on the converter power modules due to greater variation in current. The turbulent wind speed has highlighted the need to also consider the wind speed history in deriving the current throughput. Therefore the power module current throughput is complex and cannot be directly derived from the current wind speed but requires a drive train model.

As the ΔT_j is closely related to the converter current

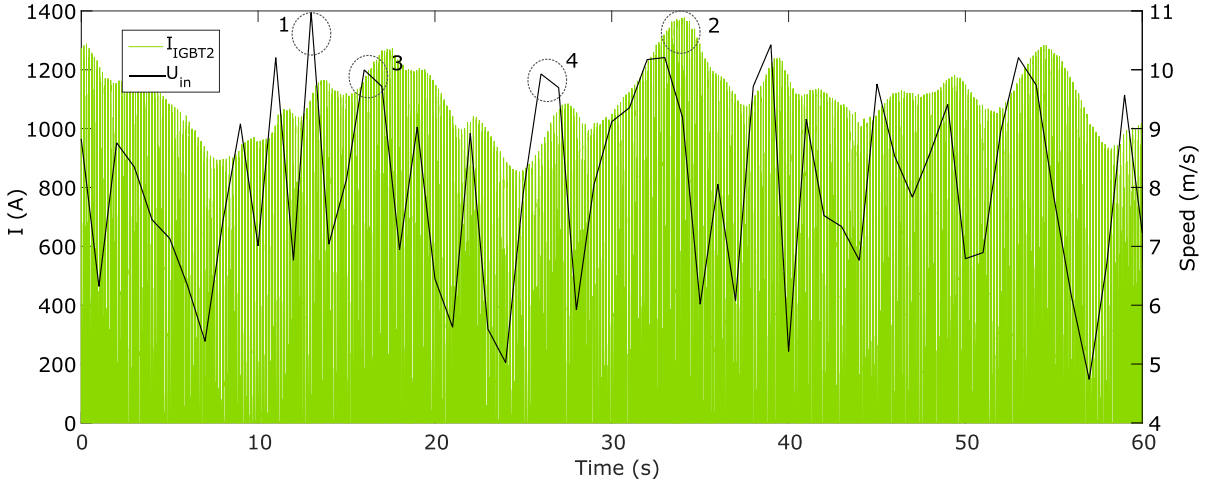

Figure 10: IGBT current response to turbulent wind speed.

[25], the characterisation of thermal loading on the devices in the converter requires this complex drive train modelling. However in these simulations it has been assumed that all aspects of the current profile, including noise due to harmonics, are important for thermal loading and damage accumulation on the converter power modules. This assumption requires further investigation through the thermal modelling of the power modules in question and experimental validation as mentioned in Section II. This investigation can determine if aspects of the drive train can be simplified for long-term simulation.

V. Conclusion

Maintaining high reliability of offshore wind turbines is essential for reducing the LCoE of offshore wind. It has been established that FRC reliability is critical for PMSG turbines and requires investigation into the reasons for their high failure rate. To address this, an experimental rig is being designed which will apply the power converter under turbine operating conditions.

Prior to this experimental work the potentially harmful operating conditions need to be characterised. The experimental rig also needs parameterisation. This paper outlines a computer simulation of a turbine drive train that is used to meet these objectives.

The drive train model consists of a 2MW FRC PMSG turbine with MPPT achieved using torque control and rated operation maintained using an active pitch system. with detailed models for rotor power extraction, drive train dynamics, generator, MSC, DC link and turbine control.

The drive train model was subjected to a reduction in wind speed in the MPPT operating region, a ramp up in wind speed from MPPT to rated operation, and a turbulent wind speed input. The turbine responded successfully to both isolated wind speed scenarios. The turbine response is dominated by the response in ω_t, smoothing the current. The current was also affected by noise from the MSC. Pitch controller overshoot caused interaction between the controllers, potentially increasing the thermal loading on the converter power modules. The turbulent wind speed highlighted the need to also consider wind speed history and drive train dynamics.

With this converter current response detailed simulation and analysis of the thermal loading on the power modules is possible. The turbine can now also be emulated using the AC power supply in the experimental rig to provide realistic operating conditions for the MSC power modules.

References

[1]. E. Davey and A. Nimmo. *Offshore Wind Cost Reduction, Pathways Study*. 2012 [cited 2015 07/10]; Available from: http://www.thecrownestate.co.uk/energy-and-infrastructure/offshore-wind-energy/working-with-us/strategic-workstreams/cost-reduction-study/.

[2]. W. Musial and B. Ram. *Large-Scale Offshore Wind Power in the United States: Assessment of Opportunities and Barriers*. 2010 [cited 2015 07/10]; Available from: http://www.nrel.gov/docs/fy10osti/40745.pdf.

[3]. F. Spinato, et al., *Reliability of wind turbine subassemblies.* Renewable Power Generation, IET, 2009. 3(4): p. 387-401.

[4]. J. Carroll, A. McDonald, and D. McMillan, *Failure rate, repair time and unscheduled O&M cost analysis of offshore wind turbines.* Wind Energy, 2015.

[5]. J. Carroll, A. McDonald, and D. McMillan, *Reliability Comparison of Wind Turbines With DFIG and PMG Drive Trains.* IEEE Transactions on Energy Conversion, 2015. 30(2): p. 663.

[6]. H. Wang, K. Ma, and F. Blaabjerg. *Design for reliability of power electronic systems*. in *IECON 2012 - 38th Annual Conference of IEEE Industrial Electronics*. 2012.

[7]. G. Van Bussel and M. Zaaijer. *Reliability, availability and maintenance aspects of large-scale offshore wind farms, a concepts study*. in *Proceedings of MAREC*. 2001.

[8]. S.S. Gjerde and T.M. Undeland. *The best suitable multilevel converters for offshore wind power generators without transformers*. in *International Power Electronics Conference (IPEC)*. 2010.

[9]. A. Sannino, H. Breder, and E.K. Nielsen. *Reliability of Collection Grids for Large Offshore Wind Parks*. in *International Conference on Probabilistic Methods Applied to Power Systems*. 2006.

[10]. K. Ma, et al., *Thermal loading and lifetime estimation for power device considering mission profiles in wind power converter.* IEEE Transactions on Power Electronics, 2015. 30(2): p. 590-602.

[11]. T. Burton, et al., *Wind energy handbook*. 2001: John Wiley & Sons.

[12]. O. Anaya-Lara, et al., *Wind energy generation: modelling and control*. 2011: John Wiley & Sons.

[13]. S.S. Rao and F.F. Yap, *Mechanical vibrations*. Vol. 4. 1995: Addison-Wesley Reading.

[14]. SEMIKRON. *SKS B1 090 GD 69/11 - MA PB Datasheet*. 2013 [cited 2015 13/10]; Available from: http://www.semikron.com/dl/service-support/downloads/download/semikron-datasheet-sks-b1-090-gd-69-11-ma-pb-08800136.

[15]. SEMIKRON. *SKiiP 1513 GB172-3DW V3 Datasheet*. 2014 [cited 2015 13/10]; Available from: http://www.semikron.com/dl/service-support/downloads/download/semikron-datasheet-skiip-1513-gb172-3dw-v3-20451120.

[16]. MathWorks. *Universal Bridge*. 2015 [cited 2015 07/10]; Available from: http://uk.mathworks.com/help/physmod/sps/powersys/ref/universalbridge.html.

[17]. SEMIKRON. *Optimised Converter for Solar and Wind*. 2014 [cited 2015/ 14/09]; Available from: http://www.semikron.com/dl/service-

support/downloads/download/semikron-flyer-semistackre-2014-04-08.
[18]. SEMIKRON. *Semistack RE Datasheets*. 2015 [cited 2015 14/09]; Available from: http://www.semikron.com/products/product-classes/stacks.html#presets/product-line=semistack-re/.
[19]. M. Chinchilla, S. Arnaltes, and J.C. Burgos, *Control of permanent-magnet generators applied to variable-speed wind-energy systems connected to the grid.* IEEE Transactions on Energy Conversion, 2006. 21(1): p. 130-135.
[20]. J. Zhang, et al. *Pitch angle control for variable speed wind turbines*. in *Third International Conference on Electric Utility Deregulation and Restructuring and Power Technologies*. 2008.
[21]. F.D. Bianchi, H. De Battista, and R.J. Mantz, *Wind turbine control systems: principles, modelling and gain scheduling design*. 2006: Springer Science & Business Media.
[22]. Mathworks. *Universal Bridge*. 2015 [cited 2015 14/09]; Available from: http://uk.mathworks.com/help/physmod/sps/powersys/ref/universalbridge.html.
[23]. B. Wu, et al., *Power conversion and control of wind energy systems*. 2011: John Wiley & Sons.
[24]. I.E. C, *Wind turbines-Part 1: Design requirements*, 2005: IEC 61400-1:2005(E).
[25]. P. Wyllie, *Electrothermal Modelling for Doubly Fed Induction Generator Converter Reliability in Wind Power*, 2014, Durham University Thesis.
[26]. J. Slootweg, H. Polinder, and W. Kling. *Dynamic modelling of a wind turbine with doubly fed induction generator*. in *Power Engineering Society Summer Meeting*. 2001.
[27]. B. Wu, Y. Lang, and S. Kouro, *Power conversion and control of wind energy systems*, 2011, John Wiley and Sons, Inc., NJ, USA.
[28]. V. Akhmatov, *Analysis of dynamic behaviour of electric power systems with large amount of wind power*, 2003, Electric Power Engineering, Ørsted-DTU, Technical University of Denmark Thesis.
[29]. J.-B. Sim, et al., *Ride-through of PMSG wind power system under the distorted and unbalanced grid voltage dips.* Journal of Electrical Engineering & Technology, 2012. 7(6): p. 898-904.
[30]. F.M. Gonzalez-Longatt, P. Wall, and V. Terzija. *A simplified model for dynamic behavior of permanent magnet synchronous generator for direct drive wind turbines*. in *2011 IEEE Trondheim PowerTech*. 2011.

Appendix A

Parameter	Value	Reference
A_t	0.22	[26]
B_t	116	[26]
C_t	0.4	[26]
D_t	0	[26]
E_t	0	[26]
F_t	5	[26]
G_t	12.5	[26]
H_t	0.08	[26]
K_t	0.035	[26]
$P_{t,rat}$	2.0MW	[27]
$\omega_{t,rat}$	22.5rpm	[27]
λ_{opt}	6.3	-
$C_{p,max}$	0.438	-
$C_{p,betz}$	0.593	[12]
u_{rat}	12.7m/s	-
r	34m	-
ρ	1.225kg/m^3	[12]
J_t	2.92x10^6 kg/m^2	[28]
J_g	200kg/m^2	[29]
K	4.0x10^7 Nm/rad	[28]
C_d	6.72x10^6 Nms/rad	-
R_s	8.21x10^{-4} Ω	[23]
L_d	1.5731H	[23]
p	52	[23]
φ	8.24Vs (peak)	[23]
V_f	0.95	[15]
V_{fd}	1.9V	[15]
T_f	0	-
T_t	0	-
R_{on}	1.2mΩ	[15]
V_{dc}	1150V	-
R_{snub}	1x10^5 Ω	[16]
C_{snub}	*inf* F	[16]
$R_{c/r}$	200	-
β_{max}	45°	SG
β_{min}	0°	SG
$\beta_{rate,max}$	8°/s	SG
$\beta_{rate,min}$	-8°/s	SG
τ	0.5s	[30]
P_p	3.357	-
I_p	0.012	-
P_{id}	-0.148	-
I_{id}	-5.377	-
P_{iq}	-0.155	-
I_{iq}	-2.689	-

Table A: Drive train parameters.

V_f is the IGBT forward voltage (V), V_{fd} is the diode forward voltage (V), $T_{f,t}$ is the IGBT fall time and tail time respectively (s), R_{on} is the IGBT on state slope resistance (Ω) is. R_{snub} is the snubber resistance (Ω), C_{snub} is the snubber capacitance (F), $P_{p,id,iq}$ are the proportional gains for the pitch, I_d and I_q controllers respectively, and $I_{p,id,iq}$ are the integral gains for the pitch, I_d and I_q controllers respectively.

Those labelled 'SG' are from the exemplar wind turbine from the Supergen wind hub: http://www.supergen-wind.org.uk/

Evaluation of Synthetic Wind Speed Time Series for Reliability Analysis of Offshore Wind Farms

C.J. Smith[a], C.J. Crabtree[a], P.C. Matthews[a]

[a]Energy Group, School of Engineering and Computing Sciences, Durham University

I. Abstract

A method for synthesising wind speed time series (WSTS) from limited data is required that can be used for reliability examination of wind farms and maintenance strategies for a range of wind speed scenarios. Key characteristics of the wind resource need to be captured, including energy availability and maintenance weather windows. 4 WSTS simulators were used to produce synthetic WSTS based on benchmark data from a meteorological mast data at the offshore Egmond aan Zee wind farm in the Netherlands.

These synthetic WSTS were compared with test criteria to determine their suitability for reliability analysis. This included comparing the synthetic WSTS to the benchmark data in terms of the energy availability in the wind and from a typical turbine, residence time at wind speeds, number of transitions between 1m/s wind speed bins, replication of seasonal characteristics including weather windows, and underlying statistical properties.

Based on the chosen criteria, the most appropriate WSTS simulator was the modified Markov process. However, no modelling technique performed best against all criteria and none capture the auto-correlation function (ACF) as closely as desired. Therefore, there is scope for a more advanced technique for wind speed modelling for reliability analysis which combines the best aspects of the models used in this work.

Keywords – Wind speed time series, reliability analysis, weather windows, evaluation criteria.

II. Introduction

To meet EU renewable energy targets for 2020 and beyond, the Levelised Cost of Energy (LCoE) of offshore wind needs to be reduced from the current £140/MWh to below £100/MWh [1]. As Operation and Maintenance (O&M) accounts for around 30% of LCoE [2], researchers have carried out reliability studies on offshore wind to explore the root causes of these costs.

A unique characteristic of wind generation that impacts O&M is the stochastic nature of the fuel. This adds complexity to turbine operation and impacts the available maintenance opportunities, known as weather windows [3]. A weather window is defined as a point in time where a maintenance team could be dispatched to repair a component as the wind speed is below a threshold for a sufficiently long time period to carry out the repair (Figure 1).

Weather windows are particularly critical for offshore O&M due the higher sustained wind speeds leading to fewer opportunities for maintenance. This is compounded by longer lead times due to the large distances from shore. As such there is a need to ensure that these weather windows are accurately represented in O&M research.

The wind resource also adds uncertainty to the expected loss of generation revenue during turbine downtime. Therefore reliability studies need to

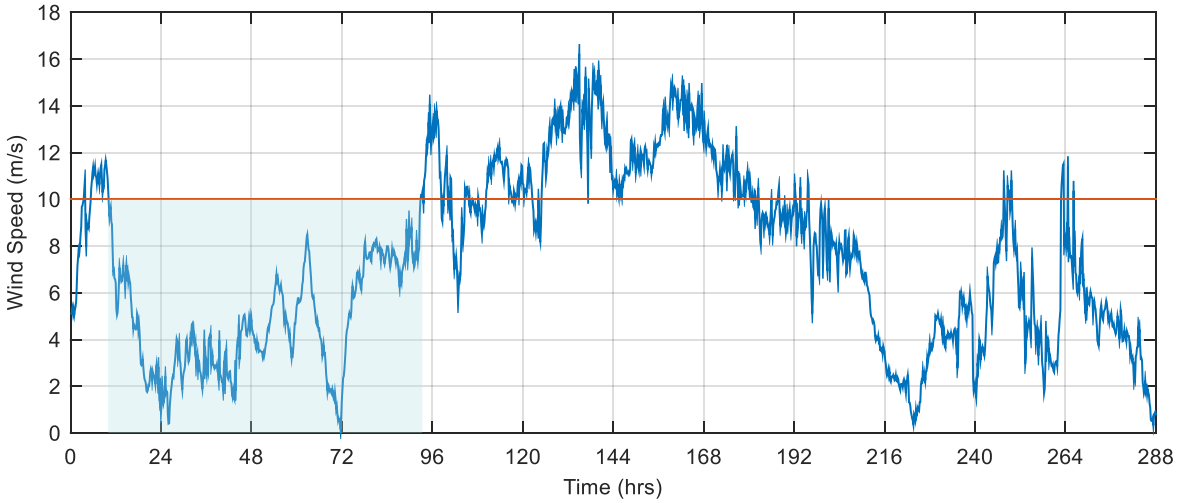

Figure 1: Example of a weather window. The weather window (shaded area) is the only time where the wind speed is below the threshold (red line) for long enough to carry out the repair.

accurately capture the elements of the wind resource that impact turbine and farm O&M.

To carry out this reliability analysis a site specific wind speed dataset for the lifetime of the farm is essential. Typically this data is collected for a year prior to turbine construction using a meteorological mast, with future data collection affected due to farm wake effects. Therefore a method for synthesising wind speed time series (WSTS) from limited data is required.

The use of synthetic WSTS facilitates detailed reliability studies and maintenance strategy evaluation under a range of wind speed scenarios. For example, a proposed maintenance strategy could be evaluated against a range of scenarios using a Monte-Carlo simulation where the weather windows are not fixed each time, but their occurrence is allowed to vary randomly with a probability determined by the original recorded data. Due to the complexity of wind speed data this is not a trivial task and all characteristics of the wind speed may not be captured using one modelling technique. To ensure a suitable model is chosen a list of reliability analysis specific criteria is needed.

This paper formalises the desirable attributes of synthetic WSTS for use in reliability analysis of offshore wind farms by formulating a list of key criteria. WSTS simulators are used to produce synthetic WSTS which are compared with these criteria to determine the most suitable simulator. From this work the following learning objectives are aimed to be fulfilled:

- To understand what characteristics of the wind speed are important for reliability analysis of offshore wind turbines.
- To provide a testing procedure for ensuring WSTS simulators for synthetic WSTS are fit for purpose.
- To determine the most promising modelling techniques of synthetic WSTS for reliability analysis.

The paper is organised as follows; Section III details past wind speed modelling techniques and why an evaluation criteria is needed, Section IV details the benchmark WSTS data used, the evaluation criteria developed and the wind speed simulators that will be evaluated including a new model methodology, Section V details the results of this evaluation, and Section V concludes the paper.

III. Past Wind Speed Modelling Techniques

A number of wind farm reliability studies have aimed to capture the stochastic nature of the wind resource, with a particular focus on a site's mean wind speed. As local wind speed data for a particular site is limited by the length of time a meteorological mast has been installed at the site, these long term reliability studies have required the wind speed to be simulated based on this limited data. This modelling has been carried out in a number of ways:

- Mathematical expectation calculations based on probability distribution functions [4-10].
- WSTS produced using hindcasting [11].
- WSTS produced by randomly sampling from probability distributions [12-14].
- WSTS produced from Markov processes [15].
- WSTS produced using an auto-regressive moving average (ARMA) model [16-18].

By far the most common of these methods is the use of probability distribution functions for expectation calculations [4-10]. This calculation uses a probability distribution function to represent the wind resource at a site. This is typically using the Weibull distribution [8, 9], or a special case of the distribution with a shape factor of 2 known as the Rayleigh distribution [4, 5, 7, 10]. This probability distribution function can also be simplified to a smaller number of points to provide simpler computation [6]. These methods are used to calculate the expected energy generated or power output, which are used to derive index values such as Availability and annual energy production (AEP). These methods can be used to quickly assess the performance of a wind farm configuration, but cannot be used to detail the effects of factors such as weather windows and maintenance delays. Therefore, this model type is not suitable for the reliability analysis that this research is targeting.

The production of WSTS is more appropriate for investigating these factors. For example, the use of a WSTS can more accurately represent the effect of a turbine failure by giving the range of impacts that may occur, along with their respective likelihood. This can give a confidence level in the energy production produced by the model. Therefore, the production of WSTS is of interest.

One way to generate this time series is to use hindcasting. This involves using the WSTS data available from the site in question directly in the model for producing WSTS for future years. The simplest method is use the original WSTS directly from an anemometer at a site [11] and repeat this data for each simulated year. Alternatively, trends in the data to predict the amplitude variation whilst maintaining the same seasonal variation. Hindcasting is a popular method in system adequacy studies for demand [19] and ensures that the data is realistic, but the stochastic element of the wind resource is not captured.

A common method used is to generate an average farm wind speed is to randomly sample from a probability distribution. Generally, this is done from a Weibull distribution [12-14]. A variation on this is done in [20], where the daily mean wind speed was produced by randomly sampling from a Weibull distribution, but the hourly wind speed is generated from a normal distribution using this mean daily wind

speed. By using random sampling from a distribution, it is ensured that the wind speeds generated are random and based on the site specific details. A large number of times series can be generated, which is required for Monte-Carlo simulation. However, whilst this method can be modified to allow for seasonal variations, it is difficult to include short term trends such as weather windows. These short term trends are important for forecasting to allow accurate maintenance dispatch characteristics.

A more novel approach is the use of a continuous Markov process to generate the WSTS [15]. This method uses the transitions between wind speeds within a real time series to dictate the likelihood of transitions occurring in the generated time series. This is then converted into transition times between states to give the time at a state before moving to the next state [21]. Like the random sampling from a probability density function, the use of probabilities retains the stochastic nature of the wind, but the integration of other characteristics such as seasonality is simpler. However, the calculation of transition rates is more complex, and the wind speed transitions in the model can only occur if they exist in the original data unless transition rate estimations are used.

Finally, analytical relationships derived from original wind speed data can be used. A common method used is known as ARMA. This was developed in [16] for reliability studies and has been used in subsequent work [17, 18]. These models can accurately replicate the original WSTS and be used to generate a number of time series. However, the accuracy of these methods are reliant on the quantity of data available. They also assume that the wind speed follows an analytical relationship across the year, rather than a probabilistic relationship. Whilst noise can be introduced to increase the stochastic characteristics, it still makes the wind speed synthesis predictable.

A number of the above methods are suitable for time series generation for Monte-Carlo simulation. Whilst each method has qualitative benefits and drawbacks that may determine which method is used, no work has been done to quantify the adequacy of these models for reliability analysis. For example factors such as energy available in the wind have not been considered when choosing the approach. This quantification is needed to justify the use of these wind speed models. This will become especially important if methods are introduced that are modifications of the above methods.

IV. Evaluation Strategy

This section outlines the field WSTS data used for benchmarking, the measurement criteria used to assess synthetic WSTS quality, and the WSTS models that are assessed.

a. Benchmark Data

To assess the quality of WSTS simulators, a field WSTS dataset is needed. The data was taken from the meteorological mast at the Egmond aan Zee offshore wind farm in the Netherlands [22]. The data has been validated by Mierij Meteo before it was made publicly available on the NoordzeeWind web pages [23].

Though there are a number of years of data they are not directly comparable. From July 2006 construction work began on the wind farm and soon afterwards the wind farm began operating. This has affected the wind speed readings from the direction of the wind farm due to wake effects. The directions that have been impacted are detailed in [24]. Therefore, for the purposes of this study only data from 01/07/2005-30/06/2006 inclusive was used.

The data reported is the raw 10-minute supervisory control and data acquisition (SCADA) average wind data at 3 heights (26, 70 and 116m) and on three booms facing north-east (NE), north-west (NW) and south (S). Depending on the wind direction each of these booms are shadowed by the mast at some point. Therefore to produce an accurate benchmark WSTS the data needed to be pre-processed.

The operator has recommended steps for derived wind speed data acquisition [25]. However there were a number of assumptions that have had to be made. The following steps were made to derive this wind speed:

1. The first step was to determine the derived wind direction in order to choose the correct boom to record the wind speed from. The derived wind direction is produced by averaging over two weather vanes for a given time stamp based on a reference wind direction (Table 1).
   The operator does not state which direction should be used as a reference so the NW boom was used. If the wind direction for the NW boom is missing then the other two vanes are checked. If no data is available or if one vane data point are used for averaging is unavailable the derived wind direction is labelled as missing. No statement has been made on what to do when data missing derived wind direction data. It has been assumed that the wind direction has not changed since the last healthy derived wind direction data point. If it is the first time step, a default of 180° is used.

Reference Wind Direction (D)	Derived D Vanes
$330° \leq D < 30°$	Average of NW & NE vanes
$30° \leq D < 90°$	Average of S & NW vanes
$90° \leq D < 150°$	Average of S & NE vanes
$150° \leq D < 210°$	Average of NW & NE vanes
$210° \leq D < 270°$	Average of NW & S vanes
$270° \leq D < 330°$	Average of NE & S vanes

Table 1: Weather vanes used for derived wind direction based on current wind direction.

Derived Wind Direction (D_d)	Anemometer
$0° \leq D_d < 120°$	NE cup anemometer
$120° \leq D_d < 240°$	S cup anemometer
$240° \leq D_d < 360°$	NW cup anemometer

Table 2: Cup anemometers used for derived wind speed based on derived wind direction

2. Using the derived wind direction, a derived wind speed can be produced. This wind speed is taken from the cup anemometer which is chosen from the current derived wind direction as detailed in Table 2.

There were some missing wind speed data points. The WSTS simulators used in this work require complete datasets and therefore the missing data was substituted rather than omitted.

A number of data cleaning methods were attempted but the following algorithm was found to provide the best results.

1. If the mean wind speed value from a different height was available the logarithmic height law (1) was used to estimate the wind speed at that time period.

$$U_z = \frac{ln\frac{z}{z_0}}{ln\frac{z}{z_{ref}}} U_{zref} \qquad (1)$$

Where U_Z is the wind speed (m/s) at the required height Z (m), Z_0 is the roughness length (m), and U_{Zref} is the wind speed (m/s) at the anemometer height Z_{ref} (m/s).

2. If both alternative wind speed heights are available, the alternative height data with the highest correlation coefficient to the healthy height data in question was used.
3. If no alternative data was available but the data point is isolated, the value was linearly interpolated between previous and future data points at that the height in question.
4. If no alternative data was available as a reference and there were a large number of corresponding missing data points, data from another year was substituted in. This only represented 0.75% of the data.

Following this procedure a cleaned derived benchmark WSTS was produced at all 3 boom heights. For this study the data at 70m was used at this had the highest data recovery rate before cleaning and is the hub height of the wind turbines found at the Egmond aan Zee wind farm. Figure 2 displays this benchmark WSTS.

To note a key assumption of using this data is that this one year is representative of the wind speed for all years the wind farm will be operating. In order to produce more data measure-correlate-predict (MCP) could be implemented. MCP is the process of using past data from nearby meteorological stations to predict what the wind speed was at the farm site. This can be done by comparing the known data at the wind farm site with the same time period of data from the meteorological stations to produce an analytical relationship between the datasets. This relationship can be then used to predict the data to give a much longer WSTS (in some cases decades). This would be an interesting extension but has not been implemented here.

To summarise, wind speeds from a meteorological mast at the Egmond aan Zee wind farm were used. This wind speed had to be derived from the raw SCADA data and cleaned to produce a complete dataset. The derived mean wind speed data was taken at 10 minute intervals at 70m above sea level for the year 01/07/2005 to 30/06/2006.

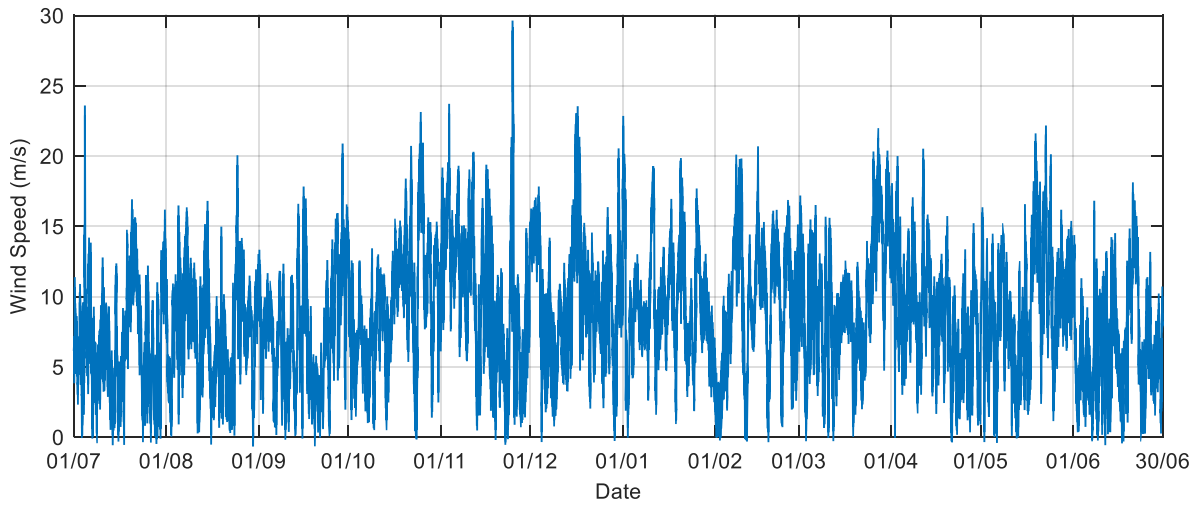

Figure 2: Cleaned derived 10-minute average wind speed data at 70m height used as the benchmark WSTS.

b. Desirable Criteria for Synthetic *WSTS*

To determine the suitability of synthetic WSTS for reliability analysis a list of criteria has been created for comparison with the benchmark WSTS. These criteria have been chosen as the results of any reliability analysis using synthetic WSTS will be sensitive to the accuracy of these parameters. The synthetic WSTS should replicate the benchmark data's:

1. Total energy availability in the wind resource.
2. Energy availability from a typical turbine.
3. Cumulative time at all wind speeds.
4. Number of transitions between wind speed states.
5. Longer term seasonal trends and occurrence of sustained low and high wind conditions.
6. The underlying statistical relationships, determined by the sample auto-correlation function (ACF), in the benchmark WSTS.

To make these criteria measurable the calculation for the benchmark and synthetic WSTS needed to be defined. Note the wind speed data was discretised into 1 m/s states.

1. To quantify energy availability in the wind, the expected power densities (*E(p)*) of benchmark and synthetic WSTS were computed (2). *E(p)* was used to remove any un-required information such as turbine size and turbine life span.

$$E(p) = \sum_{u=0}^{u_{max}} 0.5\rho u^3 F(u) \qquad (2)$$

   Where ρ is air density (kg/m^3), u is wind speed (m/s), u_{max} is the maximum wind speed (m/s) and $F(u)$ is the probability distribution function of the wind speeds.

2. The expected power from a typical turbine ($E(p_t)$) was computed similarly (3), but with limits to represent the turbine power curve (4).

$$E(p_t) = \sum_{u=0}^{u_{max}} 0.5 C_p \rho {u_t}^3 F(u) \qquad (3)$$

$$u_t = \begin{cases} 0, & u < u_{in} \\ u, & u_{in} \le u < u_{rated} \\ u_{rated}, & u_{rated} \le u < u_{out} \\ 0, & u \ge u_{out} \end{cases} \qquad (4)$$

   Where C_p is the coefficient of performance, u_t is the equivalent wind speed for a wind turbine (m/s), u_{in} is the cut-in wind speed (m/s), u_{rated} is the rated wind speed (m/s), and u_{out} is the cut-out wind speed (m/s).

   The turbine data is given in Table 3. In reality the C_p would vary to main the power extraction, rather than the wind speed itself changing, and would not be at the Betz limit.

Parameter	Value
ρ	1.225kg/m^3
C_p	0.593
u_{in}	4m/s
u_{rated}	13m/s
u_{out}	25m/s

Table 3: Wind and turbine parameters.

3. A plot was used to visually compare the cumulative time at all wind speeds between benchmark and synthetic WSTS.
4. The number of transitions between wind speed states for the benchmark and synthetic WSTS was recorded for comparison.
5. To assess the quality of replicating seasonal characteristics two tests were carried out. Firstly, the frequency spectrum of the synthetic WSTS was compared to the benchmark WSTS by using a Fourier Transform. In the spectrum, the frequencies for both WSTS should have similar amplitudes if the seasonal variation has been modelled successfully.
   The second test quantified the occurrence of weather windows. This was computed by calculating the percentage of time a maintenance team could be dispatched. The length of the weather window and the wind speed threshold is dependent on the maintenance type and the travel distance. For this work a wind speed threshold of 10m/s and a time of 48 hours was taken as a weather window, similar to those found for a jack-up vessel in [3].
6. To assess whether the underlying statistical properties of the wind speed were captured the ACF was computed for an exemplar synthetic WSTS for each modelling technique and the benchmark WSTS.

These 6 criteria produced 7 measurements to be used as a metric to assess synthetic WSTS quality. These characteristics and measurements are summarised in Table 4.

a. Synthetic WSTS Simulation

As discussed in Section III there are a number of WSTS simulators that have been used for synthesising WSTS. This section outlines the 4 modelling techniques that have been assessed, including one modified approach developed for this work.

Random sampling from probability distributions (PDF). The model used was developed in [20] and randomly samples from both Weibull and normal distributions to produce the WSTS. Figure 3 outlines this method.

WSTS Desirable Criteria	Measurement |Criterion No.|
Energy availability in the wind resource	Comparison of expected power density ($E(p)$) in wind |1|
Energy availability from a typical turbine	Comparison of expected power density ($E(pt)$) from a turbine |2|
Cumulative time at all wind speeds	Comparison of plotted time at each wind speed |3|
Number of transitions between wind speed states	Comparison of transitions between 1m/s wind speed bins |4|
Longer term seasonal trends and occurrence of sustained wind conditions	1. Comparison of Frequency spectrums from a Fourier transform |5| 2. Comparison of % of time a maintenance team could be dispatched (weather window); below 10m/s for 48 hrs |6|
Same underlying statistical relationships	Comparison of sample auto-correlation functions (ACF) |7|

Table 4: Summary of desirable criteria and corresponding measurement strategy.

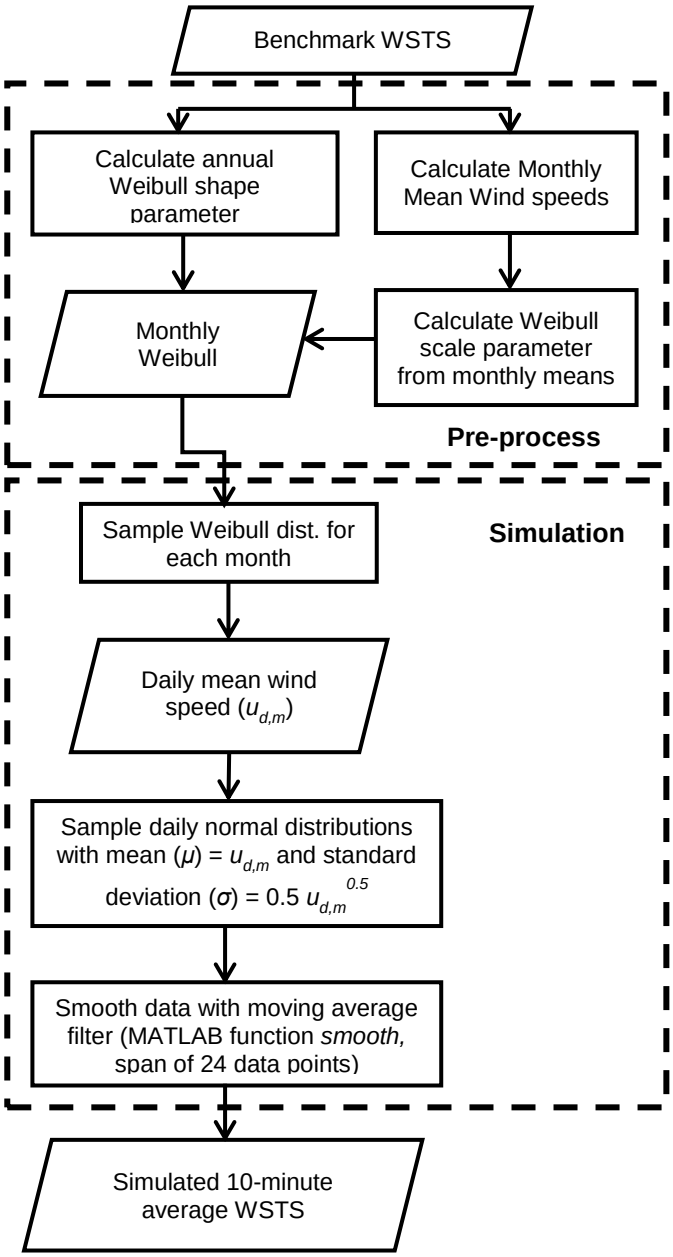

Figure 3: Flow diagram of PDF sampling model.

Continuous Markov Process: The Markov process uses the transitions between wind speeds in the original WSTS to dictate the transitions occurring in the synthetic WSTS. The next wind speed state is determined by the current state, and the shortest transition time from the current state (Figure 4).

A Markov process approach assumes that the system is memory-less; future random behaviour is dependent on the current state, and the process is stationary; the behaviour of the system is time independent. As such, the transition rates must be constant. The state residence times are assumed to follow an exponential distribution [26]. The transition rates are calculated using (4). The transitions times from the current state *i* to state *j* are calculated using (5).

$$\lambda_{ij} = \frac{N_{ij}}{T_i} \tag{4}$$

$$L_{ij} = \frac{h_{yr}}{\lambda_{ij}} \ln(R_j) \tag{5}$$

Where N_{ij} is the number of transitions between states *i* and *j*, T_j is the total time at state *i* (years), L_{ij} is the transition time (hours), h_{yr} is the number of hours in a year (8760), and R_j is a uniform random number between 0 and 1.

The Markov process model used is similar to that found in [15], with a number of variations:

- The initial state is determined by randomly sampling from a Weibull distribution.
- The input data is based on 10 minute average, rather than hourly average, wind speed data.

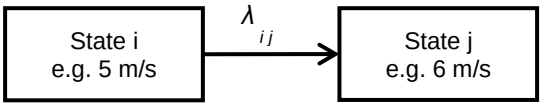

Figure 4: Schematic diagram of Markov process. λ_{ij} is the transition rate between states *i* and *j* (occurrences/year).

- Missing transition rates due to having a small dataset were filled using linear interpolation.
- Transitions can occur to any other state from the current state, unlike the birth-and-death model used in [15]. The next state is determined by the smallest transition time calculated (5) and states are represented by 1 m/s bins.
- The benchmark data was sampled at 10 minutes, so transitions times that are below 10 minutes are rejected. As a continuous process is used, transition times can be a non-integer multiple of 10 minutes to produce a continuous-time WSTS.

Modified Markov Process: This model uses the continuous Markov but consists of higher order processes that do not determine the output of the model, but do dictate which lower order states are available. In this paper the high order processes were used to produce periods of higher and lower sustained wind speeds. The process is outlined in Figure 5.

Auto-Regressive (AR(X)) model: An AR(X) model uses the weighted value of the previous X observations in a time series, alongside a randomly generated error term, to determine the next value in the series. In this case a simple third order model (AR(3)) was used. This model was used as follows:

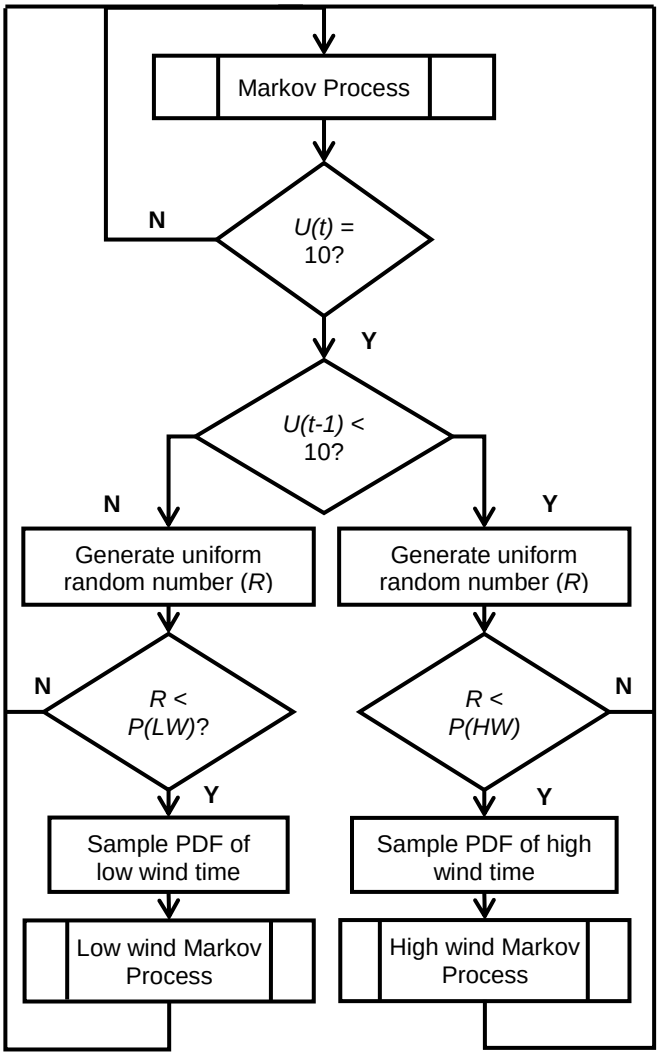

Figure 5: Flow Diagram of Modified Markov Model. *P(LW)* and *P(HW)* are the probabilities that a sustained period of low and high wind occurs respectively.

1. The mean of the benchmark WSTS was subtracted from each data point in the benchmark WSTS.
2. MATLAB's *ar* function was used to fit the AR(3) parameters.
3. The noise at each time step (*e(t)*) was calculated (6).

$$e(t) = \sigma_e R_n(t) \quad (6)$$

Where σ_e is the standard deviation of the noise from the *ar* fit and R_n is a normally distributed random number between 0 and 1.

4. The synthetic WSTS is generated using (7).

$$y(t) = a_1 y(t-1) + a_2 y(t-2) + a_3 y(t-3) + e(t) \quad (7)$$

Where *y* is the synthetic WSTS and $a_{1\text{-}3}$ are the AR coefficients. *y(1-3)* is taken from the benchmark WSTS.

Table 5 gives the values used for this AR(3) model.

Parameter	Value
σ_e	0.683m/s
a_1	0.8794
a_2	0.0047
a_3	0.1044

Table 5: Parameters for AR(3) model.

To summarise, four synthetic WSTS simulators have been modelled for comparison with the benchmark WSTS. They are a PDF model, a continuous Markov process, a modified Markov process to include weather windows, and an AR(3) model.

V. Results and Discussion

This section summarises the results. From Table 6 all models perform well against criterion 1 (within 3.2% of benchmark), with AR(3) performing marginally best (underestimated by 1.6%). There is slightly more variation in the results for criterion 2 (up to 3.8%), but this time the modified Markov performs best with the benchmark $E(p_t)$ falling within confidence bounds of the modified Markov result. From criteria 1 and 2 none of the models can be ruled out.

Results from criterion 3 (Figure 7) provide more insight. Both the Markov and modified Markov models replicate the mean bin times very accurately. This is to be expected as the models replicate the probability at being at each state in the calculation of λ_{ij}. Their slight overestimation for criteria 1 (2.8% and 1.9% respectively) and, to a lesser extent, 2 (1.3% and 0.3% respectively) may be due to the linear interpolation of λ_{ij} for higher wind speeds, increasing

Evaluation Criteria |Criterion No.|	Benchmark WSTS	PDF	Markov	Modified Markov	AR(3)
$E(p)$ (W/m^2) |1|	657.3	678.3 ±9.4	675.8 ± 6.9	669.6 ± 9.2	**646.9 ± 8.9**
$E(p_t)$ (W/m^2) |2|	510.9	491.6 ± 4.8	517.5 ± 3.8	**512.4 ± 5.4**	529.2 ± 5.5
Number of Wind Speed Transitions |4|	19378	4169 ± 18.0	11624 ± 26.9	**15838 ± 29.3**	26139 ± 32.0
Weather Window Opportunities (%) |6|	14.8	24.2 ± 0.6	4.5 ± 0.2	**13.5 ± 0.5**	6.8 ±0.3

Table 6: Results of evaluation. Best results are given in bold.

how regularly these wind speeds occur. As the energy available in the wind follows a cubic relationship, a very slight overestimation in residence times of higher wind speeds can have a noticeable impact in the results.

The PDF model performed worst for criteria 1 and 2, overestimating by 3.2% for criteria 1 and underestimating by 3.8% for criterion 2. This overestimation is due to high wind speeds increasing the $E(p)$, whilst the distribution skew to the left in the turbine operating region (Figure 7) causes the underestimation for criterion 2. The PDF also produces a different distribution to that of the benchmark WSTS, showing that the normal distribution was not a suitable estimation for the daily wind speed distribution.

The AR(3) model performs better than the PDF model against criterion 3 as it does not have the same skew to the left (Figure 7) and this is reflected in the better performance against criterion 1 and 2 (Table 6). The AR(3) model is poor at low wind speeds, with an overestimation of 0m/s bin time (Figure 7). This is not apparent in the criterion 1 and 2 results as the amount of energy is negligible in the low speed region. This overestimation may be due to the normally distributed noise variance assumption. Therefore examining the distribution of noise variance and modelling accordingly may provide a more accurate model.

None of the models accurately replicate the number of transitions in the wind speed (criterion 4, Table 1). The PDF model has only 21.5% of transitions due to the over-suppression of variation from the filter. The AR(3) model has 135% the number of transitions as the model works on a fixed time step basis with the wind speed value varying at nearly every step. The lower number of transitions for the Markov process is due to a skew towards longer transitions times from the rejection of time steps lower than 10 minutes. The discrepancy between that and the modified Markov is likely due to the elongated periods when the model is at higher wind speeds where the transition rates are much higher, causing shorter transition times than the normal Markov. This would highlight that, whilst the modified Markov performs best against criterion 4, the distribution of transitions across wind speeds needs further investigation to verify if this is desirable.

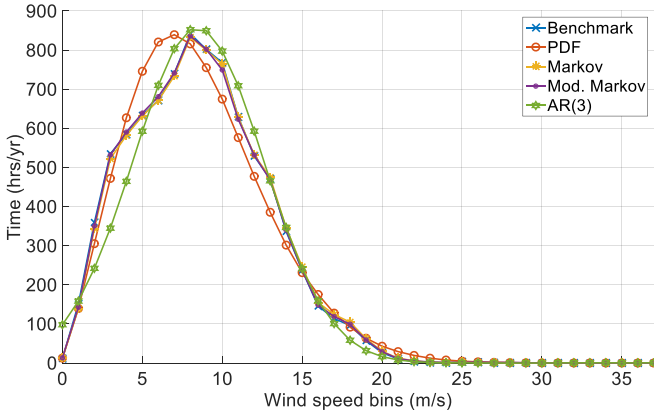

Figure 7: Wind speed mean residence times of benchmark and synthetic WSTS (criterion 3).

The modified Markov performs best against criterion 6 (Table 6). This would be expected as the model is deliberately set up to replicate weather windows, but this result verifies that it has performed this successfully. The Markov and AR(3) models do not capture these weather window opportunities, showing the need to explicitly model these windows. The PDF approach overestimates the amount of time available for maintenance by 63.5%, again due to the filter. This could have a significant impact on the results of any reliability analysis that considers weather windows.

Figure 6 reveals that the seasonality of the benchmark WSTS (represented by peaks at low frequencies) was not captured by the Markov process. The PDF model

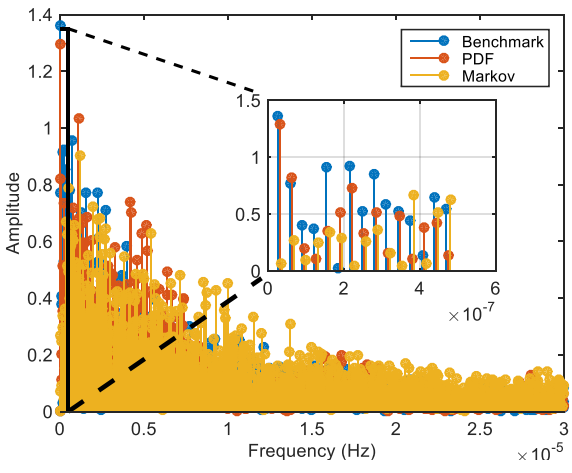

Figure 6: Frequency spectrum of benchmark and selected models. The arrow indicates 1 cycle/year.

used mean speeds for each month, and therefore replicated the high amplitudes at low frequencies of the benchmark WSTS with accuracy. The AR(3) and modified Markov results are not shown here as they perform almost identically to the Markov model results. Seasonality should be added to any WSTS simulator.

None of the models replicate the ACF of the benchmark WSTS (criterion 7, Figure 8). The AR(3) model is closest, which is expected as it uses the ACF to fit the model coefficients. This would indicate that a higher order AR model is required. The Markov and modified Markov perform the worst. This is because the Markov processes only using the previous time step to dictate the next state. Therefore a higher order AR model is likely to perform better against the ACF than any of the models represented here.

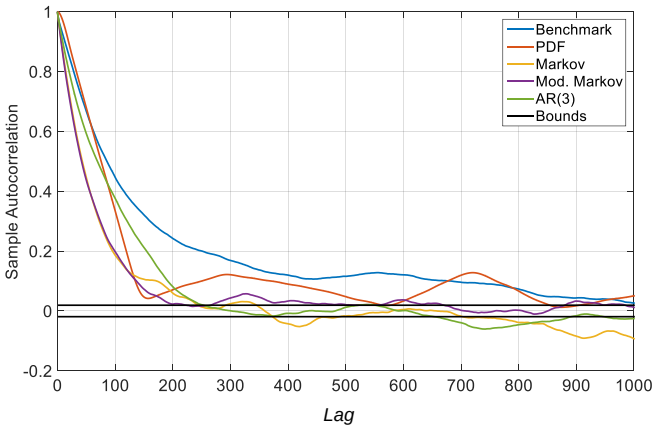

Figure 8: ACF of WSTS (criterion 7).

In summary:

- The AR(3) performed best for criterion 1 and 7, but performed poorly against criterion 3 and 6.
- The modified Markov performed best for criteria 2-4, and 6 though the result for criterion 4 needs further investigation. It performed poorly against criterion 7.
- Only the PDF model captured the seasonal variations (criterion 5).
- The PDF model performed the worst for all criteria other than criteria 5 and 7 and therefore is not suitable for this kind of reliability analysis without modification.

Arguably the wind speed residence times (criterion 3) and weather windows (criterion 5) are most important for reliability analysis as they dictate both the energy availability and maintenance opportunities, which are likely to have the highest impact on LCoE. Therefore, based on the analysis presented the most appropriate WSTS simulator is the modified Markov process.

However, no modelling technique performed best against all criteria and none captured the ACF as closely as desired. Therefore, there is scope for a more advanced technique for WSTS simulation for reliability analysis. Based on the results detailed, a combination of a more complex AR model for short term modelling and elements of the modified Markov process for short and long term weather conditions could prove the most appropriate modelling technique.

VI. Conclusion

This work has outlined 6 desirable criteria of synthetic WSTS for use in offshore wind farm reliability analysis, with 7 measures to quantify how well synthetic WSTS matched these criteria. These included considering the time spent at all wind speeds and opportunities for maintenance via weather windows. This evaluation criteria can be used to evaluate any WSTS simulators developed specifically for sequential reliability studies.

4 WSTS simulators were used and were compared with these criteria. These were based on models produced in previous reliability studies and a modified Markov model developed in this work. Based on the evaluation criteria the most appropriate WSTS simulator for reliability analysis was the modified Markov process. This is as it closely replicated a number of criteria including the weather window opportunities and the wind speed distribution.

No modelling technique performed against all criteria and none captured the ACF closely. Therefore there is scope for a more advanced technique. A combination of an AR model and elements of the modified Markov process could produce promising results.

References

[1]. E. Davey and A. Nimmo. *Offshore Wind Cost Reduction, Pathways Study*. 2012 [cited 2015 07/10]; Available from: http://www.thecrownestate.co.uk/energy-and-infrastructure/offshore-wind-energy/working-with-us/strategic-workstreams/cost-reduction-study/.

[2]. W. Musial and B. Ram. *Large-Scale Offshore Wind Power in the United States: Assessment of Opportunities and Barriers*. 2010 [cited 2015 07/10]; Available from: http://www.nrel.gov/docs/fy10osti/40745.pdf.

[3]. J. Dowell, et al., *Analysis of Wind and Wave Data to Assess Maintenance Access to Offshore Wind Farms* in *European Safety and Reliability Association Conference* 2013: Amsterdam.

[4]. M.A. Parker and O. Anaya-Lara, *Cost and losses associated with offshore wind farm collection networks which centralise the turbine power electronic converters.* IET Renewable Power Generation, 2013. **7**(4): p. 390-400.

[5]. D. Jovcic and N. Strachan, *Offshore wind farm with centralised power conversion and DC interconnection.* Generation, Transmission & Distribution, IET, 2009. **3**(6): p. 586-595.

[6]. A. Underbrink, et al. *Probabilistic Reliability Calculations for the Grid Connection of an Offshore Wind Farm*. in *International Conference on*

Probabilistic Methods Applied to Power Systems, 2006. 2006.
[7]. V. Gevorgian, M. Singh, and E. Muljadi. *Variable frequency operation of a HVDC-VSC interconnected type 1 offshore wind power plant*. in *2012 IEEE Power and Energy Society General Meeting*. 2012.
[8]. E. Spahic, et al. *Reliability model of large offshore wind farms*. in *2009 IEEE PowerTech* 2009. Bucharest.
[9]. C. Nemes and F. Munteanu. *Reliability consideration on wind farms energy production*. in *13th International Conference on Optimization of Electrical and Electronic Equipment (OPTIM)* 2012.
[10]. H. Arabian-Hoseynabadi, H. Oraee, and P.J. Tavner, *Wind turbine productivity considering electrical subassembly reliability.* Renewable Energy, 2010. **35**(1): p. 190-197.
[11]. K. Xie, Z. Jiang, and W. Li, *Effect of Wind Speed on Wind Turbine Power Converter Reliability.* IEEE Transactions on Energy Conversion, 2012. **27**(1): p. 96-104.
[12]. M. de Prada Gil, et al., *Analysis of a multi turbine offshore wind farm connected to a single large power converter operated with variable frequency.* Energy, 2011. **36**(5): p. 3272-3281.
[13]. M. de Prada Gil, et al., *Power generation efficiency analysis of offshore wind farms connected to a SLPC (single large power converter) operated with variable frequencies considering wake effects.* Energy, 2012. **37**(1): p. 455-468.
[14]. D.W. Elliott, S.J. Finney, and C. Booth. *Single converter interface for a cluster of offshore wind turbines*. in *IET Conference on Renewable Power Generation (RPG 2011)*. 2011. Edinburgh.
[15]. N.B. Negra, et al., *Aspects of Relevance in Offshore Wind Farm Reliability Assessment.* IEEE Transactions on Energy Conversion, 2007. **22**(1): p. 159-166.
[16]. R. Billinton, H. Chen, and R. Ghajar, *Time-series models for reliability evaluation of power systems including wind energy.* Microelectronics Reliability, 1996. **36**(9): p. 1253-1261.
[17]. R. Billinton, Y. Gao, and R. Karki, *Composite system adequacy assessment incorporating large-scale wind energy conversion systems considering wind speed correlation.* Power Systems, IEEE Transactions on, 2009. **24**(3): p. 1375-1382.
[18]. R. Billinton and R. Karki, *Incorporating wind power in generating system reliability evaluation.* International Journal of Systems Assurance Engineering and Management, 2010. **1**(2): p. 120-128.
[19]. Ofgem. *Electricity Capacity Assessment Report 2014*. 2014 [cited 2015 07/10]; Available from: https://www.ofgem.gov.uk/ofgem-publications/88523/electricitycapacityassessment2014-fullreportfinalforpublication.pdf.
[20]. B. Kazemtabrizi, C. Crabtree, and S. Hogg, *Reliability Evaluation of New Offshore Wind Farm Electrical Grid Connection Topologies*, in *ASME Turbo Expo 2013: Turbine Technical Conference and Exposition* 2013: Texas, USA. p. 1-10.
[21]. F. Castro Sayas and R.N. Allan, *Generation availability assessment of wind farms.* IEE Proceedings-Generation, Transmission and Distribution, 1996. **143**(5): p. 507-518.
[22]. Noordzeewind. *Noordzeewind: Reports & Data*. 2014 [cited 2015 07/10]; Available from: http://www.noordzeewind.nl/en/knowledge/reportsdata/.
[23]. S. Barth and P. Eecen. *Description of the relation of wind, wave and current characteristics*. 2007 [cited 2015 07/10]; Available from: http://www.noordzeewind.nl/wp-content/uploads/2012/02/OWEZ_R_122_Wave_2006_20080409.pdf.
[24]. A. Curvers. *Surrounding obstacles influencing the owez meteo mast measurements.* 2007 [cited 2015 07/10]; Available from: http://www.noordzeewind.nl/wp-content/uploads/2012/02/OWEZ_R_181_T0_20070821_undisturbed_wind.pdf.
[25]. P. Eecen, L. Machielse, and A. Curvers. *Meteorological Measurements OWEZ Half year report 01-01-2006 - 30-06-2006* 2007; Available from: http://www.noordzeewind.nl/wp-content/uploads/2012/02/OWEZ_R_121_20060101-20060630_wind_resource_2006_1.pdf.
[26]. R. Billinton and R.N. Allan, *Reliability evaluation of engineering systems*. 1983: Plenum press New York.

Appendix B

Drive Train Model Parameters

B.1 Drive Train Parameter Table

Table B.1: Drive train parameter values

Parameter	Value	Reference	Parameter	Value	Reference
A_t	0.22	[108]	B_t	116	[108]
C_t	0.4	[108]	D_t	0	[108]
E_t	0	[108]	F_t	5	[108]
G_t	12.5	[108]	H_t	0.08	[108]
K_t	0.035	[108]	$P_{t,rat}$	2.0MW	[111]
$\omega_{t,r}$	22.5rpm	[111]	λ_{opt}	6.3	Note 1
$C_{p,max}$	0.4832	Note 1	$C_{p,betz}$	0.593	[33]
u_{rat}	12.7m/s	Note 1	r	34m	Note 1
ρ	1.225kg/m^3	[33]	J_t	2.92×10^6kg/m^2	[112]
J_g	200kg/m^2	[113]	K	4.0×10^7Nm/rad	[112]
C_d	6.72×10^6Nms/rad	Note 2	p	52	[111]
ϕ	8.24Vs$_{(\text{peak})}$	[111]	r_s	0.821mΩ	[111]
L_d	1.5731mH	[111]	L_q	1.5731mH	[111]
V_f	0.95V	[116]	$V_{f,d}$	0.95V	[116]
T_f	0s	Note 3	T_t	0s	Note 3
R_{on}	1.2mΩ	[116]	V_{DC}	1150V	Sec. 3.2.5

Continued on next page

Table B.1 – *Continued from previous page*

Parameter	Value	Reference	Parameter	Value	Reference
R_{snub}	$1{\times}10^5\Omega$	[117]	C_{snub}	∞F	[117]
$R_{c/r}$	200	Note 4	β_{max}	45°	[123]*
β_{min}	45°	[123]	$\beta_{rate,max}$	8°/s	[123]*
$\beta_{rate,min}$	-8°/s	[123]*	τ	0.5s	[124]
P_p	3.357	Sec. 3.2.8	I_p	0.012	Sec. 3.2.8
P_{id}	-0.148	Sec. 3.2.8	I_{id}	-5.377	Sec. 3.2.8
P_{iq}	-0.155	Sec. 3.2.8	I_{iq}	-2.689	Sec. 3.2.8
β_{samp}	0.00125s	[123]*	β_{quant}	0.01	[123]*
ω_{samp}	0.00125s	[123]*	ω_{quant}	0.001	[123]*
I_{samp}	0.00125s	[123]*	I_{quant}	0.01	[123]*
T_s	$5{\times}10^{-6}$s	-	$\omega_{t,max}$	2.43rad/s	Sec. 3.2.6
τ_ω	0.01s	[123]*	f_{sw}	2kHz	[115]
f_{rat}	9.75Hz	[111]	$V_{l,rat}$	$690\text{V}_{(\text{rms})}$	[111]
I_{rat}	$1867.76\text{A}_{(\text{rms})}$	[111]	T_{rat}	848.826kNm	[111]
f_{sw}	2kHz	[115]	$R_{th,c,i}(1)$	1.5×10^{-3}K/W	-
$R_{th,c,i}(2)$	7.3×10^{-3}K/W	-	$R_{th,c,i}(3)$	5.9×10^{-3}K/W	-
$R_{th,c,i}(4)$	2.5×10^{-3}K/W	-	$R_{th,c,i}(5)$	0.37×10^{-3}K/W	-
$C_{th,c,i}(1)$	0.55Ws/K	-	$C_{th,c,i}(2)$	3.61Ws/K	-
$C_{th,c,i}(3)$	35.90Ws/K	-	$C_{th,c,i}(4)$	476.61Ws/K	-
$C_{th,c,i}(5)$	$4.81{\times}10^3$Ws/K	-	$R_{th,c,d}(1)$	2.8×10^{-3}K/W	-
$R_{th,c,d}(2)$	10.2×10^{-3}K/W	-	$R_{th,c,d}(3)$	10.5×10^{-3}K/W	-
$R_{th,c,d}(4)$	11.9×10^{-3}K/W	-	$R_{th,c,d}(5)$	8.6×10^{-3}K/W	-
$R_{th,c,d}(6)$	0.94×10^{-3}K/W	-	$C_{th,c,d}(1)$	0.773Ws/K	-
$C_{th,c,d}(2)$	1.45Ws/K	-	$C_{th,c,d}(3)$	4.90Ws/K	-
$C_{th,c,d}(4)$	36.07Ws/K	-	$C_{th,c,d}(5)$	577.76Ws/K	-
$C_{th,c,d}(6)$	1.60×10^4Ws/K	-	$R_{th,c,h}(1)$	0.79×10^{-3}K/W	-
$R_{th,c,h}(2)$	3.1×10^{-3}K/W	-	$R_{th,c,h}(3)$	4.3×10^{-3}K/W	-
$R_{th,c,h}(4)$	0.88×10^{-3}K/W	-	$R_{th,c,h}(5)$	0.14×10^{-3}K/W	-

Continued on next page

Table B.1 – *Continued from previous page*

Parameter	Value	Reference	Parameter	Value	Reference
$C_{th,c,h}(1)$	337.28Ws/K	-	$C_{th,c,h}(2)$	409.76Ws/K	-
$C_{th,c,h}(3)$	$1.37\times^{3}$Ws/K	-	$C_{th,c,h}(4)$	$1.91\times^{4}$Ws/K	-
$C_{th,c,h}(5)$	$1.30\times^{4}$Ws/K	-	$T_{j,ref}$	125°C	-
TC_{Esw}	0.003	[105]	TC_{Err}	0.006	[105]

*The values are not found in this paper, but are related to the model detailed here.

V_f is the IGBT forward voltage, V_{fd} is the diode forward voltage, $T_{f,t}$ is the IGBT fall time and tail time respectively, R_{on} is the IGBT on state slope resistance, R_{snub} is the snubber resistance, is the snubber capacitance, $P_{p,id,iq}$ are the proportional gains for the pitch, I_d and I_q controllers respectively, and $I_{p,id,iq}$ are the integral gains for the pitch, I_d and I_q controllers respectively, f_{rat} is the turbine rated frequency, $V_{l,rat}$ is the rated line voltage, I_{rat} is the rated current, T_{rat} is the rated torque and ${}_s amp$ indicates a sampling period.

B.2 Notes

B.2.1 Note 1

The $C_p - \lambda$ curve (3.2) uses values from a generic turbine rotor design and therefore did not have corresponding r and u_r values for a 2MW turbine. These were therefore calculated with λ_{opt} and ω_t values given in Table B.1 to provide a ratio between r and u_r in (3.5). This ratio was then used in (3.1) to calculate the required values to prove a 2MW turbine with the given C_p, max.

B.2.2 Note 2

No C_d value could be found for a 2 mass model, direct drive PMSG wind turbine. Therefore, an equivalent 1.5MW turbine's drive train parameters [124] were used to produce a damping ratio (ζ) using (B.1).

$$\zeta = \frac{C_d}{2\sqrt{J_t K}} = \frac{14 \times 10^6}{2\sqrt{6.1 \times 10^6 \times 83 \times 10^6}} = 0.311 \tag{B.1}$$

This ζ value was then used with the 2MW turbine parameters (Table B.1) to derive the estimated C_d.

B.2.3 Note 3

T_t and T_f are given values in the datasheet [116]. However, these times were lower than the sampling rate used for the simulation and therefore the values were reduced to 0s.

B.2.4 Note 4

$R_{c/r}$ is chosen to ensure that f_{sw} is maximum ($f_{sw,m}$) at maximum generator frequency ($f_{g,m}$). $f_{g,m}$ was estimated as 10Hz and therefore $R_{c/r}$ was calculated using (B.2).

$$R_{c/r} = \frac{f_{sw,m}}{f_{g,m}} \tag{B.2}$$